UNDERSTANDING THE STRUCTURAL, ELECTRONIC AND OPTICAL PROPERTIES OF TECHNOLOGICALLY RELEVANT MATERIALS FROM FIRST-PRINCIPLE CALCULATIONS

THESIS

SUBMITTED TO

JADAVPUR UNIVERSITY

FOR THE DEGREE OF

DOCTOR OF PHILOSOPHY

(SCIENCE)

BY

SWARUP GHOSH

DEPARTMENT OF PHYSICS

JADAVPUR UNIVERSITY

KOLKATA, INDIA

2024

CERTIFICATE FROM THE SUPERVISOR(S)

This is to certify that the thesis entitled "**Understanding the Structural, Electronic and Optical Properties of Technologically Relevant Materials from First-Principle Calculations**" submitted by Sri **Swarup Ghosh** who got his name registered on **6th November 2019** for the award of Ph.D (Science) degree of Jadavpur University, is absolutely based upon his own work under the supervision of **Prof. (Dr.) Joydeep Chowdhury** and that neither this thesis nor any part of it has been submitted for either any degree / diploma or any other academic award anywhere before.

Chowdhury 19/06/2024

Signature of the supervisor(s) with the date and official seal

Prof. Joydeep Chowdhury
Professor
Department of Physics
Jadavpur University
Kolkata - 700 032

To My Family Friends and Teachers

Abstract

First-principle calculations within the framework of density functional theory (DFT) are considered as one of the most advanced computational methods in quantum mechanics to address the microscopic properties of many body systems in finer detail. The entire research work in this dissertation is primarily focused on understanding the structural, electronic and optical properties of technologically relevant materials using first-principle calculations. In the early phase of research, technologically relevant material Mercurous Chloride (Hg_2Cl_2) is considered as a reference compound and its structural, electronic and optoelectronic properties have been studied in detail from first-principle calculations. The electronic band gap of the Hg_2Cl_2 compound has been estimated from the DFT calculations upon inclusion of different hybrid and non-hybrid exchange-correlation functionals and on-site Coulomb repulsion term. Detailed investigations show that the Hg_2Cl_2 system is a wide band gap charge transfer insulator. The Mulliken bond population, electronic charge density distribution and Bader charges analyses have been performed to unveil the covalent and ionic interactions between Hg and Cl atoms of Hg_2Cl_2. The Natural Bond Orbital analyses have been studied to gain deeper insights into the charge transfer interactions between Hg and Cl atoms of the Hg_2Cl_2 compound. The pressure-driven structural phase transitions from the body–centred tetragonal to base–centred orthorhombic and from the base–centred orthorhombic to primitive orthorhombic phases of the same compound have been explored from first-principle DFT and Born – Oppenheimer molecular dynamics (BOMD) calculations. The key phonon modes behind these phase transitions and the nature of structural phase transitions have been unveiled. The electronic and optoelectronic properties of the Hg_2Cl_2 system in its various phases have also been explored. Modulations of electronic band gaps and optoelectronic parameters such as complex dielectric functions, absorption coefficients, optical conductivities, refractive indices of the system have been critically unveiled under external pressure. Temperature-induced structural phase transition and negative thermal expansion behaviour of the Hg_2Cl_2 compound have been further studied from DFT and BOMD calculations. The key phonon modes responsible for the body–centred tetragonal to base–centred orthorhombic phase transition and negative thermal expansion of the compound have been investigated. Recently, the band gaps of nitride perovskites with general formula ABN_3 (“A” and “B” are cationic elements) have been predicted from machine learning models and DFT calculations. Four machine learning models such as multi-layer perceptron, gradient boosted decision tree,

support vector regression and random forest regression have been considered to predict the band gaps of the nitride perovskite compounds. The band gaps of two nitride perovskites $CeMoN_3$ and $CeWN_3$ have been further predicted from DFT calculations as well as machine learning methods. The entire study is expected to provide a wealth of information in understanding the structural, electronic and optical properties of technologically relevant materials from first-principle calculations.

The aforementioned research work has been framed in the form of a thesis entitled "**Understanding the Structural, Electronic and Optical Properties of Technologically Relevant Materials from First-Principle Calculations**" under Registration No: SOPHY1112119 (Dated: 06/11/2019) and **Index No: 121/19/Phys./26** for the award of Ph.D (Science) degree at Jadavpur University, Kolkata, India. The work was done under the guidance of Prof. (Dr.) Joydeep Chowdhury, at the Department of Physics, Jadavpur University. This thesis is a presentation of the original research work. All the results incorporated in the thesis have been published in different peer-reviewed journals of international repute. The list of publications with the reprints of the published papers that are included in the thesis and the list of papers presented in the international and/ or national conferences/ seminars have been incorporated into the thesis. Moreover, wherever contributions of others are involved, every effort is made to indicate this clearly, with due reference to the literature, and acknowledgement of collaborative research and discussions.

Swarup Ghosh

Acknowledgements

First and foremost, I would like to thank my supervisor Prof.(Dr.) Joydeep Chowdhury for all his guidance and support. I have benefited enormously from his enthusiastic supervision. I am very grateful to my collaborators Prof. Surojit Pande, Prof. Md Mohi Uddin and Prof. Sougata Sarkar for the science I have learnt from them. It is a pleasure to acknowledge the Vice-Chancellor, Pro-Vice-Chancellor, Registrar, Dean – Faculty Council of Science and Principal Secretary – Faculty Council of Science at Jadavpur University for their administrative guidance and support. A special thanks goes to Dr. Dirtha Sanyal for his guidance during the research advisory committee meetings. I sincerely acknowledge the Head of the Department of Physics, Jadavpur University and other faculty members of the Physics Department, Jadavpur University for their scientific guidance and support. I would also like to thank the non-teaching staff members of the Physics Department, Research Section and Faculty Council of Science for their support.

I am extremely thankful to the National Supercomputing Mission 'PARAM Kamrupa', Bioinformatics Resources and Applications Facility 'C-DAC' and DST-FIST for providing computing resources. I also acknowledge the University Grants Commission (UGC), Government of India for providing financial support in the form of NET-JRF fellowship.

I would like to thank my seniors and colleagues Dr. Rina De, Dr. Subhendu Chandra, Dr. Snehasish Bhattacharjee, Dr. Sourav Banik, Dr. Bipan Dutta, Dr. Sannak Dutta Roy, Dr. Somsubhra Saha, Dr. Saumen Saha, Dr. Sumit Kumar Das, Dr. Divya Rathore, Ms. Rati Ray Banik, Mr. Rajdeep Sinha, Mrs. Sutapa Baitalik, Mr. Sk Firoj Haque, Mr. Priyabrata Maity, Ms. Ritu Sarkar, Ms. Trisita Das, Ms. Shanwli Mallick and Mr. Chayan Kumar Mitra not only for the physics discussion I had with them but also for their support, encouragements and cheerful presence.

Most importantly, nothing would have been possible without the support and love I got from my family. I sincerely thank my parents and sister who have always been a source of great inspiration. Finally, this journey would not have been possible without the love and support of my best friend Rati and her parents.

List of Publications

List of publications included in the thesis (In ascending order of year):

1. **Swarup Ghosh**, Joydeep Chowdhury, **Pressure induced structural phase transitions of technologically significant mercurous chloride at room temperature: An account from first-principle DFT and Born–Oppenheimer molecular dynamics studies**, *Journal of Applied Phys*ics, **130**, 225103, (2021).

2. **Swarup Ghosh**, Sougata Sarkar, Joydeep Chowdhury, **Structural and electronic properties of wide band gap charge transfer insulator Hg_2Cl_2: Insights from the first-principle calculations**, *Materials Chemistry and Physics*, **276**, 125379, (2022).

3. **Swarup Ghosh**, Joydeep Chowdhury, **Pressure induced modulations in the optoelectronic properties of Hg_2Cl_2 compound: Insights from the first-principle calculations**, *Materials Science and Engineering B.*, **284**, 115903, (2022).

4. **Swarup Ghosh**, Joydeep Chowdhury, **Temperature dependent phase transition and negative thermal expansion of Hg_2Cl_2 compound: insights from first-principle DFT and Born-Oppenheimer on the fly molecular dynamics calculations**, *Phase Transitions*, **96**, 446-463, (2023).

5. **Swarup Ghosh**, Joydeep Chowdhury, **Predicting band gaps of ABN_3 perovskites: an account from machine learning and first-principle DFT studies**, *RSC Advances*, **14**, 6385-6397, (2024).

List of Publications not included in the thesis (In descending order of year):

1. M. Biswas, **Swarup Ghosh**, J. Chowdhury, M.A. Ali, M.M. Hossain, S.H. Naqib, M.M. Uddin, **An inclusive study of lead-free perovskite $CsMI_3$ materials for photovoltaic and optoelectronic appliance explored by a first principles study**, *Materials Today Communications*, **40**, 109422, (2024).
2. Divya Rathore, **Swarup Ghosh**, Astha Gupta, Joydeep Chowdhury, Surojit Pande, **Ce-Doped NiSe Nanosheets on Carbon Cloth for Electrochemical Water-Splitting**, *ACS Applied Nano Materials*, **7**, 9730–9744, (2024).
3. Rati Ray Banik, **Swarup Ghosh**, Joydeep Chowdhury, **Strain Induced Modulations in the Thermoelectric Properties of 2D SiH and GeH Monolayers: Insights from First-Principle Calculations**, *Journal of Physics: Condensed Matter*, **36**, 255706, (2024).
4. M.H. Kabir, M.Z. Hossain, M.A. Jalil, **Swaup Ghosh**, M.M. Hossain, M.A. Ali, M.U. Kh andake, D. Jana, M.M. Rahman, M.K. Hossain, J. Chowdhury, Mohsin Kazi, M.M. Uddin, **The efficacy of rare-earth doped V_2O_5 photocatalyst for removal of pollutants from industrial wastewater**, *Optical Materials*, **147**, 114724, (2024).
5. **Swarup Ghosh**, Joydeep Chowdhury, **Identifying Rashba–Dresselhaus splittings from first-principle calculations: A brief overview**, *Modern Physics Letters B*, **38**, 2330003, (2023).
6. Rati Ray Banik, **Swarup Ghosh**, Joydeep Chowdhury, **Pressure Driven Structural Phase Transitions and Modulations in Optical Properties of Lanthanum Nitride: An Account from On The Fly Molecular Dynamics and SCF vis-à-vis Non-SCF First-Principle Calculations**, *Physics Scripta*, **98**, 105914, (2023).
7. Rati Ray Banik, **Swarup Ghosh**, Joydeep Chowdhury, **Ultralow lattice thermal conductivity, negative thermal expansion, elastic and thermoelectric properties of Lanthanum Nitride: Insights from first-principle calculations**, *Physics Scripta*, **98**, 045920, (2023).
8. Divya Rathore, **Swarup Ghosh**, Joydeep Chowdhury, Surojit Pande, **Fe-Doped $NiCo_2Se_4$ Nanorod Arrays as Electrocatalysts for Overall Electrochemical Water Splitting**, *ACS Applied Nano Materials*, **6**, 3095-3110, (2023).
9. Divya Rathore, **Swarup Ghosh**, Joydeep Chowdhury, Surojit Pande, **Co-Doped Ni_9S_8 Nanostructures for Electrocatalytic Water Splitting over a Wide pH Range**, *ACS Applied Nano Materials*, **5**, 11823-11838, (2022).
10. **Swarup Ghosh**, Rati Ray Banik, Joydeep Chowdhury, **Understanding the Strongly Correlated Systems from Theoretical Perspectives: A Brief Review**, *Indian Journal of Theoretical Physics*, **69**, 43, (2021).

Contents

Page No.

Chapter 1

Introduction

1.1. Overview

"Materials" in general refer to substances that can be used in technology and medicine for the welfare of mankind. It encompasses a wide range of substances, including natural resources like wood, metal ores, and minerals, as well as synthetic materials like plastics, ceramics, and composites. Materials are essential in the manufacturing and construction industries, as they govern the properties, strength, durability, and appearance of products and structures. Advances in material science have led to the development of new materials with unique properties, enabling innovations in various fields such as aerospace, electronics, medicine, and renewable energy. From the early age of human civilization, the characterizations and use of different materials became one of the most important parts of the sustenance of living. Interestingly, the use of materials belongs to three separate periods in the historical timeline which include Stone, Bronze, and Iron Ages [1-3]. Stone Age is marked to have lasted around 3.4 million years and ended between 4000 BCE and 2000 BCE. This age was significant for the use of different tools that had sharp points, chiselled edges, and percussion surfaces and are now being recognized to have ended with the emergence of metals [4,5]. The Stone Age can further be divided into three distinct periods such as the most primitive Paleolithic era, a transitional period with finer tools reckoned as the Mesolithic era, and the final stage known as the Neolithic era. In the Neolithic era, agriculture became an important part of the lifestyle and thus the first transition from hunter-gatherer societies to the settled lifestyle of inhabiting towns and villages was observed. At the end of the Neolithic era, the use of copper was considered as the commencement of the Bronze Age. The Bronze Age spanned around 3300 BCE to 1200 BCE, where the extensive use of copper, and gold mostly for ornamentation, and bronze in proto-writing were noted [6,7]. The remarkable use of bronze is significant from the scientific point of view as well because it is not a pure metal, instead an alloy containing primarily copper and around 12% tin together with other metals (ca. Al, Mg, Ni, Zn) and sometimes metalloids like arsenic or silicon, or non-metals such as phosphorous. The practice of copper, gold, and bronze thus led to the development of early urban civilization at the later stage of the Bronze Age. Moreover, the people in the pre-historic era not only knew how to prepare alloys but were quite aware of using them in printing and state-of-the-art tools for household/ hunting applications. Iron age, which is recognized as the final epoch of the three historical metal ages, were started around 15^{th} century BCE and continued approximately till the 3^{rd} century BCE, where iron workings were explicitly practiced, the most prominent example being the Painted Grey Ware culture of India and Nok culture of Nigeria [8-12].

Since then, with the advancement of science the world has beheld different techniques for the extractions, characterizations and applications of fascinating materials that find wide range of applications in technology and medicine. However, understanding the structural, electronic and optical properties of materials were far from analytical consequences until the development of faster computations [13-23]. With the development of quantum mechanics along with the advancement of modern computational facilities and techniques, the "many-body theory" that can address the microscopic properties of materials in finer detail has experienced a paradigm shift in the offing of materials sciences, condensed matter and chemical physics.

1.2. Many-body theory

Materials on a quantum scale are polyatomic systems consisting of large number of interacting atoms. The physics of understanding the collective behaviour of such a large number of interacting atoms is designated as "many-body theory" in material sciences. A year after the discovery of the Schrödinger equation in 1926 [24], a comprehensive Hamiltonian of the many-body systems was framed and the general Hamiltonian for "N" nuclei and "n" electron systems is mathematically represented as

$$H = -\sum_{i=1}^{n}\frac{\hbar^2}{2m}\nabla_{\boldsymbol{r}_i}^2 - \frac{e^2}{4\pi\varepsilon_0}\sum_{I=1}^{N}\frac{Z_I}{|\boldsymbol{r}_i-\boldsymbol{R}_I|} + \frac{e^2}{2}\sum_{i\neq j}\frac{1}{|\boldsymbol{r}_i-\boldsymbol{r}_j|} - \sum_{I=1}^{N}\frac{h^2}{2M_I}\nabla_{\boldsymbol{R}_I}^2 + \frac{1}{2}\sum_{I\neq J}\frac{Z_I Z_J e^2}{|\boldsymbol{R}_I-\boldsymbol{R}_J|} \qquad (1.1)$$

where r_i and R_I represent the position of electron i and nucleus I with charge $-e$ and $Z_I e$ respectively of the system. The first term in the Hamiltonian is the kinetic energy associated with the "n" electrons, the second term is the attractive Coulomb potential generated from the contribution of "N" nuclei and "n" electrons of the system, the third term signifies the repulsion between electron-electron interactions, the fourth and the final terms are the respective kinetic energy and the attractive potential of the "N" nuclei of the many-body system.

However, the nucleus in an atom is ~ 1830 times heavier than the electron, so in practice, the electrons are considered to be moving in a fixed nuclear frame at a given instant of time. This approximation is known as the Born-Oppenheimer (BO) approximation [25] and under such approximation, the general Hamiltonian for "n" electron systems is expressed as

$$\hat{H} = -\sum_{i=1}^{n}\frac{\hbar^2}{2m}\nabla_{\boldsymbol{r}_i}^2 - \frac{e^2}{4\pi\varepsilon_0}\sum_{I=1}^{N}\frac{Z_I}{|\boldsymbol{r}_i-\boldsymbol{R}_I|} + \frac{e^2}{2}\sum_{i\neq j}\frac{1}{|\boldsymbol{r}_i-\boldsymbol{r}_j|} \qquad (1.2)$$

One of the major challenges in the formalism of many-body theory over the past two decades has been the correct interpretation of structural, chemical and physical (ca. electronic, optical, magnetic, transport) properties of many-body systems. The physical properties of electrons in a many-body system were tried to explain from the assumptions of independent particle approximation. This is particularly successful when one deals with broad energy bands, associated with a large value of the kinetic energy. In such cases, the valence electrons are considered to be highly itinerant and are almost delocalised over the entire solid. The typical time spent of valence electrons near a specific atom in the crystal lattice is very short. In such a scenario, the valence electrons are well described using a wave-like picture, in which individual wavefunction can be calculated from an effective one-electron periodic potential.

Two years later, in 1929, British physicist Paul Dirac emphasized the inherent difficulties in solving the Schrödinger equation for complex many-body systems [26]. The many-body Hamiltonian is hard to solve due to the existence of third term in equation (1.1) or (1.2), i.e. the electron-electron interactions. To address the issue of electron-electron correlations in the above referred Hamiltonian, several single-particle approximations in the form of first-principle calculations have been introduced to understand the physics of many-body systems [27]. In this context, the mean-field theory (MFT) [28,29], as reported by Hartree based on the self-consistent field approach, was the first prominent approach to solve the modified Hamiltonian as framed in equation (1.2) [30]. According to MFT, each electron is subjected to move in an average or mean-field created by all other electrons in an atom. The MFT takes into account the electron-electron correlation term in the Hamiltonian and the associated Schrödinger equations are then solved utilizing an iterative method. Though Hartree's theory is successful in predicting the electronic properties of some molecules and solids, however, it does not take into the anti-symmetric nature of electronic wave functions. Later, with the independent insights from Slater [31,32] and Fock [33], Hartree reformulated his theory as Hartree-Fock theory by incorporating the anti-symmetric nature of the electronic wave functions as the electronic exchange term [34]. While Hartree-Fock theory is moderately successful in predicting the electronic structures of molecules and solids, the major drawback of this theory is the neglect of electron correlations for the electrons of opposite spins. Moreover, the Hartree-Fock theory fails to describe the magnetic properties of materials accompanying with the transition metals like Fe, Pt, Pd, Mn, Cu, Ni etc. and their respective electronic properties [35-42].

An alternative approach to solve the many-body Hamiltonian is the density functional theory (DFT) which takes into account the electron correlation explicitly. The semi-classical approach of DFT was initially suggested by Thomas and Fermi (TF) [43,44]. This theory included the oversimplified electron-electron interactions classically and thus their theoretical predictions in most cases are far from experimental results. The modification of the TF model was proposed by Hohenberg, Kohn and Sham [45,46]. This DFT method uses local density approximation (LDA) and generalized gradient approximation (GGA) to address the electron correlations which is proven to be successful in predicting the electronic band structures as well as the ground state properties of some significant materials such as NaX (X = F, Cl), SiO_2, Al, B_2O_3, boron nitride (BN), LiX (X= F, Cl, Br and I) etc. [47-51] in harmony with the experimental observations.

Surprisingly, for system having transition metal (TM) and/ or heavy fermion (HF) elements, the conventional DFT approach struggles to reproduce any meaningful results and fails to explain the experimentally observed insulating behaviours of such materials. While the typical DFT suggests the metallic properties of TM compounds and HF systems, in reality they turn out to be insulators [17,52-57]. The apparent disagreement between the theoretical predictions and experimental observations for these classes of materials stems from their strong electron correlations linked with partially occupied “d” and “f” electronic orbitals.

1.3. Strongly correlated systems

Systems containing TM and/ or HF elements, the valence electrons of those compounds are found to spend larger time around a given atom in the crystal lattice and hence have tendency towards localization. In such case, the effects of statistical correlations between the motions of electrons become important. In this regard, the particle-like picture may in fact be more appropriate than a wave-like one over those time scales, involving wavefunctions localized around specific atomic sites. Materials in which electronic correlations are significant are generally associated with narrow energy bands and moderate values of the bandwidth. The small kinetic energy of valence electron implies a longer time spent on a given atomic site. It also implies that the ratio of the on-site Coulomb repulsion (U) between electrons and the available kinetic energy (W) becomes larger. As a result, delocalising the valence electrons over the whole solid may become less favourable energetically, and therefore the corresponding electrons are found to remain localised. In a simplified picture, the wavefunctions for the “d” or “f” orbitals of the TM compounds or rare-earth/ actinide elements

are localized more closely to the nucleus in comparison to the wavefunctions associated with the "s" or "p" orbitals of similar energies. Thus the relative motions of the "d" or "f" electrons are statistically more correlated than for the electrons residing in the "s" or "p" orbitals. Moreover, these "d" or "f" electrons sit on the atoms to which they belong to and refuse to move. If this happens to all the electrons close to the Fermi energy level (E_F), the solid becomes an insulator. This insulator is difficult to understand in the wave-like picture as it is not caused by the absence of available one-electron states due to destructive interference in reciprocal **k**-space, resulting in a band gap in the conventional band insulators. The mechanism of those unconventional insulators was reported by Mott and Peierls way back in 1949 [58]. Thus, the typical DFT formalism under LDA or GGA approximation cannot explicitly consider such electron correlation effect on such systems of interest and thus fails to establish the correct Hamiltonian that can reproduce closely with the experimental results. In this context, the inclusion of on-site coulomb repulsion "U" in the DFT calculations eventually splits the metallic bands of those unconventional systems into two discrete sets of Hubbard bands [ca. Upper (UHB) and Lower Hubbard bands (LHB)] leaving behind a band gap between them which is in close agreement with the experimental observations. Such insulators are recognized as Mott or Mott – Hubbard (M-H) insulators [59]. However, apart from M-H insulators, there are another type of strongly correlated insulators known to be of charge transfer (CT) type [59]. The complete picture concerning the electronic properties of the compounds behaving as insulators, in general, can be accomplished by considering the p orbitals of the anions or the ligands surrounding the TM ions or rare earth elements. An electron from the p orbitals of the anion or the ligands can be transferred to the respective TM elements of the compound resulting in an energy cost of $\Delta_{CT,}$ known as CT energy. Interestingly, the characterization of the TM compounds exhibiting insulating behaviour can be explored from the Zaanen –Sawatzky – Allen diagram (ZSA) as depicted in the seminal work way back in 1985 [60]. A schematic representation of the ZSA diagram is shown in Figure 1.1. From Figure 1.1, it is observed that while $U < \Delta_{CT}$ denotes the insulator to be of M-H type, $U > \Delta_{CT}$ on the other hand signifies the system to be of CT insulator type.

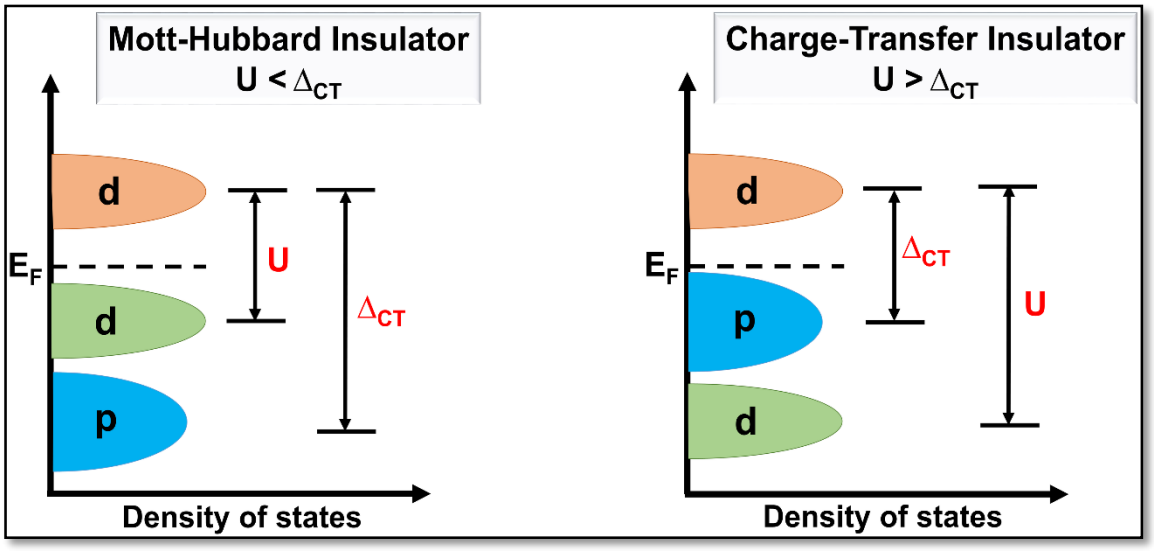

Figure 1.1. A schematic Zaanen –Sawatzky – Allen diagram representing Mott-Hubbard and charge transfer insulator [E_F denotes the Fermi energy level].

1.4. Machine learning

Despite the considerable success of first-principle calculations in estimating the physical and chemical properties of many-body systems, the major pitfalls of such calculations are that they are computationally demanding and need high-end computational facilities to run them. Recently, machine learning (ML) can be considered an effective alternative route to avoid the inherent computational costs linked with first-principle calculations and helps in establishing a simple model to predict the properties of materials in short intervals of time. ML, which is reckoned as a subset of artificial intelligence, has gained significant attention in recent years due to its widespread applications across different fields of research [61-75]. The primary objectives of ML rely on developing different algorithms that can learn and create statistical models for data analysis and prediction. ML algorithm works on a self-learning mechanism based on the data provided and makes accurate predictions between the input and predicted variables without having been programmed explicitly for a given task. To establish a more accurate ML model, the quality and quantity of the dataset used for training purposes play an important role. The identification and isolation of the training dataset are the first steps of the ML approach. The isolated data must be homogenized and cleaned before it can be used for training purposes. Therefore, the data are then processed by eliminating the possible erroneous, missing or inconsistent data points (outliers).

ML algorithms, in general, follow two different learning processes which include supervised and unsupervised learnings. While in supervised learning the training set should consist of both the input and their corresponding out variables, the unsupervised learning on the other hand draws interfaces about the input data without any prior knowledge of the associated output variables. The supervised learning is broadly categorized into two types such as classification and regression techniques where the predicted variables are designated as of categorical and continuous types, respectively. In unsupervised learning, the clustering and principle component methods are considered to identify the undetected patters in the data.

1.5. Literature review

Since the advancement of computational facilities, scientists and their research groups all over the world are trying to explore intriguing properties of many-body systems from first-principle calculations and ML methods. Recent works of some renowned research groups who are working in this area of research are highlighted below.

1.5.1. National status

U Waghmare *et al*. of Jawaharlal Nehru Centre for Advanced Scientific Research have been extensively working on exploring the underpinning physics behind the phase change materials from first-principle and spectroscopic studies. For example, their first-principle effective Hamiltonian and Raman spectroscopic studies show the pressure driven structural phase transition of Ta_2NiS_5 system from its base-centered orthorhombic (*Cmcm*) to primitive orthorhombic (*Pmnm*) at transition pressure ~ 4.2 GPa [76]. This system also exhibits semiconductor to metallic transition at pressure ~ 10.8 GPa. Their studies further reveal the topological insulating phase of $TlBiSe_2$ compound under the application of hydrostatic pressure. Moreover, their first-principle DFT calculations suggest the phonon anomalies and band inversion in the electronic band structure of the compounds are responsible for change in mirror Chern number and Z_2 topological invariant, which in turn result the pressure-induced topological crystalline insulator phase in $TlBiSe_2$ at pressure ~ 2.5 GPa. In another work, the same group has explored the superconducting state in weak topological insulator BiSe above pressure ~ 7 GPa [77]. Their combined DFT and spectroscopic studies indicate that BiSe system crystallizes to trigonal ($P\bar{3}m1$) phase, undergoes structural phase transitions from trigonal ($P\bar{3}m1$) to orthorhombic (*Cmcm*) and from orthorhombic (*Cmcm*) to cubic ($Pm\bar{3}m$) phases at transition pressures ~ 8, 13 GPa respectively. Distinct superconducting properties of

the compound have also been reported by them at the elevated pressure 8 and 13 GPa. Their studies as a whole identify the use of hydrostatic pressure as a potential pathway for exploring the structural phase transitions, topological crystalline insulating and superconducting phases of the materials.

T Saha-Dasgupta of S.N. Bose National Centre for Basic Sciences and her group are employing an understanding of the strongly correlated systems like perovskites and double perovskites from first-principle and ML calculations. Recently, one of their first-principle calculations reveals the unconventional multipolar magnetism in vacancy-ordered $5d^2$ halide double perovskite Cs_2WCl_6 stems from the interplay between the strong atomic spin-orbit coupling (SOC) and Coulomb interactions [78]. Weak interactions between the non-Kramers doublets and weak intersite hopping are also found in the Cs_2WCl_6 system. Such intersite interactions of the compound may be responsible for long-range ferro-octupolar order at temperature ~ 5.5 K. In another study, they explored the structural and magnetic properties of Hund's metal $BaRuO_3$ perovskite form DFT and dynamical mean field theory (DMFT) calculations [79]. Their findings show that while the cubic phase of $BaRuO_3$ shows ferromagnetic behaviour, the hexagonal phase of the same compound exhibits paramagnetic behaviour. Interestingly, the paramagnetic phase of hexagonal $BaRuO_3$ carries long-range antiferromagnetic order, which opens up the possibility of achieving a rare example of antiferromagnetic metal. This group also predicted thirty-three stable magnetic double oxide perovskites with general chemical formula $A_2BB'O_6$ comprised of 3d and 4d or 5d transition metals at their B and B' sites [80]. They used different ML models such as J48, random tree, random forest, and REP tree to classify between double and non-double perovskite compounds. Their study would help in discovering new magnetic double perovskites.

D Jana of University of Calcutta and his group are broadly working on the electronic optical magnetic and thermoelectric transport properties of materials, especially the two-dimensional (2D) systems, from first-principle and ML studies. Recently, they have predicted two new unexplored phases of germa-graphene structures GeC_3 and GeC_5 from first-principle calculations [81]. Electronic band structures of these compounds, as estimated from tight-binding model, exhibit semi-metallic band structures with parabolic valence band maximum (VBM) and conduction band minimum (CBM). The lattice thermal conductivities of these systems have been unveiled from the interatomic force constants which were trained from the moment tensor potential function in ML methods. GeC_3 and GeC_5 compounds are found to show thermoelectric figure of merit (ZT) in the range ~ 0.28 – 0.85, which is suggested to

endure their applications towards thermoelectric devices. In another work, they studied the optoelectronic and thermoelectric properties of two 2D C3N-based hetero-bilayers which include C_3N/Graphene and C_3N/hexagonal boron nitride (hBN) from first-principle calculations [82]. Their findings suggest that although both the monolayers exhibit low ZT at room temperature (300 K), the ZT values of the systems increase with an increase in temperature. Moreover, both compounds show high optical absorption coefficients within the visible electromagnetic energy window ranging between 1.6 and 3.1 eV. Their report also indicates the possibilities of these hetero-bilayers as potential candidates in thermal transport, waste-heat recovery and optoelectronic devices. Of late, they have also studied the thermoelectric properties of ternary metal chalcogenides Ba_2MnX_3 (X = Te, Se, S) from first-principle DFT and machine learning interatomic potential (MLIP) [83]. Their DFT calculations reveal that all these materials have direct electronic band gaps in the range of ~ 1.3 – 1.9 eV which may be suitable for photovoltaic applications. They have reported maximum ZT values of ~ 0.74, 0.66 and 0.42 that have been achieved at 700 K for Ba_2MnSe_3, Ba_2MnTe_3 and Ba_2MnS_3 systems respectively, reflecting their prospects as thermoelectric materials.

P Deb *et al*. of Tezpur University have recently investigated the thermoelectric properties and large magnetic proximity in monolayer- CrI_3/1T-MoS_2 van der Waals heterostructure from first-principle DFT followed by Boltzmann transport theory [84]. They have reported marked magnetic proximity of the said heterostructure stems from large magnetic anisotropy energy and spin polarization, which are estimated to be 2.21 meV and 12.30%, respectively. A high ZT value of ~ 6.0 of the system has been observed by them. They have suggested the significance of magnetic proximity which governed the high ZT value of the heterostructure which might bear technological relevance in low-dimensional thermoelectric devices. The group also works upon the underlying physics behind the electrocatalytic activities of different systems toward hydrogen evolution reaction (HER) process. For example, they have considered N-doped graphene/MoS_2/N-doped graphene trilayer structure [85] and metalloprotein (interaction of bacteriorhodopsin protein with metal nanoparticle Ag) [86] as model system for electrocatalysis of hydrogen using first-principle DFT calculations. By estimating the electronic structures, Gibbs free energies, Reaction pathways and volcano plot analyses of the studied systems, they have inferred that N – doping on graphene layer and Ag ion assimilation on active sites of bacteriorhodopsin protein significantly modulate the hydrogen binding energies resulting the enhancement in HER

activity. Their findings divulge the improved efficiencies of the studied compounds for HER can complement future hydrogen economy.

S Chattopadhyaya *et al*. of Tripura University are working on introspecting the electronic, optical and transport properties of different alloys from first-principle calculations. Recently they have investigated the elastic and thermal properties of quaternary alloys $Cd_xZn_{1-x}Se_yTe_{1-y}$ and $Mg_xZn_{1-x}S_yTe_{1-y}$ from DFT calculations followed by full-potential linearized augmented plane wave (FP-LAPW) approach [87,88]. Their study reveals that while the elastic stiffness constants, hardness, thermal conductivity and melting temperature of $Mg_xZn_{1-x}S_yTe_{1-y}$ ($Cd_xZn_{1-x}Se_yTe_{1-y}$) system increase nonlinearly with increasing S (Se) concentration at fixed Mg (Cd) concentration, the above-mentioned parameters of both the compounds however show reverse tendency with increasing Mg (Cd) concentration under fixed S (Se) concentration. Their findings reveal that these alloys may be used as appropriate materials for different thermal barrier coating and thermal management applications. In another work, the group has unveiled the structural, electronic and optoelectronic properties of ternary alloy $Be_xMg_{1-x}S$ from first-principle calculations [89]. While the lattice parameters and band gap of the $Be_xMg_{1-x}S$ system decrease with increasing Be concentration, the bulk modulus on the other hand increases with increasing Be concentration. The compound also shows structural and optical anisotropy and hence significant uniaxial birefringence phenomenon. The peaks of the dielectric function versus electromagnetic wave energy plots are reported to be observed in the ultraviolet (UV) region of electromagnetic spectra, which in turn suggest immense applications of the alloy in optoelectronic and luminescent devices capable of working in the UV region of electromagnetic wave.

S Bhattacharya and his group from Indian Institute of Technology Delhi are involved in understanding fascinating spin-splitting phenomena that play a pivotal role in spintronics. Recently, they have observed strong Rashba-Dresselhaus effects in ferroelectric bulk perovskites $CsPbF_3$ and KIO_3 from the first-principle calculations [90,91]. They have primarily studied the electronic band structures of the compounds with the aid of spin-orbit coupling (SOC) to unveil the Rashba-Dresselhaus spin-splitting. To further explore the nature of spin-splitting, whether it is Rashba or Dresselhaus type, they estimated the 2D contour plots of the spin texture in the $k_x - k_y$ momentum plane. For *R3c* phase of the $CsPbF_3$ system, they found the negligible contribution of out-of-plane spin component (S_z), however, distinct signature of in-plane spin components (S_x, S_y) was noticed in the spin texture plots. This result indicates the dominance of Rashba splitting over Dresselhaus splitting [91]. They have also calculated

the Rashba and Dresselhaus parameters ($\boldsymbol{\alpha_R}$ and $\boldsymbol{\alpha_D}$) for the *R3c* phase of $CsPbF_3$ compound from the DFT calculations and estimated to be ~ 1.05 (0.41) and 0.15 (0.08) eVÅ respectively for CBM (VBM) in harmony with the two-band **k.p** perturbation theory. To understand the Rashba-Dresselhaus effects for the rhombohedral *R3c* phase of KIO_3 compound[90], they have used DFT in unification with SOC to calculate the electronic properties of the compound. Interestingly, different type of Rashba spin-splitting followed by "novel spin textures" have been reported by them for the said phase of the compound. To unveil this new spin texture, they have suggested four-band **k.p** perturbation theory instead of two-band model. Moreover, they were succeed in enhancing the values of $\boldsymbol{\alpha_R}$ of the compounds under the application of external uniaxial strain and proposed both $CsPbF_3$ and KIO_3 as promising candidates for spintronics devices.

J Chowdhury *et al*. of Jadavpur University have been working on understanding the structural, electronic, optical and thermoelectric properties of technologically relevant materials from first-principle and ML studies [92-105]. Recently, this group has predicted the band gaps of nitride perovskites (ABN_3) having formation energies < -0.026 eV and band gaps ranging from ~ 1.0 to 3.1 eV, form ML and DFT calculations [103]. They have considered four supervised ML models such as multi-layer perceptron (MLP), gradient boosted decision tree (GBDT), support vector regression (SVR), random forest regression (RFR) along with electronic band structures and optoelectronic parameters such as complex dielectric functions, absorption coefficients to predict the band gaps of the ABN_3 systems. Their observation opens an alternative route to in estimating the band gaps of nitride perovskites by avoiding the inherent computational costs linked with DFT calculations. In another recent work, they have investigated the strain driven modulations in thermoelectric properties of 2D SiH and GeH monolayers from first-principle calculations [102]. Their study reveals that both SiH and GeH monolayers show minimum lattice thermal conductivities (~0.55 and 0.69 $Wm^{-1}K^{-1}$) and maximum ZT values (~1.26 and 0.81) at room temperature and under 2% compressive strain. The have suggested the efficacy of external strains in modulating the thermoelectric properties of 2D SiH and GeH monolayers which in turn will bear relevant technological applications in thermoelectric devices. The group also works upon understanding the electrocatalytic activities for water splitting in different systems such as Ce-doped NiSe, Fe-doped $NiCo_2Se_4$ and Co-doped Ni_9S_8 systems from first-principle calculations [96,100,104]. The electronic properties and electrochemical reaction pathways, which are the key players in unveiling the electrocatalytic mechanism, have been estimated in their studies.

1.5.2. International status

V Anisimov of M.N. Mikheev Institute of Metal Physics of Ural Branch of Russian Academy of Sciences and his group are extensively working on understanding the strongly correlated systems from first-principle DFT and DMFT studies. They have explored the electron correlation effects in paramagnetic face-centred cubic cobalt (Co) [106] and Co-based superconductor $CuCo_2S_4$ [107] from the DFT + DMFT approach. Their studies reveal that the momentum dependence static magnetic susceptibility of Co stems from the ferromagnetic correlations. Furthermore, they have also reported smaller local and fluctuating spin moments of $CuCo_2S_4$ in contrast to Fe-based superconductors are responsible for the pairing mechanism in $CuCo_2S_4$. In another work, the same group investigated the correlated nature of electronic energy states in the $Pb_9Cu(PO_4)_6O$ system using the DFT+DMFT level of theory [108]. Interestingly, their study shows that the p – p-orbitals of oxygen play a major role in the electronic properties of the compound and therefore the band structure cannot be solely estimated from the two-band Hubbard model. They have also reported that the doping of electrons in $Pb_9Cu(PO_4)_6O$ can alter its charge transfer insulating nature to metallic behaviour.

O K Andersen *et. al*. of Max Planck Institute for Solid State Research, Germany recently reported the structural and electronic properties of quasi-one-dimensional (1D) systems such as $LiMo_6O_{17}$ from first-principle DFT calculations [109,110]. This compound exhibits conducting behaviour and the band structure, which is localized in a large energy window around the Fermi energy level, is formed by three Mo t_{2g}-like extended Wannier orbitals. Their study also reveals that the complex shape of the Fermi surface depends strongly on the Fermi energy level in the band gap, implying significant sensitivity to Li stoichiometry of electronic properties dependent on the Fermi surface, such as Fermi surface nesting or superconductivity. In another study the group have employed first-principle based foundation to derive a formalism for numerical 3D interpolation across a hard-sphere interstitial from the cubic-harmonic projections of the target density function, $\rho(r)$, and its first three radial derivatives at the spheres. Whereas this calculation is found to suffice for closely-packed structures, additional information such as the integral of $\rho(r)$ over the interstitial and/or the values at specific points deep inside the interstitial is needed for open structures. This was illustrated by application to a constant function and to the valence charge densities in Si, ZnSe, and CuBr compound, interpolated across either the bcc- or the zinc-blende-structured interstitial, depending on whether or not the voids were filled with empty spheres [111].

S H Naqib *et al*. of University of Rajshahi, Bangladesh are working on understanding the elastic, electronic, optical and thermoelectric properties of novel materials under their pristine or defect conditions. Recently, they have studied the elastic, thermal and optoelectronic properties of XBi_2 (X = K, Rb) [112] and XIr_3 (X = La, Th) [113] compounds from first-principle DFT calculations. Detailed investigations of optical absorption, reflectivity spectra and the refractive index of XBi_2 (X = K, Rb) indicate that these systems can be used as solar reflectors and ultraviolet absorbers. Moreover, they have calculated the superconducting transition temperature (T_c) for $LaIr_3$ and $ThIr_3$ compounds and are estimated to be ~ 4.91 and 5.01 K, respectively [113]. In another article, they reported the modulations of electronic, optical, mechanical and thermoelectric properties of the $KTaO_3$ compound with sulfur (S) substitution [114]. Surprisingly, their study unveiled fascinating structural phase transitions where the cubic $KTaO_3$ undergoes to tetragonal phase for $KTaO_2S$ and $KTaOS_2$ compounds, eventually remaining in the cubic phase for $KTaS_3$ system. The modified band gap and optical properties of $KTaO_2S$ compound reflect considerable potential for its application in photovoltaics, presenting promising opportunities in improving solar energy conversion efficiency.

S Picozzi *et al*. and her group from Consiglio Nazionale delle Ricerche (CNR-SPIN), Italy are mainly focussed to explore different intriguing quantum phenomena and spin-splitting of novel materials from first-principle calculations. Recently they have showed the Rashba effect of $BiCoO_3$ compound from the DFT calculations [115]. $BiCoO_3$ crystal shows perovskite like structure and exhibits multiferroic (ferroelectric and antiferromagnetic) behaviour below Néel temperature (T_N) = 420 K. Their study unveiled larger Rashba parameter (= 0.74 eVÅ) of the system and suggested $BiCoO_3$ as a potential candidate for spin – field effect transistor [115]. They suggested the general trend of multiferroic materials which exhibit Rashba-Dresselhaus spin-splitting. According to them, the Rashba-Dresselhaus effects are generally observed in non-centrosymmetric crystals which either exhibit ferroelectric (FE) – nonmagnetic (NM) or FE – antiferromagnetic (AFM) properties. On contrary, ferromagnetic (FM) systems do not exhibit RD splittings as their on-site exchange interaction term (J) largely splits the electronic bands and form an unpaired band consisting of both up and down spins. Paraelectric (PE) compounds also do not show any such effect due to the absence of spontaneous electrical polarization. In another paper, the group has explored the spin-chirality driven multiferroicity in van der Waals 2D Monolayers from first-principle calculations [116]. This work shows a remarkable role of spin-lattice coupling on magnetoelectricity, which in turn indicates a

significant contribution of spin-orbit coupling driven by anions. Moreover, their study further reveals such multiferroic compounds exhibit considerable spin-driven structural distortions which may promote the multifunctional spin-electric-lattice couplings [116].

1.6. Summary of thesis chapters

The dissertation aims to understand the structural, electronic and optical properties of technologically relevant materials from first-principle calculations. The thesis report has been framed in the following way. After discussing a general introduction to material sciences, many-body theory, strongly correlated systems and machine learning in Chapter 1, Chapter 2 focuses on the computational methodologies such as the first-principle DFT framework, calculations of phonon dispersion relations, Born-Oppenheimer molecular dynamics (BOMD) simulations, calculations of optical properties and machine learning methods. Chapter 3 aims to understand the structural and electronic properties of the Mercurous Chloride (Hg_2Cl_2) compound from first-principle DFT calculations. The charge-transfer insulating property of the Hg_2Cl_2 compound has been elaborately discussed in Chapter 3. In Chapter 4, the pressure-driven structural phase transitions of the Hg_2Cl_2 compound at room temperature (T = 300 K) have been deliberated. The transition pressures linked with the structural phase transitions of Hg_2Cl_2 system from its body-centred tetragonal [*I4/mmm* (D_{4h}^{17})] → base-centred orthorhombic [*Cmcm* (D_{2h}^{17})] phase and from base-centred orthorhombic [*Cmcm* (D_{2h}^{17})] → primitive orthorhombic [*Pnma* (D_{2h}^{16})] phase have been unveiled in Chapter 4. The key vibrational phonon modes linked with these structural phase transitions and the type of phase transition have also been shared. Chapter 5 discusses the alterations of electronic and optoelectronic properties of the Hg_2Cl_2 system under the application of pressure. The electronic band structures, anisotropic optoelectronic parameters such as complex dielectric function [$\varepsilon(\omega)$], absorption coefficient [$\alpha(\omega)$], optical conductivity [$\sigma(\omega)$], refractive indices (n_e, n_o), optical birefringence (Δn) of Hg_2Cl_2 at ambient conditions and under external pressures have been enlightened in Chapter 5. Chapter 6 is framed with the temperature-dependent structural phase transition and negative thermal expansion behaviour of the Hg_2Cl_2 compound. The transition temperature associated with the structural phase transition of the system from *I4/mmm* (D_{4h}^{17}) → *Cmcm* (D_{2h}^{17}) phase has been revealed in this chapter. The corresponding order parameter, key phonon modes responsible for structural phase transition and negative thermal expansion behaviour have also been highlighted in Chapter 6. In Chapter 7, the band gaps of nitride perovskites, with general chemical formula ABN_3, have been predicted from machine learning

and DFT calculations. Four machine learning models such as support vector regression (SVR), gradient boosted decision tree (GBDT), random forest regression (RFR) and multi-layer perceptron (MLP) have been considered for predicting the band gaps of the ABN_3 – type compounds. The band gaps of two nitride perovskites $CeMoN_3$ and $CeWN_3$, so predicted from their electronic band structures, dielectric functions, absorption coefficients and machine learning models, have also been highlighted in Chapter 7. The overall conclusions and future perspective of research work have been discussed under Chapter 8.

Bibliography

[1] A. Lele, *Disruptive Technologies for the Militaries and Security* (Springer Singapore, 2018).

[2] B. A. Kipfer, *Encyclopedic Dictionary of Archaeology* (Springer US, 2000).

[3] M. A. Morse, Proc. Prehist. Soc. **65**, 1 (1999).

[4] J. Goody, *Metals, Culture and Capitalism: An Essay on the Origins of the Modern World* (Cambridge University Press, Cambridge, 2012).

[5] P. Sillitoe and K. Hardy, Antiquity **77**, 555 (2003).

[6] M. Gross, Curr. Biol. **22**, R981 (2012).

[7] H. Pilcher, Nature (2003).

[8] T. Shaw, P. L. Shinnie, O. Davies, and N. J. Van Der Merwe, Curr. Anthropol. **10**, 226 (1969).

[9] M. Stuiver and N. J. van der Merwe, Curr. Anthropol. **9**, 54 (1968).

[10] A. L. Stanton, *Cultural Sociology of the Middle East, Asia, and Africa: An Encyclopedia* (SAGE Publications, 2012).

[11] J. P. Mallory and D. Q. Adams, *Encyclopedia of Indo-European Culture* (Fitzroy Dearborn, 1997).

[12] K. C. Jain, *Malwa Through The Ages* (Motilal Banarsidass Publishers (Pvt. Limited), 1972).

[13] in *Condensed-Matter and Materials Physics: Basic Research for Tomorrow's Technology*, edited by N. R. Council (The National Academies Press, Washington, DC, 1999), p. 31.

[14] J. Schmidt, M. R. G. Marques, S. Botti, and M. A. L. Marques, npj Comput Mater **5**, 83 (2019).

[15] S. Hao, V. P. Dravid, M. G. Kanatzidis, and C. Wolverton, npj Comput Mater **5**, 58 (2019).

[16] G. Kotliar, S. Y. Savrasov, K. Haule, V. S. Oudovenko, O. Parcollet, and C. A. Marianetti, Rev. Mod. Phys. **78**, 865 (2006).

[17] K. Held, Adv. Phys. **56**, 829 (2007).

[18] M. Hacene, A. Anciaux-Sedrakian, X. Rozanska, D. Klahr, T. Guignon, and P. Fleurat-Lessard, J. Comput. Chem. **33**, 2581 (2012).

[19] M. C. Bennett, Nat Rev Phys **3**, 725 (2021).

[20] S. Lehtola, Int J Quantum Chem. **119**, e25968 (2019).

[21] N. Govind, Y. A. Wang, and E. A. Carter, J. Chem. Phys. **110**, 7677 (1999).

[22] P. Kratzer and J. Neugebauer, Front. Chem. **7** (2019).

[23] M. V. Malyshkina and A. S. Novikov, Compounds **1** (2021).

[24] E. Schrödinger, Phys. Rev. **28**, 1049 (1926).

[25] M. Born and R. Oppenheimer, Ann. Phys. **389**, 457 (1927).

[26] P. A. M. Dirac and R. H. Fowler, Proc. R. Soc. A: Math. Phys. Eng. Sci. **123**, 714 (1929).

[27] R. K. Nesbet, Rev. Mod. Phys. **33**, 28 (1961).

[28] P. Chaikin, & Lubensky, T., in *Principles of Condensed Matter Physics*, edited by P. M. Chaikin, and T. C. Lubensky (Cambridge University Press, Cambridge, 1995), pp. i.

[29] P. Weiss, J. Phys. Theor. Appl. **6**, 661 (1907).

[30] D. R. Hartree, Math. Proc. Camb. Philos. Soc. **24**, 111 (1928).

[31] J. C. Slater, Phys. Rev. **35**, 210 (1930).

[32] J. C. Slater, Phys. Rev. **32**, 339 (1928).

[33] V. Fock, Z. Physik **61**, 126 (1930).

[34] D. R. Hartree and W. Hartree, Proc. R. Soc. A: Math. Phys. Eng. Sci. **150**, 9 (1935).

[35] T. G. Williams, N. J. DeYonker, and A. K. Wilson, J. Chem. Phys. **128**, 044101 (2008).

[36] K. Fægri and J. Almlöf, Chem. Phys. Lett. **107**, 121 (1984).

[37] H. P. Lüthi, J. H. Ammeter, J. Almlöf, and K. Faegri, J. Chem. Phys. **77**, 2002 (1982).

[38] J. O. Noell, M. D. Newton, P. J. Hay, R. L. Martin, and F. W. Bobrowicz, J. Chem. Phys. **73**, 2360 (1980).

[39] M. Pelissier, J. Chem. Phys. **75**, 775 (1981).

[40] P. S. Bagus and H. F. Schaefer, J. Chem. Phys. **58**, 1844 (1973).

[41] P. J. Hay, J. Am. Chem. Soc. **103**, 1390 (1981).

[42] H. P. Lüthi, J. Ammeter, J. Almlöf, and K. Korsell, Chem. Phys. Lett. **69**, 540 (1980).

[43] L. H. Thomas, Math. Proc. Camb. Philos. Soc. **23**, 542 (1927).

[44] E. Fermi, Accademia Nazionale dei Lincei **6**, 602 (1927).

[45] W. Kohn and L. J. Sham, Phys. Rev. **140**, A1133 (1965).

[46] P. Hohenberg and W. Kohn, Phys. Rev. **136**, B864 (1964).

[47] S. L. Phutela, S. Arora, D. S. Ahlawat, and S. Kansal, AIP Conf Proc **2093**, 020043 (2019).

[48] U. Engberg, Phys. Rev. B **55**, 2824 (1997).

[49] A. Francis, G. Abdu, S., Haruna, A., & Danladi, E., Phys. Sci. Int. J. **11**, 1 (2016).

[50] C. Schmidt, P. B. Allen, T. Baruah, and M. R. J. B. o. t. A. P. S. Pederson, arXiv:cond-mat/0411009 (2004).

[51] J. Wang, M. Deng, Y. Chen, X. Liu, W. Ke, D. Li, W. Dai, and K. He, Mater. Chem. Phys. **244**, 122733 (2020).

[52] V. I. Anisimov, J. Zaanen, and O. K. Andersen, Phys. Rev. B **44**, 943 (1991).

[53] S. Ghosal, K. Dutta, S. Chowdhury, and D. Jana, J. Phys. D: Appl. Phys. **55**, 375303 (2022).

[54] A. Georges, AIP Conf Proc **715**, 3 (2004).

[55] J. Kuneš, V. I. Anisimov, S. L. Skornyakov, A. V. Lukoyanov, and D. Vollhardt, Phys. Rev. Lett. **99**, 156404 (2007).

[56] V. I. Anisimov, F. Aryasetiawan, and A. I. Lichtenstein, J. Phys.: Condens. Matter **9**, 767 (1997).

[57] E. Pavarini, La Rivista del Nuovo Cimento **44**, 597 (2021).

[58] N. F. Mott, Proc. Phys. Soc. A **62**, 416 (1949).

[59] X. Bu and Y. Li, Phys. Rev. B **106**, L241101 (2022).

[60] J. Zaanen, G. A. Sawatzky, and J. W. Allen, Phys. Rev. Lett. **55**, 418 (1985).

[61] O. Allam, B. W. Cho, K. C. Kim, and S. S. Jang, RSC Adv. **8**, 39414 (2018).

[62] F. Wang, Z. Yang, F. Li, J.-L. Shao, and L.-C. Xu, RSC Adv. **13**, 31728 (2023).

[63] W. Z. Tawfik, S. N. Mohammad, K. H. Rahouma, G. M. Salama, and E. Tammam, Phys. Scr. **99**, 026001 (2024).

[64] X. Li, Y. Qin, G. He, F. Lian, S. Zuo, and C. Cai, J. Phys. D: Appl. Phys. **57**, 135303 (2024).

[65] H. J. Kulik *et al.*, Electron. Struct. **4**, 023004 (2022).

[66] L. Ward, A. Agrawal, A. Choudhary, and C. Wolverton, npj Comput Mater **2**, 16028 (2016).

[67] G. Pilania, A. Mannodi-Kanakkithodi, B. P. Uberuaga, R. Ramprasad, J. E. Gubernatis, and T. Lookman, Sci Rep **6**, 19375 (2016).

[68] V. Gladkikh, D. Y. Kim, A. Hajibabaei, A. Jana, C. W. Myung, and K. S. Kim, J. Phys. Chem. C **124**, 8905 (2020).

[69] E. Bedolla, L. C. Padierna, and R. Castañeda-Priego, J. Phys.: Condens. Matter **33**, 053001 (2021).

[70] S. Chibani and F.-X. Coudert, APL Mater. **8**, 080701 (2020).

[71] Y. Zhang, W. Xu, G. Liu, Z. Zhang, J. Zhu, and M. Li, PLOS ONE **16**, e0255637 (2021).

[72] M. Gao, B. Cai, G. Liu, L. Xu, S. Zhang, and H. Zeng, Phys. Chem. Chem. Phys. **25**, 9123 (2023).

[73] R. Pederson, B. Kalita, and K. Burke, Nat Rev Phys **4**, 357 (2022).

[74] L. D. Jones, D. Golan, S. A. Hanna, and M. Ramachandran, Bone Joint Res. **7**, 223 (2018).

[75] R. Cioffi, M. Travaglioni, G. Piscitelli, A. Petrillo, and F. De Felice, in *Sustainability*2020).

[76] S. Pal, A. Sinha, L. Harnagea, P. Telang, D. V. S. Muthu, U. V. Waghmare, and A. K. Sood, Phys. Rev. B **109**, 155202 (2024).

[77] P. Malavi, A. Paul, A. Bera, D. V. S. Muthu, K. Majhi, P. S. A. Kumar, U. V. Waghmare, A. K. Sood, and S. Karmakar, Phys. Rev. B **107**, 024506 (2023).

[78] K. Pradhan, A. Paramekanti, and T. Saha-Dasgupta, Phys. Rev. B **109**, 184416 (2024).

[79] H. Banerjee, H. Schnait, M. Aichhorn, and T. Saha-Dasgupta, Phys. Rev. B **105**, 235106 (2022).

[80] A. Halder, A. Ghosh, and T. S. Dasgupta, Phys. Rev. Materials **3**, 084418 (2019).

[81] S. Ghosal, N. S. Mondal, S. Chowdhury, and D. Jana, Appl. Surf. Sci. **614**, 156107 (2023).

[82] D. Mondal, S. Ghosal, S. Jana, A. Roy, Asfakujjaman, K. Basak, M. Ghosh, and D. Jana, J. Phys.: Condens. Matter **36**, 285705 (2024).

[83] M. Rakshit, S. Chowdhury, A. Majumdar, D. Banerjee, and D. Jana, Comput. Mater. Sci. **230**, 112526 (2023).

[84] A. K. Singh, W. Gao, and P. Deb, J. Phys.: Condens. Matter **36**, 305704 (2024).

[85] S. K. Behera, P. Deb, and A. Ghosh, ChemistrySelect **2**, 3657 (2017).

[86] S. K. Behera, P. Deb, and A. Ghosh, Phys. Chem. Chem. Phys. **18**, 23220 (2016).

[87] S. Chanda, M. Debbarma, D. Ghosh, S. Das, B. Debnath, R. Bhattacharjee, and S. Chattopadhyaya, Mater. Today Commun. **27**, 102136 (2021).

[88] D. Ghosh, S. Chanda, M. Debbarma, B. Debnath, and S. Chattopadhyaya, Indian J Phys **96**, 747 (2022).

[89] B. Debnath, D. Ghosh, M. Debbarma, S. Chanda, S. Das, R. Bhattacharjee, and S. Chattopadhyaya, Mater. Chem. Phys. **258**, 123946 (2021).

[90] S. Sheoran, M. Kumar, P. Bhumla, and S. Bhattacharya, Mater. Adv. **3**, 4170 (2022).

[91] P. Bhumla, D. Gill, S. Sheoran, and S. Bhattacharya, J. Phys. Chem. Lett. **12**, 9539 (2021).

[92] S. Ghosh, R. R. Banik, and J. Chowdhury, Indian J. Theor. Phys. **69**, 43 (2021).

[93] S. Ghosh and J. Chowdhury, J. Appl. Phys. **130**, 225103 (2021).

[94] S. Ghosh and J. Chowdhury, Mater Sci Eng B. **284**, 115903 (2022).

[95] S. Ghosh, S. Sarkar, and J. Chowdhury, Mater. Chem. Phys. **276**, 125379 (2022).

[96] D. Rathore, S. Ghosh, J. Chowdhury, and S. Pande, ACS Appl. Nano Mater. **5**, 11823 (2022).

[97] R. R. Banik, S. Ghosh, and J. Chowdhury, Phys. Scr. **98**, 105914 (2023).

[98] S. Ghosh and J. Chowdhury, Phase Transit. **96**, 446 (2023).

[99] S. Ghosh and J. Chowdhury, Mod. Phys. Lett. B **38**, 2330003 (2023).

[100] D. Rathore, S. Ghosh, J. Chowdhury, and S. Pande, ACS Appl. Nano Mater. **6**, 3095 (2023).

[101] R. Ray Banik, S. Ghosh, and J. Chowdhury, Phys. Scr. **98**, 045920 (2023).

[102] R. R. Banik, S. Ghosh, and J. Chowdhury, J. Phys.: Condens. Matter **36**, 255706 (2024).

[103] S. Ghosh and J. Chowdhury, RSC Adv. **14**, 6385 (2024).

[104] D. Rathore, S. Ghosh, A. Gupta, J. Chowdhury, and S. Pande, ACS Appl. Nano Mater. **7**, 9730 (2024).

[105] M. H. Kabir *et al.*, Opt. Mater. **147**, 114724 (2024).

[106] A. S. Belozerov and V. I. Anisimov, Jetp Lett. **117**, 854 (2023).

[107] S. L. Skornyakov, I. O. Trifonov, and V. I. Anisimov, Jetp Lett. **117**, 588 (2023).

[108] D. M. Korotin, D. Y. Novoselov, A. O. Shorikov, V. I. Anisimov, and A. R. Oganov, Phys. Rev. B **108**, L241111 (2023).

[109] L. Dudy, J. W. Allen, J. D. Denlinger, J. He, M. Greenblatt, M. W. Haverkort, Y. Nohara, and O. K. Andersen, Phys. Rev. B **109**, 115143 (2024).

[110] L. Dudy, J. W. Allen, J. D. Denlinger, J. He, M. Greenblatt, M. W. Haverkort, Y. Nohara, and O. K. Andersen, Phys. Rev. B **109**, 115145 (2024).

[111] Y. Nohara and O. K. Andersen, Phys. Rev. B **94**, 085148 (2016).

[112] J. Hassan, M. A. Masum, and S. H. Naqib, Comput. Condens. Matter **39**, e00905 (2024).

[113] M. S. Islam, R. Ahmed, M. M. Hossain, M. A. Ali, M. M. Uddin, and S. H. Naqib, Results Mater. **22**, 100568 (2024).

[114] H. Akter, M. M. Hossain, M. M. Uddin, S. H. Naqib, and M. A. Ali, J. Phys. Chem. Solids **190**, 112021 (2024).

[115] K. Yamauchi, P. Barone, and S. Picozzi, Phys. Rev. B **100**, 245115 (2019).

[116] C. Liu, W. Ren, and S. Picozzi, Phys. Rev. Lett. **132**, 086802 (2024).

Chapter 2

Computational methodology

2.1. Introduction

This chapter is focused on the computational methodologies that have been employed in the entire research work of the thesis. The first-principle calculations have been carried out within the density functional theory (DFT) framework as implemented in Quantum ESPRESSO (QE) software [1-3]. The single particle approximation such as DFT in the form of first-principle calculations may be considered as one of the most advanced approximate methods to address the microscopic properties of the materials in finer detail [4-6]. First-principle calculations in general estimate the atomistic properties of the compounds from charge (e) and mass (m) of the electrons for the systems in hand and are found to be extremely successful not only in reproducing the experimental observations [4-11], but may also in predicting the properties of new materials before experiments [12-19]. The DFT method as formulated by Hohenberg, Kohn and Sham [20,21], has drawn significant attention over the last thirty years in the theoretical advancements of both chemical and condensed matter physics [22-26]. DFT method not only simplifies the complexities of using multidimensional abstract wavefunctions but leverages the use of experimentally observable electron density function $\rho(r)$ for many-body systems.

2.2. Formalism of DFT

In the DFT framework, the total ground state energy ($\boldsymbol{E_0}$) of a many-body system is formulated in terms of functional of electron density [$\boldsymbol{\rho(r)}$]. The energy functional ($\boldsymbol{E_0[\rho(r)]}$) can be expressed as:

$$E_0[\rho(\boldsymbol{r})] = \langle T_K[\rho(\boldsymbol{r})]\rangle + \langle V_{ne}[\rho(\boldsymbol{r})]\rangle + \langle V_{ee}[\rho(\boldsymbol{r})]\rangle \tag{2.1}$$

where T_K and V_{ee} are the respective kinetic energy and repulsive Coulomb potential functionals of electron densities. The "<….>" bracket symbolises the expectation value of the quantity located inside it. Here, V_{ne} denotes the attractive potential between the electrons and nuclei and is expressed as:

$$\langle V_{ne}[\rho(\boldsymbol{r})]\rangle = \int d\boldsymbol{r}\, V_{ne}\, \rho(\boldsymbol{r}) = -\sum_{nuclei\, I} Z_I \int \frac{\rho(\boldsymbol{r}_1)}{\boldsymbol{r}_{1I}}\, d\boldsymbol{r}_1 \tag{2.2}$$

where Z_I is the atomic number of the nucleus "I" and $\boldsymbol{r}_{1I}$ denotes the distance between the electron and nucleus I.

Equation (2.1) is now represented as:

$$E_0[\rho(\boldsymbol{r})] = \langle T_K[\rho(\boldsymbol{r})]\rangle + \int d\boldsymbol{r}\, V_{ne}\, \rho(\boldsymbol{r}) + \langle V_{ee}[\rho(\boldsymbol{r})]\rangle$$

or

$$E_0[\rho(\boldsymbol{r})] = \langle T_K[\rho(\boldsymbol{r})]\rangle - \sum_{nuclei\, I} Z_I \int \frac{\rho(\boldsymbol{r}_1)}{\boldsymbol{r}_{1I}} d\boldsymbol{r}_1 + \langle V_{ee}[\rho(\boldsymbol{r})]\rangle \quad (2.3)$$

To grapple with equation (2.3), a fictitious reference model of non-interacting electrons has been considered [20,21]. These non-interacting electrons exhibit similar electron density distribution to a real ground state system. Deviations (Δ) of $\langle T_K[\rho(\boldsymbol{r})]\rangle$ and $\langle V_{ee}[\rho(\boldsymbol{r})]\rangle$ from their respective reference (ref) systems can then be expressed as [27]:

$$\Delta\langle T_K[\rho(\boldsymbol{r})]\rangle = \langle T_K[\rho(\boldsymbol{r})]\rangle - \langle T_K[\rho(\boldsymbol{r})]\rangle_{ref} \quad (2.4)$$

$$\Delta\langle V_{ee}[\rho(\boldsymbol{r})]\rangle = \langle V_{ee}[\rho(\boldsymbol{r})]\rangle - \langle V_{ee}[\rho(\boldsymbol{r})]\rangle_{ref} \quad (2.5)$$

where $$\langle V_{ee}[\rho(\boldsymbol{r})]\rangle_{ref} = \frac{1}{2}\iint \frac{\rho(\boldsymbol{r}_1)\rho(\boldsymbol{r}_2)}{|\boldsymbol{r}_2 - \boldsymbol{r}_1|} d\boldsymbol{r}_1 d\boldsymbol{r}_2 \quad (2.6)$$

Equation (2.3) is further modified to

$$E_0[\rho(\boldsymbol{r})] = \int d\boldsymbol{r}\, V_{ne}\, \rho(\boldsymbol{r}) + \langle T_K[\rho(\boldsymbol{r})]\rangle_{ref} + \frac{1}{2}\iint \frac{\rho(\boldsymbol{r}_1)\rho(\boldsymbol{r}_2)}{|\boldsymbol{r}_2 - \boldsymbol{r}_1|} d\boldsymbol{r}_1 d\boldsymbol{r}_2 + E_{XC}[\rho(\boldsymbol{r})] \quad (2.7)$$

where

$$E_{XC}[\rho(\boldsymbol{r})] = \Delta\langle T_K[\rho(\boldsymbol{r})]\rangle + \Delta\langle V_{ee}[\rho(\boldsymbol{r})]\rangle \quad (2.8)$$

Here, E_{XC} is termed as exchange-correlation (XC) functional.

Now, in Equation (2.7), $\langle T_K[\rho(\boldsymbol{r})]\rangle_{ref}$ refers to the expectation value of the sum of one-electron kinetic energy operators in the ground state wavefunction $[\varphi_{ref}(\boldsymbol{r}_1, \boldsymbol{r}_2, \boldsymbol{r}_3, \ldots\ldots \boldsymbol{r}_n)]$ of the reference system, and is represented as:

$$\langle T_K[\rho(\boldsymbol{r})]\rangle_{ref} = \langle \varphi_{ref}| -\frac{1}{2}\sum_{i=1}^{2n} \boldsymbol{\nabla}_i^2 |\varphi_{ref}\rangle \quad (2.9)$$

Since these hypothetical electrons are non-interacting, φ_{ref} can be written in the form of a Slater determinant [20,28] with Kohn-Sham (KS) orbitals of the ith particle (ϕ_i^{KS}) and spin functions (α, β). More precisely for a four-electron system

$$\varphi_{ref} = \begin{vmatrix} \phi_1^{KS}(1)\alpha(1) & \phi_1^{KS}(1)\beta(1) & \phi_2^{KS}(1)\alpha(1) & \phi_2^{KS}(1)\beta(1) \\ \phi_1^{KS}(2)\alpha(2) & \phi_1^{KS}(2)\beta(2) & \phi_2^{KS}(2)\alpha(2) & \phi_2^{KS}(2)\beta(2) \\ \phi_1^{KS}(3)\alpha(3) & \phi_1^{KS}(3)\beta(3) & \phi_2^{KS}(3)\alpha(3) & \phi_2^{KS}(3)\beta(3) \\ \phi_1^{KS}(4)\alpha(4) & \phi_1^{KS}(4)\beta(4) & \phi_2^{KS}(4)\alpha(4) & \phi_2^{KS}(4)\beta(4) \end{vmatrix} \quad (2.10)$$

The quantity $\langle T_K[\rho(\boldsymbol{r})]\rangle_{ref}$ can thus be expressed in terms of ϕ_i^{KS} and is represented as:

$$\langle T_K[\rho(\boldsymbol{r})]\rangle_{ref} = -\frac{1}{2}\sum_{i=1}^{2n}\langle\phi_i^{KS}|\boldsymbol{\nabla}_i^2|\phi_i^{KS}\rangle \quad (2.11)$$

In this context, Equation (2.7) can again be expressed as:

$$E_0[\rho(\boldsymbol{r})] = \int dr\, V_{ne}\,\rho(\boldsymbol{r}) - \frac{1}{2}\sum_{i=1}^{2n}\langle\phi_i^{KS}\left|\boldsymbol{\nabla}_i^2\right|\phi_i^{KS}\rangle + \frac{1}{2}\iint\frac{\rho(\boldsymbol{r}_1)\rho(\boldsymbol{r}_2)}{|\boldsymbol{r}_2-\boldsymbol{r}_1|}d\boldsymbol{r}_1 d\boldsymbol{r}_2 + E_{XC}[\rho(\boldsymbol{r})] \quad (2.12)$$

Since,

$$\rho = \sum_{i=1}^{2n}\left|\phi_i^{KS}\right|^2 \quad (2.13)$$

Now, substituting ρ in Equation (2.12) and differentiating $E_0[\rho(\boldsymbol{r})]$ with respect to ϕ_i^{KS} by considering ϕ_i^{KS} as orthonormal [29] lead to the KS equation which is mathematically represented as:

$$\left[-\frac{\hbar^2}{2m}\boldsymbol{\nabla}^2 + V_{ne}(\boldsymbol{r}) + \int\frac{\rho(\boldsymbol{r}_2)}{|\boldsymbol{r}_2-\boldsymbol{r}_1|}d\boldsymbol{r}_2 + \frac{\partial E_{XC}[\rho(\boldsymbol{r})]}{\partial\rho(\boldsymbol{r})}\right]\phi_i^{KS} = E_i^{KS}\phi_i^{KS}$$

or

$$\left[-\frac{\hbar^2}{2m}\boldsymbol{\nabla}^2 - \sum_{nuclei\,I}\frac{Z_I}{\boldsymbol{r}_{1I}} + \int\frac{\rho(\boldsymbol{r}_2)}{|\boldsymbol{r}_2-\boldsymbol{r}_1|}d\boldsymbol{r}_2 + \frac{\partial E_{XC}[\rho(\boldsymbol{r})]}{\partial\rho(\boldsymbol{r})}\right]\phi_i^{KS} = E_i^{KS}\phi_i^{KS} \quad (2.14)$$

where E_i^{KS} is the KS orbital energy eigenvalues of ith particle. Moreover, the clever choice of XC functional $E_{XC}[\rho(\boldsymbol{r})]$ in Equation (2.14) is considered an important factor in estimating the electronic and/or optical band gaps of the compounds with profound accuracies in line with the experimental results [30-38].

The DFT formalism was successfully implemented in the first-principle calculations by Roberto Car and Michele Parrinello for the first-time way back in 1985 [39]. Car and Parrinello in their seminal work pointed out two key features which include the plane wave basis for electronic wavefunctions and pseudopotentials instead of ionic interactions for DFT calculations. The choice of plane wave basis set in the first-principle DFT calculations is advantageous as it is complete, unbiased and independent of atomic positions of the system [40,41].

2.3. The exchange-correlation functional

DFT is an elegant technique not only in reproducing the experimental observations [4-11] but also in predicting the electronic, optical and magnetic properties of new materials prior to experiments [12-19**]**. Both the electronic as well as the optoelectronic properties are primarily guided by the band gap (E_g) of the materials. While DFT calculations with local density approximation (LDA) and generalized gradient approximation (GGA) are found to underestimate E_g values in general [33,42-44], the unscreened hybrid and Perdew–Burke–Ernzerhof–Hartree–Fock exchange (PBE0) functionals on the other hand overestimate band gap energies of the compounds relative to their experimental counterparts [45-47]. In this context, DFT calculations, as accomplished from single-shot GW (G_0W_0) approximation and hybrid XC functionals such as Heyd–Scuseria–Ernzerhof (HSE), Becke-3-parameter-Lee-Yang-Parr (B3LYP), B3PW91 are known to predict the E_g values of the compounds close to the experimental results [30-32,34,42,48-53]. The primary driving force behind the success of hybrid functional stems from the mutual effects of both the Hartree–Fock (HF) exchange and LDA/ GGA approximation that are incorporated into the hybrid functional. For example, while the Perdew–Burke–Ernzerhof (PBE) XC energy functional (E_{XC}^{GGA}), which is a simplified parametrization form of GGA, is represented as [54]:

$$E_{XC}^{GGA}(n_\uparrow, n_\downarrow) = \int d^3r \; n \, \epsilon_X(n) F_{XC}(r_s, s, \zeta) \tag{2.15}$$

the mathematical form of HSE functional (E_{XC}^{HSE}) on the other hand can be expressed as [55]:

$$E_{XC}^{HSE} = {}^1\!/_4 \, E_X^{HF,SR}(\omega) + {}^3\!/_4 \, E_X^{PBE,SR}(\omega) + E_X^{PBE,LR}(\omega) + E_C^{PBE} \tag{2.16}$$

where "n" is the sum of electron spin densities $n_\uparrow$ and $n_\downarrow$. The quantities ϵ_X and F_{XC} denote the exchange energy per electron and non-local spin-polarized enhancement factor, respectively. The parameters r_s, s, ζ symbolize local Seitz radius, dimensionless density gradient factor and relative spin-polarization respectively. The symbols "X", "C", "SR" and "LR" represent the exchange, correlation, short-range and long-range terms respectively in the energy functional. "ω" governs the extent of short-range interactions. The difference of E_g values between HSE and PBE functionals can be rationalized from the fact that the HSE functional, which consists of screened Coulomb potential for HF exchange, considers the exact mixing of both the HF and PBE exchange only for short-range interactions. This mixing allows the exchange hole to become delocalized among its nearest neighbours, which in turn results in E_g values that are

reported to be closer to experimental observations in contrast to the same being performed with PBE functional [55].

2.4. DFT calculations linked with strongly correlated systems

The simplest model which can describe the physics of these strongly correlated systems is the "Hubbard model" [56-61]. The Hubbard Hamiltonian ($H_{Hubbard}$) is mathematically represented as:

$$H_{Hubbard} = -t \sum_{<i,j>,\sigma} (c_{i,\sigma}^{\dagger} c_{j,\sigma} + c_{j,\sigma}^{\dagger} c_{i,\sigma}) + U \sum_i n_{i,\uparrow} n_{i,\downarrow} \quad (2.17)$$

where $< i, j >$ signifies nearest-neighbour atomic sites. The quantities $c_{i,\sigma}^{\dagger}$, $c_{j,\sigma}$ and $n_{i,\sigma}$ are the respective creation, annihilation and number operators for electrons of spin σ located at atomic site i or j. Here, "t" and "U" are the hopping amplitude and on-site Coulomb interaction respectively. The total energy within the LDA+U or GGA+U approach can be expressed as:

$$E_{LDA/GGA+U}[\rho(\boldsymbol{r})] = E_{LDA/GGA}[\rho(\boldsymbol{r})] + E_{Hubbard}\left[\left(n_{m,m'}^{I,\sigma}\right)\right] - E_{dc}[(n^{I,\sigma})] \quad (2.18)$$

where E_{dc} represents the double-counting term; $n_{m,m'}^{I,\sigma}$ are called occupation numbers, which define the projections of occupied KS orbitals (ϕ_{kb}^{σ}) on localized wavefunctions ψ_m^I, and are denoted as

$$n_{m,m'}^{I,\sigma} = \sum_{k,b} F_{k,b}^{\sigma} < \phi_{kb}^{\sigma} | \psi_{m'}^{I} >< \psi_m^I | \phi_{kb}^{\sigma} > \quad (2.19)$$

where $F_{k,b}^{\sigma}$ is the Fermi-Dirac occupation for KS energy states having band indices "b" and k-points "k".

Besides the success of LDA+U and/ or GGA+U methods in describing the physical phenomena of many strongly correlated systems, the most surprising situation for strongly correlated systems is observed when the electrons are neither localized nor itinerant but settle in between the two extremes. To understand the correct physics of such systems, the dynamical mean field theory (DMFT) is considered as one of the most prominent methods [62,63]. The DMFT Hamiltonian is mathematically represented as

$$H_{DMFT} = U \sum_{i,\sigma,i,l} n_{i,l}^{\sigma} n_{i,l}^{\sigma'} + \sum_{i,\sigma,i,l\neq m} (V - \delta_{\sigma,\sigma'}) n_{i,l}^{\sigma} n_{i,m}^{\sigma'} - \frac{J}{2} \sum_{i,\sigma,i,l\neq m} c_{i,l,\sigma}^{\dagger} c_{i,l,\sigma'} c_{i,m,\sigma'}^{\dagger} c_{i,m,\sigma} - \frac{J'}{2} \sum_{i,\sigma,i,l\neq m} c_{i,l,\sigma}^{\dagger} c_{i,l,\sigma'}^{\dagger} c_{i,m,\sigma} c_{i,m,\sigma'} - \sum_{i,\sigma,l} \Delta\epsilon \, n_{i,l}^{\sigma} \quad (2.20)$$

where V denotes the inter-orbital Coulomb interaction of electrons, J and J' represent the Hund exchange and pair hopping terms respectively of the orbitals (l and m) at site i. However, the calculations involving DMFT are outside the scope of this dissertation and hence have not been elaborated here.

2.5. Optimization and convergence criteria

The crystal structures are primarily optimized using the "variable-cell relaxation" (VC-relax) method followed by the Broyden-Fletcher-Goldfarb-Shanno scheme [64-67]. The projector augmented wave (PAW) pseudopotentials [68] have been considered to incorporate the electron-ion interactions of the compounds and the XC term of the pseudopotential has been accomplished from any of the above-referred functionals. The crystal structures of the system are allowed to relax until the Hellmann–Feynman force, total electronic energy, and cell pressure attain their specified convergence criteria. The plane wave kinetic energy cut-off for the valance electrons and the size of the **k**-point mesh, as obtained from the Monkhorst-Pack grid scheme, have been to be fixed for DFT calculations.

2.6. Calculations of phonon dispersion relations

Phonons are quasiparticles that represent the collective vibrational modes of atoms in a crystalline material. In simpler terms, they're the units of vibrational energy that propagate through a material, similar to how photons are units of light energy. These vibrations can be thought of as waves travelling through a material's atomic lattice, affecting its thermal, and elastic properties. Phonons play a crucial role in understanding phenomena like lattice thermal conductivity, superconductivity, and thermal expansion in materials.

Here, the phonon dispersion relations have been estimated from both the density functional perturbation theory (DFPT) and supercell approach as implemented in QE [1-3] and Phono3py [69] suites of software. The DFPT calculation is in general performed on the unitcell geometry of the crystal whose phonon data have been estimated through the diagonalization and sampling of dynamical matrix D(**k**) for any arbitrary wave vector **k**. The second-order (harmonic) interatomic force constants (IFCs) on the real-space grid have been extracted from the backward Fourier transform approach of calculated D(**k**). The supercell approach, however, follows the finite atomic displacements and calculates the phonon frequencies by considering both the second-order as well as third-order (anharmonic) IFCs of the systems.

2.7. Born-Oppenheimer molecular dynamics simulations

In Born-Oppenheimer molecular dynamics (BOMD) simulations, the motion of the atoms is calculated by solving Newton's equations of motion using the forces derived from the potential energy surface, which represents the total energy of the system as a function of nuclear coordinates. The potential energy surface is typically obtained from quantum mechanical calculations such as DFT.

Here, the BOMD simulations have been accomplished from the NPT ensemble whose temperature is controlled by the Andersen or Nose-Hoover thermostat. The simulations have been performed over a time step of 1 or 2 fs and the estimated free energies (F) of the compounds have been calculated using the following relation [70]:

$$F(T,\mathrm{V}) = E(\mathrm{V}) + F_{el}(T,\mathrm{V}) + F_{ph}(T,\mathrm{V}) \tag{2.21}$$

where E measures the total ground state energy of the supercell, V signifies the supercell volume at temperature T, $F_{el}(T,\mathrm{V})$ and $F_{ph}(T,\mathrm{V})$ are the free energies of the electrons and phonons respectively. $F_{el}(T,\mathrm{V})$ can be estimated using the following mathematical relation [71,72]:

$$F_{el}(T,\mathrm{V}) \approx k_B T \int d\upsilon\, N_{el}(\upsilon)\,[n \ln n + (1-n)\ln(1-n)] \tag{2.22}$$

where $N_{el}(\upsilon)$ is the electronic density of states and n is the Fermi occupation number.

$F_{ph}(T,\mathrm{V})$ has been calculated under the thermodynamic integration approach [72,73] and is expressed as:

$$F_{ph}(T,\mathrm{V}) = \int_0^1 d\upsilon\, \langle F_{el}(\{R_I\}) - F_{el}(\{R_I^0\}) - \sum_{i,j} \frac{m}{2}\, u_i u_j\, D_{ij}(T,\mathrm{V})\rangle_\upsilon \tag{2.23}$$

where "$F_{el}(\{R_I\}) - F_{el}(\{R_I^0\})$" corresponds to the difference in electronic free energies at a certain point of ionic coordinates $\{R_I\}$. $u_i = \{R_i\} - \{R_i^0\}$, m is the atomic mass and D represents the dynamical matrix of the system. "$\langle \ldots\ldots\ldots \rangle_\upsilon$" represents the thermodynamic average and has been estimated using the BOMD simulations.

2.8. Calculations of optical properties

The optical properties of a system have been estimated from the linear response theory and these properties of a crystal under electromagnetic radiation can be readily envisaged from

the frequency-dependent (ω) complex dielectric function $\varepsilon(\omega)$. The complex function $\varepsilon(\omega)$ is mathematically expressed as:

$$\varepsilon(\omega) = \varepsilon_1(\omega) + i\varepsilon_2(\omega) \tag{2.24}$$

where $\varepsilon_1(\omega)$ and $\varepsilon_2(\omega)$ are the real and imaginary parts of $\varepsilon(\omega)$.

While $\varepsilon_1(\omega)$ depicts the linear polarization and dispersion of the incident light passing through the crystal, $\varepsilon_2(\omega)$ on the other hand may be directly correlated with the electronic band structure and absorption of incident radiation by the crystals. The imaginary part of the dielectric function $\varepsilon_2(\omega)$ is estimated from the first-order time-dependent perturbation theory following the simple dipole approximation. In the long wavelength ($q \rightarrow 0$) limit, $\varepsilon_2(\omega)$ is represented as [74]:

$$\varepsilon_2(\omega) = \frac{8\pi^2 e^2}{\omega^2 m^2 V} \sum_{i\,\epsilon\,c, f\,\epsilon\,v} \sum | < \boldsymbol{k}, i\,|\boldsymbol{u}.\boldsymbol{r}|\,\boldsymbol{k}, f > |^2 \times \delta\,[E_i(\boldsymbol{k}) - E_f(\boldsymbol{k}) - \hbar\omega] \tag{2.25}$$

where V is the volume of unitcell. The quantities $|\,\boldsymbol{k}, i >$ and $|\,\boldsymbol{k}, f >$ represent the valance and conduction band states respectively over the wave vector $\boldsymbol{k}$, $\boldsymbol{u}$ and $\boldsymbol{r}$ are the polarization and position vectors of the electromagnetic wave respectively. The real part of $\varepsilon_1(\omega)$ can be accomplished from $\varepsilon_2(\omega)$ using the Kramers – Kronig relation [75,76] and is depicted as follows:

$$\varepsilon_1(\omega) = \frac{1}{\pi} P \int_{-\infty}^{\infty} \frac{\varepsilon_2(\omega\prime)}{\omega' - \omega}\, d\omega' \tag{2.26}$$

where P is the Cauchy principal value.

The frequency-dependent complex dielectric function of any dispersive materials carries a wealth of information relating to their optical properties. For example, the complex refractive index $\mathrm{N}(\omega)$ is related to $\varepsilon(\omega)$ through the following simple relation:

$$\mathrm{N}(\omega) = \sqrt{\varepsilon(\omega)} = n(\omega) + ik(\omega) \tag{2.27}$$

where the real part of the complex refractive index is expressed as:

$$n(\omega) = \left(\frac{\sqrt{\varepsilon_1^2 + \varepsilon_2^2} + \varepsilon_1}{2} \right)^{\frac{1}{2}} \tag{2.28}$$

and the corresponding imaginary part, known as the extinction coefficient (k), is expressed by the following equation:

$$k\ (\omega) = \left(\frac{\sqrt{\varepsilon_1^2 + \varepsilon_2^2} - \varepsilon_1}{2} \right)^{\frac{1}{2}} \tag{2.29}$$

The absorption coefficient $[\alpha(\omega)]$ refers to the attenuation of incident radiation in percentage as it propagates per unit distance through the materials. It is closely associated with the extinction coefficient of the material and also with $\varepsilon_2(\omega)$ through the following relation

$$\alpha\ (\omega) = \frac{2k\omega}{c\hbar} = \frac{\omega}{nc}\varepsilon_2(\omega) \tag{2.30}$$

where c is the speed of light in vacuum.

The imaginary part of the dielectric function $\varepsilon_2(\omega)$ is closely related to the optical conductivity $\sigma(\omega)$, which provides valuable information about the conduction of free charge carriers over a defined range of energies of incident photons. The optical conductivity $\sigma(\omega)$ is mathematically expressed as:

$$\sigma\ (\omega) = \frac{\omega\varepsilon_2}{4\pi} \tag{2.31}$$

2.9. Machine learning methods

The data-driven machine learning (ML) models between the characteristics features and the target variable can be framed and the accurate prediction of data will be estimated from their respective performances. The characteristics of the ML model can be estimated from the Pearson correlation coefficient (p) which is expressed as [77]:

$$p = \frac{\sum_{i=1}^{N}(x_i - \bar{x})(y_i - \bar{y})}{\sqrt{\sum_{i=1}^{N}(x_i - \bar{x})^2}\sqrt{\sum_{i=1}^{N}(y_i - \bar{y})^2}} \tag{2.32}$$

where x_i and y_i are the comparative features of x and y respectively, $\bar{x}$ and $\bar{y}$ are their respective average values, N represents the total number of samples in the training set. The performance of the ML model has been determined from root-mean-square error (RMSE), mean absolute error (MAE) and evaluation coefficient (R^2) values. RMSE, MAE and R^2 have been calculated using the following relations:

$$RMSE = \sqrt{\frac{1}{N}\sum_{i=1}^{N}(y_i - y)^2} \quad (2.33)$$

$$MAE = \frac{1}{N}\sum_{i=1}^{N}|y_i - y| \quad (2.34)$$

$$R^2 = 1 - \frac{\sum_{i=1}^{N}(y_i - y)^2}{\sum_{i=1}^{N}(y_i - \bar{y})^2} \quad (2.35)$$

respectively. Where y_i and y are the respective input and predicted values of the dataset. A schematic diagram of ML workflow in predicting the materials' properties such as band gaps of materials is shown in Figure 2.1.

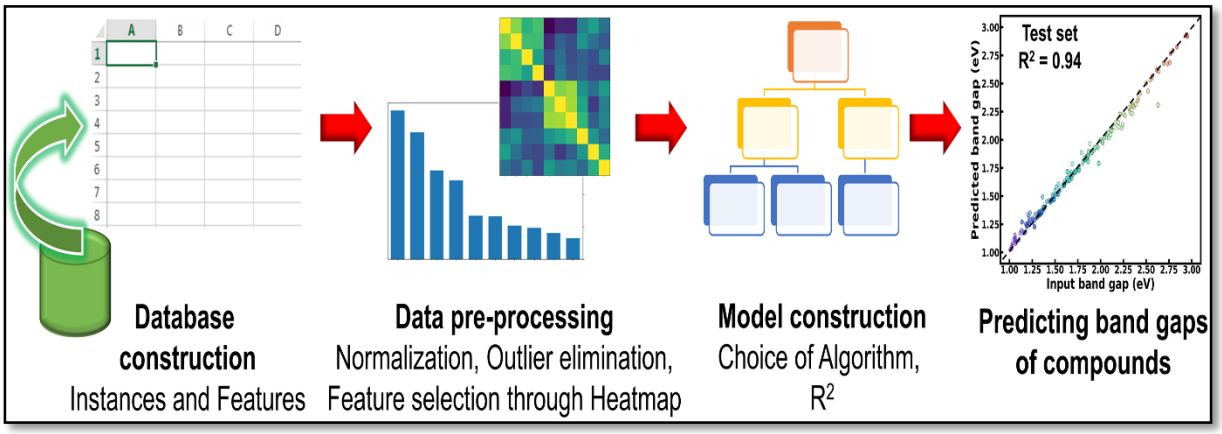

Figure 2.1. Schematic representation of machine learning workflow in predicting band gaps of the materials.

Here, the supervised models such as support vector regression (SVR), gradient boosted decision tree (GBDT), random forest regression (RFR) and multi-layer perceptron (MLP) algorithms were considered in the research works [78]. The algorithms were realized using the *Scikit-learn* software package within the *Python 3.9* framework [79]. The parameters of the algorithms were optimized and the model performances were estimated using the grid search of the average RMSE of each model validation set. The target variable was predicted from the SVR model using the following mathematical relation:

$$f_{SVR}(y) = \sum_{i=1}^{N}(a_i - a_i^*)K(y_i, y) + b \quad (2.36)$$

where a_i and a_i^* are non-negative multipliers for each observation y_i, K is the kernel or radial basis function which is used to calculate the difference between training (y_i) and predicted (y) values of the target variable, "b" can be estimated from the Lagrange function.

The values of the target variable, so predicted from the GBDT algorithm, are represented using the following expression:

$$f_{GBDT}(y) = f_0(y) + \sum_{m=1}^{M} \sum_{j=1}^{J} \Theta_{m,j} I(y \in R_{m,j}) \quad (2.37)$$

where $f_0(y)$ is an initial single decision tree; M, J and $\Theta_{m,j}$ are the number of regression trees, number of leaf nodes of the trees and the best fitting value respectively for each set of leaf nodes $R_{m,j}$.

Using the RFR model the predicted target variable can be represented as:

$$f_{RFR}(y) = \sum_{t=1}^{T} \sum_{n=1}^{N} C_n I(y \in D_n)/t \quad (2.38)$$

where t runs from 1 to T and T represents the number of formed classification or regression trees. C_n signifies the mean value of dataset D_n for randomly selecting N training samples from the said dataset.

The target variable, so predicted from the neural network-based MLP framework, can be expressed using the following mathematical function:

$$f_{MLP}(y) = \sum_{j=1}^{N} W_0^{ij} \theta\left(W_l^{ij} y_j + b_1\right) + b_0 \quad (2.39)$$

where W_0^{ij} and W_l^{ij} are the weights of i^{th} neurons in the output and l^{th} layers respectively, b_0 and b_1 represent the respective output layer and hidden biases.

Bibliography

[1] P. Giannozzi *et al.*, J. Chem. Phys. **152**, 154105 (2020).

[2] P. Giannozzi *et al.*, J. Phys.: Condens. Matter **29**, 465901 (2017).

[3] P. Giannozzi *et al.*, J. Phys.: Condens. Matter **21**, 395502 (2009).

[4] F. Nilsson and F. Aryasetiawan, in *Comput.*2018).

[5] A. F. Lima and M. V. Lalic, Opt. Mater.: X **15**, 100185 (2022).

[6] K. M. Rabe, Annu. Rev. Condens. Matter Phys. **1**, 211 (2010).

[7] H. Liu, Y. Li, F. Tian, and G. Li, Mod. Phys. Lett. B **30**, 1650206 (2016).

[8] L. Li, Mod. Phys. Lett. B **22**, 2937 (2008).

[9] M. Hoffmann, A. Ernst, W. Hergert, V. N. Antonov, W. A. Adeagbo, R. M. Geilhufe, and H. Ben Hamed, Phys. Status Solidi B **257**, 1900671 (2020).

[10] S. M. Woodley and R. Catlow, Nature Mater **7**, 937 (2008).

[11] F. Calle-Vallejo and M. T. M. Koper, Electrochim. Acta **84**, 3 (2012).

[12] S. Moshat, H. Luitel, and D. Sanyal, Int. J. Mod. Phys. B **36**, 2250202 (2022).

[13] Y. P. Feng, A. T. L. Lim, and J. C. Zheng, in *Recent Advances in Computational Science and Engineering* (PUBLISHED BY IMPERIAL COLLEGE PRESS AND DISTRIBUTED BY WORLD SCIENTIFIC PUBLISHING CO., 2002), pp. 23.

[14] H. Weng, X. Dai, and Z. Fang, J. Phys.: Condens. Matter **28**, 303001 (2016).

[15] S. Bhandari Sharma, I. Qattan, S. Kc, and S. Abedrabbo, in *Nanomater.*2022).

[16] Q. Xie, J. Yuan, N. Yu, L. Wang, and J. Wang, Comput. Mater. Sci. **135**, 160 (2017).

[17] X. L. Wang, Z. He, Y. M. Ma, T. Cui, Z. M. Liu, B. B. Liu, J. F. Li, and G. T. Zou, J. Phys.: Condens. Matter **19**, 425226 (2007).

[18] C. Park, S. W. Kim, and M. Yoon, Phys. Rev. Lett. **120**, 026401 (2018).

[19] Z. Wang, T.-Y. Lü, H.-Q. Wang, Y. P. Feng, and J.-C. Zheng, Sci Rep **7**, 609 (2017).

[20] W. Kohn and L. J. Sham, Phys. Rev. **140**, A1133 (1965).

[21] P. Hohenberg and W. Kohn, Phys. Rev. **136**, B864 (1964).

[22] M. O. Lynn, D. Ologunagba, B. B. Dangi, and S. Kattel, Phys. Chem. Chem. Phys. **25**, 5156 (2023).

[23] P. Verma and D. G. Truhlar, Trends Chem. **2**, 302 (2020).

[24] A. J. Cohen, P. Mori-Sánchez, and W. Yang, Chem. Rev. **112**, 289 (2012).

[25] N. Mardirossian and M. Head-Gordon, Mol. Phys. **115**, 2315 (2017).

[26] R. O. Jones, Rev. Mod. Phys. **87**, 897 (2015).

[27] E. G. Lewars, *Computational Chemistry* (Springer Dordrecht, 2010).

[28] J. C. Slater, Phys. Rev. **34**, 1293 (1929).

[29] R. G. Parr and Y. Weitao, (Oxford University Press, 1995).

[30] S. Ghosh, S. Sarkar, and J. Chowdhury, Mater. Chem. Phys. **276**, 125379 (2022).

[31] R. Ray Banik, S. Ghosh, and J. Chowdhury, Phys. Scr. **98**, 045920 (2023).

[32] S. Śmiga and L. A. Constantin, J. Phys. Chem. A **124**, 5606 (2020).

[33] H. Xiao, J. Tahir-Kheli, and W. A. Goddard, III, J. Phys. Chem. Lett. **2**, 212 (2011).

[34] A. J. Garza and G. E. Scuseria, J. Phys. Chem. Lett. **7**, 4165 (2016).

[35] F. Viñes, O. Lamiel-García, K. Chul Ko, J. Yong Lee, and F. Illas, J. Comput. Chem. **38**, 781 (2017).

[36] M. Marsman, J. Paier, A. Stroppa, and G. Kresse, J. Phys.: Condens. Matter **20**, 064201 (2008).

[37] M. Nishiwaki and H. Fujiwara, Comput. Mater. Sci. **172**, 109315 (2020).

[38] M. Gerosa, C. E. Bottani, C. Di Valentin, G. Onida, and G. Pacchioni, J. Phys.: Condens. Matter **30**, 044003 (2018).

[39] R. Car and M. Parrinello, Phys. Rev. Lett. **55**, 2471 (1985).

[40] G. P. Francis and M. C. Payne, J. Phys.: Condens. Matter **2**, 4395 (1990).

[41] M. D. Segall, J. D. L. Philip, M. J. Probert, C. J. Pickard, P. J. Hasnip, S. J. Clark, and M. C. Payne, J. Phys.: Condens. Matter **14**, 2717 (2002).

[42] S. Ghosh, R. R. Banik, and J. Chowdhury, Indian J. Theor. Phys. **69**, 43 (2021).

[43] V. I. Anisimov, J. Zaanen, and O. K. Andersen, Phys. Rev. B **44**, 943 (1991).

[44] I. N. Yakovkin and P. A. Dowben, Surf. Rev. Lett. **14**, 481 (2007).

[45] D. S. Lambert and D. D. O'Regan, Phys. Rev. Research **5**, 013160 (2023).

[46] S. Tomić and N. M. Harrison, AIP Conf. Proc. **1199**, 65 (2010).

[47] D. Wing, G. Ohad, J. B. Haber, M. R. Filip, S. E. Gant, J. B. Neaton, and L. Kronik, PNAS **118**, e2104556118 (2021).

[48] S. Ghosh and J. Chowdhury, Mater Sci Eng B. **284**, 115903 (2022).

[49] S. Ghosh and J. Chowdhury, Mod. Phys. Lett. B **38**, 2330003 (2023).

[50] R. R. Banik, S. Ghosh, and J. Chowdhury, Phys. Scr. **98**, 105914 (2023).

[51] H. Einollahzadeh, R. S. Dariani, and S. M. Fazeli, Solid State Commun. **229**, 1 (2016).

[52] J. M. Crowley, J. Tahir-Kheli, and W. A. Goddard, III, J. Phys. Chem. Lett. **7**, 1198 (2016).

[53] Y. Duan, L. Qin, L. Shi, and G. Tang, Comput. Mater. Sci. **101**, 56 (2015).

[54] J. P. Perdew, K. Burke, and M. Ernzerhof, Phys. Rev. Lett. **77**, 3865 (1996).

[55] J. Heyd, G. E. Scuseria, and M. Ernzerhof, J. Chem. Phys. **118**, 8207 (2003).

[56] J. Hubbard and B. H. Flowers, Proc. R. Soc. A: Math. Phys. Eng. Sci. **276**, 238 (1997).

[57] J. Hubbard and B. H. Flowers, Proc. R. Soc. A: Math. Phys. Eng. Sci. **277**, 237 (1997).

[58] J. Hubbard and B. H. Flowers, Proc. R. Soc. A: Math. Phys. Eng. Sci. **281**, 401 (1997).

[59] J. Hubbard and B. H. Flowers, Proc. R. Soc. A: Math. Phys. Eng. Sci. **285**, 542 (1997).

[60] J. Hubbard and B. H. Flowers, Proc. R. Soc. A: Math. Phys. Eng. Sci. **296**, 82 (1997).

[61] J. Hubbard and B. H. Flowers, Proc. R. Soc. A: Math. Phys. Eng. Sci. **296**, 100 (1997).

[62] A. Georges, G. Kotliar, W. Krauth, and M. J. Rozenberg, Rev. Mod. Phys. **68**, 13 (1996).

[63] K. Held, Adv. Phys. **56**, 829 (2007).

[64] D. F. Shanno, Math. Comp. **24**, 647 (1970).

[65] D. Goldfarb, Math. Comp. **24**, 23 (1970).

[66] R. Fletcher, Comput. J. **13**, 317 (1970).

[67] C. G. Broyden, IMA J. Appl. Math. **6**, 76 (1970).

[68] A. Dal Corso, Comput. Mater. Sci. **95**, 337 (2014).

[69] A. Togo, L. Chaput, and I. Tanaka, Phys. Rev. B **91**, 094306 (2015).

[70] S. Ghosh and J. Chowdhury, Phase Transit. **96**, 446 (2023).

[71] R. Phillips, *Crystals, Defects and Microstructures: Modeling Across Scales* (Cambridge University Press, Cambridge, 2001).

[72] B. Grabowski, P. Söderlind, T. Hickel, and J. Neugebauer, Phys. Rev. B **84**, 214107 (2011).

[73] B. Grabowski, T. Hickel, and J. Neugebauer, Phys. Status Solidi B **248**, 1295 (2011).

[74] P. O. Nilsson, *Solid State Physics* Academic Press, New York, 1974), 1st edn., Vol. 29, p.^pp. 387.

[75] R. d. L. J. J. o. t. O. S. o. A. Kronig, J. Opt. Soc. Am. **12**, 547 (1926).

[76] H. A. Kramers, Atti Del Congresso Internationale Dei Fisici, Como., 545 (1927).

[77] J. Hauke and T. Kossowski, Quaest. Geogr. **30**, 87 (2011).

[78] S. Ghosh and J. Chowdhury, RSC Adv. **14**, 6385 (2024).

[79] G. V. Fabian Pedregosa, Alexandre Gramfort, Vincent Michel, Bertrand Thirion, Olivier Grisel, Mathieu Blondel, Peter Prettenhofer, Ron Weiss, Vincent Dubourg, Jake Vanderplas, Alexandre Passos, David Cournapeau, Matthieu Brucher, Matthieu Perrot, Édouard Duchesnay, J. Mach. Learn Res. **12**, 2825 (2011).

Chapter 3

Structural and electronic properties of Mercurous Chloride

3.1. Introduction

In this chapter, the structural and electronic properties of Mercurous chloride (Hg_2Cl_2) have been studied. Hg_2Cl_2 commonly referred to as "calomel", is an insulator and finds extensive applications as white pigment and electrodes in electrochemistry [1,2]. Moreover, the compound is known to exhibit unique anisotropic behaviour with strong birefringence, effective for making polarizing prism [3,4]. Recently, Hg_2Cl_2 has shown early promises to be used as acousto-optic tunable filters for the development of hyperspectral imagers covering the UV-Vis-LWIR region [5]. Here, the electronic band gap of the compound in its body-centred tetragonal [*I4/mmm* (D_{4h}^{17})] phase has been comprehensively studied under different exchange-correlation (XC) functionals and on-site Coulomb repulsion ($+U_{dd}$) in DFT calculations. Additionally, the nature of the insulator, whether it is Mott-Hubbard (M-H) or of charge transfer (CT) type is also unveiled in detail.

3.2. Crystal structure of Hg_2Cl_2 compound

Mercurous Chloride at room temperature and under ambient pressure crystallizes to the tetragonal phase and falls under *I4/mmm* (space group no. 139) space group symmetry. The crystal structure and the associated lattice parameters of the Hg_2Cl_2 compound in its *I4/mmm* phase are reported from the experimentally determined X-ray [6] and neutron diffraction [7] data. The unitcell of Hg_2Cl_2 comprises of one formula unit (Z = 2) with 8 atoms, where Hg and Cl are at 4e (0, 0, 0.11577) and 4e (0, 0, 0.3380) Wyckoff sites. Starting from the experimentally determined lattice parameters a = b and c (a = b = 4.4795 Å, c = 10.9054 Å), the unit cell associated with the *I4/mmm* phase of Hg_2Cl_2 has been optimized from GGA calculations using PBE, PBEsol, BLYP, B3LYP and HSE functionals. Before the relaxation of the structure, the plane wave kinetic energy (KE) cut-off for valence electrons and **k**-point mesh were fixed. While the specific KE cut-off for the valance electrons of the Hg_2Cl_2 compound has been estimated from the total self-consistent field (SCF) energy versus KE cut-off plots for different XC functionals, the mesh of the **k**-point grid has been accomplished from the variations of total SCF energy as a function of **k** points for a fixed KE cut-off. The changes in total SCF energies of Hg_2Cl_2 compound as functions of plane wave KE cut-off and **k**-point mesh are shown in Figure 3.1(a) and 3.1(b) respectively. From Figure 3.1(a), it is seen that the KE cut-off ~ 50 Ry is sufficient to carry out further calculations to estimate the size of the **k** – point grid. For a fixed energy cut-off at 50 Ry, Figure 3.1(b) shows successful convergences

of total energies for the **k** – point mesh $\geq 5 \times 5 \times 5$. These results collectively suggest that the **k**- point mesh of $9 \times 9 \times 9$ and 50 Ry KE cut-off are sufficient to carry out the first-principle DFT calculations for predicting the optimized structure of the Hg_2Cl_2 compound. However, denser k-point mesh can be further considered for non-SCF calculations of the compounds.

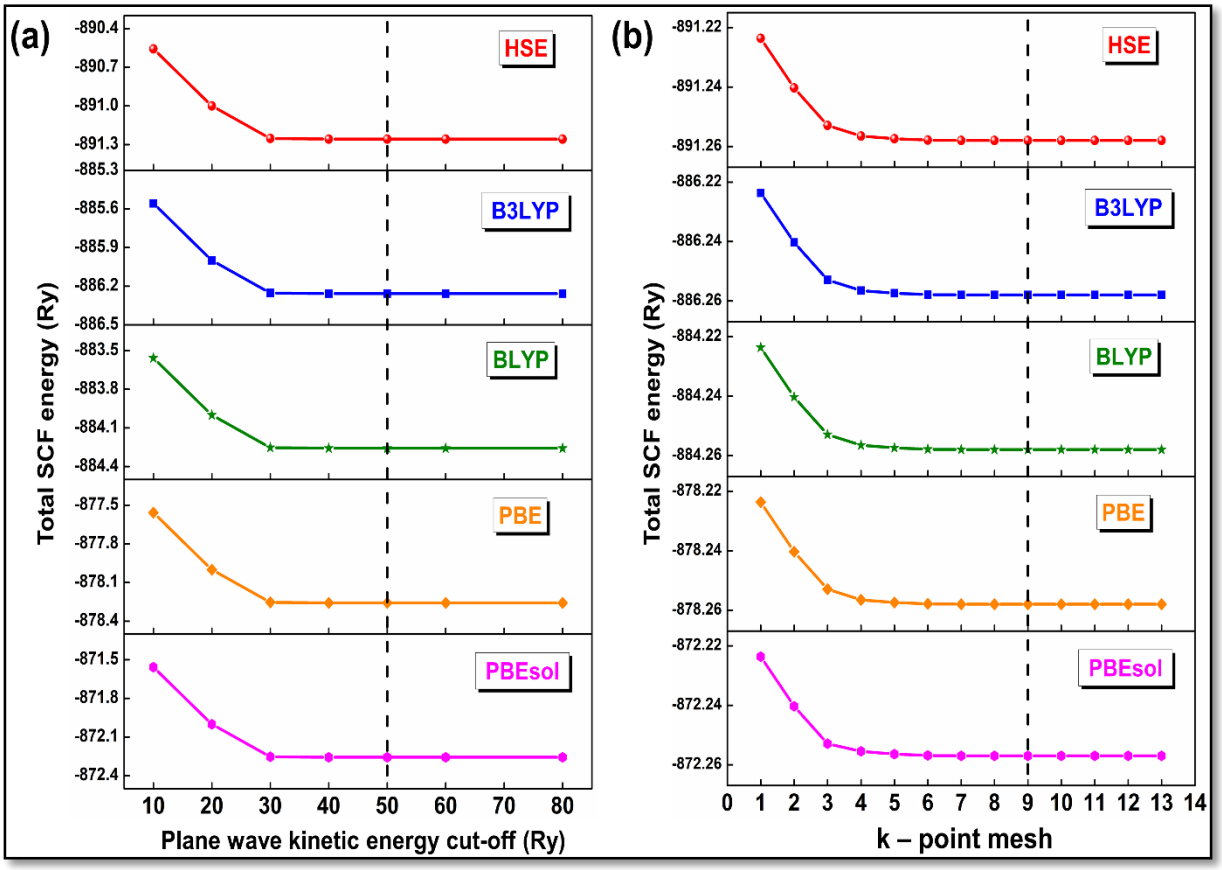

Figure 3.1. Total SCF energy versus **(a)** plane wave kinetic energy cut-off and **(b)** **k**-point mesh plots for HSE, B3LYP, BLYP, PBE and PBEsol functionals [The KE cut-off of 50 Ry and **k**-point mesh of $9 \times 9 \times 9$are marked with vertical dashed vertical lines].

The optimized lattice parameters and unitcell volume of the Hg_2Cl_2 system have been estimated from PBE, PBEsol, BLYP, B3LYP and HSE functionals. The results are shown in Table 3.1. From Table 2.1, it is clearly seen that the estimated lattice parameters and unitcell volume of Hg_2Cl_2, as obtained from HSE functional, are in exact agreement with the experimental results as reported elsewhere [8]. However, no significant alterations in lattice parameters and unitcell volume of the compound have been observed for PBE, PBEsol, BLYP, B3LYP functionals in comparison to the experimental result [8]. Hence, to reduce the computational cost the non-hybrid XC functionals like PBE, PBEsol, BLYP can be used in

estimating the optimized lattice and structural parameters of the materials in the DFT calculations.

Table 3.1. Lattice parameters and unitcell volume of Hg_2Cl_2 as estimated from HSE, B3LYP, BLYP, PBE and PBEsol functionals.

Exchange-correlation functionals	a = b (Å)	c (Å)	Volume ($Å^3$)
HSE	4.482	10.910	219.164
B3LYP	4.482	10.890	218.762
BLYP	4.478	10.900	218.572
PBE	4.481	10.910	219.065
PBEsol	4.479	10.890	218.470
Experiment [8]	4.482	10.910	219.164

The associated optimized structural parameters such as bond length, bond and dihedral angles of the Hg_2Cl_2 compound as enumerated from the GGA-HSE level of theory are also shown in Table 3.2. From Table 3.2, it is found that the estimated parameters from HSE functional are in excellent agreement with the experimental results in general and with the observations as reported by Dorm *et al.* [8].

Table 3.2. Optimized lattice and structural parameters for the tetragonal phase of Hg_2Cl_2 compound.

Measured parameters	Havighurst (1926) [6]	Dorm *et al.* (1971) [8]	Kleier *et al.* (1980) [9]	Pelant *et al.* (1987) [4]	Nicholas *et al.* (1989) [7]	This Study
Lattice parameters (Å)						
a = b	4.470	4.482	-	4.478	4.479	4.482
c	10.890	10.910	-	10.910	10.905	10.910
Statistical average of bond lengths (Å)						
Hg(C) – Cl(L)	-	2.430	2.430	2.420	2.362	2.424
Hg(A) – Hg(C)	-	2.526	2.600	2.530	2.595	2.526
Hg(C) – Cl(V)	-	3.209	3.210	3.210	3.206	3.210
Statistical average of bond angles (degree)						
Hg(A) – Hg(C) – Cl(L)	-	180	180	180	180	180
Cl(V) – Hg(C) – Cl(V)	-	-	-	-	-	161.92
Hg(A) – Hg(C) – Cl(V)	-	-	-	-	-	99.04
Statistical average of dihedral angle (degree)						
Cl(L) – Hg(C) – Hg(A) – Cl(L)	180	180	180	180	180	180

The optimized geometrical structure of Hg_2Cl_2, as obtained from GGA-HSE level of theory is shown in Figure 3.2. The crystal structure marks the presence of apparently distorted octahedral environments with corner-sharing Hg (Cent) atoms. The magnified view of the quasi-octahedral environment is shown in Figure 3.2(c). From Figure 3.2(c), it is seen that the neighbouring chlorine [Cl(V)] and apical mercury [Hg(Ap)] atoms at the vertices form the distorted octahedron Hg(Cent)Hg(Ap)$[Cl(V)]_5$ with Hg (Cent) at its centre. Several distorted octahedra are dispensed in three-dimensional space over the crystal lattice whose depiction is

shown in Figure 3.2(a). Each of the distorted corner-sharing octahedron will now be designated as Hg(C)Hg(A)[Cl(V)]$_5$ henceforth just for the sake of simpler nomenclature. The distortion in the octahedron is manifested by the decrease in Cl(V)–Hg(C)–Cl(V) angle ~ 161.92^0 along the a-b plane [Figure 3.2(c)]. Interestingly, the Hg(C) – Cl(V) bond lengths for each of the Cl(V) pairs are equal and are ~ 3.21 Å. However, one of the neighbouring Cl(V) atom form a Cl(V)–Hg(C)–Hg(A) linear chain with the associated angles ~ 180^0. To distinguish the chlorine atom [Cl(V)] involved in the linear chain from the rest, we designate it as Cl(L). The linear Cl(L)–Hg(C)–Hg(A)–Cl(L) chain of Hg_2Cl_2 in the *I4/mmm* phase is considered to be responsible for large anisotropy, birefringence and low transverse acoustic wave velocity of the compound [3,4]. In this new nomenclature, the associated octahedron in the crystal lattice of the Hg_2Cl_2 compound will be designated as Hg(C)Hg(A)[Cl(V)]$_4$Cl(L) hereafter. The Cl(L)–Hg(C), Hg(C)–Hg(A) bond lengths are not equal and estimated to be 2.424Å, 2.526 Å respectively. The deviation in bond length of ~ 0.102Å primarily signifies that Hg(C) is off-centred and shifted more towards the vertex, albeit lying undeviated on the local c-axis. Closer inspection of the supercell unveils another interesting feature concerning dispositions of the octahedral domains. The repetitive octahedra are connected through Cl(L)–Hg(C)–Hg(A)–Cl(L) linear chain with the corresponding dihedral angle ~ 180^0 (Figure 3.2(a)).

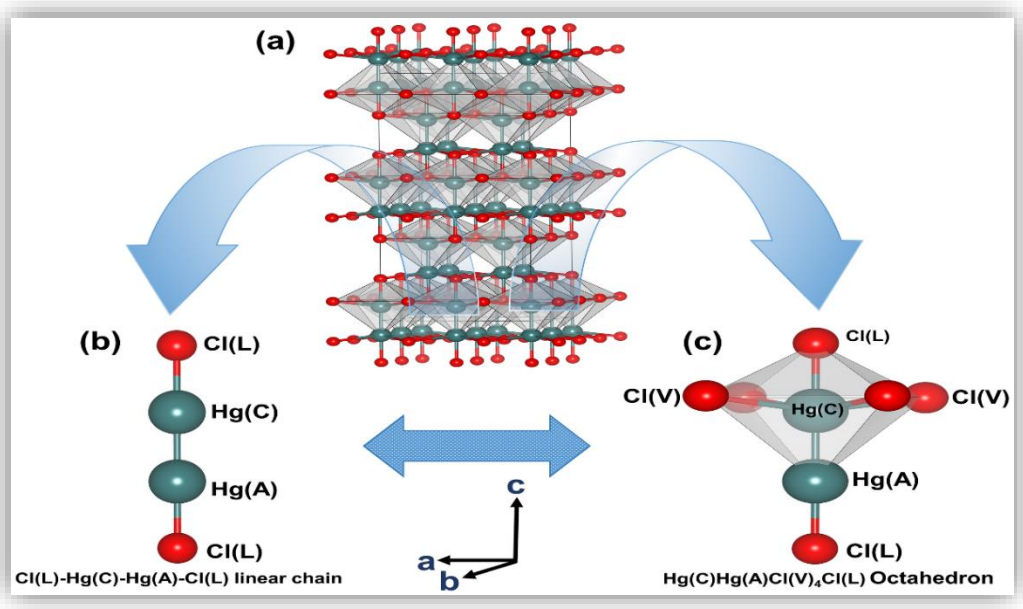

Figure. 3.2 (a) Supercell (2 × 2 × 2) of the tetragonal phase (*I4/mmm*) of Hg_2Cl_2 compound. The magnified view of the supercell showing **(b)** linear chain comprising of Cl(L)–Hg(C) Hg(A)–Cl(L) atoms **(c)** the octahedral environment. [Cl atoms are shown in red and the Hg atoms are shown in emerald blue].

3.3. Dynamical stability of Hg_2Cl_2 compound

To ensure the dynamical stability of the Hg_2Cl_2 compound, the phonon dispersion curve along the Γ→M→X→Γ→P high symmetry direction has been estimated from GGA calculations in conjunction with HSE functional. The dispersion curves together with phonon density of states (PhDOS) are shown in Figure 3.3. From the dispersion plot, it is seen that all the twenty-four phonon modes at any **k** points on the dispersion spectra (Figure 3.3) show positive values thereby affirming the dynamical stability of the system. The phonon frequencies of the Hg_2Cl_2 crystal system span a narrow wave number window ranging from 0 to 300 cm^{-1}. The optical phonon modes at relatively higher frequencies ~ 85 – 300 cm^{-1} emanated mainly from Cl atoms, while those at ~ 85 – 150 cm^{-1} frequency window, both Cl and Hg atoms are seen to contribute. At a comparatively lower frequency window (55 – 65 cm^{-1}), the optical phonons explicitly originate from the Hg atoms. The wide dispersions of optical phonon modes in three distinctively different frequency windows are owed to different atomic masses of the constituent Hg and Cl atoms of the Hg_2Cl_2 system. The acoustic phonon modes are also observed at the lowest frequency window spanning in the range 0 - 45 cm^{-1}. The cross-over regions between the optical and acoustical phonon vibrational modes are observed in the frequency range 35 – 45 cm^{-1}. Moreover, this mixing of low-frequency optical phonons with transverse acoustic and longitudinal acoustic modes may primarily suggest considerable thermal conductivity [10] of the Hg_2Cl_2 compound.

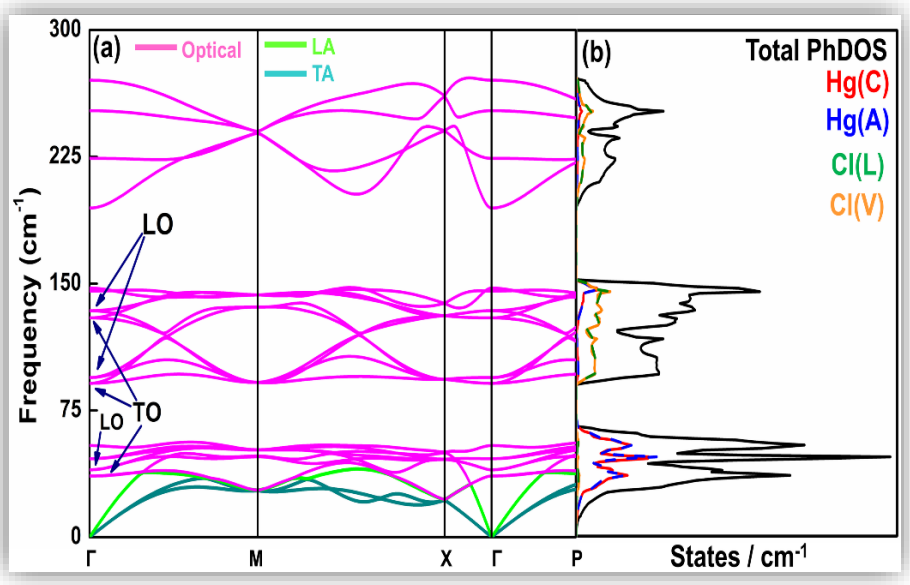

Figure 3.3. (a) Phonon dispersion curve along the high-symmetry points Γ→M→X→Γ→P and **(b)** the total and partial PhDOS of the tetragonal phase of Hg_2Cl_2 compound calculated at ambient pressure in GGA – HSE level of theory. (Magenta colour traces indicate optical phonon modes, while those with cyan and light green colours illustrate transverse and longitudinal acoustic phonon modes in the phonon dispersion curve. [Distinct LO – TO splitting are marked in the figure.]

Since Hg_2Cl_2 is an ionic solid the phonon dispersion calculations have been performed by considering the coupling between the macroscopic electric field and the atomic displacements. These calculations help to identify the Longitudinal Optical - Transverse Optical (LO-TO) splitting, resulting from loss of degeneracies of the optical phonon vibrations. The LO-TO splitting are observed near the Γ point at 84 cm^{-1} and 135 cm^{-1} in the phonon dispersion spectrum. The LO modes are estimated to have greater frequencies than the TO modes ($\omega_{LO} > \omega_{LO}$). The rationale behind it is due to the fact that the local field around the neighbouring atoms induce polarization in opposite direction for the LO modes, while the polarization is induced in the same direction for the TO modes. The Longitudinal Acoustic-Transverse Acoustic (LA –TA) modes are also observed in the lowest phonon branches at ~ 14.723 cm^{-1} near the Brillouin zone boundary. The various LO-TO and LA-TA splitting of the phonon modes are marked in Figure 3.3(a).

3.4. Electronic properties of Hg_2Cl_2 compound

The electronic band gap (E_g) value of the *I4/mmm* phase of Hg_2Cl_2 under ambient pressure has been estimated from the DFT calculations with varied levels of theory using different XC functionals. The estimated values of E_g are shown in Table 3.3. From Table 3.3, it is observed that the E_g values, as attained from the HSE, B3LYP and BLYP functionals, predict a larger band gap (3.43eV - 3.93 eV), while for the functionals PBE and PBEsol the calculated E_g values are grossly underestimated. The predicted E_g value (~ 3.93 eV) for the *I4/mmm* phase of the Hg_2Cl_2 compound, as obtained from the HSE functional, closely matches its optical band gap (~ 4.0 eV) at room temperature as reported elsewhere [11]. Thus we primarily believe that the hybrid HSE functional can reproduce the band gaps of the materials quite satisfactorily with the experimental observation.

Table 3.3. The estimated values of band gap of Hg_2Cl_2 in the tetragonal phase as obtained from different exchange-correlation functionals.

Exchange-correlation Functionals	Band Gap (eV)
HSE	3.93
B3LYP	3.78
BLYP	3.43
PBE	2.80
PBEsol	2.79

Figure 3.4(a) shows the E – **k** diagram of the tetragonal phase of Hg_2Cl_2 along the high symmetry direction Γ→M→X→Γ→P in the reciprocal **k** space, as estimated from GGA – HSE calculations. Direct E_g ~ 3.93 eV is observed at the high symmetry point M. No trace of dispersive energy states is noted near the Fermi level (E_F) in the E-**k** diagram. These results signify that the *I4/mmm* phase of Hg_2Cl_2 compound represent a wide band gap insulator.

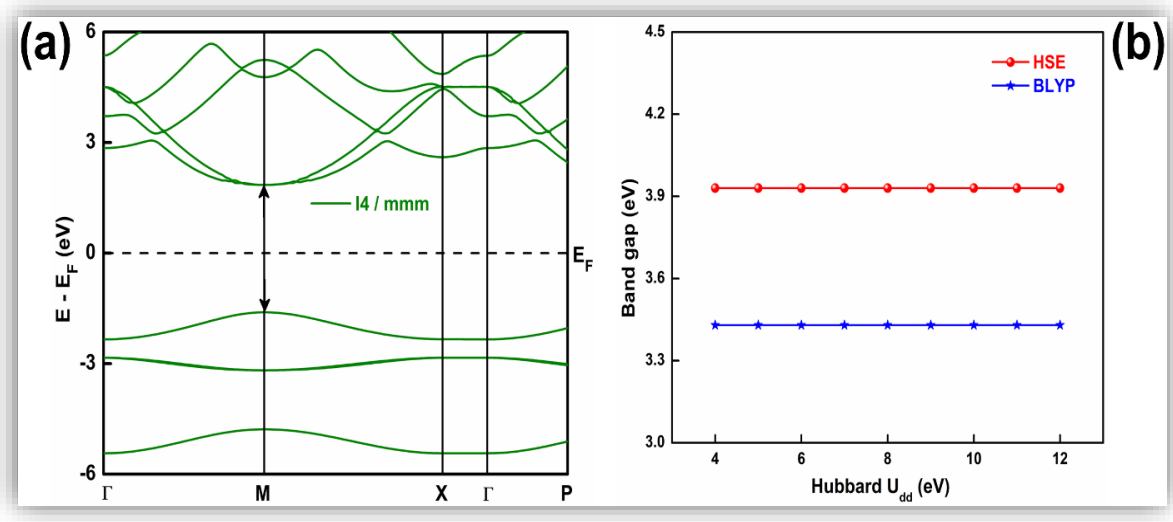

Figure 3.4. (a) Electronic band structure for the tetragonal phase of Hg_2Cl_2 as estimated from GGA calculations in conjunction with HSE functional along the high-symmetry direction Γ→M→X→Γ→P [The band gap and the Fermi energy (E_F) are shown in black arrow and black dashed line respectively]. **(b)** Variations of E_g for Hg_2Cl_2 compound as a function of on-site Coulomb repulsion $+U_{dd}$. The E_g values have been estimated from the GGA - HSE (red trace) and GGA - BLYP (blue trace) calculations.

Interestingly, Hg is a post transition metal whose "d" orbitals are completely filled. We are interested to see the effect of on-site coulomb repulsion on the estimated E_g value of Hg_2Cl_2 compound. The strength of Hubbard "$+U_{dd}$" interaction has been varied over a wide range from 4 to 12 eV. Figure 3.4(b) shows the variation of E_g for different values of $+U_{dd}$ as obtained from the GGA calculations with hybrid HSE and non-hybrid BLYP functionals. No change in E_g value of Hg_2Cl_2 has been observed upon the inclusion of $+U_{dd}$ term for the GGA calculations with both the functionals HSE and BLYP. These observations indicate that the incorporation of the Hubbard $+U_{dd}$ term does not affect the estimated band gap value of Hg_2Cl_2. The apparent inertness on the variation of the band gap of Hg_2Cl_2 upon inclusion of the Hubbard $+U_{dd}$ parameter may be rationalised. The Hg atoms of Hg_2Cl_2 have completely filled $5d^{10}$ orbitals. This precludes the electrons to hop from any degenerate d orbitals to the other upon excitation, resulting in no energy cost $+U_{dd}$ associated with them ($d^n d^n \nrightarrow d^{n-1}d^{n+1}$). This result suggests that Hg_2Cl_2 is an insulator but not of strongly correlated M–H type. However, in this context, it may be mentioned that electrons from the occupied 6s orbital of Hg are free to hop towards the vacant 3p orbital of Cl atoms, whose possibility will be explored later.

3.5. Electronic density of states

To introspect the bonding configurations of the Hg_2Cl_2 compound and to explore the possibility of whether the compound falls under the class of charge transfer insulator or not, the total and orbital resolved projected atomic density of states (TDOS and PDOS) of the studied system have been performed within DFT framework for GGA – HSE level of theory. The results of the calculations are shown in Figure 3.5. The TDOS calculations clearly show the depletion of electronic energy states in the vicinity of the E_F, signifying the insulating behaviour of the compound. The orbital resolved PDOS for the atoms Hg(C), Hg(A) - 5d, 6s orbitals and Cl(L), Cl(V) - 3p and 4s orbitals have been estimated and are shown in Figure 3.5(b) and 3.5(c) respectively. The top of the valance bands of the compound, ranging between - 4 and 0 eV, are mainly dominated by Cl(L) - 3p, 4s; Cl(V) - 4s and Hg(C), Hg(A) - 6s orbitals. Partial overlap of the 6s orbitals of Hg(C) and Hg(A) may suggest weak to moderate s-s hybridization between two Hg atoms [12,13]. Significantly enough, substantial overlap between the 3p orbital of Cl(L) atom with Hg(C), Hg(A) - 6s orbitals have been noticed. These observations may signify strong covalent interactions resulting in the formation of directional σ bond between Hg(C), Hg(A) and Cl(L) atoms as a result of s-p hybridizations. The result follows the earlier report that depicts the molecular structure of Mercurous Halides [9].

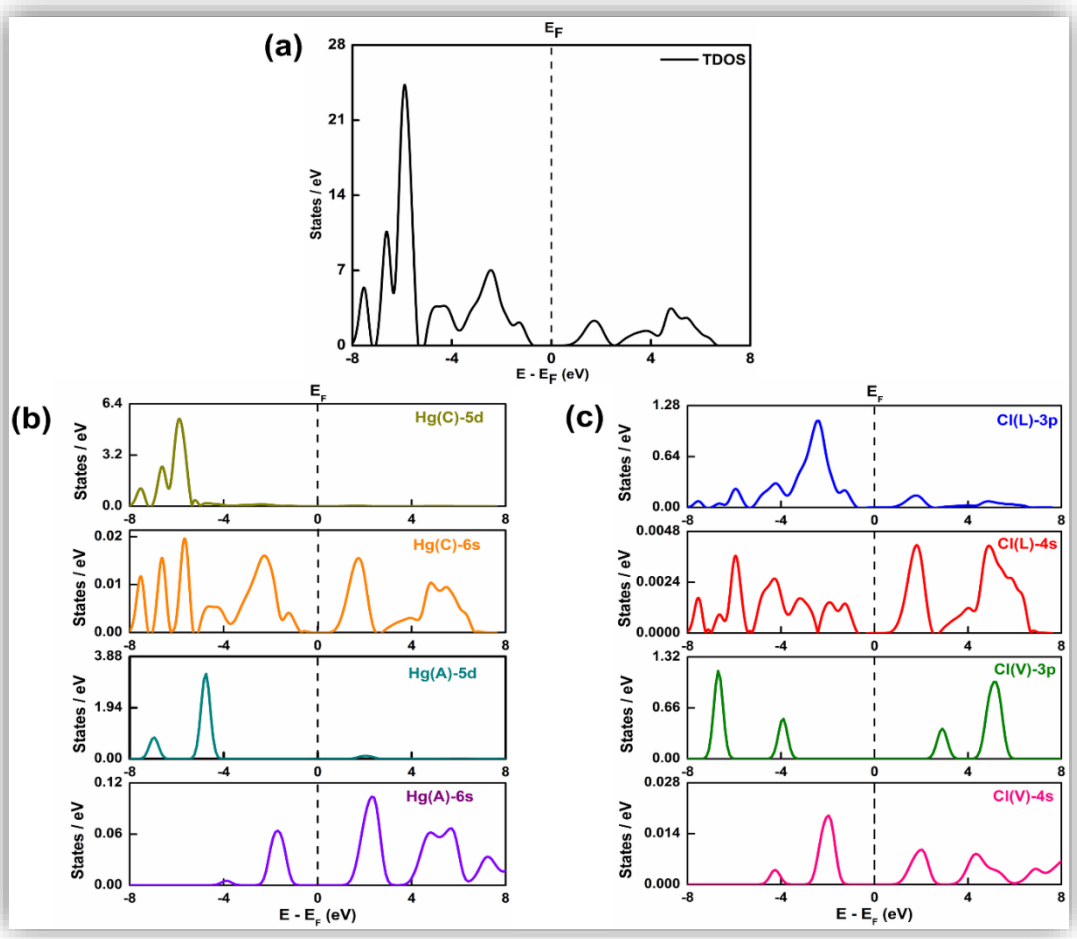

Figure 3.5. (a) TDOS spectrum of the tetragonal phase of Hg_2Cl_2 as estimated from GGA level of theory in conjunction with HSE functional. **(b)** Orbital resolved PDOS plots of the 5d and 6s orbitals of Hg(C) and Hg(A) atoms. **(c)** PDOS spectra of the 3p and 4s orbitals of Cl(L) and Cl(V) atoms.

Interestingly, Figure 3.5 further shows that the bottom of the conduction band is dominated by Hg(C), Hg(A) - 6s; Cl(L), Cl(V) – 4s orbitals with weak trace from the contributions of Cl(L) and Cl(V) - 3p orbitals. The relative weights from the contributions of Hg - 6s or Cl - 3p orbitals in the conduction band of the compound can be readily envisaged from the PDOS plots. While the 6s orbitals from both the Hg(C) and Hg(A) atoms show intense peaks around -4 to 4 eV, the peaks emanating from the 3p orbital of Cl(V) are comparatively weak and ill resolved. No prominent trace of bands originating from the 5d orbitals of either of Hg atoms is observed. These observations collectively suggest strong s-p and comparatively weak s-s hybridizations between Hg(C), Hg(A) - 6s with Cl(L) -3p and Hg(C) - 6s with Hg(A) - 6s atoms respectively. The strong s-p hybridizations may result in charge transfer (CT)

interactions [14-17] between Hg(C and A) and the surrounding Cl(L) atoms forming the linear Cl(L)–Hg(C)–Hg(A)–Cl(L) chains of Hg_2Cl_2compound. Moreover, the weak but definite overlap between Hg(C) - 6s and Cl(V) - 3p, 4s may also suggest remote possibility of CT interactions between Hg(C and A) and neighbouring Cl(V) atoms. In the absence of on-site Coulomb repulsion $+U_{dd}$ (*vide ante*) resulting in upper and lower Hubbard bands, the transfer of electrons between Hg and Cl is associated with energy cost leading to CT interaction energy (Δ_{CT}). This in turn results in wide band gap opening, thereby identifying the compound to behave like a CT insulator. Significantly enough, the energy dispositions in the PDOS plots (Figure 3.5) in the case of Hg_2Cl_2 do not follow the nature of Zaanen – Sawatzky – Allen (ZSA) diagram [18], as frequently observed for CT insulators with p-d hybridizations. The above observations further indicate that the ZSA diagram, which is considered the hallmark of CT insulators for TM compounds, is not necessary to be strictly obeyed in the case of CT insulators for post-transition metals like Hg. However, in this connection, it may be relevant to mention that apart from being a CT insulator Hg and Cl atoms of the Hg_2Cl_2 compound can undergo long-range ionic interactions between the Hg^+ cation and Cl^- anions as evinced from the LO-TO splitting of the phonon modes near the rpoint (*vide ante*).

3.6. Bond population analysis

To gain deeper insights concerning the covalent and/or ionic characters of bonding in Hg_2Cl_2, the Mulliken bond population analyses [19] have been carried out in terms of atomic, orbitals and effective valance charges of Hg and Cl atoms present in the compound. The results of the Mulliken bond population analysis have been illustrated in Table 3.4. From Table 3.4 it is observed that the atomic Mulliken charges for Hg(C), Hg(A), Cl(L) and Cl(V) atoms are 0.13, 0.15, – 0.10 and – 0.18 respectively. In general, the normal atomic charge values for pure ionic states of Hg and Cl atoms are +12 and –7 respectively. The deviation of Mulliken charge values from pure ionic states of Hg and Cl atoms indicates the prevalence of covalent interactions between Hg and Cl atoms. The key contribution for the CT interaction between Hg(C / A) and Cl(L / V) atoms has been significantly noticed from the individual 6s and 3p orbital charges of Hg (+1.05 e, +1.01 e) and Cl (+5.30 e, +5.19 e) atoms respectively. This implies CT interaction from 6s orbitals of Hg(C / A) to 3p orbitals of Cl(L / V) atoms. The estimated observations are in line with the PDOS as discussed earlier (*vide ante*). Moreover, the effective valence charges on Hg(C) / Hg(A) atoms have been estimated to be +11.87e / +

11.85e. The non–zero values of effective valance [20] signify the presence of both the covalent and ionic bonds in Hg_2Cl_2, albeit the covalent bond dominates in the compound [21].

Table 3.4. Charge spilling parameter (%), individual Orbital, Mulliken and Effective Valance charges on Hg and Cl atoms in Hg_2Cl_2 compound.

Atoms	Charge spilling parameter (%)	s	p	d	Total charge	Mulliken charge	Effective Valance charge
Hg(C)	0.002	1.05	0.91	9.91	11.87	+ 0.13	+ 11.87
Hg(A)		1.01	0.91	9.93	11.85	+ 0.15	+11.85
Cl(L)		1.79	5.30	0.00	7.10	- 0.10	-
Cl(V)		1.99	5.19	0.00	7.18	- 0.18	-

3.7. Electronic charge density distribution and the Bader charge analyses

To understand more closely the covalent and long-range ionic interactions between Hg and Cl atoms and the CT mechanism (*vide ante*) of Hg_2Cl_2, the electron charge density in the valance band of the compound has been estimated and is shown in Figure 3.6. From Figure 3.6 it is seen that the electronic charge density distributions around Hg(C / A) and Cl(L) atoms in the linear Cl(L)–Hg(C)–Hg(A)–Cl(L) chains of Hg_2Cl_2 compound are non – spherical, suggesting covalent interactions between them [21]. This is further substantiated by the considerable overlap of electron clouds between Hg(C), Cl(L) and Hg(A), Cl(L) atoms. All these observations are in close agreement with the orbital resolved PDOS of the compound (Figure 3.5).

The electron cloud density distribution, as shown in Figure 3.6, further unveils some interesting aspects. Depletion of electronic charge cloud density between Hg(C), Cl(V); Hg(A), Cl(V) and Hg(C), Hg(A) atoms have been noticed. While the depletion of electron cloud between the former pairs of Hg(C), Cl(V) and Hg(A), Cl(V) atoms may portend long-range ionic interactions between them, however for the latter pair [ca. Hg(C) and Hg (A) atoms] appreciable charge transfer from Hg(C / A) to the neighbouring Cl atoms may be presaged.

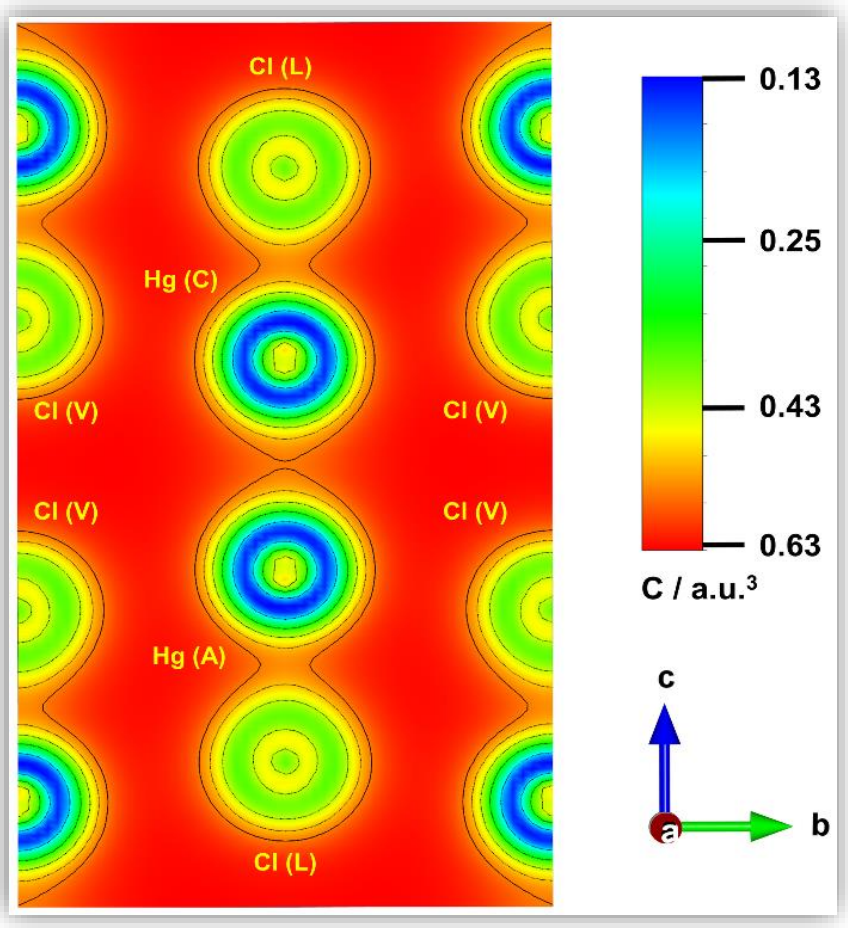

Figure 3.5. The electronic charge density distribution map of Hg_2Cl_2 compound. (Isosurface value = 0.009).

This result is further substantiated from the differential charge density distribution map as shown in Figure 3.7. From Figure 3.7, it is found that the differential Bader charge densities on Hg(C) and Hg(A) atoms are 0.14 e and 0.16 e respectively, while for Cl(L) it is -0.09 e and for Cl(V) it is estimated to be -0.20 e. Positive values of differential charge densities on Hg (+0.14 e, +0.16 e) and negative values of the same in the Cl atoms (-0.09 e, -0.20 e) indicate charge transfer from Hg to Cl atoms [89, 90].

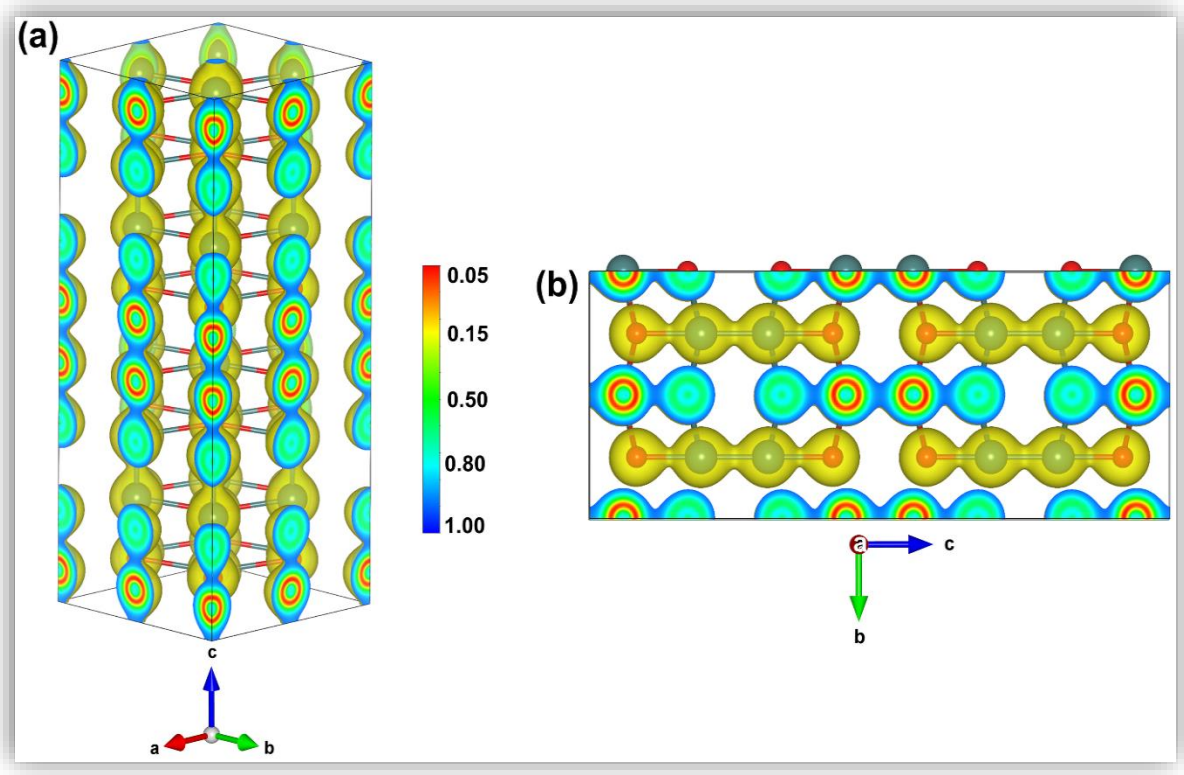

Figure 3.6. Differential charge density distribution **(a)** side view and **(b)** planer view along bc - plane of the 2 × 2 × 2 supercell of Hg_2Cl_2 compound as estimated from the Bader charge analysis. [Emerald blue and the red colour balls in the ball and stick model of Hg_2Cl_2 compound indicate Hg and Cl atoms respectively. Isosurface level = 0.010].

3.8. Natural bond orbital analysis

To gather more information concerning the CT interactions between Hg and Cl atoms of the Hg_2Cl_2 compound, the Natural Bond orbital (NBO) analyses have been performed. The basic concept behind the NBO analyses was suggested by Löwdin in his seminal work and had been reported elsewhere [22]. NBO analyses generate molecular orbitals of the compound from the Lewis concept that depict localized and doubly occupied electron pair orbitals in one, two or three-centred regions representing lone pairs (LPs) and chemical bonds (BD, 3C) respectively. NBO calculations have been performed by considering the probable interactions between the donor (filled) and the acceptor (vacant) NBOs in terms of stabilization energy E_2, as estimated from the second-order perturbation theory. The stabilization energy E_2 associated with the delocalization ($i \rightarrow j$) energy (ΔE_{ij}) is represented as:

$$E_2 = \Delta E_{ij} = q_i \frac{<\sigma_j|\hat{F}|\sigma_i>}{\varepsilon_j - \varepsilon_i} \quad (3.1)$$

where q_i is the orbital occupancy of the donor, $\hat{F}$ is the Fock or Kohn-Sham matrix and also known as effective orbital Hamiltonian. The diagonal elements ε_i ($\sim < \sigma_i|\hat{F}|\sigma_i >$) and ε_j ($\sim < \sigma_j|\hat{F}|\sigma_j >$) are the orbital energies of donor and acceptor respectively. The stabilization energies (E_2) of the relevant bond-bond Hg(C) – Hg(A) (σ) / Hg(C) – Cl(L) (σ) and bond-antibond Hg(C) – Hg(A) (σ) / Cl(L) – Cl(V) (σ^*) interactions have been estimated and are shown in Table 3.5. From Table 3.5 it is seen that the interaction between Hg(C) – Hg(A) (σ) / Hg(C) – Cl(L) (σ) shows strong stabilization accounting for the large E_2 value (5.85 kcal / mol) in comparison to the Hg(C) – Cl(V) (σ) / Cl(L) – Cl(V) (σ^*) interaction. The large stabilization energy (E_2) depicting bond-bond Hg(C) – Hg(A) (σ) / Hg(C) – Cl(L) (σ) interactions signify considerable CT from Hg(C / A) to Cl(L) atoms in accordance to our earlier conjecture (*vide ante*).

Table 3.5. Bond–bond and bond – antibond interactions for the Hg and Cl atoms of Hg_2Cl_2 compound.

Bond – bond/antibond Interactions	**Stabilization energy (E_2) (kcal / mol)**	**Fock matrix element (F_{ij}) (a.u.)**
Hg(C) – Hg(A) (σ) / Hg(C) – Cl(L) (σ)	5.85	0.033
Hg(C) – Hg(A) (σ) / Cl(L) – Cl(V) (σ^*)	0.58	0.010

Figure 3.8 further shows the 2D- contour plots depicting bond-bond Hg(C) – Hg(A) (σ) / Hg(C) – Cl(L) (σ) and bond-antibond Hg(C) – Cl(V) (σ) / Cl(L) – Cl(V) (σ^*) interactions. The 2D contour plot for the Hg(C) – Hg(A) (σ) / Hg(C) – Cl(L) (σ) bonding orbital reveals considerable overlap in the region of Hg(C) - Hg(A) and Hg(C) - Cl(L) bonds (F_{ij} = 0.033 a.u.) thereby promoting the CT interactions .

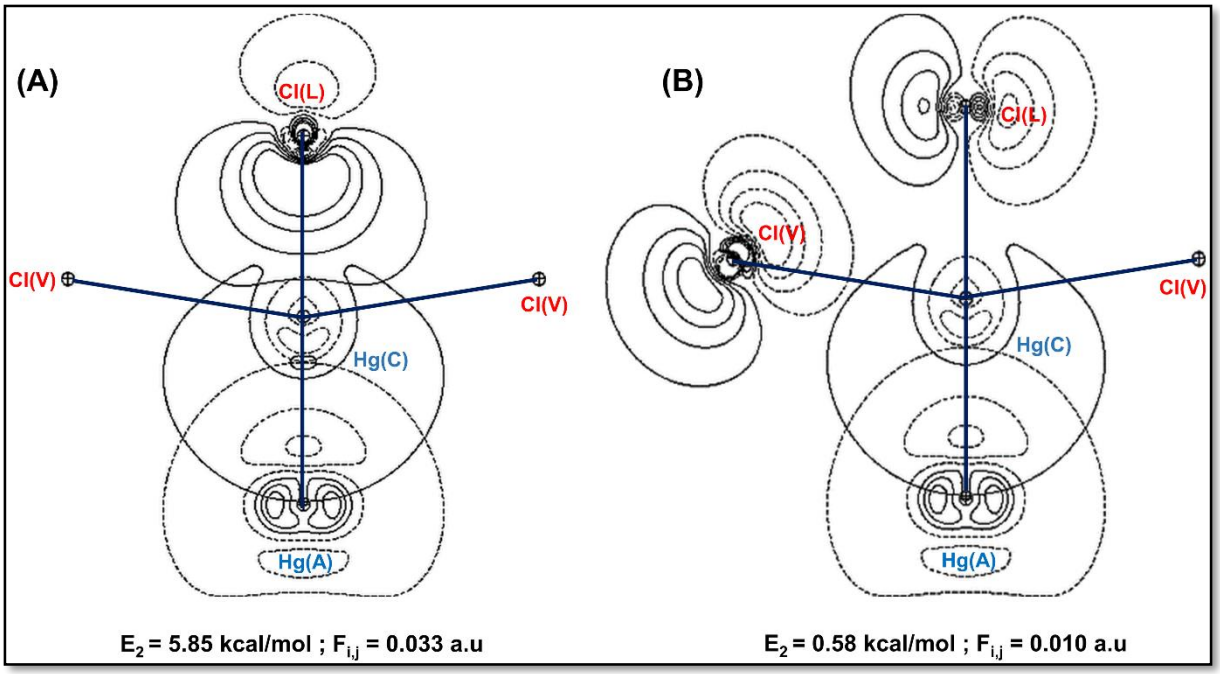

Figure 3.7. 2D orbital contour diagram for**(A)** Hg(C) – Hg(A) (σ) bonding and Hg(C) – Cl(L) (σ) bonding, **(B)** Hg(C) – Cl(V) (σ) bonding and Cl(L) – Cl(V) (σ^*) antibonding pre-NBO.

3.9. Distortions of the octahedral domains within the crystal lattice

From the analyses of the PDOS, as discussed in the earlier section, we believe the self-consistent energy alignment through hybridization may primarily stand responsible in the formation of distorted octahedral domains of Hg(C)Hg(A)[Cl(V)]$_4$Cl(L) in the crystal structure of the Hg_2Cl_2 compound. In each octahedral domain [*vide supra*, *cf.* Figure 3.2 (c)] one Hg(A) and five Cl [among them four are neighbouring Cl(V) and one is Cl(L)] atoms form the vertices of the octahedron with Hg(C) at the centre. We are interested to see how the presence of the neighbouring Cl [Cl(V) and /or Cl(L)] atoms influence the energy levels associated with the 5d orbitals of both Hg(C) and Hg(A) atoms despite screening from their respective 6s orbitals. The orbital-resolved PDOS of the 5d orbital of Hg(C) and Hg(A) atoms are shown in Figure 3.9. From Figure 3.9(A) (upper left panel) it is seen that near the valence band edge, loss of degeneracy of the 5d orbitals of Hg(C) has been observed. The splitting of d orbitals in the PDOS spectrum appears as two distinct branches. While the former branch at higher energy is dominated by the overlapped $d_{x^2-y^2}$, d_{xy} and d_{zx} orbitals, the latter is mostly comprised of overlapped $d_{x^2-y^2}$, $d_{3z^2-r^2}$, d_{xy}, d_{yz} and d_{zx} orbitals. Interestingly the 5d orbitals of Hg(A) atom around the valence band do not show any loss of degeneracy [Figure 3.9(A) (lower left panel)].

These results may suggest that the loss of degeneracy in the 5d orbitals of Hg(C) atom in the valence band may result in the structural distortion of the octahedral domains in the lattice of the Hg_2Cl_2 compound (*vide ante*) in pursuit for achieving the minimum energy configuration.

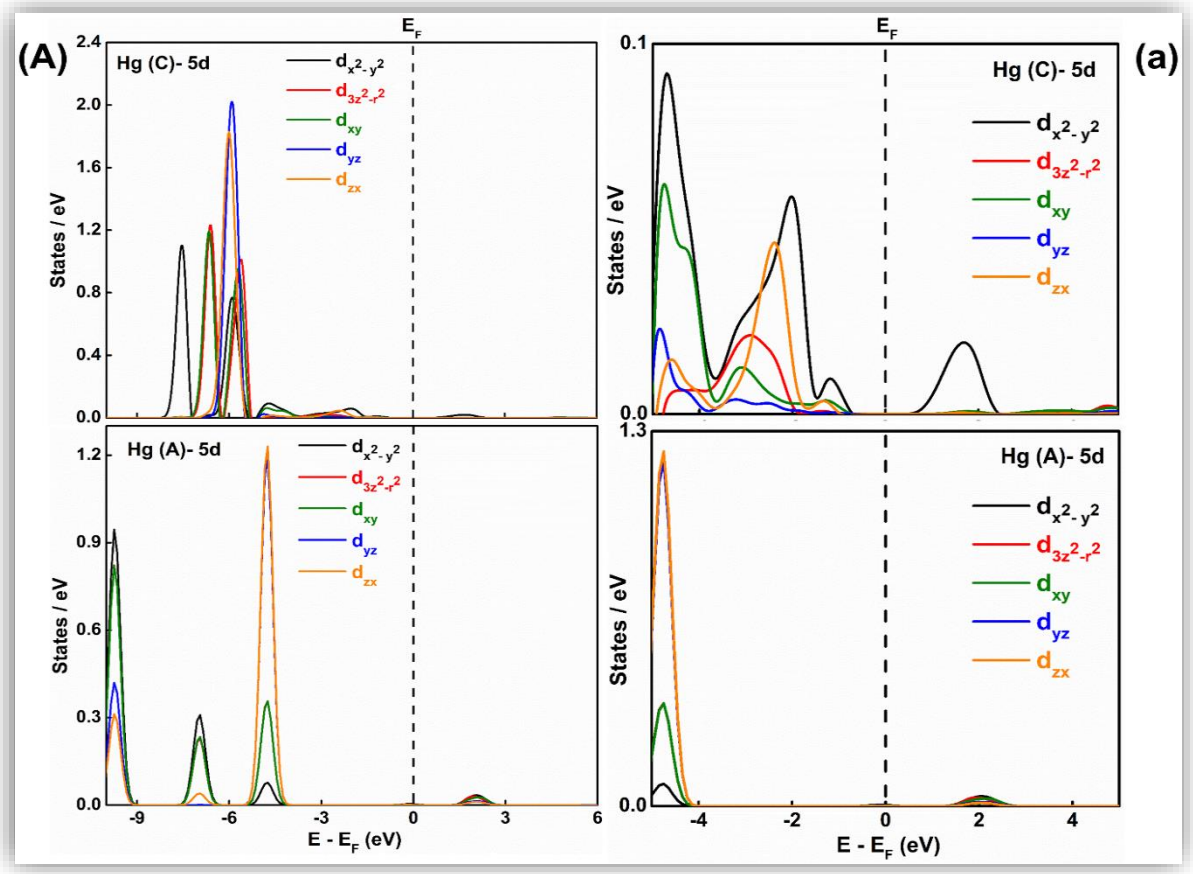

Figure 3.9. (A) Splitting of 5d orbitals of Hg(C) and Hg(A) atoms in presence ligand Cl(L) and neighbouring Cl(V) atoms in the octahedral environment. **(a)** Right panel shows the magnified views of the splitting of 5d orbitals of Hg(C) and Hg(A) atoms near the Fermi energy.

3.10. Conclusions

The structural and electronic properties of Hg_2Cl_2 in its tetragonal phase have been investigated from density functional theory calculations. The SCF energies and the associated lattice parameters and of the above-referred compound have been estimated from the GGA calculations in conjunction with PBE, PBEsol, BLYP, B3LYP and HSE correlation functionals. Detail calculations using the GGA-HSE level of theory suggest that Hg_2Cl_2 is a wide band gap CT insulator with a band gap ~ 3.93 eV. Moreover, the effects of on-site

Coulomb repulsion $+U_{dd}$ on the E_g of the compound have also been explored. Interestingly although the compound is suggested to be a CT insulator, however the corresponding energy dispositions in the orbital resolved PDOS plots do not obey the ZSA diagram. These observations suggest that the ZSA diagram, which is considered as the hallmark of CT insulators for transition metal compounds, is not seen to be followed in the case of CT insulators of the post-transition metals like Hg. The PDOS spectra further revealed strong covalent as well as CT interactions between Hg(C)/ Hg(A) and Cl(L) atoms in the linear Cl(L)–Hg(C)–Hg(A)–Cl(L) chains of the compound. The Mulliken bond population analyses and the electronic charge density distributions unveiled the existence of weak ionic interactions (in addition to the covalent and CT interactions) mostly among the Hg(C / A) and Cl(V), that form the distorted octahedral domains in the crystal lattice of Hg_2Cl_2. The NBO analyses had also been carried out to gain deeper insights into the CT interactions between Hg and Cl atoms of the compound. Distortions of the octahedral domains within the crystal lattice of Hg_2Cl_2 have been deciphered from the loss of degeneracies in the 5d orbitals of Hg(C) atom in the valence band of the Hg_2Cl_2 compound.

Bibliography

[1] W. W. Ewing, J. Am. Chem. Soc. **47**, 301 (1925).

[2] M. Crippa, S. Legnaioli, C. Kimbriel, and P. Ricciardi, J Raman Spectrosc. **52**, 15 (2021).

[3] T. Henningsen and N. B. Singh, J. Cryst. Growth **96**, 114 (1989).

[4] I. Pelant, M. N. Popova, J. Hála, M. AmbroŽ, V. Lhotská, and K. Vacek, Czech. J. Phys. **37**, 1183 (1987).

[5] A. Pierson and C. Philippe, in *Proc.SPIE*2019).

[6] R. J. Havighurst, J. Am. Chem. Soc. **48**, 2113 (1926).

[7] C. L. K. NicholasJ. Calos, Z. Krist. Cryst. Mater. **187**, 305 (1989).

[8] E. Dorm, J. Chem. Soc. D, 466 (1971).

[9] D. A. Kleier and W. R. Wadt, J. Am. Chem. Soc. **102**, 6909 (1980).

[10] Y. Luo, J. Wang, Y. Li, and J. Wang, Sci Rep **6**, 29801 (2016).

[11] V. V. Sobolev, V. V. Sobolev, and D. V. Anisimov, Semiconductors **50**, 29 (2016).

[12] H. M. Tütüncü, H. Y. Uzunok, E. Karaca, S. Bağcı, and G. P. Srivastava, Intermetallics **106**, 107 (2019).

[13] Y. Liu, N. Zhang, Y. Jia, Q. Sun, and M. Chao, Phys. Lett. A **379**, 2756 (2015).

[14] Y. K. Chang, K. P. Lin, W. F. Pong, M.-H. Tsai, H. H. Hseih, J. Y. Pieh, P. K. Tseng, J. F. Lee, and L. S. Hsu, J. Appl. Phys. **87**, 1312 (2000).

[15] T. Abtew, B.-C. Shih, S. Banerjee, and P. Zhang, Nanoscale **5**, 1902 (2013).

[16] M. N. Grisolia *et al.*, Nature Phys **12**, 484 (2016).

[17] S. Sahu, M. R. Sahoo, A. K. Kushwaha, G. C. Rout, and S. K. Nayak, Carbon **142**, 685 (2019).

[18] J. Zaanen, G. A. Sawatzky, and J. W. Allen, Phys. Rev. Lett. **55**, 418 (1985).

[19] R. C. D. Richardson, Wear **10**, 291 (1967).

[20] M. D. Segall, J. D. L. Philip, M. J. Probert, C. J. Pickard, P. J. Hasnip, S. J. Clark, and M. C. Payne, J. Phys.: Condens. Matter **14**, 2717 (2002).

[21] M. I. Naher and S. H. Naqib, Sci Rep **11**, 5592 (2021).

[22] P.-O. Löwdin, Phys. Rev. **97**, 1474 (1955).

Chapter 4

Pressure driven structural phase transitions of Mercurous Chloride

4.1. Introduction

This chapter reports the pressure-driven structural phase transitions of the Hg_2Cl_2 compound at room temperature (T = 300 K). Phase transitions are considered as one of the fundamental physical processes that have drawn significant attention over the years among physicists and chemists. During the phase transition, the physical and thermodynamic parameters of a system can alter significantly, as it transforms one physical state to another. The most familiar example of phase transitions in nature is the conversion of ice to water and then into vapour with the temperature rise [1-3]. However, in de facto there exist many exotic examples of phase transitions in physics that include conversions of ferromagnetic/ antiferromagnetic materials into paramagnetic at the Curie point (T_{Curie})/ Neel temperature (T_N) [4-11], the transformation of conducting materials into superconductors at the critical temperature [12,13], conversion of the normal fluid Helium-I to the superfluid Helium-II at the lambda point [14-16], order-disorder phase transition in brass [17], the temperature and/or pressure driven structural phase transitions in the crystals [18-38], to name a few. Here, the pressure-driven phase transitions of Hg_2Cl_2 have been estimated from from first-principle density functional theory (DFT) and Born-Oppenheimer molecular dynamics (BOMD) calculations. The associated phonon dispersion relations, key phonon modes and the nature of the phase transition whether it is "displacive" or of "order-disorder" type have been highlighted here.

4.2. Alterations of lattice and structural parameters of Hg_2Cl_2 under pressure

Figure 4.1(a) shows the variation in the ratio of the refined unitcell volume ratio (V/V_0, where V_0 is the unitcell volume of *I4/mmm* phase at P = 0 GPa) of Hg_2Cl_2 compound as a function of external pressure. Interestingly, with a slight increase in P, the V/V_0 ratio shows a sharp rise with a peak at 0.25 GPa, beyond which the V/V_0 ratio falls monotonically until around P between 8 and 10 GPa, where a definite change in the gradient of the slope is observed. Significantly enough the pressure $P_T \sim 0.25$ GPa at which the V/V_0 ratio attains the maximum value corresponds to the first structural phase transition of Hg_2Cl_2 crystal from its tetragonal phase to the base-centered orthorhombic one [*I4/mmm* (D_{4h}^{17}) → *Cmcm* (D_{2h}^{17})] as reported elsewhere [39-41]. Our first-principle calculations further suggest a nearly two-fold

increase in the unitcell volume at P = 0.25 GPa, mostly involving larger increments of the associated lattice parameters "a" and "b" in comparison to "c". Changes in the lattice parameters of the Hg_2Cl_2 crystal as a function of P are shown in Figure 4.1(b). Such doubling of the unit cell is also reported for the Hg_2Cl_2 crystal as it undergoes temperature-driven structural phase transition from tetragonal to base-centered orthorhombic [*I4/mmm* (D_{4h}^{17}) → *Cmcm* (D_{2h}^{17})] phase at 185 K [42,43]. With an increase in the external pressure P > 0.25 GPa, the V/V_0 decreases smoothly till ~ 8 GPa, while beyond that pressure, distinct change in the slope is noticed at ~ 9 GPa, primarily signifies the occurrence of the second phase transition for the crystal. Presence of second phase transition ~ 9 GPa has recently been estimated experimentally by Roginskii *et al.* from the low frequency Raman spectroscopic studies [44]. The associated lattice parameters ~ P = 9 GPa show overall small decrement in the "a", "b" and "c" values in comparison to that estimated between 0.5 GPa and 8 GPa external pressure [Figure 4.1(b)]. In fact the external pressure P = 9 GPa may mark the pressure driven second phase transition of Hg_2Cl_2 crystal from base-centered orthorhombic [*Cmcm* (D_{2h}^{17})] to primitive orthorhombic [*Pnma* (D_{2h}^{16})] phase. The experimental observation further suggests that the base-centered orthorhombic phase of Hg_2Cl_2 remains stable within 0.25 < P < 9 GPa external pressure just before the onset of the second phase transition [44]. However, in general both the phase transitions at P= 0.25 GPa and 9 GPa for the Hg_2Cl_2 compound are accompanied by the discrete changes in volumes, thereby suggesting such transitions to be of first order type.

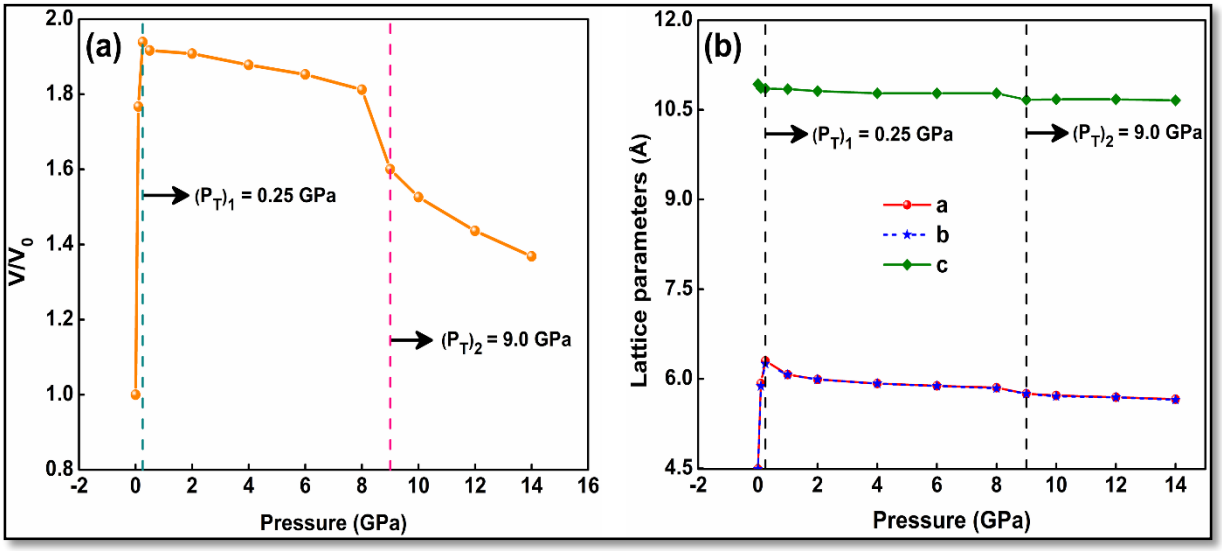

Figure 4.1. (a) V/V_0 and **(b)** lattice parameters versus pressure plots under different external pressure ranging from 0 GPa to 14 GPa. [The transitions pressures $(P_T)_1$ and $(P_T)_2$ are marked in the figures as vertical dotted (---) lines].

Figure 4.2(a) shows the refined optimized geometries depicting the crystal structures of Hg_2Cl_2 compound at 0.25 GPa, 6 GPa and 9 GPa, representing the *Cmcm* (D_{2h}^{17}) and *Pnma* (D_{2h}^{16}) phases respectively. The corresponding lattice and the structural parameters associated with the above referred *Cmcm* (D_{2h}^{17}) and *Pnma* (D_{2h}^{16}) phases of the compound are also shown in Table 4.1. The experimentally determined lattice parameters for *Pnma* (D_{2h}^{16}) phase of the compound is not available in the literature, however for the *Cmcm* (D_{2h}^{17}) phase the available experimental results are depicted in Table 4.1. The structural and lattice parameters associated with the base-centered orthorhombic *Cmcm* (D_{2h}^{17}) phase of Hg_2Cl_2, as estimated from the first-principle calculations, are in close harmony with the experimental result [43]. The refined structural parameters as reflected from the Table 4.1 show alterations in Hg(C)–Hg(A), Hg(C)–Cl(L), Hg(C)–Cl(V) bond lengths of the compound as it undergoes structural phase changes from the body-centered tetragonal to base-centered orthorhombic (*I4/mmm* → *Cmcm*) and primitive orthorhombic phases (*Cmcm* → *Pnma*) at two different pressures. These structural phase changes also lead to variations in the bond angles Cl(V)–Hg(C)–Cl(V), Hg(A)–Hg(C)–Cl(V) involving Hg(C & A) and neighbouring Cl(V) of the compound which in turn results in the distortion of the octahedral domains within the crystal lattice. Significantly enough, the average dihedral angle of Cl(L)–Hg(C)–Hg(A)–Cl(L) shows deviation from planarity and loses its linear form as the system undergoes pressure-driven phase transition from the body-centered tetragonal to base-centered orthorhombic (*I4/mmm* → *Cmcm*) and primitive orthorhombic phases (*Cmcm* → *Pnma*). The variation of the above-referred dihedral angle with pressure is shown in Figure 4.2(b).

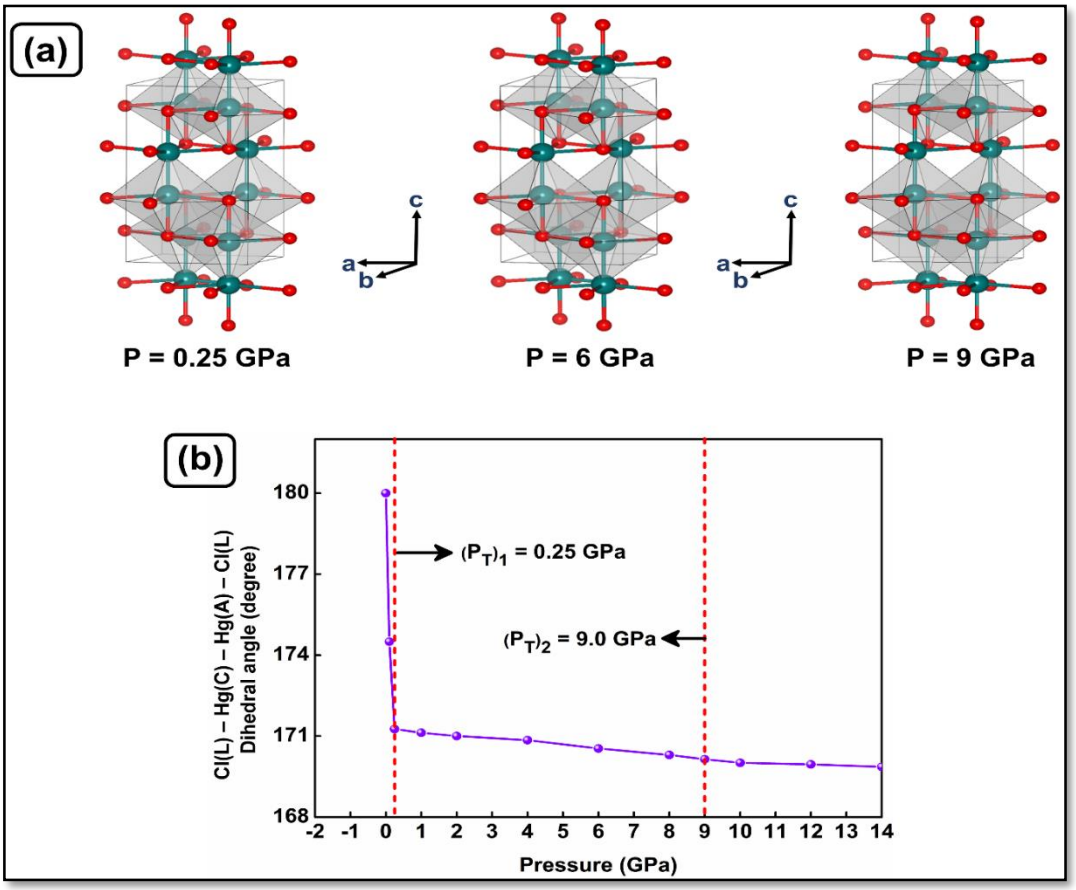

Figure 4.2. (a) Refined structures of the I4/mmm phase at 0.25 GPa, Cmcm phase at 6 GPa and 9 GPa external pressure for the Hg_2Cl_2 compound calculated at room temperature (Hg atoms are shown in emerald blue and Cl atoms are shown in red). **(b)** Variation in Cl(L)–Hg(C)–Hg(A)–Cl(L) average dihedral angle as function of pressure as calculated from the refined structures.

Table 4.1. Computed refined lattice and structural parameters for tetragonal *I4/mmm*, *Cmcm* and *Pnma* phase of Hg_2Cl_2 compound as obtained from BOMD simulations.

Measured parameters	Phases				
	I4/mmm		Cmcm		Pnma
	This study	Experiments [45,46]	This study	Experiments [43]	This study
Lattice Parameters (Å)					
a	4.489	4.470, 4.480	6.299	6.290	5.752
b	4.489	4.470, 4.480	6.249	6.240	5.751
c	10.929	10.890, 10.910	10.857	10.860	10.677
Volume ($Å^3$)					
V	220.23 (V_0)	217.60, 218.97	427.36	426.25	342.14
Average bond length (Å)					
Hg(C)–Hg(A)	2.526	2.526	2.617	-	2.624
Hg(C)–Cl(L)	2.424	2.434	2.522	-	2.528
Average bond angle (degree)					
Hg(C)–Cl(V)	3.210	3.209	3.160	-	3.154
Cl(V)–Hg(C)–Cl(V)	161.920	162.240	169.290	-	171.120
Hg(A)–Hg(C)–Cl(V)	99.040	-	95.270	-	95.130
Cl(L)–Hg(C)–Hg(A)–Cl(L)	180.000	180.00	171.260	-	170.140

To estimate precisely the transition pressure (P_T), the variation of enthalpy (H) with pressure for *I4/mmm*, *Cmcm* and *Pnma* phases of Hg_2Cl_2 crystal at room temperature have been estimated using the following relation:

$$H = E + PV \quad (4.1)$$

where E, V are the total energy and volume of the respective unitcells associated with *I4/mmm*, *Cmcm* and *Pnma* phases of the Hg_2Cl_2 compound respectively and P is the applied external pressure on them. The respective variations of H for *I4/mmm*, *Cmcm* and *Cmcm*, *Pnma* phases of Hg_2Cl_2 as a function P are shown in Figure 4.3. The transition pressure (P_T) corresponds to the point on the H-P plots where the two enthalpy values for the above mentioned phase pairs of the compound [ca. *I4/mmm*, *Cmcm* and *Cmcm*, *Pnma*] become equal. From Figure 4.3(a) and 4.3(b), it is observed that the H-P plots for *I4/mmm*, *Cmcm* and *Cmcm*, *Pnma* phases of Hg_2Cl_2 intersect at P = $(P_T)_1$ = 0.25 GPa and P = $(P_T)_2$ = 9 GPa. Thus the external pressures $(P_T)_1$ and $(P_T)_2$ are related to the transition pressures that correspond to the respective first *I4/mmm* (D_{4h}^{17}) → *Cmcm* (D_{2h}^{17}) and second *Cmcm* (D_{2h}^{17}) → *Pnma* (D_{2h}^{16}) structural phase transitions of the system. The results are in concordance with the experimental observations that clearly predict the pressure induced phase transition of the Hg_2Cl_2 crystal at P ~ 0.25 GPa and 9 GPa [39-41,44].

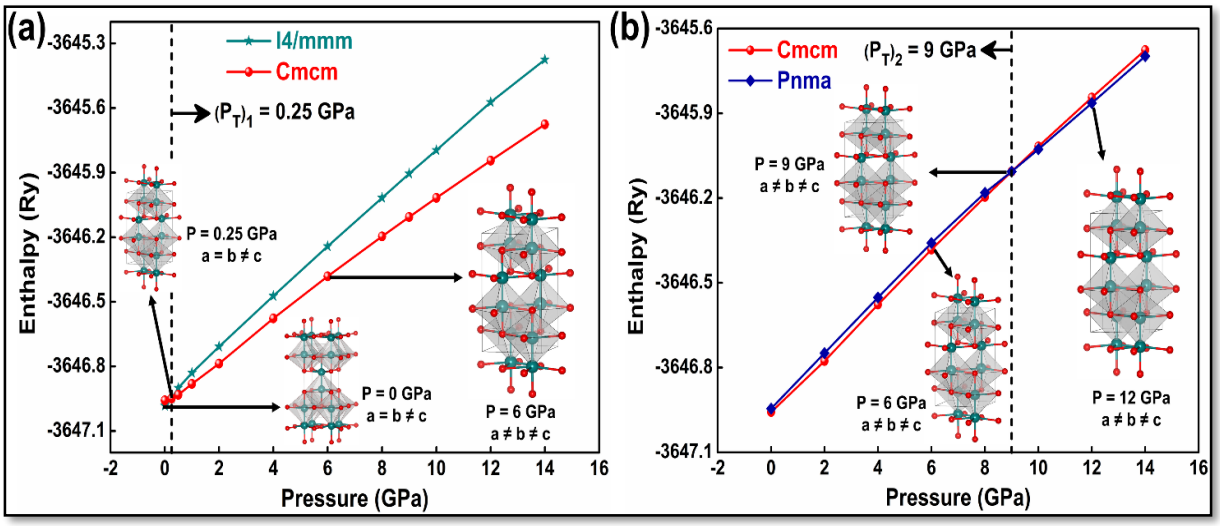

Figure 4.3. The enthalpy – pressure plots and associated structural evolutions for **(a)** *I4/mmm*, *Cmcm* phase and **(b)** *Cmcm*, *Pnma* phases of Hg_2Cl_2 compound [The transitions pressures are marked in the figures as vertical dotted lines].

4.3. Phonon dispersion relations and phonon density of states of Hg_2Cl_2 compound at various phases

The Hg_2Cl_2 crystal at ambient pressure crystallizes to *I4/mmm* space group symmetry. However, under different external pressures at P = 3, 6 GPa the compound belongs to *Cmcm*

phase while at 12 GPa, we observe *Pnma* space group. The Hg_2Cl_2 crystal in each of the above-referred phases contains eight atoms in their respective unitcells. Thus 21 optical and 3 acoustic phonon branches are expected to appear in their phonon dispersion spectra. The left panels of Figures 4.4 [Figure 4.4(A, B)] and 4.5 [Figure 4.5(A)] show the phonon dispersion curves of the Hg_2Cl_2 crystal representing *I4/mmm* and *Cmcm*, *Pnma* phases respectively along the high symmetry directions Γ→M→X→Γ→P and Γ→Z→X→Γ→Y of the Brillouin zone. The total and atom resolved phonon density of states (PhDOS) related with the dispersion curves are also shown in the right panels of the Figure 4.4 [Figure 4.4 (a, b)] and Figure 4.5 [Figure 4.5 (a)]. The phonon dispersion curves for the crystal in general show the distinct presence of transverse acoustic (TA) and longitudinal acoustic (LA) phonon branches in the expected lower frequency window ranging from ~ 0 cm^{-1} – 40 cm^{-1}. Among them the TA branch is doubly degenerate along X→Γ direction for the tetragonal and along Γ→ Z for the orthorhombic phases of the crystal. From Figure 4.4 nesting of the optical phonon branches for the *I4/mmm* phase of the compound at ambient pressure are seen in three distinct frequency regions spanning from ~ 27.9 cm^{-1} - 54.1 cm^{-1}, 91.6 cm^{-1} - 143.3 cm^{-1} and 195 cm^{-1} - 271.4 cm^{-1}. The dispersions of the phonon branches in the high frequency region are little more pronounced than for the low lying phonon branches ~ 27.9 cm^{-1} – 54.1 cm^{-1} and 91.6 cm^{-1} – 143.3 cm^{-1} frequency regions. The corresponding total and atom resolved PhDOS [Figure 4.4 (a)] reveal that the phonon branches in the low frequency range (~ 27.9 cm^{-1} – 54.1 cm^{-1}) are linked with vibrations involving Hg atoms, while in the high frequency region (91.6 cm^{-1} – 143.3 cm^{-1} and 195 cm^{-1} - 271.4 cm^{-1}) larger weights on the PhDOS are owed to the vibrations of the Cl sublattices. However, the phonon branches for the Hg_2Cl_2 crystal with space group *I4/mmm* at ambient pressure do not show any imaginary frequencies, signifying the structure to be dynamically stable. Interestingly, upon compression the phonon dispersion spectrum of the compound at P = 0.25 GPa shows remarkable changes in their general features. It is marked by the decrease in frequencies of the optical Γ_{15}, M_{15}, X_{11}, P_{11} and slowest transverse acoustic (TA_1) X_1 phonon modes of vibrations at the respective high symmetry points Γ, M, X, P and X in the Brillouin zone. Among them, the decrease in frequency of the TA_1 X_1 mode at the X high symmetry point of the Brillouin zone boundary for the Hg_2Cl_2 crystal in the tetragonal *I4/mmm* phase at room temperature is reported to decrease with increase in P from 0 to 0.25 GPa [41]. Moreover, hardening in the optical phonon frequencies of the Γ_{24}, M_{24}, X_{22} and P_{24} modes are also observed. The corresponding PhDOS as shown in the Figure 4.4(b) exhibits broadening and shifts in the peak positions associated with Hg and Cl atoms in the frequency range ~ 0 cm^{-1} – 69.5 cm^{-1} and ~ 84.6 cm^{-1} - 155.6 cm^{-1}. The reason behind the broadening of PhDOS

spectra of Hg_2Cl_2 at an external pressure P = 0.25 GPa in contrast to that estimated for P = 0 GPa may be attributed to the increase of phonon energy states in the above-referred frequency range (~ 84.6 cm^{-1} - 155.6 cm^{-1}). Incidentally, experimental results and our first-principle calculations suggest that external pressure P ~ 0.25 GPa happens to be the transition pressure $(P_T)_1$ which is explicitly linked with the first *I4/mmm* (D_{4h}^{17}) → *Cmcm* (D_{2h}^{17}) structural phase transition of the system.

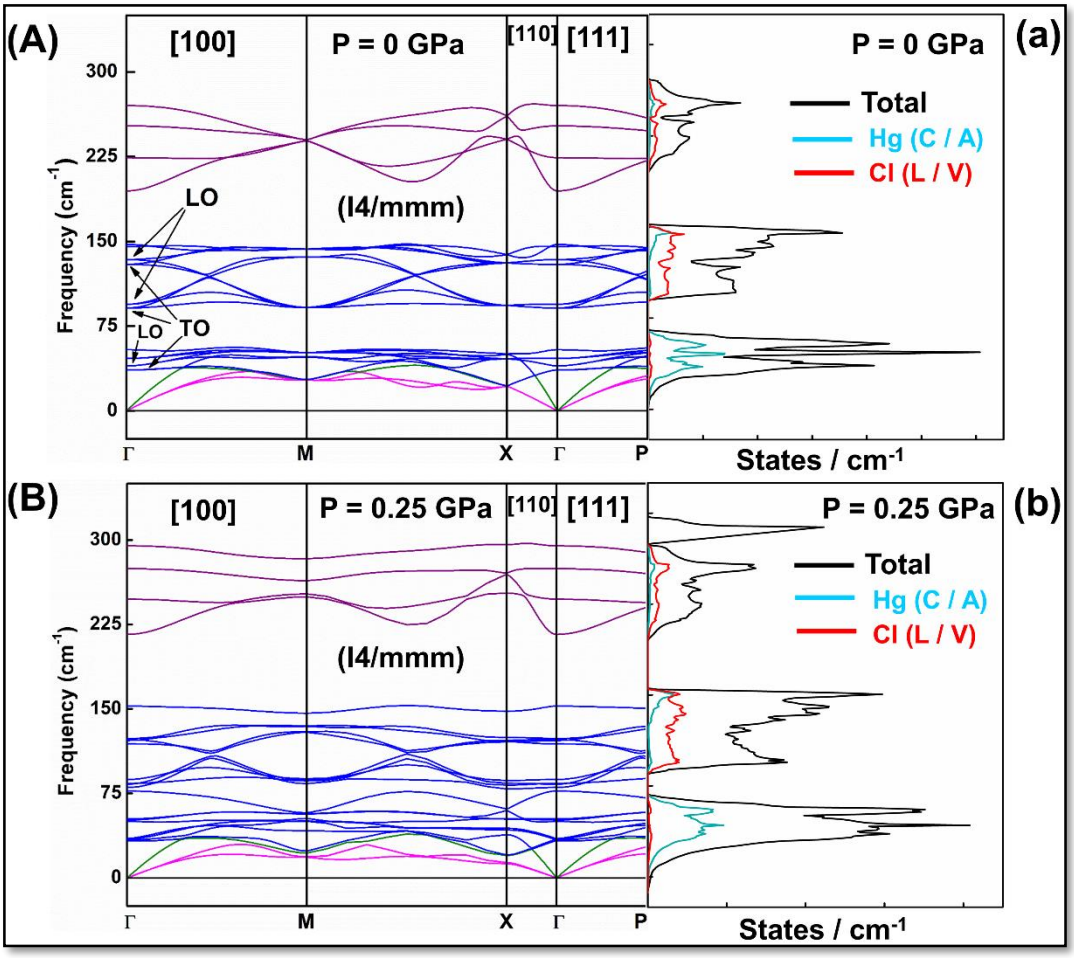

Figure 4.4. Left panel shows the phonon dispersion curves along the high-symmetry points Γ→M→X→Γ→P and the right panel depicts the total and partial PhDOS of the BOMD refined structure of Hg_2Cl_2 compound at P = 0 GPa and P = 0.25 GPa as estimated from the HSE level of theory. [Blue and purple colour traces indicate optical phonon modes in 27.9 cm^{-1} - 143.3 cm^{-1} and 195 cm^{-1} - 271.4 cm^{-1} frequency windows respectively, while those with magenta and green colours illustrate transverse and longitudinal acoustic phonon modes respectively in the phonon dispersion curve. LO-TO splittings are marked in the Figure 4.4(A).]

Interestingly after the first phase transition at $(P_T)_1$, at higher external P > 0.25 GPa the Hg_2Cl_2 compound exits in the *Cmcm*. The system is known to remain dynamically stable in the same phase over the external pressure range 0.25 GPa < P < 9 GPa [44]. The phonon dispersion spectra of the Hg_2Cl_2 crystal and their related PhDOS at the external pressures P = 3, 6 GPa thus show no significant alterations in the dispersion behaviour of the phonon branches. These features are apparent in Figure 4.5(A). At pressure P = 9 GPa, appreciable changes in the dispersive features of the phonon branches are noticed. While decrement in frequencies of the phonons linked with Γ_{15}, Z_1, Z_{15}, X_{11} and Y_{11} modes of vibrations are estimated from the first-principle calculations, concomitant upshifts of Γ_{24}, Z_{24}, X_{22} and Y_{24} modes at the respective high symmetry points Γ, Z, X and Y in the Brillouin zone are also observed. Figure 4.5(a) shows the associated PhDOS of the compound at P = 9 GPa. The PhDOS shows remarkable changes in the features displaying significant shifts in the peak positions linked with Hg and Cl atoms of the compound together with the emergence of energy states particularly in the frequency window ~ 84 cm^{-1} – 162 cm^{-1}. Significantly enough the external pressure ~ P = 9 GPa is the transition pressure $(P_T)_2$ that signifies the second phase transition of the Hg_2Cl_2 crystal leading to *Cmcm* → *Pnma* structural changes (*vide supra*). The condensations of Y_{11} and Z_1 phonons in *Cmcm* → *Pnma* phase transition are in excellent agreement with the results of the earlier studies as reported by Roginskii *et al*. [44]. At P > 9 GPa, Hg_2Cl_2 is dynamically stable and exists in primitive orthorhombic phase with *Pnma* space group symmetry. A representative phonon dispersion spectrum along with its associated PhDOS for the *Pnma* phase of the compound at P = 12 GPa is shown in Figure 4.5.

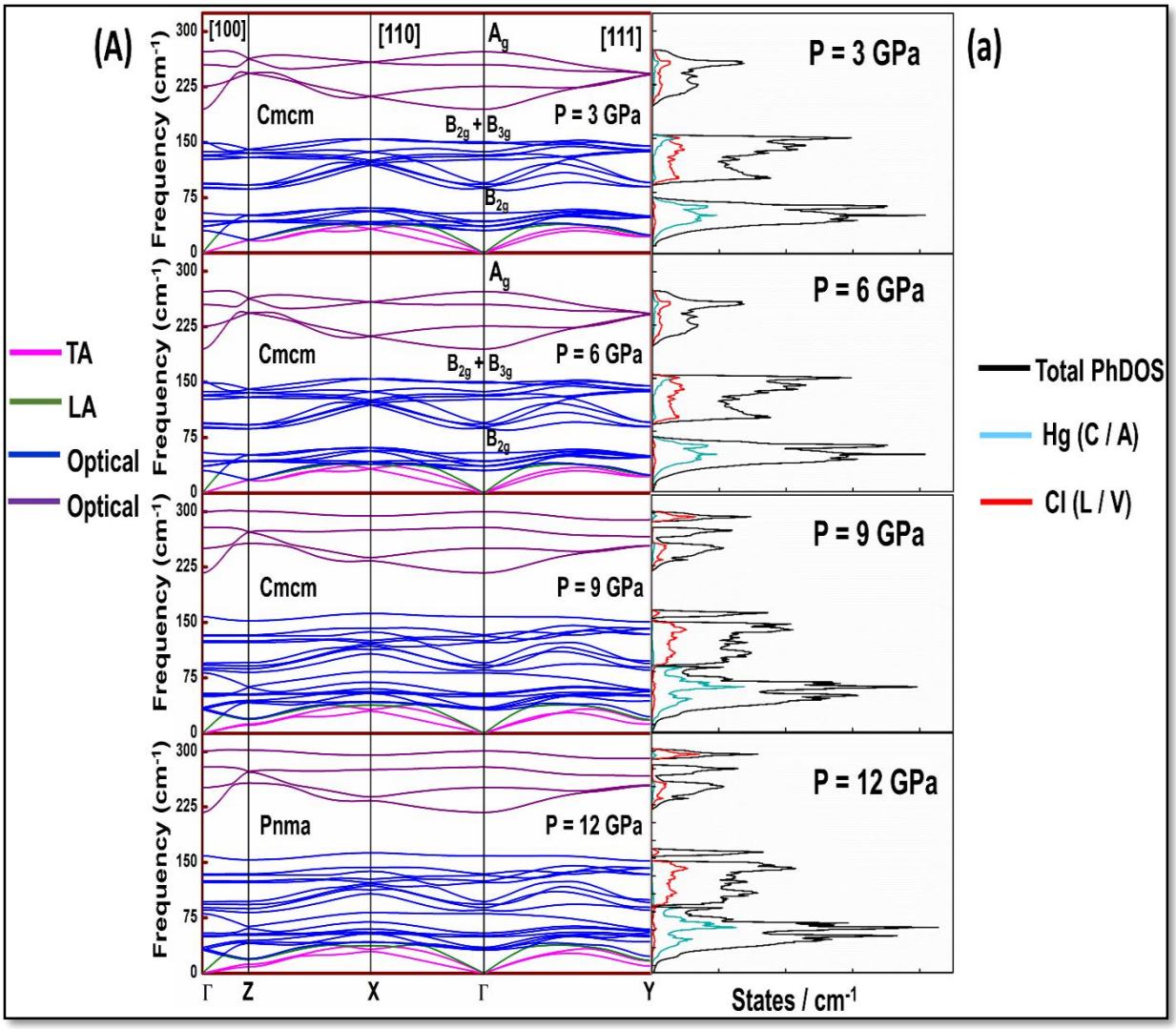

Figure 4.5. (A) Phonon dispersion curves of the orthorhombic (Cmcm and Pnma) phases of Hg_2Cl_2 along the high-symmetry points Γ→Z→X→Γ→Y and the **(a)** total and partial PhDOS of the compound calculated at P = 3, 6, 9 and 12 GPa as estimated from the HSE level of theory.

4.4. Pressure dependence key phonon modes and their corresponding Cartesian displacements

To gain more insights on the dependence of phonon frequencies as function of external pressures leading to the first *I4/mmm* → *Cmcm* and second *Cmcm* → *Pnma* structural phase transitions at $(P_T)_1$ = 0.25 GPa and $(P_T)_2$ = 9 GPa respectively of the Hg_2Cl_2 compound, the variations of the phonon frequencies at different high-symmetry points in the Brillouin zone of the *I4/mmm* and *Cmcm* phases of the system with pressure have been estimated. The respective variations are shown in Figure 4.6(a) and Figure 4.6(b). From Figure 4.6(a) and Figure 4.6(b),

it is found that the low frequency phonons in the frequency range 27.9 cm^{-1} – 143.3 cm^{-1} undergo noticeable downshifts while the high frequency ones in ~ 195 cm^{-1} – 271.4 cm^{-1} region is appreciably hardened. The other striking feature of the frequency vs pressure plots is the distinct changes in the slopes at P = 0.25 GPa and 9 GPa, which incidentally correspond to the transition pressures $(P_T)_1$ and $(P_T)_2$ linked with the first and the second pressure driven phase transitions of the Hg_2Cl_2 compound, respectively. Surprisingly, beyond $(P_T)_1$ = 0.25 GPa and $(P_T)_2$ = 9 GPa, the phonon frequencies show no significant variations with P, suggesting the presence of *Cmcm* and *Pnma* phases of the Hg_2Cl_2 compound over a wide range of external pressures ranging from ~ 0.5 GPa – 8 GPa and above 9 GPa respectively. Figure 4.6(b) further entails the variation in frequencies of the optical phonon branches associated with Γ_{15}, Z_1, Z_{15}, X_{11}, Y_{11} and Γ_{24}, Z_{24}, X_{22} and Y_{24} modes with pressure. The former phonon modes show a gradual decrease in frequencies while the latter reflects the opposite trend at the onset of the second phase transition pressure $(P_T)_2$ = 9 GPa. At P > 9 GPa, the phonon frequencies show no appreciable variations with P again suggesting the second structural phase transition from base-centered orthorhombic (*Cmcm*) to primitive orthorhombic (*Pnma*) phase of the compound at pressure 9 GPa.

In this connection, considerable attention may be drawn from the estimated low-frequency Raman active modes of the *Cmcm* and *Pnma* systems at the Γ point. The experimental observations of the low-frequency Raman mode ν_1' at ~ 59 cm^{-1} (calculated 44 cm^{-1}) and the liberational mode ~ 137 cm^{-1} (calculated 126.9 cm^{-1}) belonging to B_{2g} and B_{2g} + B_{3g} irreducible representations respectively closely match with our calculated frequencies [44]. Among them the B_{2g} mode at ~ 59 cm^{-1} had been experimentally reported to get soften and downshifted to ~ 56 cm^{-1} (calculated. 41.1 cm^{-1}) during *Cmcm* → *Pnma* structural phase transition of the Hg_2Cl_2 compound at 9 GPa in concordance with our theoretical estimations. However, discrepancies in the assignment of the low-frequency Raman active mode belonging to the A_g irreducible representation have been noted. While this mode was experimentally observed to be at ~ 46 cm^{-1} by Roginskii *et al.* [44], however, A. A. Kaplyanskii reported the same to be at much higher frequency ~ 275 cm^{-1} [47]. Our theoretical calculations estimate the frequency of this mode to be at 272.5 cm^{-1} in close agreement with the report of A. A. Kaplyanskii. Although our estimated frequency does not match with the result of Roginskii *et al.*, yet subsequent hardening of this A_g mode (from 272.5 to 298.7 cm^{-1}) with increase in pressure is still reflected from our first-principle calculations in harmony with that observed in the experimental observations [44,47].

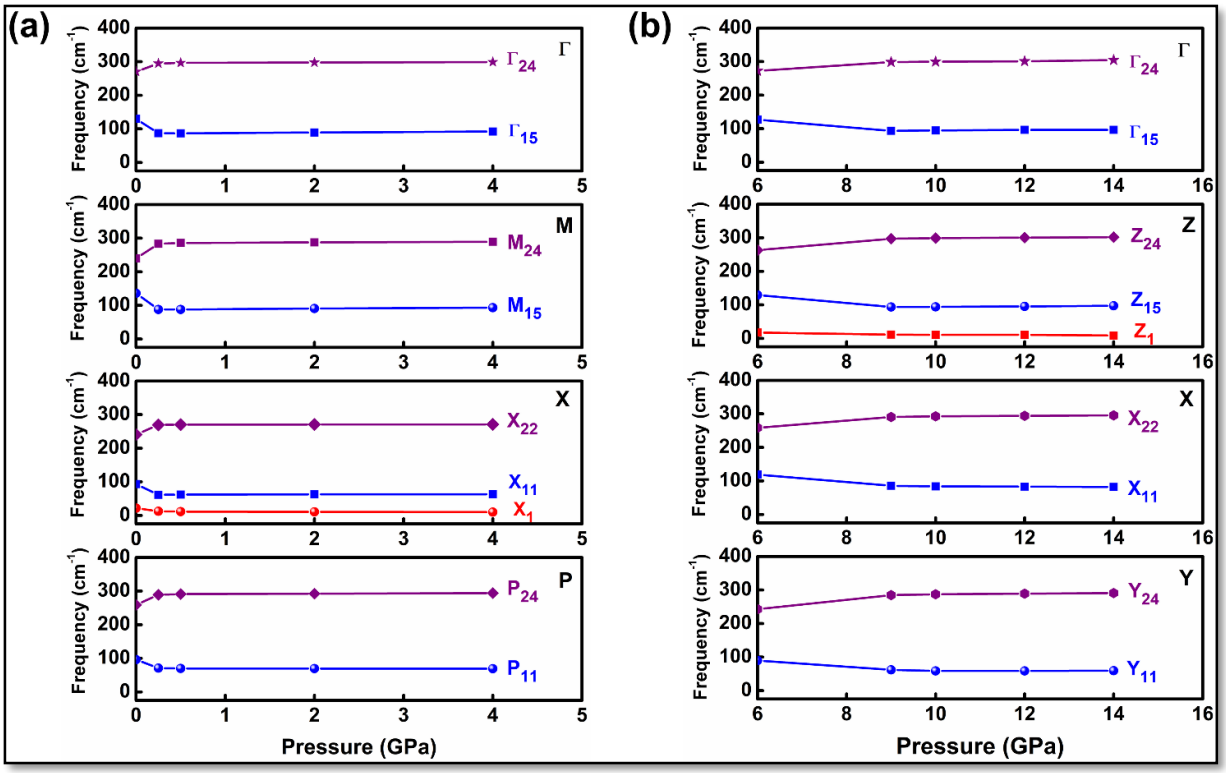

Figure 4.6. Pressure-dependent phonon frequencies at high-symmetry q points **(a)** Γ, M, X, P for the tetragonal (I4/mmm) phase and **(b)** Γ, Z, X, Y for the orthorhombic (Cmcm) phase of the Hg_2Cl_2 compound.

To understand the structural deformations associated with the decrement and hardening of the optical phonon frequencies of Hg_2Cl_2 compound under external pressures leading to *I4/mmm* (D_{4h}^{17}) → *Cmcm* (D_{2h}^{17}) and *Cmcm* (D_{2h}^{17}) → *Pnma* (D_{2h}^{16}) structural phase transitions at $(P_T)_1$ = 0.25 GPa and $(P_T)_2$ = 9 GPa respectively, the cartesian displacements of atoms for some of the representative phonon modes are considered. The results are shown in Figure 4.7(a) and Figure 4.7(b). From Figure 4.7(a), it is clearly seen that the phonon modes Γ_{15} and X_{11} of the Hg_2Cl_2 compound involve displacements of the Cl atoms only along the basal ab-plane, while the Hg atoms remain stationary. The phonon mode X_1 involves displacements of both Hg and Cl atoms in the ab-plane. These modes of vibrations may not only result in the bending of linear Cl(L)–Hg(C)–Hg(A)–Cl(L) chain but also may promote increments in the lattice parameters "a" and "b" of the compound. Figure 4.7(a) also shows the atomic displacements of Γ_{24} and X_{22} phonon modes mostly involving stretching of the linear Cl(L)–Hg(C)–Hg(A)–Cl(L) chain Cl atoms in opposite directions along the crystallographic c – axis. These results collectively signify some alterations in the lattice parameters of the Hg_2Cl_2 at P= 0.25 GPa which in turn may result in the first phase transition of the compound from the body-centered tetragonal *I4/mmm* (D_{4h}^{17}) to the base-centered orthorhombic *Cmcm* (D_{2h}^{17}) phase.

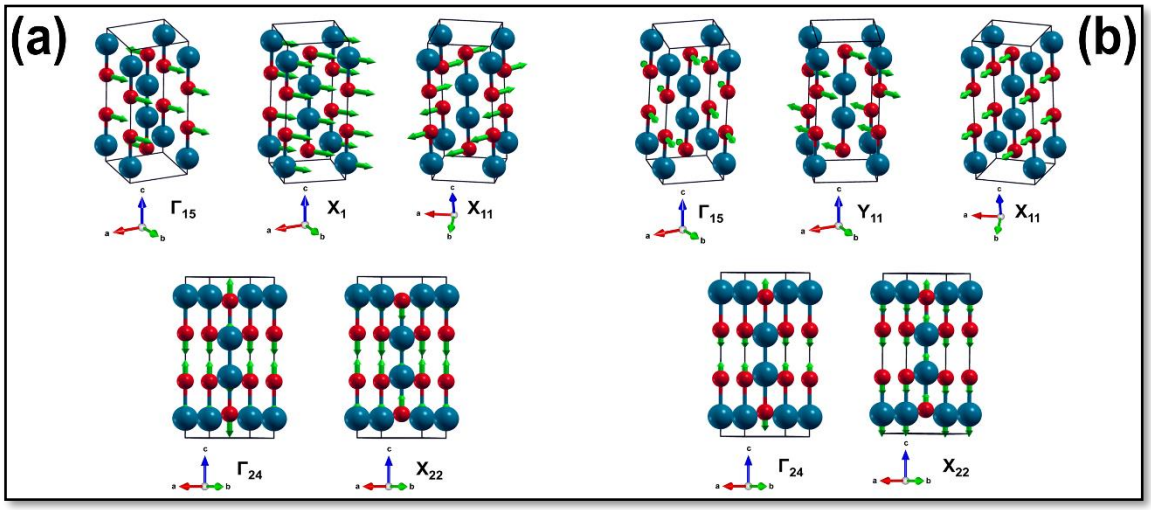

Figure 4.7. (a) Schematic representations of eigenvectors and atomic displacements for Γ_{15}, X_1, X_{11}, Γ_{24} and X_{22} phonon modes of the tetragonal (I4/mmm) phase of Hg_2Cl_2 at 0.25 GPa. (Large Hg atoms are shown in emerald blue and small Cl atoms are shown in red. The green arrows signify the atomic displacements). **(b)** Schematic diagrams of eigenvectors and atomic displacements for Γ_{15}, Γ_{24}, Y_{11}, X_{11} and X_{22} phonon modes of the orthorhombic (Cmcm) phase of Hg_2Cl_2 at P = 9 GPa. (Large Hg atoms are shown in emerald blue and small Cl atoms are shown in red. The green arrows signify the atomic displacements).

Similar observations may be drawn from the representative Γ_{15}, Y_{11}, X_{11}, Γ_{24} and X_{22} phonon modes linked with the *Cmcm* phase of Hg_2Cl_2 at 9 GPa. The cartesian displacements of the above referred modes are shown in Figure 4.7(b). The atomic displacements of the phonon vibrational signatures, as shown in Figure 4.7(b), in general suggest small variations in the lattice parameters of the compound which may lead to the second structural phase transition from *Cmcm* to *Pnma* phase of Hg_2Cl_2 crystal at P = 9 GPa.

4.5. Nature of the structural phase transitions

Two types of structural phase transitions have been observed in general. In an "order-disorder" type structural phase transition the potential energy hypersurface for the collective atomic displacements shows multiple potential wells of equal depths. Atoms jump over the finite potential barrier between the two nearest local potential minima within longer intervals of time. However, for "displacive" type structural phase transition, the potential energy hypersurface of the Cartesian displacements of atoms exhibits a single global minimum at equilibrium. The atoms move to and fro about the equilibrium of the potential energy

hypersurface with frequencies that link with the order of the phonon frequencies. The magnitude of $K_{ij}(\lambda)$ determines the curvature, while its sign signifies the nature of the potential energy hypersurface. Positive values of $K_{ij}(\lambda)$ suggest the single minimum on the local potential energy hypersurface signifying a "displacive" type structural phase transition. The negative values of $K_{ij}(\lambda)$ on the other hand correspond to the multiwell nature of the potential energy hypersurface and link the phase transition to be of "order-disorder" type [22,48-53].

The Hellmann-Feynman forces have been estimated separately from the independent displacements of Hg and Cl atoms of Hg_2Cl_2 crystal along x, y and z directions for the tetragonal (*I4/mmm*) and orthorhombic phases (*Cmcm*, *Pnma*) of the compound. To understand the nature of the pressure-driven structural phase transitions the on-site force constants K_{ij}(Hg) and K_{ij}(Cl) for the Hg_2Cl_2 system belonging to its *I4/mmm* and *Cmcm*, *Pnma* phases have been calculated. The calculations reveal force constants $K_{ij}(Hg) = K_{ij}(Cl) = 0$ for $i \neq j$, while K_{ii}(Hg) and K_{ii}(Cl) exhibit non-zero values. The non-zero values of the force constants K_{ii}(Hg) and K_{ii}(Cl) along xx, yy and zz directions are shown in Table 4.2. Interestingly, the non-zero on-site force constants for Hg and Cl atoms are found to be positive in the first *I4/mmm* (D_{4h}^{17}) → *Cmcm* (D_{2h}^{17}) phase transition. These results signify the displacive nature of the first structural *I4/mmm* → *Cmcm* phase transition of the Hg_2Cl_2 compound at P = 0.25 GPa. Interestingly, the z - z-components of the non-zero value of force constant K_{zz} for Hg and Cl atoms show negative values for the second phase transition associated with *Cmcm* → *Pnma* transition at 9 GPa. This observation suggests that the second phase transition for the Hg_2Cl_2 compound at P = 9 GPa represents an order-disorder type.

Table 2. Calculated non-zero components of on-site force constants for different phases of Hg_2Cl_2 compound.

Phases	**On-site force constants (N/m)**					
	K_{xx}(Hg)	**K_{yy} (Hg)**	**K_{zz} (Hg)**	**K_{xx} (Cl)**	**K_{yy} (Cl)**	**K_{zz} (Cl)**
***I4/mmm* (P = 0.25 GPa)**	0.50	0.50	0.92	1.58	1.58	2.07
***Cmcm* (P = 9 GPa)**	0.17	0.21	-0.07	0.17	1.07	-0.17

4.6. Conclusions

This chapter reports the underpinning physics behind the pressure-induced structural phase transitions of the Hg_2Cl_2 compound at room temperature. The phonon modes linked with the phase transitions of the compound have been critically explored for its tetragonal and orthorhombic phases from their corresponding phonon dispersion relations and PhDOS. Pressure dependence of the phonon modes at the respective high-symmetry points has also been investigated to get deeper insights into their role in the structural phase transitions of the compound. The nature of the phase transition, whether it is "displacive" or of "order-disorder" type, has been predicted.

Bibliography

[1] E. M. Lifshitz and L. P. Pitaevskii, *Statistical Physics: Theory of the Condensed State* (Elsevier Science, 2013), v. 9.

[2] P. V. Hobbs, *Ice Physics* (OUP Oxford, 2010).

[3] M. Marcellini, F. M. Fernandes, D. Dedovets, and S. Deville, J. Chem. Phys. **146**, 144504 (2017).

[4] R. E. Kirby, E. Kisker, F. K. King, and E. L. Garwin, Solid State Commun. **56**, 425 (1985).

[5] D. Küpper, S. Easton, and J. A. C. Bland, J. Appl. Phys. **102**, 083902 (2007).

[6] V. Usov, S. Murphy, and I. V. Shvets, J. Magn. Magn. Mater. **290-291**, 764 (2005).

[7] B. Binaei Ghotbabadi, A. Sheykhi, and G. H. Bordbar, Phys. Lett. B **797**, 134896 (2019).

[8] A. K. Pramanik and A. Banerjee, Phys. Rev. B **79**, 214426 (2009).

[9] S. W. Biernacki, Phys. Rev. B **68**, 174417 (2003).

[10] L. Zu, S. Lin, Y. Liu, J. C. Lin, B. Yuan, X. C. Kan, P. Tong, W. H. Song, and Y. P. Sun, Appl. Phys. Lett. **108**, 031906 (2016).

[11] Z. He, T. Taniyama, and M. Itoh, Phys. Rev. B **73**, 212406 (2006).

[12] M. Marik, D. Jana, K. C. Majumder, and B. K. Chaudhuri, Mol. Cryst. Liq. Cryst. **606**, 111 (2015).

[13] X. Li *et al.*, PNAS **116**, 17696 (2019).

[14] J. K. Hoffer, W. R. Gardner, C. G. Waterfield, and N. E. Phillips, J. Low Temp. Phys. **23**, 63 (1976).

[15] J. F. Allen and A. D. Misener, Nature **142**, 643 (1938).

[16] J. F. Allen and A. D. Misener, Nature **141**, 75 (1938).

[17] A. Madsen, J. Als-Nielsen, J. Hallmann, T. Roth, and W. Lu, Phys. Rev. B **94**, 014111 (2016).

[18] B. D. Sahoo, K. D. Joshi, and T. C. Kaushik, J. Appl. Phys. **128**, 035902 (2020).

[19] M. Kurban, C. Kürkçü, Ç. Yamçıçıer, and F. Göktaş, J. Phys.: Condens. Matter **31**, 305401 (2019).

[20] K. A. Irshad, P. Anees, S. Sahoo, N. R. Sanjay Kumar, V. Srihari, S. Kalavathi, and N. V. Chandra Shekar, J. Appl. Phys. **124**, 155901 (2018).

[21] Y. Tao, S. Xie, T. Lu, C. Hu, H. Liu, H. Zhang, X. Cheng, M. Liu, and Z. Qi, J. Appl. Phys. **131**, 165901 (2022).

[22] S. Ghosh and J. Chowdhury, J. Appl. Phys. **130**, 225103 (2021).

[23] B. A. Zakharov, A. A. L. Michalchuk, C. A. Morrison, and E. V. Boldyreva, Phys. Chem. Chem. Phys. **20**, 8523 (2018).

[24] A. Krylov, I. Yushina, E. Slyusareva, S. Krylova, A. Vtyurin, S. Kaskel, and I. Senkovska, Phys. Chem. Chem. Phys. **24**, 3788 (2022).

[25] G. V. Pushkarev, V. G. Mazurenko, V. V. Mazurenko, and D. W. Boukhvalov, Phys. Chem. Chem. Phys. **21**, 22647 (2019).

[26] H.-W. Chen, C.-Y. Huang, G.-J. Shu, and H.-L. Liu, RSC Adv. **11**, 40173 (2021).

[27] Y. Duan, J. Li, T. Li, X. Zhang, Z. Wang, and H. Li, Phys. Chem. Chem. Phys. **20**, 9337 (2018).

[28] A. Dudka, S. Nesterenko, and A. Tursina, J. Alloys Compd. **890**, 161759 (2022).

[29] X. Yang, S.-Q. Jiang, H.-C. Zhang, K.-P. Zhao, X. Shi, and X.-J. Chen, J. Alloys Compd. **766**, 813 (2018).

[30] A. Nonato, P. H. M. Lima, W. C. Ferreira, R. X. Silva, N. L. M. Costa, A. R. Paschoal, A. P. Ayala, and C. W. A. Paschoal, J. Alloys Compd. **787**, 1195 (2019).

[31] D. Shrivastava and S. P. Sanyal, J. Alloys Compd. **745**, 240 (2018).

[32] A. Nag, A. Kumari, and J. Kumar, J. Solid State Chem. **304**, 122600 (2021).

[33] Y. Peng, X. Wei, C. Jin, Y. Zhang, and J. Cao, J. Solid State Chem. **300**, 122194 (2021).

[34] S. Sharma, R. Nandan, J. Shah, R. K. Kotnala, and N. S. Negi, Phase Transit. **95**, 609 (2022).

[35] V. Kapustianyk, S. Semak, Y. Chornii, and M. Rudko, Phase Transit. **95**, 626 (2022).

[36] Y. de Armas Figueroa, J. Portelles, R. López-Noda, J. Fuentes, H. L. Hmŏk, Z. I. Bedolla-Valdez, and J. M. Siqueiros, Phase Transit. **95**, 466 (2022).

[37] I. Bejaoui Ouni, H. Aroui, and M. D. Fontana, Phase Transit. **95**, 749 (2022).

[38] R. H. Chen, S. C. Chen, and T. M. Chen, Phase Transit. **53**, 15 (1995).

[39] M. Midorikawa, Y. Ishibashi, S.-i. Nakashima, and A. Mitsuishi, J. Phys. Soc. Jpn. **49**, 554 (1980).

[40] W. Dultz and E. Rehaber, J. Phys. C: Solid State Phys. **12**, L137 (1979).

[41] A. A. Kvasov, Y. F. Markov, E. M. Roginskii, and M. B. Smirnov, Ferroelectrics **397**, 81 (2010).

[42] S. Ghosh and J. Chowdhury, Phase Transit. **96**, 446 (2023).

[43] I. Pelant, M. N. Popova, J. Hála, M. AmbroŽ, V. Lhotská, and K. Vacek, Czech J Phys **37**, 1183 (1987).

[44] E. M. Roginskii, A. S. Krylov, Y. F. Markov, and M. B. Smirnov, Bull. Russ. Acad. Sci. Phys. **80**, 1033 (2016).

[45] R. J. Havighurst, J. Am. Chem. Soc. **48**, 2113 (1926).

[46] E. Dorm, J. Chem. Soc. D, 466 (1971).

[47] A. A. Kaplyanskii, in *Theory of Light Scattering in Condensed Matter*, edited by B. Bendow, J. L. Birman, and V. M. Agranovich (Springer US, Boston, MA, 1976), pp. 31.

[48] A. I. Lebedev, Phys. Solid State **51**, 362 (2009).

[49] K. Parlinski, Y. Kawazoe, and Y. Waseda, J. Chem. Phys. **114**, 2395 (2001).

[50] K. Parlinski and Y. Kawazoe, Eur. Phys. J. B **16**, 49 (2000).

[51] K. Parlinski, Z. Q. Li, and Y. Kawazoe, Phys. Rev. B **61**, 272 (2000).

[52] T. Schneider and E. Stoll, Phys. Rev. B **13**, 1216 (1976).

[53] U. D. Wdowik, K. Parlinski, S. Rols, and T. Chatterji, Phys. Rev. B **89**, 224306 (2014).

Chapter 5

Pressure driven modulations in the electronic and optical properties of Mercurous Chloride

5.1. Introduction

In this chapter, the pressure-driven modulations in optoelectronic properties of the Hg_2Cl_2 compound have been discussed. The system exhibits pressure-induced structural phase transitions from body-centred tetragonal [*I4/mmm* (D_{4h}^{17})] → base-centred orthorhombic [*Cmcm* (D_{2h}^{17})] phase and from *Cmcm* (D_{2h}^{17}) to the primitive orthorhombic [*Pnma* (D_{2h}^{16})] phase at external pressure 0.25 and 9 GPa respectively [1]. The electronic and the associated optical properties of the Hg_2Cl_2 compound in terms of complex dielectric function [$\varepsilon(\omega)$], absorption coefficient [$\alpha(\omega)$], optical conductivity [$\sigma(\omega)$], refractive indices (n_e, n_o), optical birefringence (Δn) under ambient conditions and external pressures have been highlighted in this chapter.

5.2. Electronic band structures of Hg_2Cl_2 compound under ambient and external pressures

Figure 5.1 shows the electronic band structures of the body-centred tetragonal (*I4/mmm*) and orthorhombic (*Cmcm, Pnma*) phases of the Hg_2Cl_2 crystal under ambient conditions and external pressures. From Figure 5.1 it is apparent that at ambient pressure (ca. P = 0 GPa), where Hg_2Cl_2 crystallizes to *I4/mmm* phase, shows a direct gap opening around the Fermi energy level (E_F) with electronic band gap energy (E_g) ~ 3.93eV, where both the valence band maximum (VBM) and the conduction band minimum (CBM) are located at the same high-symmetry point M. The estimated value of E_g ~ 3.93 eV, so obtained from the GGA-HSE level of theory, is in close harmony with the experimentally determined optical band gap (~ 4.0 – 4.1 eV) for *I4/mmm* phase of the compound at room temperature [2]. Small deviation (~ + 0.07 eV) in the recorded optical band gap energy from the estimated E_g value may be due to the contribution from the excitonic effects which are not considered in the band structure calculations.

With the application of pressure in the range of 0.25 - 14 GPa, small increments in the E_g values of the compound have been noticed, although both the VBM and CBM are now shifted from M to Γ, the Brillouin zone centre. The shift in the direct band gap position from M to Γ high symmetry points may be identified with the pressure-dependent structural phase transition of the Hg_2Cl_2 crystal, which eventually leads to the overall reduction in symmetry from tetragonal [*I4/mmm*] to orthorhombic [*Cmcm, Pnma*] phases of the compound. The

reduction in symmetry due to phase transition is not only limited to the obvious changes in the high symmetric points [Γ→M→X→Γ→P in tetragonal (*I4/mmm*) as compared to X→Γ →Z→Y→Γ for base-centred (*Cmcm*) and primitive (*Pnma*) orthorhombic phases) in the E-**k** diagrams but also depict distinguishable variations in the dispersion relations of the energy bands, as evinced in Figure 5.1. The alterations in the electronic band structures linked with different phases of the compound at P = 0, 6 and 12 GPa in turn may modulate their corresponding optical properties, whose detail discussions will be presented in the next section of the chapter. However, the E_g values, as estimated from the DFT calculations with GGA-HSE level of theory, for all the three phases (ca. P = 0, 6 and 12 GPa) of Hg_2Cl_2 crystal, further recognize them as wide band gap insulators where electronic transitions from valence to the conduction bands account for their respective optical absorptions.

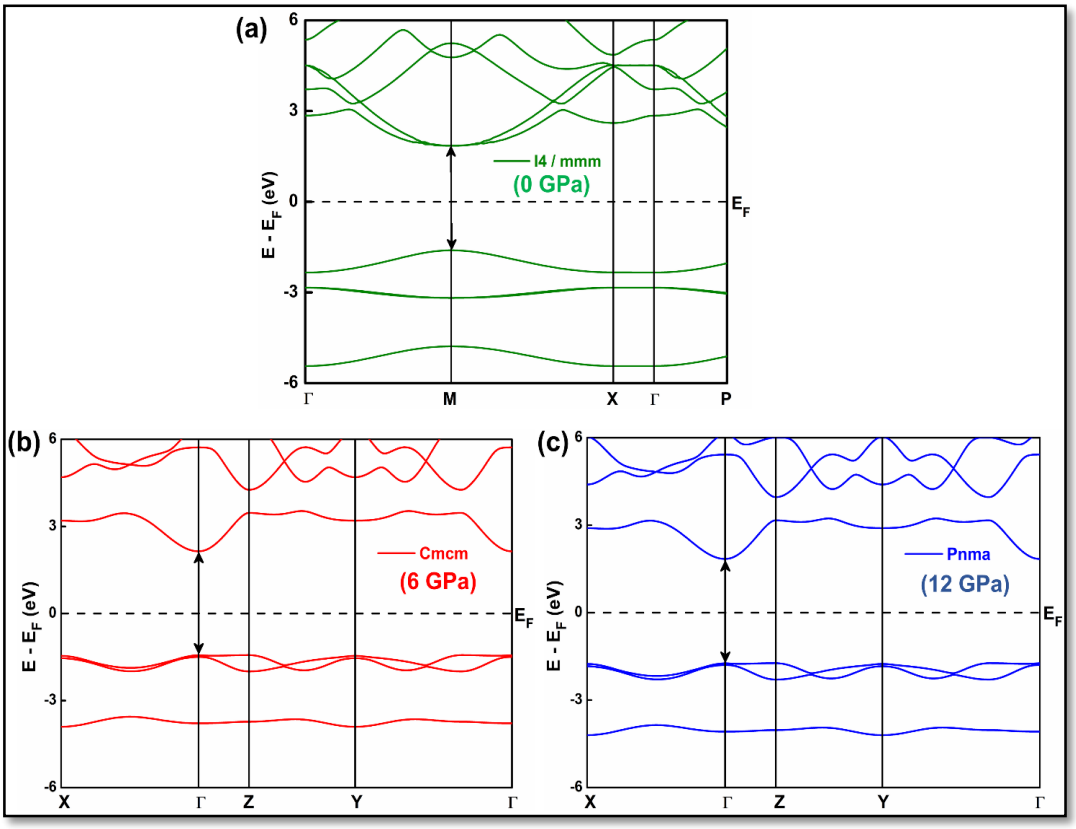

Figure 5.1. Electronic band structure for **(a)** tetragonal (*I4/mmm*) and orthorhombic **(b)** *Cmcm* and **(c)** *Pnma* phases of the Hg_2Cl_2 compound along the high symmetry points Γ→M→X→Γ→P and X→Γ→Z→Y→Γ respectively. The band gaps and the Fermi energies (E_F) are shown as black vertical arrows and black horizontal dashed lines respectively.

5.3. Optoelectronic properties of Hg_2Cl_2 crystal under ambient and external pressures

Hg_2Cl_2 crystal is known to possess large elastic and structural anisotropies at room temperature and under ambient pressure [3]. The anisotropies in the physical properties of the compound are mainly attributed to the presence of parallel Cl(L)–Hg(C)–Hg(A)–Cl(L) linear chains directed along the crystallographic c-axis representing [001] direction [4]. The ingrained anisotropies associated with the elastic and physical properties of the compound may presage similar direction dependence behaviour in the optical properties as well. The optical properties of the Hg_2Cl_2 crystal are thus initially investigated for all the three [100], [010] and [001] polarization directions of the incident electric field. However, the optical properties of the compound are found to be identical in both [100] and [010] polarization directions, but are substantially altered along the [001] direction. The electric field components along [100]/ [010] and [001] directions are owed to $E_\perp$ and $E_\parallel$ respectively.

5.3.1. The dielectric function $\varepsilon_1(\omega)$

Figure 5.2(a) shows the variation of the real part of the complex dielectric function $[\varepsilon_1(\omega)]$ as a function of the incident electromagnetic field energy (E_{EM}) for Hg_2Cl_2 crystal under ambient pressure P = 0 GPa and at P = 6, 12 GPa, where the compound exists in tetragonal [*I4/mmm* (D_{4h}^{17})] and orthorhombic [*Cmcm* (D_{2h}^{17}), *Pnma* (D_{2h}^{16})] phases respectively. The static dielectric constant $\varepsilon_1(0)$ of the compound at P = 0 GPa has been estimated to be ~ 4.9 for [001]/ $E_\parallel$ while it is close to zero along [100] and [010]/ $E_\perp$ polarization directions of the electric field. The estimated value of $\varepsilon_1(0)$ ~ 4.9 for Hg_2Cl_2 crystal under ambient pressure P is in close agreement with the calculated value ~ 4.6 reported by Sobolev *et al.* [2]. Distinct anisotropies in the $\varepsilon_1(\omega)$ values are also noted for two different polarization directions of the incident electromagnetic wave. For $E_\parallel$ polarization of the electric field, $\varepsilon_1(\omega)$ shows the maximum positive value at ~ 4.5 eV, beyond which it gradually decreases and becomes negative over the energy range ~ 5 – 7 eV. The real part of the dielectric function $\varepsilon_1(\omega)$ is linked with the dispersion and linear polarization of light as it propagates through the material medium [5-7]. The maximum dispersion is achieved at the resonance frequency that corresponds to E_{EM} value at ~ 4.5 eV for $E_\parallel$ polarization. However, for E_{EM} > 9 eV, $\varepsilon_1(\omega)$ becomes nearly zero. Interestingly, the dispersive nature of $\varepsilon_1(\omega)$ for $E_\perp$ is markedly different from that estimated for the $E_\parallel$ polarization. Over a wide energy range from 0 - 4 eV, $\varepsilon_1(\omega)$

remains nearly zero and is consistent with the static value of the dielectric constant $\varepsilon_1(0)$. However, within ~ 4.6 - 7.5 eV, it becomes negative, beyond which $\varepsilon_1(\omega)$ increases and becomes zero in the high energy limit. The negative values of $\varepsilon_1(\omega)$ for the Hg_2Cl_2 crystal under ambient pressure at room temperature in the 5.12 – 6.97 eV and 4.6 – 7.5 eV energy windows for $E_\parallel$ and $E_\perp$ polarization directions of the electric field respectively signify the metallic Drude like features of the compound.

Interestingly, under the application of external pressures (ca. P = 6 and 12 GPa), the variations in $\varepsilon_1(\omega)$ for Hg_2Cl_2 as a function of incident E_{EM} for both $E_\parallel$ and $E_\perp$ polarizations show remarkable differences in their features in comparison to that recorded under ambient condition at P = 0 GPa. The static dielectric constant $\varepsilon_1(0)$ of the compound at P = 6 and 12 GPa have been estimated to be ~ 4.86 and 4.65 respectively for [001]/ $E_\parallel$ polarization directions of the electric field, while both the values of $\varepsilon_1(0)$ are 2.2 and 1.68 along [100]/ [010]/ $E_\perp$ polarization directions respectively. The variations in $\varepsilon_1(\omega)$ of the Hg_2Cl_2 compound at P = 6, 12 GPa with change in incident E_{EM} for $E_\parallel$ and $E_\perp$ polarizations follow similar traces, although clear anisotropies in the values of $\varepsilon_1(\omega)$ are noted for two different polarization states of the incident radiation. However, both the traces show a resonance peak maximum at ~ 4.8 eV, which is slightly shifted towards a higher frequency in comparison to that estimated under ambient pressure (~ 4.5 eV, P = 0 GPa). The slight change in the resonance frequency may be attributed to the variation in electronic band energy states as reflected from the corresponding E-**k** diagram in the first Brillouin zone (*vide supra, cf.* Section 5.2). Significantly enough, the $\varepsilon_1(\omega)$ vs energy plots for the Hg_2Cl_2 crystal at P = 0 and 6, 12 GPa, as shown in Figure 5.2(a), show unique characteristic features that can be directly correlated with the tetragonal and orthorhombic phases of the compound under study. The tetragonal phase of Hg_2Cl_2 crystal is known to exist under ambient pressure (P = 0 GPa) while under external pressure the system undergoes structural phase transitions from tetragonal [*I4/mmm* (D_{4h}^{17})] to orthorhombic [*Cmcm* (D_{2h}^{17}), *Pnma* (D_{2h}^{16})] phases at transition pressures $(P_T)_1$ = 0.25 GPa and $(P_T)_2$ = 9 GPa [1]. The other striking observation has been the small decrements in the $\varepsilon_1(0)$ values of the compound with an increase in P. This is an expected observation as $\varepsilon_1(0)$ scales inversely with E_g following Penn's model [8].

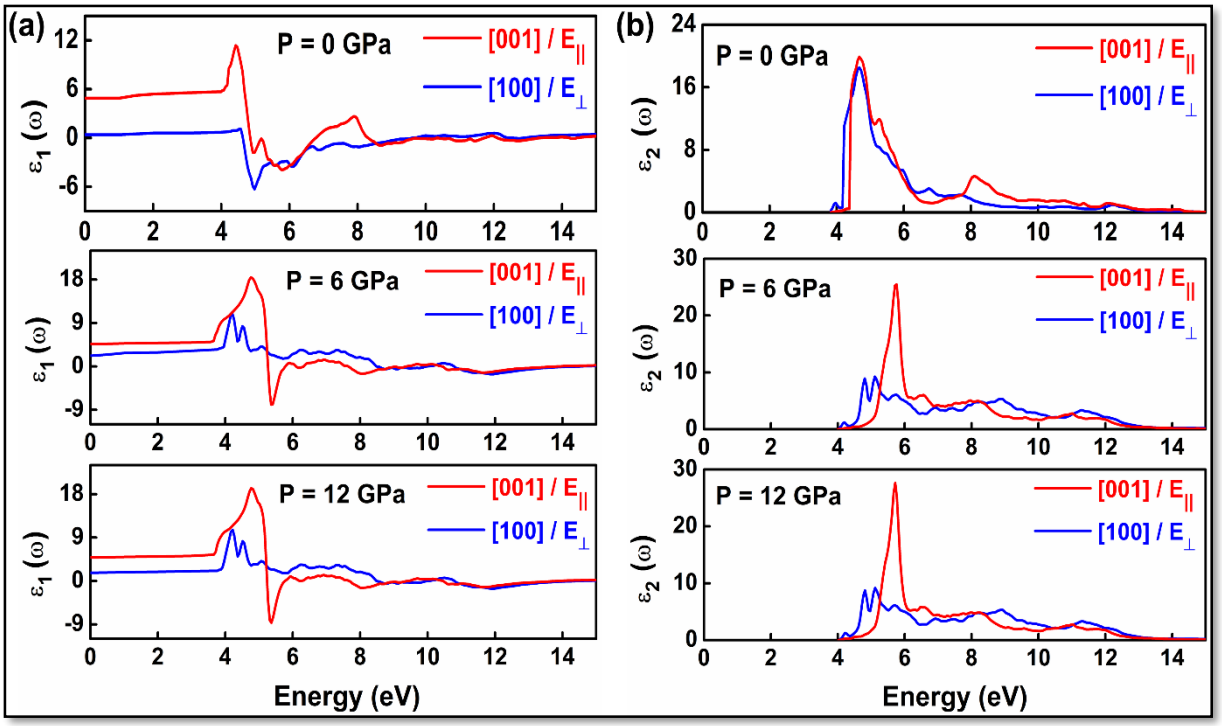

Figure 5.2. The **(a)** real and **(b)** imaginary part of the complex dielectric function of Hg_2Cl_2 compound as a function of energy under ambient pressure P = 0 GPa and under external pressures P = 6 GPa and 12 GPa along [001]/ $E_{\parallel}$ and [100]/ $E_{\perp}$ directions of polarization as estimated from GGA – HSE level of theory.

5.3.2. The dielectric function $\varepsilon_2(\omega)$

The variations of the imaginary part of the complex dielectric function $[\varepsilon_2(\omega)]$ with energy for Hg_2Cl_2 crystal under ambient (P = 0 GPa) and external pressures P = 6 and 12 GPa are shown in Figure 5.2(b). The dielectric function $\varepsilon_2(\omega)$ signifies the interband transitions and identifies frequency-dependent attenuation of incident electromagnetic field energy (E_{EM}) by the materials. The take-off or critical value of $\varepsilon_2(\omega)$ is intrinsically related to the E_g of the compound [9,10]. The critical values of $\varepsilon_2(\omega)$ for both $E_{\parallel}$ and $E_{\perp}$ polarization directions of the electric field have been estimated to be ~ 3.92, 4.00 and 4.05 eV when the crystal is subjected to external pressures P = 0, 6 and 12 GPa respectively. These results follow the estimated E_g values of the compound under similar perturbations (*cf.* Section 5.2). The critical value of $\varepsilon_2(\omega)$ of the compound at room temperature and under ambient pressure is in close agreement with the result as suggested by Sobolev *et al.* [2]. The structured bands are visible in $\varepsilon_2(\omega)$ versus energy plots [Figure 5.2(b)] whose peaks are owed to the interband transitions of the

compound. The peak positions of these bands at ~ 4.67 and ~ 5.71 eV under ambient and external pressures P = 6, 12 GPa respectively have unique characteristics of their kind that allow one to identify the tetragonal and orthorhombic phases of the compound under investigation. Furthermore, the anisotropies in the $\varepsilon_2(\omega)$ values of the compound under ambient conditions and external pressures are distinctly identified for both the polarization directions of the incident electric field. However, large to moderate positive values of $\varepsilon_2(\omega)$ in the energy range 4.5- 12 eV for both $E_{\parallel}$ and $E_{\perp}$ polarizations [Figure 5.2(b)] may signify strong absorption of the incident electromagnetic wave by this compound in this energy window. This is also reflected in $\alpha(\omega)$ and $\sigma(\omega)$ plots as shown in Figure 5.3, where both the absorption coefficient and the optical conductivity exhibit appreciable values in the 4.5 - 12 eV energy window of the electromagnetic spectrum.

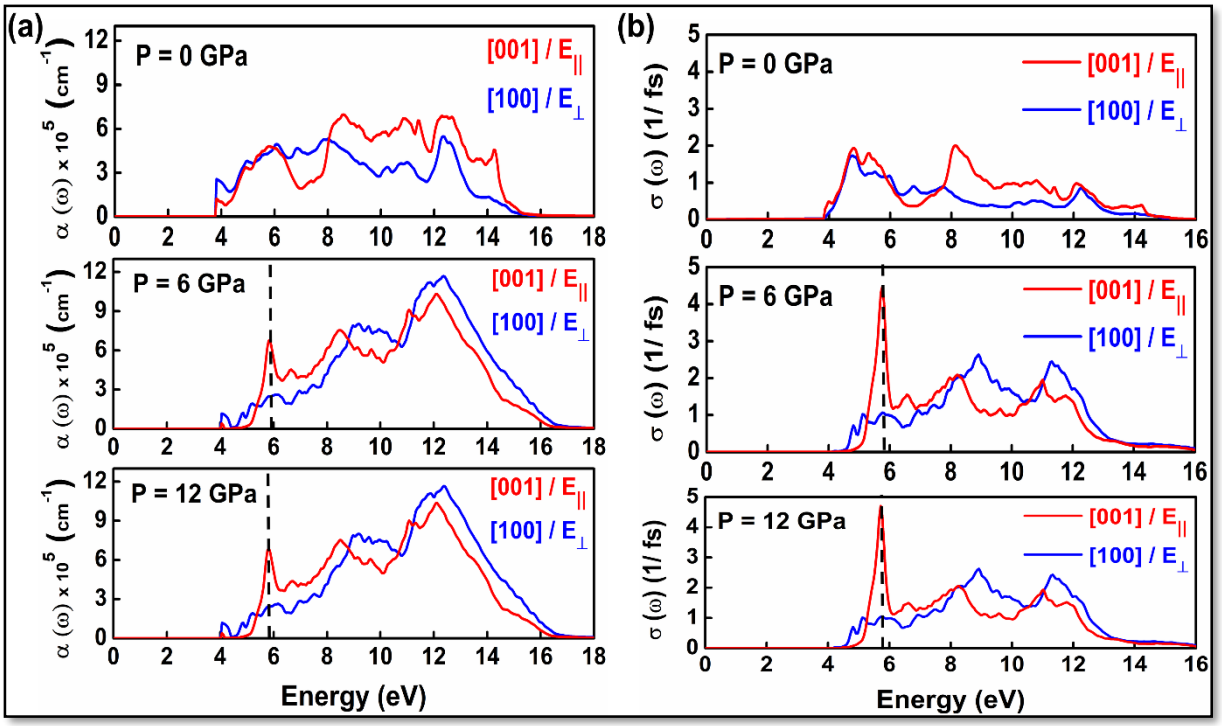

Figure 5.3. (a) Optical absorption coefficient and **(b)** optical conductivity of Hg_2Cl_2 compound as a function of energy under ambient (P = 0 GPa) and external pressures (P = 6 GPa and 12 GPa) along [001]/ $E_{\parallel}$ and [100]/ $E_{\perp}$ directions of polarization as obtained from GGA – HSE level of theory. [The characteristic peaks in the orthorhombic phases of the Hg_2Cl_2 compound are marked with dotted arrows].

Closer inspections of $\alpha(\omega)$ and $\sigma(\omega)$ plots (Figure 5.3) reveal certain interesting features. Both these plots show the appearance of a well-resolved band peaked at ~ 5.80 eV for

$E_{\parallel}$ polarization (along [001] direction) of the incident electric field. This band appears in $\alpha(\omega)$ and $\sigma(\omega)$ plots for the Hg_2Cl_2 under external pressures P = 6 and 12 GPa, where the crystal exists in the orthorhombic phase at room temperature. This peak eventually disappears when the system crystallizes to the tetragonal phase under ambient pressure. The physical origin of the peak at ~ 5.80 eV in the absorption coefficient $\alpha(\omega)$ and optical conductivity $\sigma(\omega)$ for $E_{\parallel}$ [001] polarization of the incident electromagnetic field energy (E_{EM}) at P = 6 and 12 GPa [Figure 5.3(a)] may be rationalised from the corresponding crystal structures of the compound. Interestingly, the crystallographic c-axes representing [001] direction of the compound under elevated pressures (ca. P = 6 and 12 GPa) are marked by the presence of parallel Cl(L)–Hg(C)–Hg(A)–Cl(L) distorted chains in contrast to parallel linear chains of the same under ambient pressure [1]. The distortions of the linear Cl(L)–Hg(C)–Hg(A)–Cl(L) chains at P = 6 and 12 GPa result in the alterations of electronic arrangements which in turn may promote excitonic transitions leading to a large increase in the absorption coefficients [$\alpha(\omega)$] and associated optical conductivities [$\sigma(\omega)$] for $E_{\parallel}$ polarization of the incident electric field at ~ 5.80 eV [11]. The variations in electronic arrangements of the Hg_2Cl_2 compound under ambient (P = 0 GPa) and elevated pressures (P = 6 and 12 GPa) are reflected from their corresponding E-**k** diagrams as depicted in Figure 5.1 (*vide supra, cf.* Section 5.2). The appearance of this characteristic peak at ~ 5.80 eV thus may be intrinsically related to the orthorhombic phase of Hg_2Cl_2 crystal at elevated pressure. The appearance and disappearance of the band peaked at ~ 5.80 eV in $\alpha(\omega)$, $\sigma(\omega)$ plots as a function of energy, akin to ~ 4.67 and ~ 5.71 eV peaks in the $\varepsilon_2(\omega)$ plots (*vide supra*) may be considered as a signature band that carries the latent information regarding the crystal system (tetragonal or orthorhombic) of the compound not only under ambient condition but also when subjected to elevated pressure.

Interestingly both $\alpha(\omega)$ and $\sigma(\omega)$ plots at ambient and under external pressures (P = 6 and 12 Pa) for $E_{\parallel}$ and $E_{\perp}$ polarizations begin at ~ 3.92, 4.00 and 4.05 eV respectively which corresponds to the take-off or critical values $\varepsilon_2(\omega)$ of the compound under study. The critical values $\varepsilon_2(\omega)$ of the compound in turn are linked with E_g of the systems. These calculations thus help us to cross-check the E_g values of the compounds from their corresponding optical properties. It may be relevant to mention that although in a strict sense, $\alpha(\omega)$ signifies the optical band gap of a compound, for wide band gap insulators as in the case of Hg_2Cl_2, this energy gap value closely resembles E_g where interband transitions account for the optical absorption. Moreover, in the energy windows ~ 0 – 3.9 eV, and beyond ~ 15 eV, the $\alpha(\omega)$ value of the compound under external pressures P = 0 and 6, 12 GPa for both $E_{\parallel}$ and $E_{\perp}$

polarizations of the incident electric field show zero or almost negligible values. These results suggest that Hg_2Cl_2 crystal remains highly transparent in the energy windows ~ 0 - 4 eV, and above 15 eV under a wide range of external pressures spanning between 0 – 14 GPa regardless of the structural phase transitions at $(P_T)_1$ = 0.25 GPa and $(P_T)_2$ = 9 GPa. The wide spectral range of transparency covering UV-Vis-LWIR and extreme UV regions of the electromagnetic spectrum together with pronounced optical properties make Hg_2Cl_2 a promising material for various applications in acousto-optic devices.

5.3.3. Refractive indices (n_e, n_o) and the optical birefringence (Δn) of Hg_2Cl_2

Anisotropic crystals are composed of complex atomic lattice orientations with varying electrical, optical and mechanical properties depending upon the polarization direction of the incident electromagnetic field energy (E_{EM}). As a result, the refractive indices of the anisotropic crystals also vary with the polarization direction of the electromagnetic wave, giving rise to direction-dependence trajectories and velocities of the emergent ray. This phenomenon is designated as double refraction and the emergent ray whose velocity is independent (dependent) of propagation direction is termed as ordinary (extraordinary) ray. The corresponding refractive indices for the ordinary (O) ray are designated as n_o while that for the extraordinary (E) ray as n_e. The difference in refractive indices ($\Delta n = n_e - n_o$) between the extraordinary and ordinary rays is termed as optical birefringence of the doubly refracting crystal [12]. In the present context, the directions of the O and E- rays after double refraction through the Hg_2Cl_2 crystal have been identified with $E_\perp$ and $E_\parallel$ polarizations of the electric field along [100]/ [010] and [001] directions respectively. The anisotropic response of the complex dielectric functions $\varepsilon_1(\omega)$ and $\varepsilon_2(\omega)$ for the uniaxial Hg_2Cl_2 crystal under ambient (P = 0 GPa) and external pressures P = 6 and 12 GPa for both $E_\perp$ and $E_\parallel$ polarizations of the incident electric field invoke us to study in details the real part of the complex refractive index $[n(\omega)]$ and the corresponding birefringence (Δn) value of the material.

Figure 5.4(a) shows the variations of refractive indices n_o and n_e as a function of incident E_{EM} for the Hg_2Cl_2 crystal under ambient and external pressures P = 6 and 12 GPa. From Figure 5.4(a), it is observed that n_o and n_e values of the compound under ambient (ca. P = 0 GPa) and external pressures (ca. P = 6 and 12 GPa) are nearly independent of incident E_{EM} in the energy window ~ 0 to 4.1 eV. However, beyond this energy window both n_o, n_e values

of Hg_2Cl_2 under ambient condition/ under external pressures (P = 6, 12 GPa) increase, attaining maximum values at ~ 4.62, 4.52 eV/ 4.71, 5.35 eV and then decrease again with an increase in E_{EM} within the energy window ~ 4.70 – 6.50 eV/ 5.73 – 6.05 eV. The increase in the values of refractive indices with E_{EM} in the above-referred energy window may be related to large opacity and low phase velocities of the propagating electromagnetic rays inside the compound [13,14]. The shifts in the peak values of n_o and n_e for the compound are intrinsically related to the corresponding complex dielectric functions [$\varepsilon(\omega)$] which in turn are linked with the electronic band structures of the compound under ambient (P = 0 GPa) and external pressures (P = 6, 12 GPa). Interestingly, the characteristic peaks in $n(\omega)$ versus energy plots for n_o, (n_e) at ~ 4.62, (4.52) eV owed to Hg_2Cl_2 crystal in ambient condition (ca. P = 0 GPa) and ~ 4.71 (5.35) eV under external pressures P = 6, 12 GPa may be directly related with the tetragonal and orthorhombic phases of the system under study. The Hg_2Cl_2 crystal at ambient conditions and under external pressures at P = 6, 12 GPa is indeed known to exist in body-centred tetragonal (*I4/mmm*) and orthorhombic (*Cmcm, Pnma*) phases respectively [1].

Moreover, Figure 5.4(a) also shows marked differences between the values of n_o and n_e not only for the crystal under ambient conditions but also under high external pressures. The difference (Δn) between the values of n_o and n_e makes the Hg_2Cl_2 crystal optically birefringent and is expected to show the birefringence phenomenon. The calculated birefringence value $\Delta n = 0.64$ at ~ 2 eV for the studied compound under ambient conditions is in excellent agreement with the reported value ~ 0.65 – 0.66, as depicted in the available works of literature [15]. This result further justifies the level of theory used in the first-principle calculations which has the unique power to reproduce the experimentally determined optical band gap, imaginary part of the complex dielectric function, refractive indices and optical birefringence of the compound [2,15]. In this connection, it may be worth mentioning that the first-principle calculations with the GGA-HSE level of theory are known to reproduce the experimentally determined band gaps and optical properties of different materials with profound accuracies and have been reported elsewhere [4,16-19].

Figure 5.4(a) further reveals that both the values of the refractive indices (n_o, n_e) of the compound in ambient condition and under external pressures P = 6, 12 GPa are less than 1 for the incident energies above ~ 9 and 12 eV respectively. These results signify that the phase velocity (v_p) of the incoming wave within the crystal exceeds the speed of light "c" in vacuum at the energy windows above ~ 9 eV for the tetragonal (*I4/mmm*) phase and above ~ 12 eV for

the orthorhombic (*Cmcm*, *Pnma*) phases of the compound. Beyond the above-referred energy windows, the Hg_2Cl_2 crystal is thus turned into exotic metamaterials or left-handed materials and is expected to show non-linear optical properties and superluminal characteristic features [20-23].

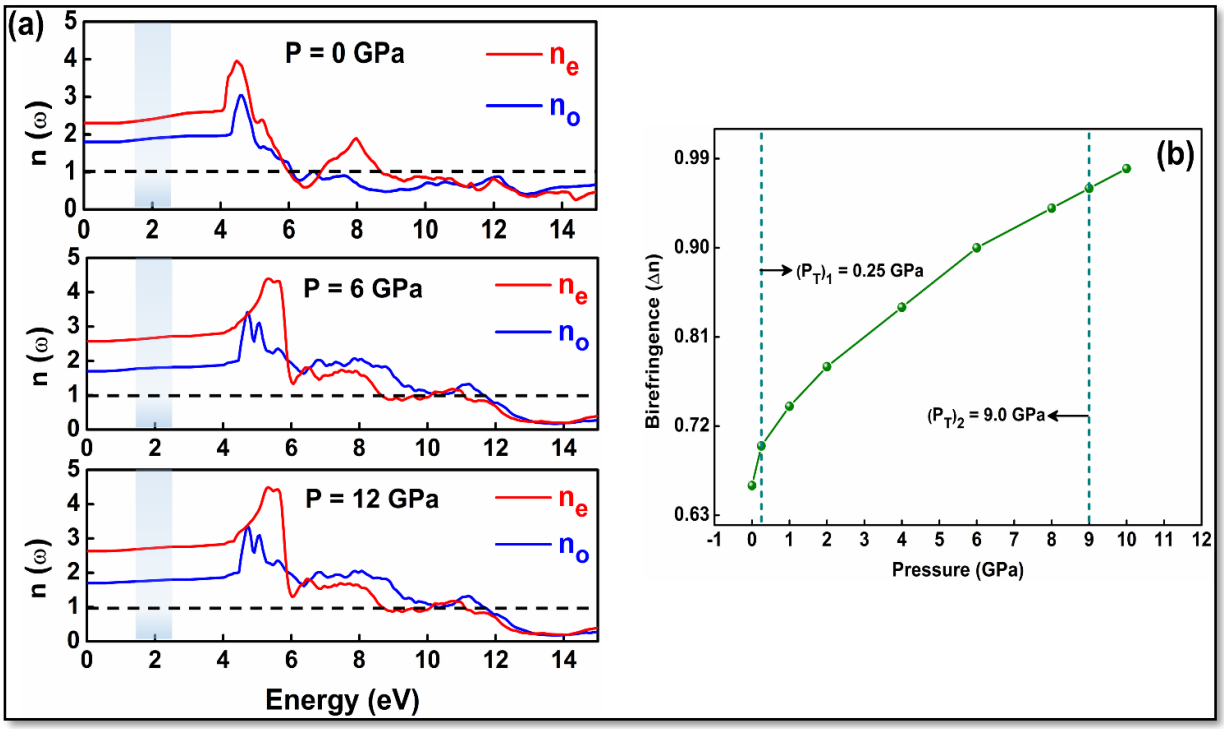

Figure 5.4. (a) Real part of the refractive index $n(\omega)$ of the Hg_2Cl_2 compound computed as a function of energy under ambient (P = 0 GPa) and external pressures (P = 6 GPa and 12 GPa) along [001]/ $E_{\parallel}$ and [100]/ $E_{\perp}$ directions of polarization. The visible region (~ 1.5 eV to 3 eV) is shaded with blue in each plot. **(b)** The birefringence (Δn) as a function of external pressure for Hg_2Cl_2 compound as estimated from GGA – HSE level of theory. [The transition pressures are marked in the figures as vertical dotted lines].

The variation in Δn for Hg_2Cl_2 crystal as a function of external pressure is shown in Figure 5.4(b). From Figure 5.4(b) it is seen that Δn increases with an increase in P. However, deeper inspection further reveals distinct changes in the slopes of the curve at P ~ 0.25 and 9 GPa which incidentally correspond to the transition pressures $(P_T)_1$ and $(P_T)_2$ associated with *I4/mmm* $(D_{4h}^{17}) \rightarrow$ *Cmcm* (D_{2h}^{17}) and *Cmcm* $(D_{2h}^{17}) \rightarrow$ *Pnma* (D_{2h}^{16}) structural phase transitions of the compound. Appreciable increments in the optical birefringence with pressure are associated with an increase in the anisotropic behaviour of the crystal as it undergoes two consecutive phase transitions from tetragonal to the orthorhombic phases of the compound at P = 0.25 and

9 GPa. We believe that such changes in the optical birefringence with P will help in designing improved optoelectronic devices such as polarized lasers, waveguides and fibre-optic communication systems in future endeavours [9,24-27].

5.4. Conclusions

Pressure-induced modulations in the optoelectronic properties of the Hg_2Cl_2 compound have been explored in detail for the first time from first-principle calculations. Crystal structures and the pressure-driven structural phase transitions from the tetragonal [*I4/mmm* (D_{4h}^{17})] to orthorhombic [*Cmcm* (D_{2h}^{17}) and *Pnma* (D_{2h}^{16})] phases of the compound have been critically explored. Variations in the optoelectronic properties of the material in ambient conditions and under external pressures have been explored in terms of complex dielectric functions, absorption coefficients, optical conductivities, refractive indices and optical birefringences.

Bibliography

[1] S. Ghosh and J. Chowdhury, J. Appl. Phys. **130**, 225103 (2021).

[2] V. V. Sobolev, V. V. Sobolev, and D. V. Anisimov, Semiconductors **50**, 29 (2016).

[3] A. A. Kaplyanskii, in *Theory of Light Scattering in Condensed Matter*, edited by B. Bendow, J. L. Birman, and V. M. Agranovich (Springer US, Boston, MA, 1976), pp. 31.

[4] S. Ghosh, S. Sarkar, and J. Chowdhury, Mater. Chem. Phys. **276**, 125379 (2022).

[5] S. Ghosal, A. Bandyopadhyay, and D. Jana, Phys. Chem. Chem. Phys. **22**, 19957 (2020).

[6] M. I. Naher and S. H. Naqib, Sci Rep **11**, 5592 (2021).

[7] R. Saniz, L.-H. Ye, T. Shishidou, and A. J. Freeman, Phys. Rev. B **74**, 014209 (2006).

[8] D. R. Penn, Phys. Rev. **128**, 2093 (1962).

[9] S. Ghosh and J. Chowdhury, Mater Sci Eng B **284**, 115903 (2022).

[10] M. Kaur, G. Sharma, M. Rérat, and K. B. Joshi, J Mater Sci **55**, 5099 (2020).

[11] M. W. Kim, P. Murugavel, S. Parashar, J. S. Lee, and T. W. Noh, New J. Phys. **6**, 156 (2004).

[12] F. A. Jenkins and H. E. White, *Fundamentals of Optics* (McGraw-Hill, 1976).

[13] M. Born and E. Wolf, *Principles of Optics: Electromagnetic Theory of Propagation, Interference and Diffraction of Light* (Cambridge University Press, Cambridge, 1999), 7 edn.

[14] R. R. Banik, S. Ghosh, and J. Chowdhury, Phys. Scr. **98**, 105914 (2023).

[15] A. Pierson and C. Philippe, in *Proc.SPIE*2019).

[16] S. Ghosh and J. Chowdhury, RSC Adv. **14**, 6385 (2024).

[17] S. Ghosh and J. Chowdhury, Mod. Phys. Lett. B **38**, 2330003 (2023).

[18] M. Nishiwaki and H. Fujiwara, Comput. Mater. Sci. **172**, 109315 (2020).

[19] M. Ramzan, Y. Li, R. Chimata, and R. Ahuja, Comput. Mater. Sci. **71**, 19 (2013).

[20] L. J. Wang, A. Kuzmich, and A. Dogariu, Nature **406**, 277 (2000).

[21] G. V. Viktor, Sov. Phys. Usp. **10**, 509 (1968).

[22] D. R. Smith, W. J. Padilla, D. C. Vier, S. C. Nemat-Nasser, and S. Schultz, Phys. Rev. Lett. **84**, 4184 (2000).

[23] Q. Mahmood, M. Hassan, and N. A. Noor, J. Phys.: Condens. Matter **28**, 506001 (2016).

[24] A. Berezin, Mater. Chem. Front. (2023).

[25] J. Hu *et al.*, Appl. Surf. Sci. **590**, 152910 (2022).

[26] S. Abedini Dereshgi, Y.-S. Lee, M. C. Larciprete, M. Centini, V. P. Dravid, and K. Aydin, Adv. Optical Mater. **11**, 2202603 (2023).

[27] D. Ghosh, S. Chanda, B. Debnath, M. Debbarma, R. Bhattacharjee, and S. Chattopadhyaya, Physica B Condens. Matter **574**, 411669 (2019).

Chapter 6

Temperature dependent structural phase transition and negative thermal expansion of Mercurous Chloride

6.1. Introduction

The present chapter aims to understand the temperature-dependent structural phase transition and negative thermal expansion (NTE) behaviour of the Hg_2Cl_2 system. At room temperature (T = 300 K) and under ambient pressure (P = 0 GPa) Hg_2Cl_2 is known to crystallise in the body-centred tetragonal [*I4/mmm* (D_{4h}^{17})] phase. Experimental observations suggest that Hg_2Cl_2 compound at low temperature (T ~ 186 K) encounters *I4/mmm* (D_{4h}^{17}) → base-centered orthorhombic [*Cmcm* (D_{2h}^{17})] structural phase transition and finally end up in the *Cmcm* (D_{2h}^{17}) phase [1-5]. Here, the temperature-dependent *I4/mmm* (D_{4h}^{17}) → *Cmcm* (D_{2h}^{17}) structural phase transition and NTE of the compound have been unveiled from the first-principle density functional theory (DFT) and Born-Oppenheimer on the fly molecular dynamics (BOMD) simulations. The order parameter, the nature of the phase transition and the Grüneisen parameters have also been unveiled. The present study will help to identify the key phonon modes that stand responsible for the above referred phase transition and NTE behaviour of the said compound.

6.2. Modulations of lattice and structural parameters of Hg_2Cl_2 compound with temperature

The Hg_2Cl_2 compound, at room temperature (T = 300 K) and at P = 0 GPa, crystallizes in the body-centered tetragonal phase with *I4/mmm* (D_{4h}^{17}) space group symmetry (space group no. 139). The variations in the supercell energy ($\tilde{E}$) of the Hg_2Cl_2 compound in its *I4/mmm* phase at room temperature (T = 300 K) with time is shown in Figure 6.1(a). After primary relaxations marked by concomitant rise in energy with time, the system attains equilibrium energy value after a lapse of ~ 10 ps. The refined supercell geometry of the system, so extracted from the BOMD simulation run at 30 ps time scale, is depicted in Figure 6.1(b).

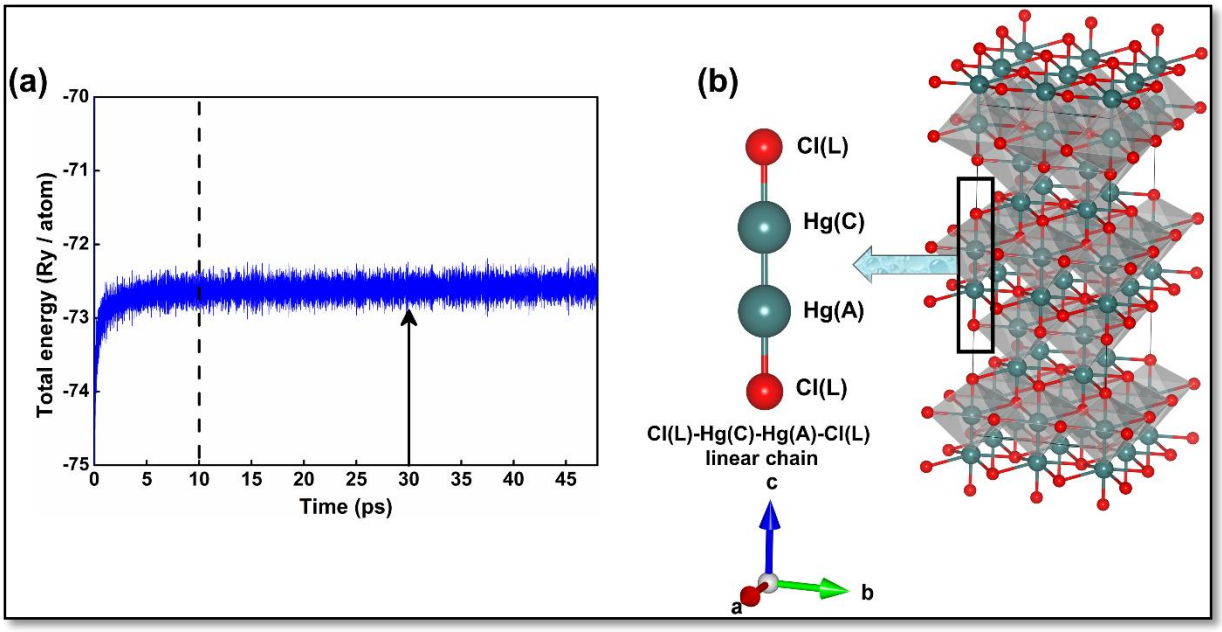

Figure 6.1. (a) Temporal variations of total energy and **(b)** the optimized geometry of 2×2×2 supercell for the *I4/mmm* phase of Hg_2Cl_2 crystal at room temperature (T = 300 K) as accomplished from the BOMD simulations. [Emarald blue and red colours show Hg and Cl atoms respectively].

To comprehend the temperature-dependent structural phase transition of the studied system, variation in the supercell volume (V) of Hg_2Cl_2 crystal in its *I4/mmm* phase as a function of temperature has been primarily estimated. The result is shown in Figure 6.2(a). Interestingly, with a decrease in temperature from 300 K, a slight increase in V has been noticed until the temperature (T) attains 188 K, where distinct discontinuity in V-T curve has been observed. Before this discontinuity, the system remains in the *I4/mmm* phase. The sharp discontinuity in the V-T curve is followed by an appreciable rise in the supercell volume from ~ 1779.89 to 3420.44 $Å^3$. Supercell volume ~ 3420.44 $Å^3$ corresponds to the base-centred orthorhombic [*Cmcm* (D_{2h}^{17})] phase of the compound. Such doubling of volume is also reported for the Hg_2Cl_2 crystal as it undergoes temperature-dependent structural phase transition from *I4/mmm* (D_{4h}^{17}) → *Cmcm* (D_{2h}^{17}) phase at T = 185 K [6]. However, with further decrease in temperature from T = 188 K, the supercell volume of the system increases monotonically. The prominent discontinuity in the V-T curve at T = 188 K indicates structural phase transition of the Hg_2Cl_2 compound from body-centered tetragonal [*I4/mmm* (D_{4h}^{17})] to base-centered orthorhombic [*Cmcm* (D_{2h}^{17})] phase. Strikingly enough this temperature T = 188 K closely corresponds to the transition temperature (T_c) ~ 186 K where the compound is experimentally

reported to undergo temperature dependent *I4/mmm* (D_{4h}^{17}) → *Cmcm* (D_{2h}^{17}) structural phase transition [1]. Furthermore, the structural phase transition at T_c = 188 K for Hg_2Cl_2 system is associated with the discrete changes in supercell volume with temperature. The alterations in the lattice parameters (a, b, c) of Hg_2Cl_2 compound as a function of temperature are shown in Figure 6.2(b). Akin to the V-T plot [Figure 6.2(a)], the variations in the lattice parameters of the compound with temperature are marked by noticeable discontinuities at T = 188 K, which further corresponds to T_c that leads to the *I4/mmm* (D_{4h}^{17}) → *Cmcm* (D_{2h}^{17}) structural phase transition of the system under study.

In this connection, it is worth mentioning that the decrease in supercell volume with temperature [Figure 6.2(a)] promotes the negative thermal expansion (NTE) behaviour of the compound in the temperature window ranging between 300 and 80 K. To understand the NTE of the system, the volumetric coefficient of thermal expansion (α) has been estimated using the following relation

$$\alpha = \frac{1}{V}\frac{\partial V}{\partial T} \tag{6.1}$$

The α values for the *I4/mmm* and *Cmcm* phases of the Hg_2Cl_2 compound at T = 300 and 185 K are found to be -1.34×10^{-4} K^{-1} and -7.62×10^{-4} K^{-1} respectively. The α value for the *I4/mmm* phase of the compound at T = 300 K closely resembles to the experimental observations as reported elsewhere [7,8]. Moreover, the NTE of the system may be linked with the variation of the crystallographic c-axis which is found to be significantly decreased with increase in T [Figure 6.2(b)]. The detail discussion on NTE of Hg_2Cl_2 compound will be unveiled in the later section.

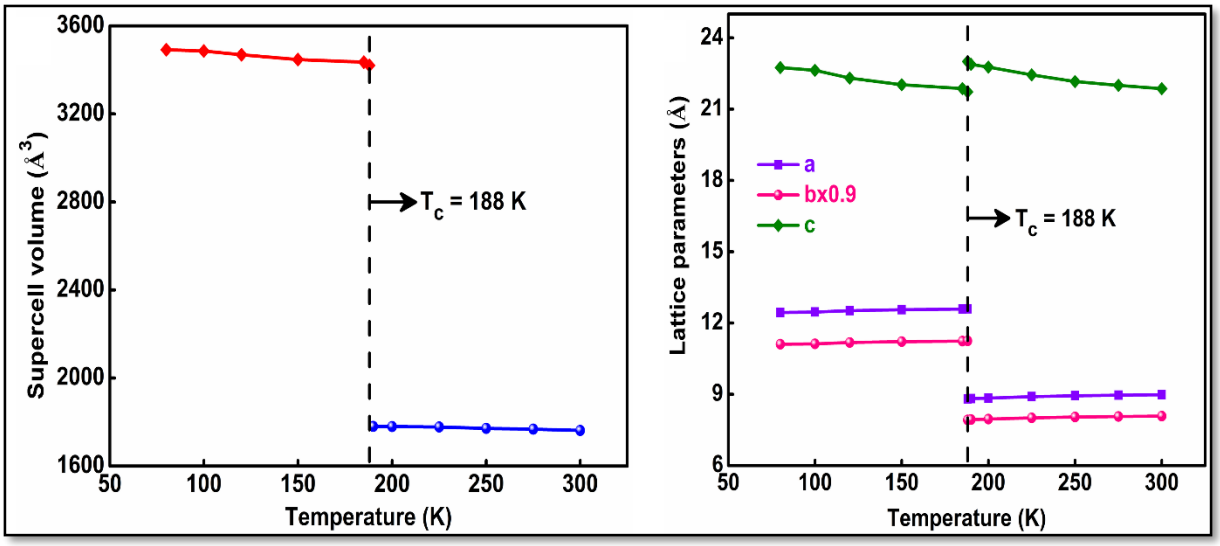

Figure 6.2. (a) Supercell volume and **(b)** lattice parameters versus temperature plots as obtained from the BOMD simulations [The transition temperature T_c has been marked with vertical dotted (---) lines.]

The optimized crystal structure for the *Cmcm* (D_{2h}^{17}) phase (that is experimentally known to remain stable at T < 186 K [1]) of Hg_2Cl_2 at temperature T = 185 K, so accomplished from the BOMD simulations is shown in Figure 6.3(a). The variation of the average Cl(L)-Hg(C)-Hg(A)-Cl(L) dihedral angle as a function of temperature is shown in Figure 6.3(b). From Figure 6.3(b) it is seen that the average value of Cl(L)-Hg(C)-Hg(A)-Cl(L) dihedral angle deviates from planar dispositions (from 180^0 to 170.54^0) of the associated atoms as the compound undergoes temperature dependent structural phase transition from the body-centered tetragonal to base-centered orthorhombic [*I4/mmm* → *Cmcm*] phase at T_c = 188 K. Deviation from planarity of the Cl(L)-Hg(C)-Hg(A)-Cl(L) chain in the Hg_2Cl_2 system in turn can alter its anisotropic behaviour and this anisotropy may become more prominent as the compound undergoes phase transition at the specified T_c.

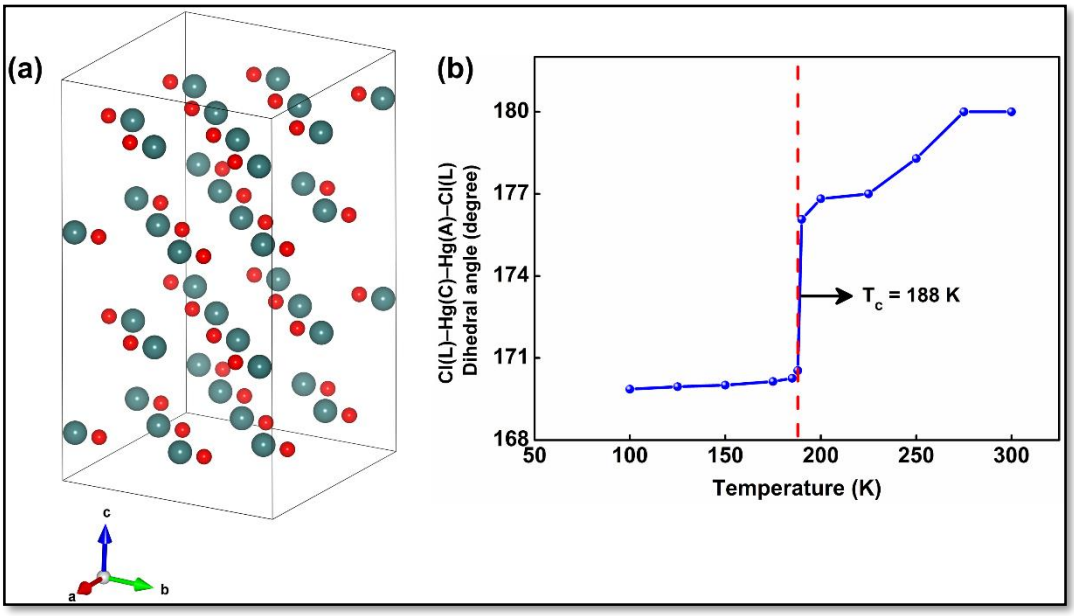

Figure 6.3. (a) Optimized 2×2×2 supercell for the *Cmcm* phase of Hg_2Cl_2 at T = 185 K (Hg atoms are shown in emerald blue, while Cl atoms are in red colours). **(b)** Average Cl(L)-Hg(C)-Hg(A)-Cl(L) dihedral angle as a function of temperature as obtained from the BOMD simulations.

6.3. Order parameter associated with the paraelastic to ferroelastic phase transition

The order parameter associated with *I4/mmm* (D_{4h}^{17}) → *Cmcm* (D_{2h}^{17}) structural phase transition of the Hg_2Cl_2 compound at T_c =188 K has been estimated from the second rank strain tensor function (e_{ij}) [9-11]. Hg_2Cl_2 is known to undergo ferroelastic to paraelastic phase transition with temperature [1,12,13]. While spontaneous strain is harboured in the ferroelastic phase of the compound, the paraelastic phase on the other hand does not show any such behaviour. In this temperature-dependent paraelastic to ferroelastic phase transition of Hg_2Cl_2 compound, the strain tensor function e_{ij} is thus considered as the order parameter. Strain tensor e_{ij} = 0 represents the paraelastic phase of the compound with no spontaneous strain. However, $e_{ij} \neq 0$ suggests the ferroelastic behaviour of the system with spontaneous strain.

The tensor function is represented as

$$e_{ij} = \frac{1}{\sqrt{2}} (e_{xx} - e_{yy}) \qquad (6.2)$$

where

$$e_{xx} = \frac{(c_o - c)}{a} \tag{6.3}$$

and

$$e_{yy} = \frac{(\frac{a_0}{\sqrt{2}} - a)}{a} \tag{6.4}$$

where "a", "c" and "a_0", "c_0" are the lattice parameter of the body-centered tetragonal (*I4/mmm*) structure and base-centered orthorhombic (*Cmcm*) phases of the compound respectively. Figure 6.4(a) shows the variation of e_{ij} (here the order parameter) as a function of temperature. Interestingly while e_{ij} shows near zero value for T > 188 K, however, for T < 188 K non-zero value of e_{ij} has been estimated. Zero and non-zero values of e_{ij} indicate that the Hg_2Cl_2 system belongs to the respective paraelastic *I4/mmm* and ferroelastic *Cmcm* phases above and below T = 188 K. Furthermore, the marked changes in the order parameters for the Hg_2Cl_2 compound at T = 188 K, not only corroborates *I4/mmm* $(D_{4h}^{17}) \rightarrow$ *Cmcm* (D_{2h}^{17}) structural phase transition at the pre referred temperature but also unveil T_c = 188 K for such transition.

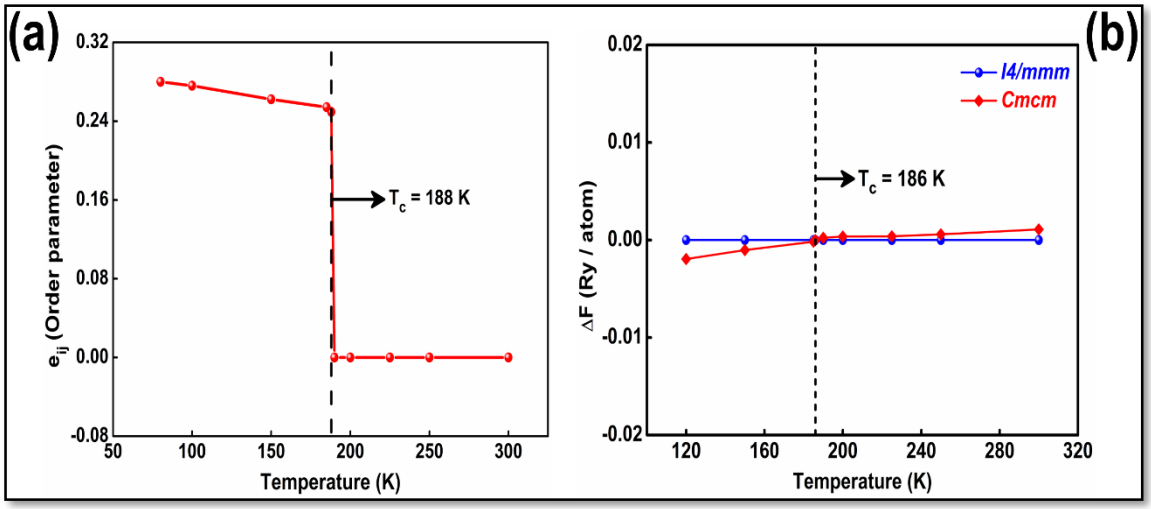

Figure 6.4. (a) Variations of e_{ij} (order parameter) as a function of temperature as obtained from BOMD simulations. **(b)** The Helmholtz free energy difference versus temperature plots for *I4/mmm* and *Cmcm* phases of the Hg_2Cl_2 compound.

6.4. Helmholtz free energy and transition temperature

To precisely determine the transition temperature (T_c) linked with *I4/mmm* (D_{4h}^{17}) → *Cmcm* (D_{2h}^{17}) structural phase transition of Hg_2Cl_2 compound, the Helmholtz free energies (F) of the systems have been estimated using the following relation:

$$F(T, V) = E(V) + F_{el}(T, V) + F_{ph}(T, V) \quad (6.5)$$

where E is the total ground state energy of the respective supercells, V signifies the supercell volume at temperature T, $F_{el}(T, V)$ and $F_{ph}(T, V)$ are the Helmholtz free energies of the electrons and phonons respectively.

The variations of Helmholtz free energy difference (ΔF) as a function of temperature for the *I4/mmm* and *Cmcm* phases of the compound are shown in Figure 6.4(b). From Figure 6.4(b), it is seen that the ΔF-T plots for the *I4/mmm* and *Cmcm* phases of the system intersect at temperature T = 186 K. The point of intersection at T = 186 K not only signifies the isoenergetic point where both the phases of Hg_2Cl_2 share the common Helmholtz free energy but also marks the transition temperature (T_c) that is linked with *I4/mmm* (D_{4h}^{17}) → *Cmcm* (D_{2h}^{17}) structural phase transition of the compound. Interestingly, the result is in complete agreement with the experimental observation where reported T_c =186 K associated with *I4/mmm* (D_{4h}^{17}) → *Cmcm* (D_{2h}^{17}) structural phase transition of the system was reported [1]. The ΔF-T plots further divulge that body-centered tetragonal (*I4/mmm*) phase of the compound is thermodynamically more stable above T_c = 186 K, while below T_c ($T < T_c$) it is the base-centered orthorhombic (*Cmcm*) phase that is estimated to be thermodynamically stable.

6.5. Phonon dispersion relations at various temperatures

Figure 6.5(A) and Figure 6.6(A) show the phonon dispersion spectra for the *I4/mmm* and *Cmcm* phases of Hg_2Cl_2 compound along the high symmetry directions Γ→M→X→Γ→P and Γ→Z→X→Γ→Y respectively. The total and partial phonon density of states (PhDOS) for the *I4/mmm* phase of system at T = 300 K is shown in Figure 6.5(a) while that for the *Cmcm* phase at T= 185 K is depicted in Figure 6.6(a). The transverse acoustic (TA), longitudinal acoustic (LA) phonon modes are observed in the low frequency window of the phonon dispersion spectra ranging between ~ 0 – 1 THz and 0 – 0.95 THz for the *I4/mmm* and *Cmcm* phases of Hg_2Cl_2 compound respectively. The TA phonon branches are found to be doubly degenerate between Γ→M, X→ Γ and Γ→P directions for the *I4/mmm* phase of the compound,

while the same is observed along Γ→Z, Z→X and Γ→Y directions for the *Cmcm* phase. The optical phonon branches for both the *I4/mmm* and *Cmcm* phases of the Hg_2Cl_2 compound at T = 300 and 185 K respectively are localized in two disparate frequency regions ranging from ~ 0.69 – 4.41 THz, 7.07 – 8.85 THz and 0.64 – 4.56 THz, 6.76 – 8.76 THz. The corresponding PhDOS plots for the *I4/mmm*, *Cmcm* phases of the system [Figure 6.5(a), 6.6(a)] indicate that the low and high frequency phonons are dominated by twisting/ wagging/ scissoring and stretching modes of the compound respectively. Interestingly, no imaginary or negative frequency has been noticed in the phonon dispersion curves. This result signifies that *I4/mmm* and *Cmcm* phases of the Hg_2Cl_2 compound at T = 300 and 185 K are dynamically stable.

Surprisingly, at T = 186 K, the phonon dispersion spectra [Figure 6.5(B)] exhibit prominent changes in the dispersions of the phonon branches, of which the slowest transverse acoustic X_1, low-lying optical X_8, Γ_6, Γ_{10}, M_{15} and P_{11} phonon modes undergo remarkable softening by decreasing their frequencies at the respective high symmetry points, X, Γ, M and P. Besides, at T = 186 K, hardening of the optical Γ_{23}, X_{24} and M_{24} phonon modes have also been noticed at the high-symmetry points Γ, X and M respectively in the Brillouin zone. The alterations in phonon frequencies of Γ_6 and Γ_{23} modes with temperature are in close agreement with the temperature dependent ν_1 (E_g) and ν_4 (A_{1g}) Raman active vibrations respectively as the compound suffers *I4/mmm* → *Cmcm* structural phase transition at T ~ 186 K [2,4,5].

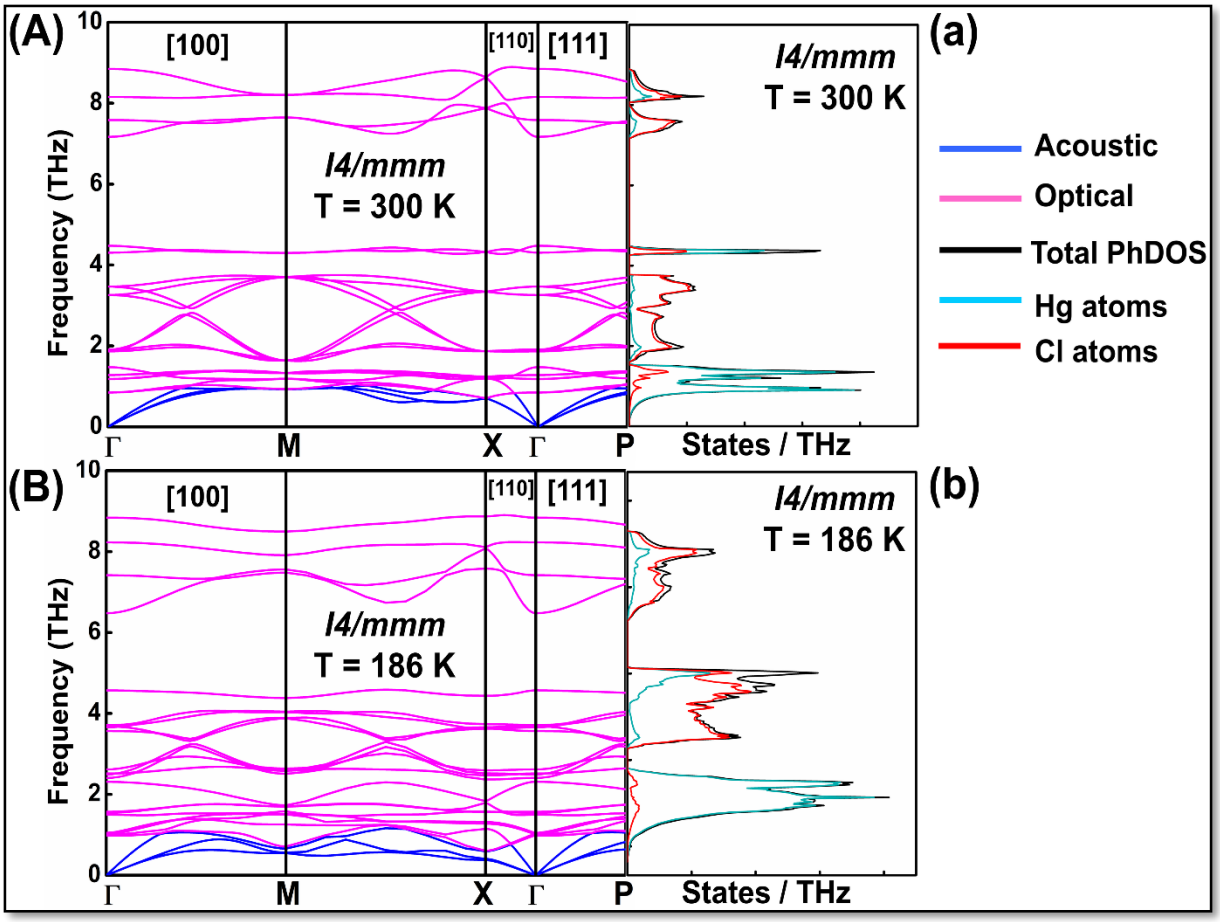

Figure 6.5. The phonon dispersion spectra along the high-symmetry points Γ→M→X→Γ→P for the *I4/mmm* phase of Hg_2Cl_2 at T = **(A)** 300 K and **(B)** 186 K. The total and atom resolved PhDOS for *I4/mmm* phase of the compound for temperature **(a)** 300 K and **(b)** 186 K.

Moreover, below T_c = 186 K, the base-centered orthorhombic [*Cmcm* (D_{2h}^{17})] phase the compound is again found to be dynamical stable as it is evident from the corresponding phonon dispersion spectra [Figure 6.6(A)]. The phonon dispersion spectra at T = 185 K show noticeable changes in their spectral features with respect to the phonon modes as estimated at T = 186 K and are marked by hardening of X_1 and Γ_{10} phonons and softening of Γ_{23} and X_{24} phonon modes. The hardening and softening of these phonon modes in phonon dispersion spectra at T = 185 K thereby allow the system to achieve dynamical stability. In this connection it is relevant to mention that similar softening of X_1, X_8, Γ_6, Γ_{10} and Γ_{15} phonon modes and hardening of Γ_{23} and X_{24} phonons have also been observed in the phonon dispersion spectra for the *Cmcm* phase of the system at T = 186 K. The corresponding phonon dispersion spectra and PhDOS for the *Cmcm* phase of the compound at T = 186 K are shown in Figure 6.6(B) and 6.6(b) respectively.

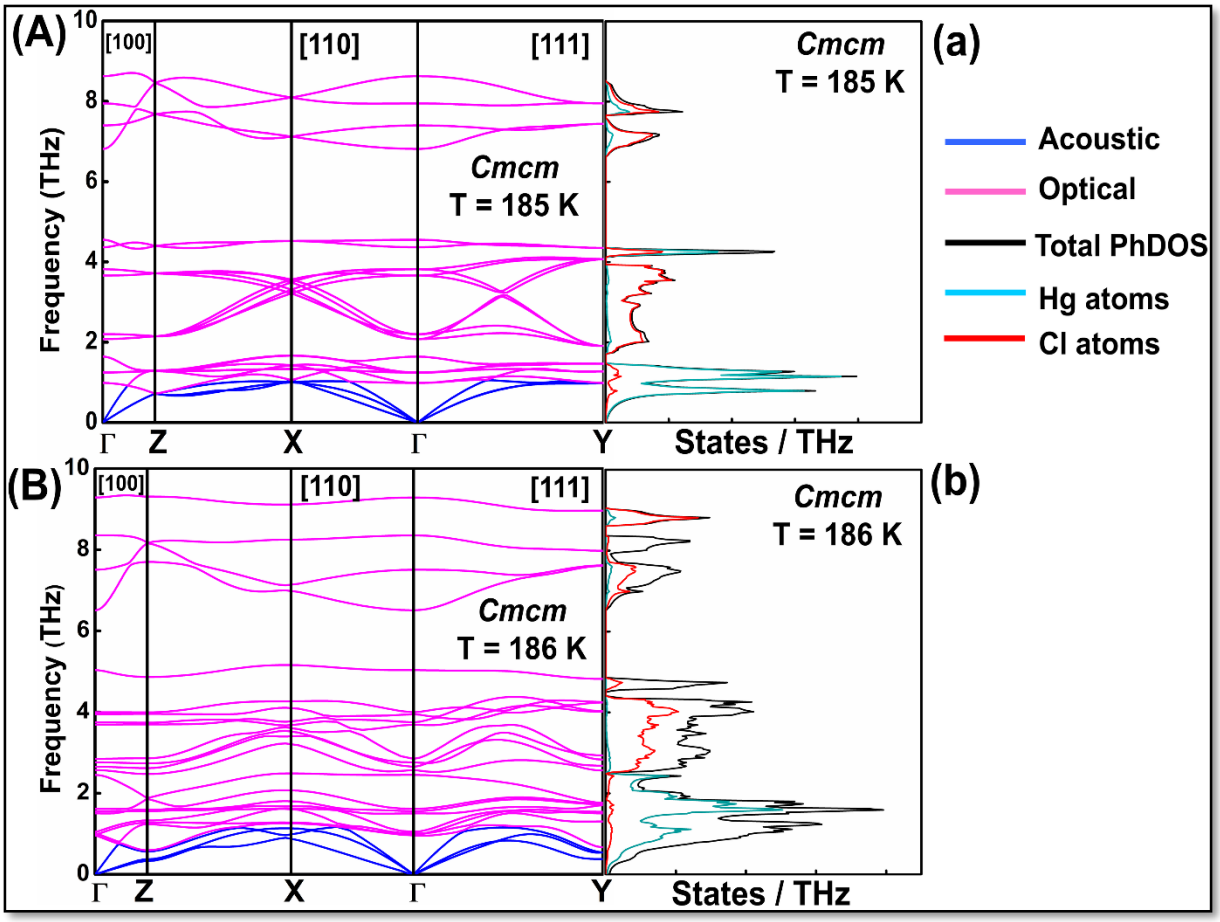

Figure 6.6. (A) The phonon dispersion curves along the high-symmetry points Γ→Z→X→Γ→Y for the *Cmcm* phase of Hg_2Cl_2 compound at T = **(A)** 185 K and **(B)** 186 K. The total and atom resolved PhDOS for *Cmcm* phase of the compound estimated at temperature **(a)** 185 K and **(b)** 186 K.

6.6. Identifying the key phonon modes responsible for structural phase transition

To identify the key phonon modes responsible for the temperature dependent phase transition of the Hg_2Cl_2 compound, the variations in vibrational frequencies for some of the representative X_1, X_8, X_{24}, Γ_6, Γ_{10} and Γ_{23} phonon modes with temperature have been estimated. The results are shown in Figure 6.7. From Figure 6.7, it is observed that the frequencies of the acoustic X_1 and low-lying optical phonon modes X_8, Γ_6, Γ_{10} at $186 < T \leq 300$ K are almost independent of temperature. However, at T = 186 K, these modes undergo sharp drop in frequencies portending the transition temperature T_c associated with temperature dependent

structural phase transition of the system. Furthermore, the high-frequency X_{24} and Γ_{23} optical phonon modes, like the acoustic phonons, remain independent with temperature except at T = 186 K, where instead of softening exhibit appreciable hardening of the vibrational frequencies. All these observations collectively suggest that acoustic X_1 and optical X_8, X_{24}, Γ_6, Γ_{10}, Γ_{23} phonon vibrations may be responsible for the temperature-dependent *I4/mmm* (D_{4h}^{17}) → *Cmcm* (D_{2h}^{17}) structural phase transition of the Hg_2Cl_2 compound at the transition temperature (T = T_c = 186 K).

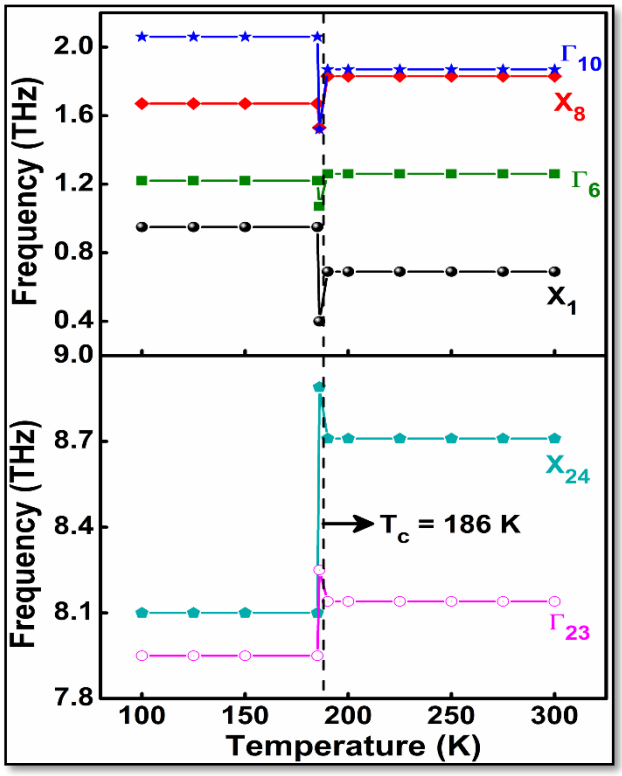

Figure 6.7. Variations of phonon frequencies as a function of temperature for the phonon normal modes X_1, X_8, X_{24} and Γ_6, Γ_{10}, Γ_{23} along the respective high-symmetry points X and Γ.

The cartesian displacements of the relevant X_1, X_8, X_{24}, Γ_{10}, Γ_{23}, and M_{24} phonon modes, as estimated from the first-principle calculations are shown in Figure 6.8. From Figure 6.8, it is observed that the high frequency optical X_{24} and Γ_{23} phonon modes are strongly linked with the vibrations of Hg atoms along the crystallographic c - axis. While the acoustic X_1 and optical X_8, M_{24} phonon modes are involved with the atomic displacements of both Hg and Cl atoms, the Γ_{10} phonon is associated with the vibrations of Cl atoms of the compound. Visual inspections of the cartesian displacements linked with the pre referred phonon modes of the compound not only suggest perturbations in the lattice parameters (a, b, c) of the system but

also signify considerable alterations of the linear Cl(L)-Hg(C)-Hg(A)-Cl(L) chain from its planar dispositions as the compound undergoes structural phase transition from the body-centered tetragonal to base-centered orthorhombic [*I4/mmm* (D_{4h}^{17}) → *Cmcm* (D_{2h}^{17})] phase at T_c = 186 K.

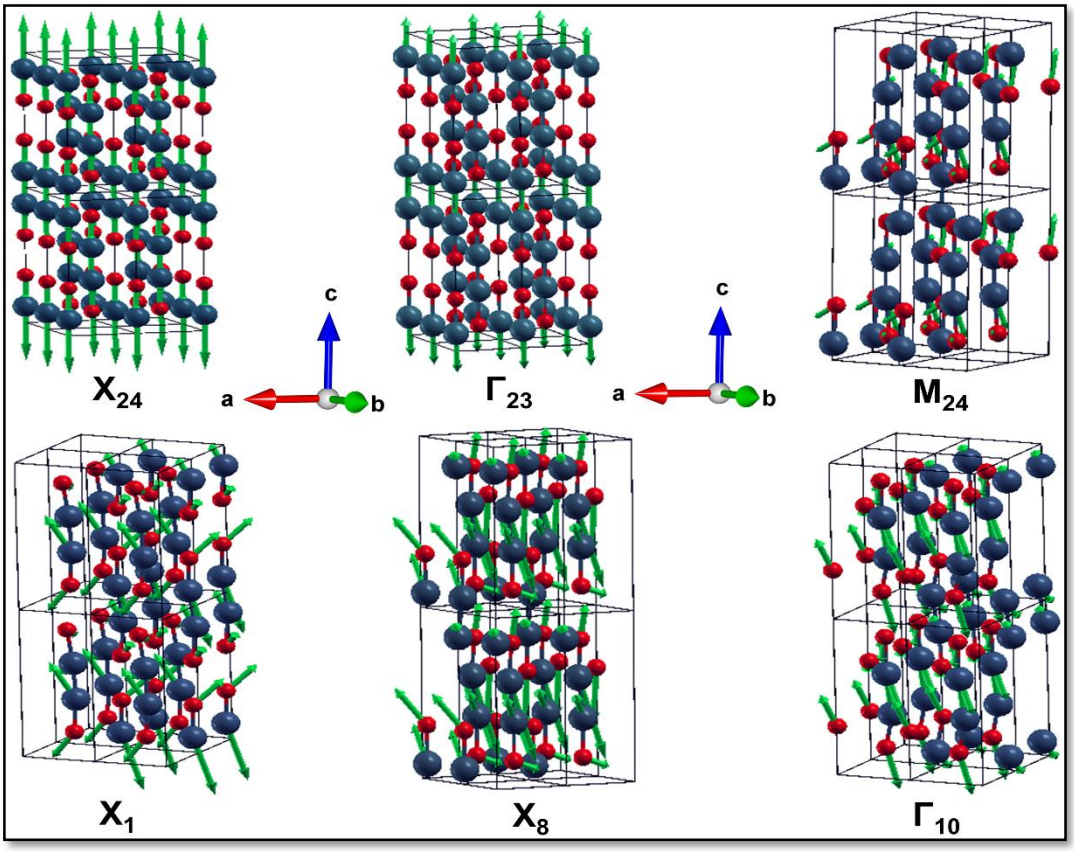

Figure 6.8. Schematic diagrams of eigenvectors and cartesian displacements of X_1, X_8, X_{24}, Γ_{10}, Γ_{23}, and M_{24} phonon modes for the *I4/mmm* phase of Hg_2Cl_2 compound at T = 186 K. (Emarald blue and red colours represent Hg and Cl atoms respectively. The green arrows illustrate the directions of cartesian displacements).

6.7. Nature of structural phase transition

To understand the nature of the structural phase transition whether it is "displacive" or of "order-disorder" type, the on-site interatomic force constants [$K_{ij}(\lambda)$] for an atom λ have been calculated from the respective supercells of the compound. The magnitude of $K_{ij}(\lambda)$ determines the curvature, while its sign signifies the nature of the potential energy hypersurface. Positive values of $K_{ij}(\lambda)$ suggest the single minimum on the local potential energy hypersurface signifying "displacive" type structural phase transition. The negative values of

$K_{ij}(\lambda)$ on the other hand correspond to the multiwell nature of the potential energy hypersurface and linked the phase transition to be of "order - disorder" type [14-20].

The on-site interatomic forces have been calculated by displacing the Hg and Cl atoms with an amplitude of ±0.03 Å from their respective equilibrium positions along the crystallographic x, y and z directions for the *I4/mmm* (D_{4h}^{17}) and *Cmcm* (D_{2h}^{17}) phases of the Hg_2Cl_2 compound. The off-diagonal ($i \neq j$) IFCs K_{ij}(Hg) and K_{ij}(Cl) for the *I4/mmm* phase of the compound are found to be zero, however, the diagonal components ($i = j$) of the IFCs K_{ii}(Hg) and K_{ii}(Cl) are estimated to have non-zero values at transition temperature T_c = 186 K. The non-zero positive values of force constants along xx, yy and zz directions [K_{xx}(Hg) = K_{yy}(Hg) = 0.18 N/m, K_{zz}(Hg) = 0.61 N/m, K_{xx}(Cl) = K_{yy}(Cl) = 0.33 N/m, K_{zz}(Cl) = 1.39 N/m] thereby suggest the nature of *I4/mmm* (D_{4h}^{17}) → *Cmcm* (D_{2h}^{17}) structural phase transition is of "displacive" type in harmony with the available experimental observations [1].

6.8. Grüneisen parameter and NTE of Hg_2Cl_2 compound

To precisely understand the NTE behaviour of the Hg_2Cl_2 compound, the mode Grüneisen parameters for the phonon modes have been estimated. The volume-dependent mode Grüneisen parameter $\gamma_j(\mathbf{k})$ is defined as [21]:

$$\gamma_j(\mathbf{k}) = -\frac{\partial\,[\ln \omega_j(\mathbf{k})]}{\partial(\ln V)} \tag{6.6}$$

where $\omega_j(\mathbf{k})$ is the phonon frequency of the j-th phonon mode with wavevector **k** while V is the volume of the unitcell of the compound. The weighted average Grüneisen parameter γ_{avg} can be expressed as:

$$\gamma_{avg} = \frac{\sum_{\boldsymbol{k}} \gamma_j(\boldsymbol{k})\, C_j(\boldsymbol{k})}{\sum_{\boldsymbol{k}} C_j(\boldsymbol{k})} \tag{6.7}$$

The specific heat [$C_j(\boldsymbol{k})$] of the j-th phonon mode for the wave-vector **k** is calculated using the following relations [22]:

$$C_j(\boldsymbol{k}) = k_B \left[\frac{\hbar\omega_j(\boldsymbol{k})}{k_B T}\right]^2 \frac{\exp[\hbar\omega_j(\boldsymbol{k}) / k_B T]}{[\exp[\hbar\omega_j(\boldsymbol{k}) / k_B T] - 1]^2} \tag{6.8}$$

where k_B and $\hbar$ are the Boltzmann and reduced Planck's constants respectively.

Variation of mode Grüneisen parameter as a function of frequency for the body-centered tetragonal (*I4/mmm*) and base-centered orthorhombic (*Cmcm*) phases of the Hg_2Cl_2 compound are shown in Figure 6.9(a) and 6.9(b) respectively. Interestingly, from Figure 6.9(a) and 6.9(b), the average values of Grüneisen parameter are found to be -0.56 and -0.64 respectively for *I4/mmm* and *Cmcm* phases of the compound. The negative values of γ_{avg} of Hg_2Cl_2 in its high and low-temperature phases (*I4/mmm* and *Cmcm*), however represent an unconventional phenomenon called NTE. The low-temperature *Cmcm* phase shows stronger NTE behaviour ($\gamma_{avg} = -0.64$) than that of its high-temperature counterpart ($\gamma_{avg} = -0.56$). This result is in harmony with the inference so predicted from the corresponding volumetric coefficient of thermal expansion (α) values [*vide supra*, section 6.2]. Figure 6.9(a) and 6.9(b) further depict that, the acoustic phonon modes (TA and LA) in the low frequency window ranging from ~ 0 – 1 THz and the low-lying optical phonons in the frequency region ranging between ~ 0 – 4 THz show significant negative values of mode Grüneisen parameters, while small negative values of mode Grüneisen parameters come from the high-frequency optical phonon modes localized in the frequency window ranging from ~ 7 to 8.85 THz. The larger negative Grüneisen parameters, as observed for the LA, TA and low-lying optical phonon modes, are the key candidates for the generation of soft phonon modes which further promote the structural instability and the phase transition of the compound [23,24].

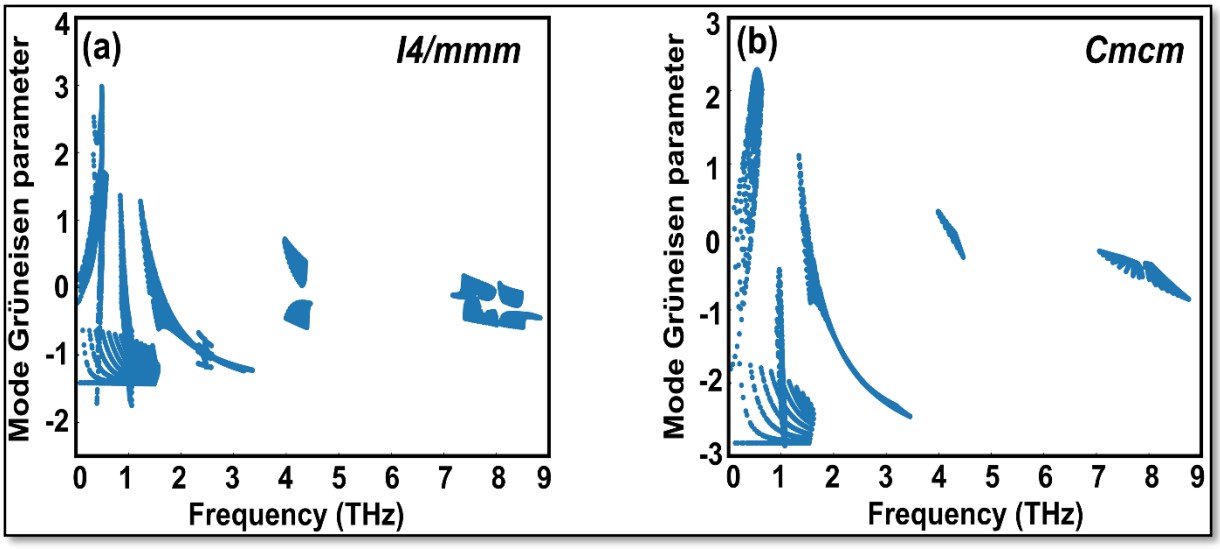

Figure 6.9. Mode Grüneisen parameters as a function of frequency for the **(a)** *I4/mmm* and **(b)** *Cmcm* phases of Hg_2Cl_2 compound.

6.9. Conclusions

Temperature dependent structural phase transition of Hg_2Cl_2 compound has been studied from the first-principle DFT and BOMD calculations. At transition temperature T_c = 186 K, the system is found to transform from the body-centered tetragonal (*I4/mmm*) to the base-centered orthorhombic (*Cmcm*) phase. The structural deformation of Hg_2Cl_2 compound with temperature has been primarily predicted from the alterations of structural parameters and Helmholtz free energy difference. The phonon dispersion relations have been estimated to explore the key phonon modes associated with the phase transition of the compound. While the order parameter e_{ij} suggests its paraelastic to ferroelastic phase transition at T_c, the on-site force constants $K_{ij}(\lambda)$ indicate the phase transition to be of "displacive" in nature. The negative values of mode Grüneisen parameters reveal the NTE of Hg_2Cl_2 compound.

Bibliography

[1] M. E. Boiko, M. D. Sharkov, A. M. Boiko, and S. G. Konnikov, Crystallogr. Rep. **63**, 196 (2018).

[2] G. F. Dobrzhanskii, A. A. Kaplyanskii, M. F. Limonov, and Y. F. Markov, Ferroelectrics **48**, 69 (1983).

[3] J. P. Benoit, C. X. An, Y. Luspin, J. P. Chappelle, and J. Lefebvre, J. Phys. C: Solid State Phys. **11**, L721 (1978).

[4] C. Barta, A. Kaplyanskiĭ, V. Kulakov, and Y. Markov, JETP Lett. **21**, 121 (1974).

[5] A. A. Kaplyanskii, in *Theory of Light Scattering in Condensed Matter*, edited by B. Bendow, J. L. Birman, and V. M. Agranovich (Springer US, Boston, MA, 1976), pp. 31.

[6] I. Pelant, M. N. Popova, J. Hála, M. AmbroŽ, V. Lhotská, and K. Vacek, Czech J Phys **37**, 1183 (1987).

[7] Y. C. Venudhar, L. Iyengar, and K. V. K. Rao, Cryst. Res. Technol. **21**, 151 (1986).

[8] P. M. Amarasinghe, J.-S. Kim, S. Trivedi, S. B. Qadri, E. P. Gorzkowski, G. Imler, J. Soos, N. Gupta, and J. Jensen, J. Electron. Mater. **48**, 7063 (2019).

[9] A. Grzechnik, K. Friese, V. Dmitriev, H.-P. Weber, J.-Y. Gesland, and W. A. Crichton, J. Phys.: Condens. Matter **17**, 763 (2005).

[10] V. K. Wadhawan, Bull. Mater. Sci. **6**, 733 (1984).

[11] E. Salje, U. Bismayer, and M. Jansen, J. Phys. C: Solid State Phys. **20**, 3613 (1987).

[12] A. V. Petrova, O. V. Nedopekin, B. Minisini, and D. A. Tayurskii, Phase Transit. **88**, 534 (2015).

[13] S. Tsunekawa, T. Kamiyama, K. Sasaki, H. Asano, and T. Fukuda, Acta Cryst. **49**, 595 (1993).

[14] A. I. Lebedev, Phys. Solid State **51**, 362 (2009).

[15] K. Parlinski, Y. Kawazoe, and Y. Waseda, J. Chem. Phys. **114**, 2395 (2001).

[16] K. Parlinski and Y. Kawazoe, Eur. Phys. J. B **16**, 49 (2000).

[17] K. Parlinski, Z. Q. Li, and Y. Kawazoe, Phys. Rev. B **61**, 272 (2000).

[18] T. Schneider and E. Stoll, Phys. Rev. B **13**, 1216 (1976).

[19] S. Ghosh and J. Chowdhury, J. Appl. Phys. **130**, 225103 (2021).

[20] U. D. Wdowik, K. Parlinski, S. Rols, and T. Chatterji, Phys. Rev. B **89**, 224306 (2014).

[21] E. Grüneisen, Ann. Phys. **344**, 257 (1912).

[22] A. Togo, L. Chaput, and I. Tanaka, Phys. Rev. B **91**, 094306 (2015).

[23] L. Wei, X. P. Wang, B. Liu, Y. Y. Zhang, X. S. Lv, Y. G. Yang, H. J. Zhang, and X. Zhao, AIP Adv. **5**, 127236 (2015).

[24] M. K. Gupta, R. Mittal, and S. L. Chaplot, Phys. Rev. B **88**, 014303 (2013).

Chapter 7

Predicting band gaps of nitride perovskites

7.1. Introduction

In this chapter, the band gaps of nitride perovskites have been predicted from machine learning (ML) and first-principle DFT calculations. Perovskites are ternary compounds with a general chemical formula ABX_3 where "A" and "B" are cationic elements and "X" can be either oxygen or halogens in anionic forms. While "A" atoms are located in the cuboctahedral cavities of the crystal, "X" atoms on the other hand form corner-sharing BX_6 octahedra. Despite considerable successes of oxide and halide perovskites, recently much attention has been focused on the syntheses and first-principle density functional theory (DFT) calculations of nitride perovskites having general formula ABN_3 [1-5]. Of late, ABN_3 systems have found potential applications as topological insulators, photovoltaic cells and are being successfully used as optical luminescent materials [4,6,7]. Here, the band gaps (E_g) of ABN_3 perovskites have been predicted from different ML models. The DFT studies have been performed to estimate the electronic band structures, E_g values and optoelectronic properties of two new nitride perovskites $CeBN_3$ (B = Mo, W).

7.2. Machine learning

7.2.1. Data cleaning and pre-processing for machine learning

The raw data of inorganic ABN_3–type perovskite compounds have been obtained from the available works in the literature [1-5,7-13]. By selecting all possible combinations of cations as "A" and "B", a set of 5566 inorganic ABN_3 – type perovskites have been initially selected for model evaluation. Lead (Pb) containing perovskites in all combinations, due their inherent toxic characters, are not considered in the above mentioned dataset. In the next step, the samples have been primarily identified according to their respective formation energies (E_f). Using support vector classification (SVC), the samples are then categorized by eliminating those candidates that show E_f > thermal excitation energy (E_{Th} ~ -0.026 eV) at room temperature (T = 300 K) [14]. To implement SVC, initially, 5566 samples were randomly divided into 4866 (~ 87%) and 700 (~ 13%) samples as training and test set, respectively. Figure 7.1(a) shows the E_f as a function of sample number of the test dataset as obtained from SVC algorithm. From Figure 7.1(a), it is observed that the samples are segregated into $E_f < E_{Th}$ and $E_f > E_{Th}$ classes. The merit of this SVC algorithm is then tested from confusion matrix and receiver operating characteristics (ROC) curve [15]. The results are shown in Figure 7.1(b) and 7.1(c) respectively. From Figure 7.1(b), the correctly identified compounds with $E_f < E_{Th}$ and

$E_f > E_{Th}$ classes are observed to be 482 [true positive (TP)] and 181 [true negative (TP)], respectively. However, the number of incorrectly identified samples under $E_f < E_{Th}$ and $E_f > E_{Th}$ classes are found to be 18 [false positive (FP)] and 19 [false negative (FN)], respectively. Out of 700 test dataset, it is found that only 5% samples (37 out of 700) have been misclassified, which in turn suggests the reliability of the SVC model to segregate the samples into their respective classes. The F1 score of the model, as attained from confusion matrix, is mathematically expressed as

$$F1\ score = \frac{2 \times Recall \times Precision}{Recall + Precision} \tag{7.1}$$

where

$$Precision = \frac{TP}{TP + FP} \tag{7.2}$$

and

$$Recall = \frac{TP}{TP + FN} \tag{7.3}$$

The F1 score is calculated to be 96.2% which also suggests the better performance of the said model. The ROC curve, as depicted in Figure 7.1(c), represents the relation between the TP rate (sensitivity) and FP rate (1 - specificity). From Figure 7.1(c), the area under curve (AUC) is estimated to be 0.98. The AUC closer to 1 further signifies the excellent segregation between the $E_f < E_{Th}$ and $E_f > E_{Th}$ classes.

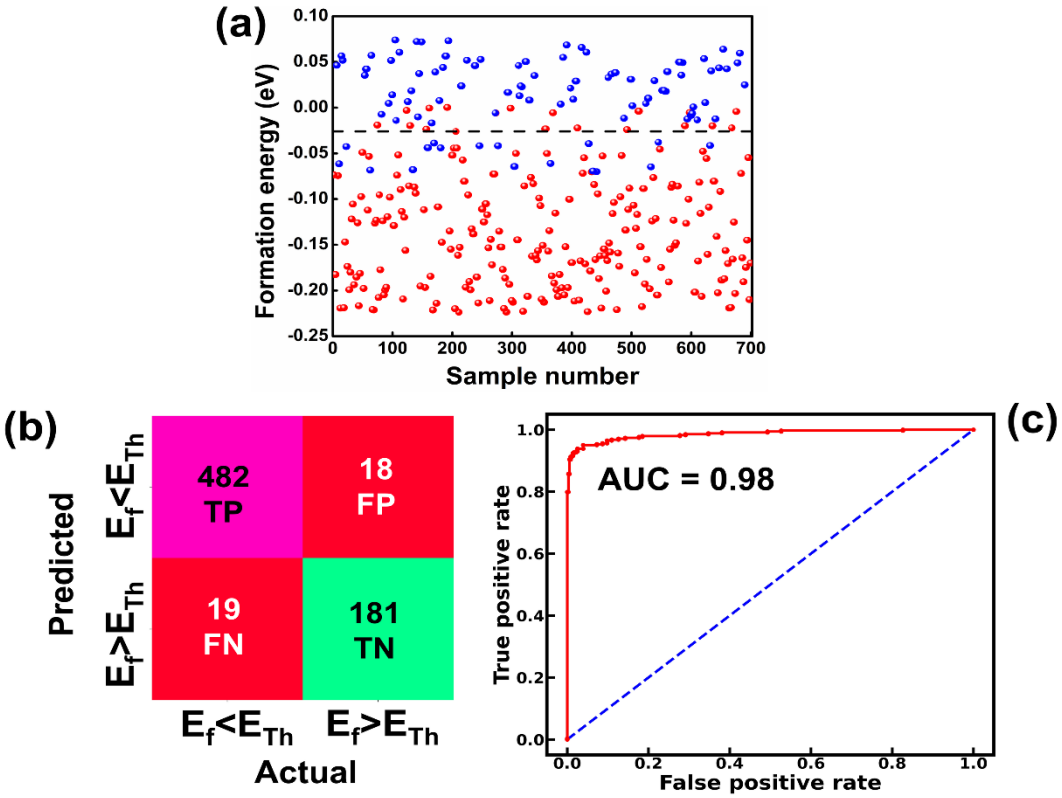

Figure 7.1. **(a)** Formation energy as a function of sample numbers for 700 test sets as estimated from SVC model. [The horizontal dashed line represents formation energy (E_f) = -0.026 eV]. **(b)** Confusion matrix representing the correlation between predicted and actual values in form of true positive (TP), false negative (FN), false positive (FP) and true negative (TN) values for the tested samples. [$E_f < E_{Th}$ and $E_f > E_{Th}$ symbolize the formation energies below and above E_{Th} (= -0.026 eV), respectively]. **(c)** The ROC curve illustrating the TP and FP rates of the test datasets.

Here we primarily focused on ABN_3 compounds which bear potential applications as photovoltaic and optical luminescent materials, the selection space has thus been further narrowed down to 1563 samples which exhibit E_g values spanning in the range from 1.0 to 3.1 eV. The E_g of the compounds in general are linked with the proposed 145 feature descriptors which include electronegativity, atomic weight, covalent radius, d valance electrons etc. [14,16]. Out of 145 feature descriptors, 117 feature attributes such as Mendeleev number, electronegativity, covalent radius, d valance electrons etc. of ABN_3 perovskites have been initially framed for the target variable E_g. With these 117 features, the Pearson correlation heatmap is constructed and the result is shown in Figure 7.2(a). The features having absolute correlation values < 0.89 and with multiple collinearities between them have been eliminated. The final top 10 feature descriptors which include electronegativity, d valance electrons,

formation energy, p valance electrons, Mendeleev number, specific volume of ground state, mean covalent radius, space group number, melting temperature and atomic weight, have been selected using the de-correlation method for further model evaluation. The heatmap portraying the evaluated top 10 feature descriptors and their order of importance are shown in Figure 7.2(b) and 7.2(c), respectively. From Figure 7.2(c), it is clearly seen that the electronegativity, d valance electrons and mean covalent radius show predominant contributions in predicting E_g values of the ABN_3 compounds.

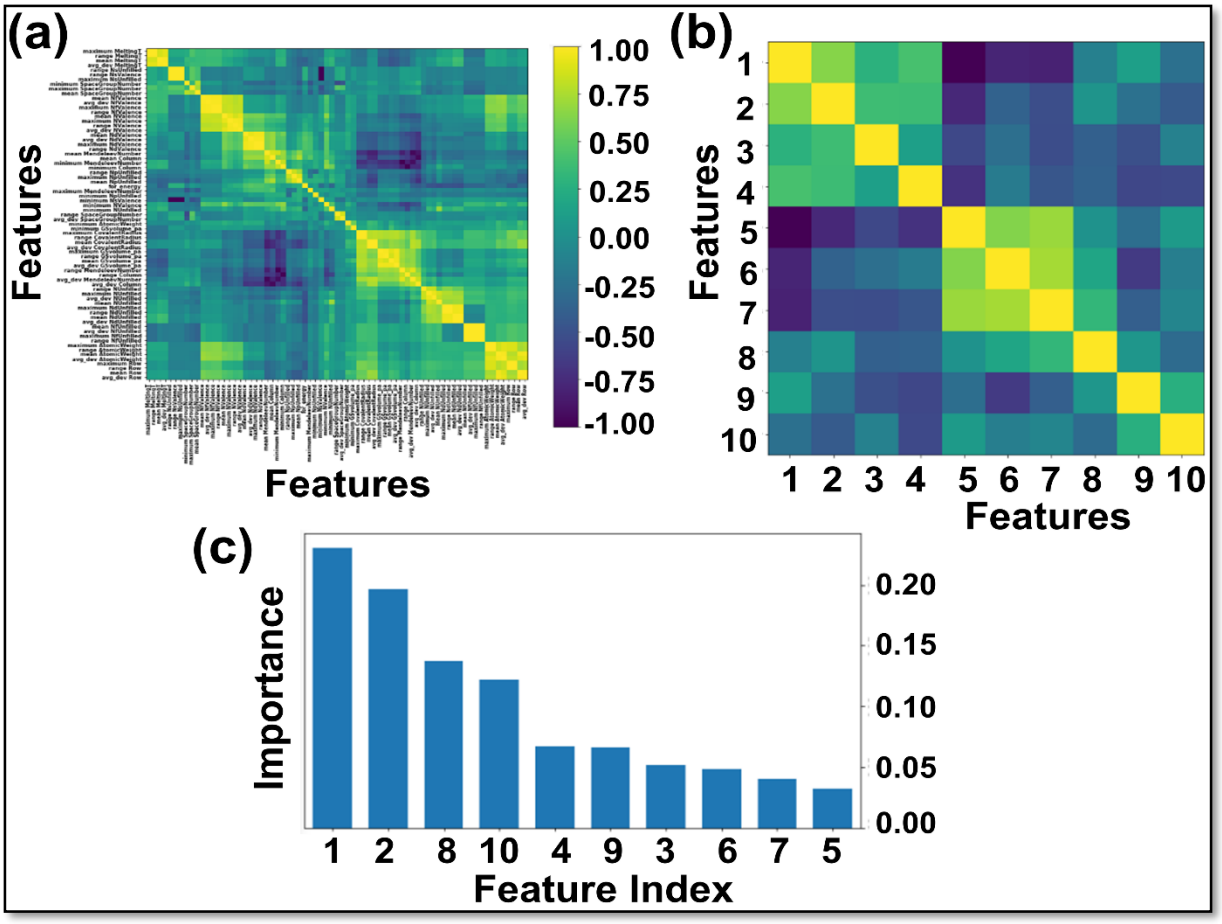

Figure 7.2. **(a)** and **(b)** Heatmap representing the initial 117 and final top 10 features respectively of ABN_3 perovskites [Yellow and dark blue colors in the heatmap represent the respective strong and weak correlations among the features]. **(c)** The relative importance of top 10 features of the compounds. [Feature indices (in the order of importance): 1- electronegativity, 2- d valance electrons, 3- formation energy, 4- p valance electrons, 5- Mendeleev number, 6- specific volume of ground state, 7- atomic weight, 8- mean covalent radius, 9- melting temperature and 10- space group number].

The correlations between E_g and electronegativity, mean covalent radius and d valance electrons can be rationalized. Electronegativity is a measure of ability to attract electrons of two bonded atoms towards their valence electrons. This ability results the delocalized distribution of valence electrons, which in turn influences the nature of the bonding as well as the E_g values of the compounds [17-19]. The mean covalent radii of the constituent atoms are intrinsically linked with the electronegativity of the system. Systems with constituent atoms having larger mean covalent radii thus result in decrease in electronegativity of the compounds in general [20]. Hence, the mean covalent radius is considered as an important feature descriptor in modulating the E_g values of the systems. The d valence electrons play major roles in the formation of energy bands in the electronic band structure and has direct impact on the E_g of the materials. Larger number of d valence electrons can realign the Fermi energy level (E_F) through p-d and s-d hybridizations, which in turn may alter the E_g values of the compounds [14].

7.2.2. Machine learning model training and validation

To precisely predict the band gaps of ABN_3 –type perovskite compounds, four ML models such as support vector regression (SVR), gradient boosted decision tree (GBDT), random forest regression (RFR) and multi-layer perceptron (MLP) have been considered. The accuracy of each model has been tested by selecting their respective hyperparameters. The list of hyperparameters of each model are shown in Table 7.1. From the dataset of 1563 ABN_3 perovskites and their top 10 feature descriptors (*vide supra*), 1363 (~ 87%) samples have been randomly selected for training and the rest 200 (~ 13%) samples have been set for testing of each model. The random selection has been considered two times for each model to confirm the statistical validity of the results. The performance of ML model has been estimated by calculating the RMSE, MAE and R^2 values. The RMSE, MAE and R^2 values of each model for the test dataset, so attained from the 10 – dimensional feature space, are illustrated in Table 7.1.

Table 7.1. Statistics of different ML models and their corresponding hyperparameters for predicting bandgaps of ABN_3 perovskites.

Models	Hyperparameters	MAE	RMSE	R^2
MLP	solver = adam, alpha = 1e-8, tol = 1e-6, max_iter = 5000, random_state = 0	0.16	0.22	0.74
GBDT	n_estimators = 2000, max_depth = 30, min_samples_split = 2	0.10	0.15	0.90
SVR	c = 50, gamma = 10, epsilon = 0.05, kernel = 'rbf'	0.08	0.13	0.91
RFR	max_depth = 30, min_samples_split = 2, n_estimators = 2000, min_samples_leaf = 1, random_state = 0	0.03	0.11	0.94

From Table 7.1, it is observed that while RFR predicts the E_g values of the compound with 3% MAE; SVR, GBDT and MLP predict the same E_g within MAEs of 8%, 10% and 16% respectively. From Table 7.1, the RFR algorithm shows lowest RMSE (= 0.11 eV) and highest R^2 (= 0.94) values in contrast to the other models. R^2 (RMSE) values of GBDT, SVR and MLP models are estimated to be 0.90 (0.15 eV), 0.91 (0.13 eV) and 0.74 (0.22 eV) respectively. These results collectively suggest the reliability of the RFR model in predicting the band gaps of ABN_3 – type perovskite compounds. The bivariate plots from the RFR model showing both the predicted, input band gap values for the training and testing datasets are shown in Figure 7.3(a). From Figure 7.3(a), strong linear correlation [with R^2 = 0.98 (training set) and 0.94 (test set)] between the predicted and input E_g values have been observed in both the training and test datasets. This result further justifies the accuracy of RFR model in predicting the band gaps of ABN_3 perovskites. The corresponding bivariate plots between the predicted and input values of E_g, as accomplished from SVR, GBDT and MLP ML models, are also shown in Figure 7.3(b), 7.3(c) and 7.3(d) respectively. From Figure 7.3(b, c, d), moderate to weak linear correlations between the predicted and input E_g values have been observed as the model goes from SVR, GBDT to MLP algorithms. The above results as a whole suggest the superiority of

the RFR algorithm as an effective ML model is predicting the band gaps of ABN_3 compounds in contrast to SVR, GBDT and MLP algorithms.

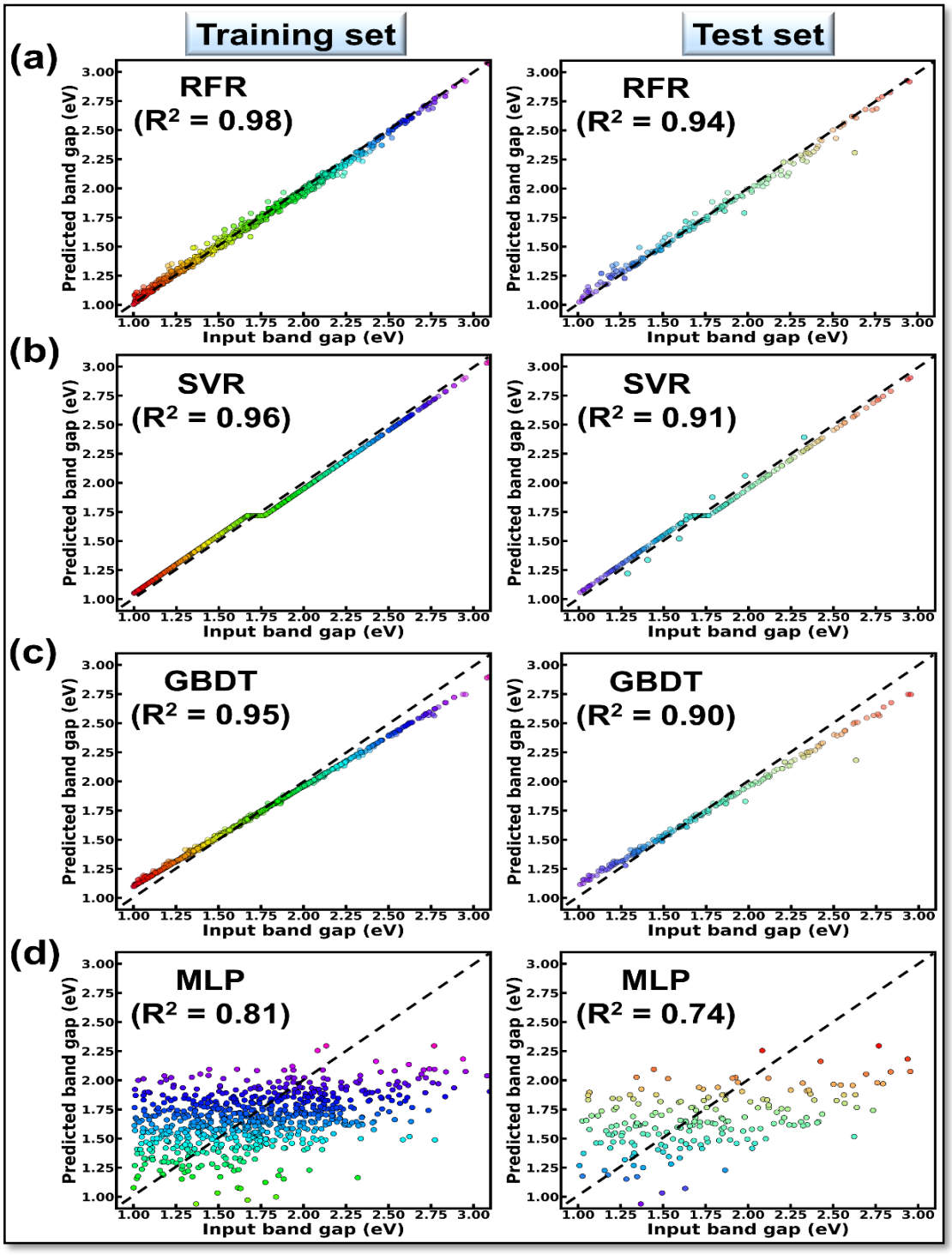

Figure 7.3. Fitted bivariate plots showing the variations of predicted and input band gaps of ABN_3 perovskites for both the training and test datasets as obtained from **(a)** RFR **(b)** SVR **(c)** GBDT and **(d)** MLP models.

Additionally, two newly synthesized nitride perovskites $CeMoN_3$ and $CeWN_3$, as reported elsewhere [11], have been selected for first-principle DFT calculations. Their electronic band structures, E_g values and optoelectronic properties have been studied from DFT calculations. The E_g values of the said systems have been predicted from both the DFT as well as RFR ML model to verify the accuracy of ML model in predicting E_g values of ABN_3 compounds.

7.3. Crystal structures and thermal stabilities of the $CeBN_3$ (B = Mo, W) compounds

At room temperature (T = 300 K) and under ambient pressure (P = 0 GPa), $CeBN_3$ (B = Mo, W) crystalize to primitive orthorhombic phase and belong to *Pmc2₁* space group symmetry with space group no. 26. The optimized unitcell geometries of the compounds, as obtained from first-principle DFT calculations with GGA – PBE level of theory, are shown in the upper panel of Figure 7.4. The lattice parameters of the $CeMoN_3$ ($CeWN_3$) crystal system have been estimated to be a = 5.789 Å (5.686 Å), b = 5.854 Å (5.667 Å) and c = 7.776 Å (8.027 Å) which are in close agreement with the experimentally determined X-ray diffraction data as reported elsewhere [11]. From Figure 7.4(a, b), it is observed that B (= Mo, N) and N atoms from several distorted octahedral environments within the crystal structure and B atom, which is located at the center of each BN_6 octahedron, is found to be shifted towards the apical N atom. The distorted octahedron, aka pyramidal coordination and large c/a ratio of $CeBN_3$ may result large spontaneous ferroelectric polarization in the said systems under study [21,22]. To comprehend the thermal stabilities of the compounds at T = 300 K, the BOMD simulation has been performed over a time span of 20 ps under time step of 1 fs. Temporal variations of free energies of $CeBN_3$ systems at T = 300 K are shown in the lower panel of Figure 7.4. From Figure 7.4(c, d) it is found that both the crystal structures attain their respective stabilizing free energy values after a time lapse of ~ 5 ps. The refined geometries of the compounds, so obtained from the BOMD simulation run at 15 ps, are shown in the inset of Figure 7.4(c, d).

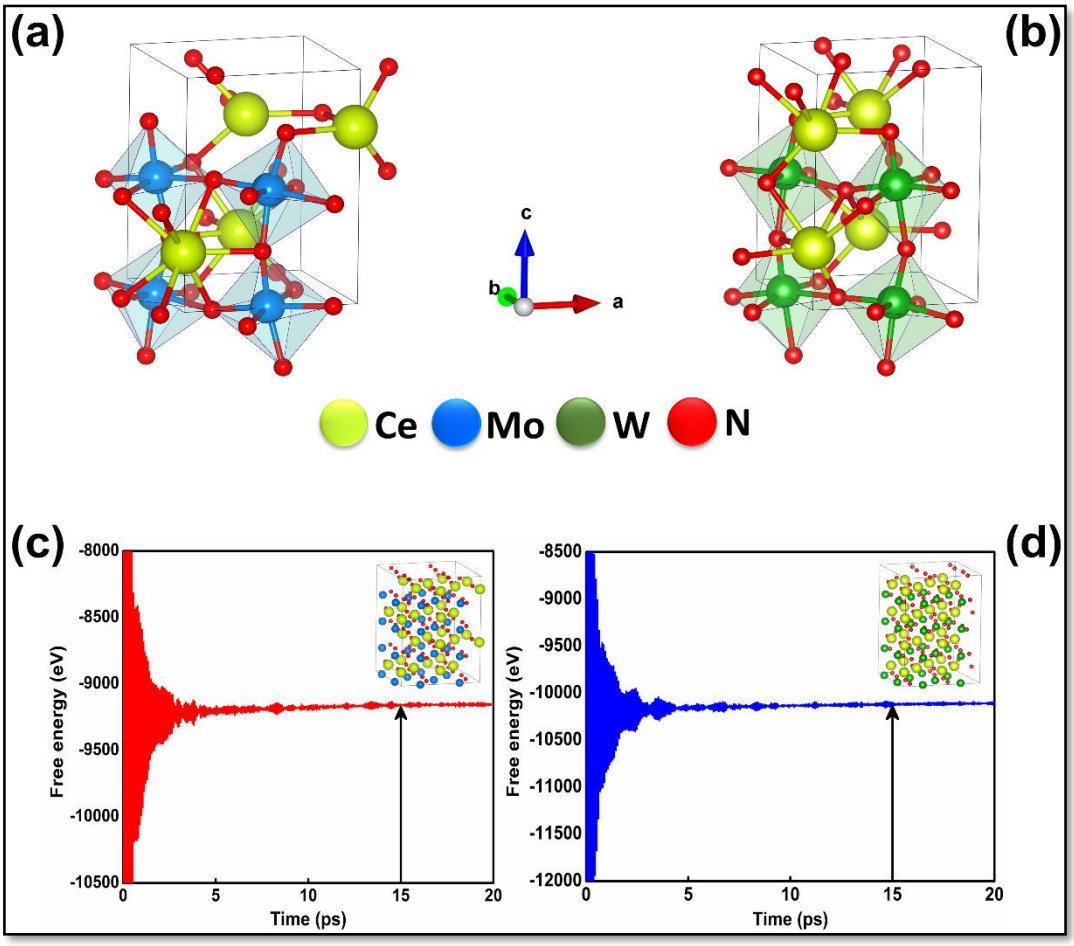

Figure 7.4. Optimized crystal structures of **(a)** $CeMoN_3$ and **(b)** $CeWN_3$ compounds as obtained from DFT calculations. Free energy as a function of time for **(c)** $CeMoN_3$ and **(d)** $CeWN_3$ systems as attained from BOMD simulation. [Inset of **(c)** and **(d)** show the respective supercell geometries of $CeMoN_3$ and $CeWN_3$ so obtained from the BOMD simulation run at 15 ps which is marked with vertical arrows.]

7.4. Estimation of band gaps for $CeBN_3$ (B = Mo, W) compounds

The E-**k** diagrams of $CeBN_3$ systems for B = Mo, W along Γ→Y→S→X→Γ →R→U→T→Z high-symmetry direction have been estimated from DFT calculations at PBE, HSE06, G_0W_0@PBE and G_0W_0@HSE06 level of theories. The results are shown in Figure 7.5. The estimated E_g values of the compounds from the corresponding E-**k** diagrams are listed in Table 7.2. Interestingly the E-**k** diagrams for both $CeMoN_3$ and $CeWN_3$ compounds show the existence of indirect band gaps ranging from 0.94 – 1.60 and 1.00 – 1.81 eV, respectively.

Presence of indirect band gaps with gap openings in the range 0.94 – 1.81 eV may render their applications in photovoltaics [23-27].

The E_g values of $CeMoN_3$ and $CeWN_3$ compounds are predicted to be ~ 1.55 and 1.76 eV from RFR ML model for the G_0W_0@HSE06 input of 1.60 and 1.81 eV respectively. While the DFT calculations at HSE06 and G_0W_0@HSE06 level of theories can closely predict the experimentally observed E_g values of the systems within < 1% error [28-34], the predicted E_g values of $CeBN_3$ (B = Mo, W) compounds as obtained from RFR ML model are estimated within an error of ~ 3% with standard deviation of ~ 0.035. The selective choice of G_0W_0@HSE06 level of theory in the DFT calculation as input for the prediction of band gaps is thus meaningful, given its efficacy in reproducing the experimental band gaps of many such compounds as reported elsewhere [35-38].

Table 7.2. Band gap of $CeBN_3$ (B = Mo, W) compounds under different levels of theory in the DFT calculations

Level of theories	Band gaps (eV)	
	$CeMoN_3$	**$CeWN_3$**
PBE	0.94	1.00
HSE06	1.57	1.80
G_0W_0@PBE	1.46	1.71
G_0W_0@HSE06	1.60	1.81

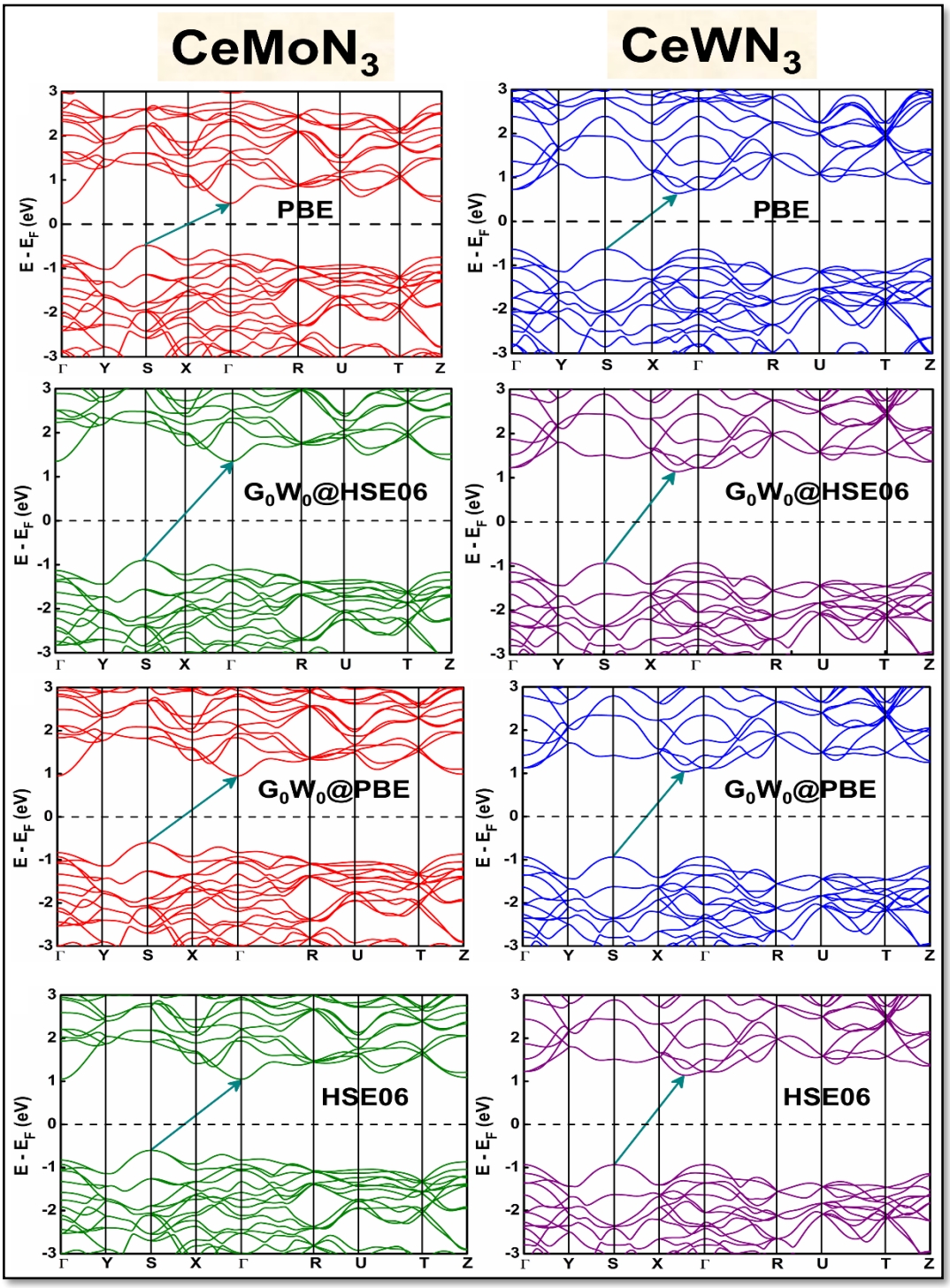

Figure 7.5. E-**k** diagrams of $CeMoN_3$ (left panel) and $CeWN_3$ (right panel) compounds along Γ→Y→S→X→Γ→R→U→T→Z high-symmetry direction as obtained from PBE and G_0W_0@HSE06 levels of theory. [Horizontal dashed line and inclined arrow represent Fermi energy level and band gap respectively].

7.5. Optoelectronic properties of $CeBN_3$ (B = Mo, W) systems

Electronic band structures are intrinsically linked with the optoelectronic properties of the systems in general. The optoelectronic properties of $CeBN_3$ (B = Mo, W) crystal systems have been estimated from the frequency (ω) dependent complex dielectric function [$\varepsilon(\omega)$]. Since, the *Pmc2₁* phase of the compounds are structurally anisotropic, the incident electromagnetic (EM) field components along the direction of a, b and c – crystallographic axes are designated as xx, yy and zz, respectively in the consequent calculations. Figure 7.6(A) and 7.6(B) show the variations of real part of $\varepsilon(\omega)$ [$\varepsilon_1(\omega)$] as a function of incident EM wave energy ($\tilde{E}_M$), so obtained from G_0W_0@HSE06 level of theory, for $CeMoN_3$ and $CeWN_3$ compounds respectively. From the upper panel of Figure 7.6, static values of $\varepsilon_1(\omega)$ [$\varepsilon_1(0)$] have been estimated to be ~ 5.85 (5.80), 4.77 (5.99) and 5.93 (5.90) for $CeMoN_3$ ($CeWN_3$) system along xx, yy and zz polarization directions respectively of the incident EM wave. These non-zero values of $\varepsilon_1(0)$ for all the three polarization directions indicate their semiconducting nature so attained from the E-**k** diagrams [*vide ante*, Figure 7.5]. The most intense structure band of $\varepsilon_1(\omega)$ for $CeMoN_3$ ($CeWN_3$) compound is obtained at $\tilde{E}_M$ ~ 1.45 (1.85) eV which corresponds to maximum dispersion of the EM wave. However, beyond $\tilde{E}_M$ ~ 3.75 (6.86) eV, $\varepsilon_1(\omega)$ values of $CeMoN_3$ ($CeWN_3$) system gradually decrease and attain negative values within the energy window $\tilde{E}_M$ ~ 4.72 (7.86) – 10.42 (13.39) eV. The negative values of $\varepsilon_1(\omega)$ signify metallic Drude – like behaviour of the compounds within the said energy windows [29,39,40].

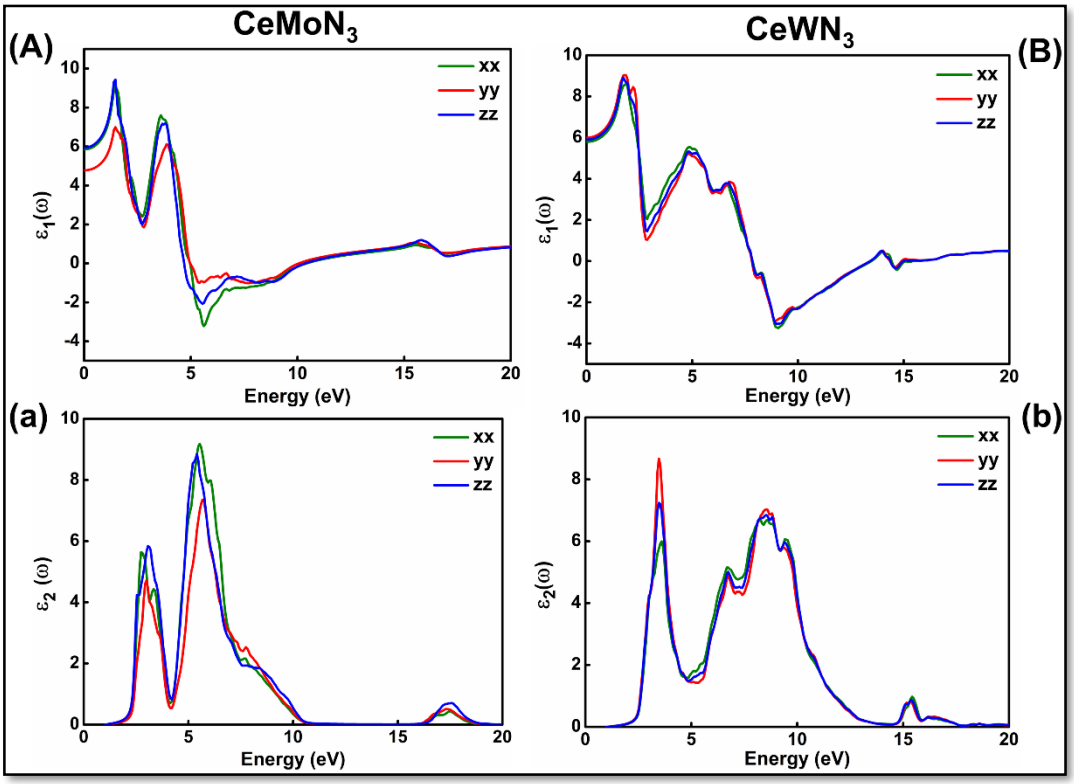

Figure 7.6. **Left panel: (A)** Real and **(a)** imaginary parts of dielectric function versus incident EM wave energy for $CeMoN_3$ compound. **Right panel: (B)** Real and **(b)** imaginary parts of $\varepsilon(\omega)$ as a function of EM wave energy for $CeWN_3$ compound.

The $\varepsilon_2(\omega)$ is known to correlate directly with the band gaps of the compounds in general. Figure 7.6(a) and 7.6(b) depict the variations of $\varepsilon_2(\omega)$ as a function of $\tilde{E}_M$ for $CeMoN_3$ and $CeWN_3$ systems respectively, so attained from G_0W_0@HSE06 level of theory. From Figure 7.6(a, b) the critical or take-off values of $\varepsilon_2(\omega)$ have been observed at $\tilde{E}_M \sim 1.60$ (1.81) eV for $CeMoN_3$ ($CeWN_3$) compound for all the three polarization directions. The critical or take-off values of $\varepsilon_2(\omega)$ are in exact agreement with the E_g values of the systems, as obtained from the G_0W_0@HSE06 level of theory (*vide ante*, Table 7.2). Interestingly, the take-off values of $\varepsilon_2(\omega)$ are found to be independent of polarization directions of EM wave. Moreover, finite values of $\varepsilon_2(\omega)$ between $\tilde{E}_M \sim 2.30$ (2.40) and 10.01 (12.50) eV for $CeMoN_3$ ($CeWN_3$) crystal corroborate strong attenuation of the incident EM wave by the systems within the said energy window [29,39].

The response of strong attenuation of the incident EM wave inside the $CeBN_3$ (B = Mo, W) compounds, so reflected in the $\varepsilon_2(\omega)$ - $\tilde{E}_M$ plots (Figure 7.6), can also be attributed from their absorption coefficients [$\alpha(\omega)$] and optical conductivities [$\sigma(\omega)$]. Figure 7.7 shows the

variations of $\alpha(\omega)$ and $\sigma(\omega)$ as function of $\tilde{E}_M$ of the systems. Akin to $\varepsilon_2(\omega)$ - $\tilde{E}_M$ plots, the critical values of both $\alpha(\omega)$ and $\sigma(\omega)$ are found at $\tilde{E}_M$ ~ 1.60 (1.81) eV for $CeMoN_3$ ($CeWN_3$) crystal system for all the three polarization directions. Hence these calculations help to recheck the E_g values as obtained from electronic band structures and $\varepsilon_2(\omega)$ - $\tilde{E}_M$ plots. From Figure 7.7, finite values of $\alpha(\omega)$/ $\sigma(\omega)$ have been observed within $\tilde{E}_M$ ~ 2.30/ 2.30 to 11.43/ 10.01 eV, 16.47/ 16.55 to 18.77/ 18.64 eV and 2.40/ 2.40 to 17.90/ 12.50 eV for $CeMoN_3$ and $CeWN_3$ compounds, respectively. The finite values of $\alpha(\omega)$ and/ or $\sigma(\omega)$ within the specified energy window signify large opacity and high optical conductivity of the said systems [29,39]. Moreover, the high transparency of $CeMoN_3$ ($CeWN_3$) compound within the energy window ~ 0 – 1.60 eV (0 - 1.81 eV) has also been noticed in $\alpha(\omega)$ - $\tilde{E}_M$ and $\sigma(\omega)$ - $\tilde{E}_M$ plots (Figure 7.7). The high transparency of the said systems covering visible and Infrared (IR) regions of the EM wave may promote them as potential candidates for optical luminescent materials and IR detectors [39,41,42].

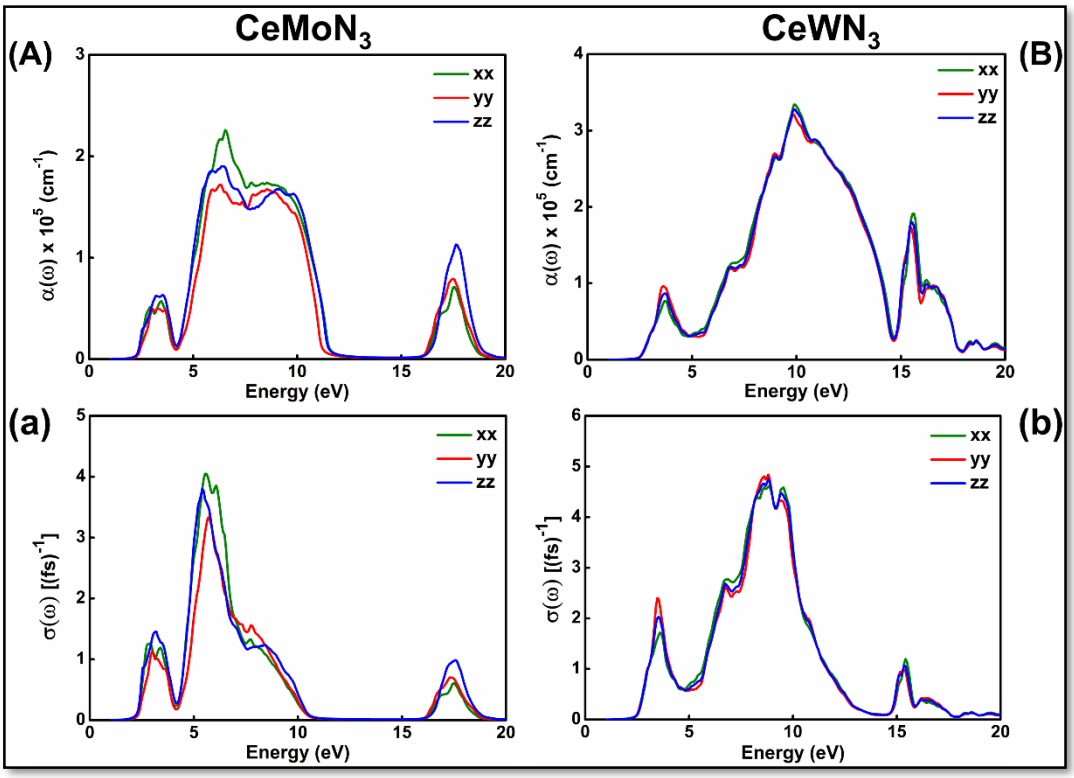

Figure 7.7. Left panel: (A) Optical absorption and **(a)** conductivity as a function of incident EM wave energy for $CeMoN_3$ compound. **Right panel: (B)** Optical absorption and **(b)** conductivity as a function of EM wave energy for $CeWN_3$ compound.

7.6. Conclusions

The band gaps of ABN_3 perovskites have been predicted from ML models based on the feature descriptors. The dataset of 1563 ABN_3 perovskites, which show E_f < -0.026 eV and E_g values spanning in the range from 1.0 to 3.1 eV, have been selected from initial 5566 samples for ML model evaluation. The E_g values of the compounds are found to be linked with 117 feature descriptors. The top 10 feature descriptors have been selected by eliminating those features which show absolute correlation values < 0.89 and low rank of importance. Correlations between the band gap and the topmost 3 features such as electronegativity, mean covalent radius and d valance electrons have also been discussed. Four supervised ML models such as MLP, GBDT, SVR and RFR have been considered to predict their band gaps. The accuracy of each model has been tested from MAE, RMSE and R^2 values. The RFR algorithm shows lowest RMSE (= 0.11 eV) and highest R^2 (= 0.94) values in comparison to other models. R^2 values and the corresponding bivariate plots suggest the superiority of RFR algorithm as an effective ML model is predicting the band gaps of ABN_3 perovskites in contrast to SVR, GBDT and MLP algorithms. Two newly synthesized ABN_3 – type perovskites $CeBN_3$ (B = Mo, W) have been further chosen and their electronic band structures and optoelectronic properties have been studied from DFT calculations. The E_g values of $CeBN_3$ (B = Mo, W) compounds have been estimated from DFT calculations at PBE, HSE06, G_0W_0@PBE and G_0W_0@HSE06 level of theories. The E_g values of $CeMoN_3$ and $CeWN_3$ compounds have been predicted to be 1.55 and 1.76 eV from RFR algorithm for the G_0W_0@HSE06 input of 1.60 and 1.81 eV respectively. The E_g values of the systems have also been verified from their respective optoelectronic parameters such as $\varepsilon_2(\omega)$, $\alpha(\omega)$ and $\sigma\ (\omega)$.

Bibliography

[1] C. Gui, J. Chen, and S. Dong, Phys. Rev. B **106**, 184418 (2022).

[2] J. A. Flores-Livas, R. Sarmiento-Pérez, S. Botti, S. Goedecker, and M. A. L. Marques, J. Phys. Mater. **2**, 025003 (2019).

[3] B. F. Grosso, D. W. Davies, B. Zhu, A. Walsh, and D. O. Scanlon, Chem. Sci. **14**, 9175 (2023).

[4] V.-A. Ha, H. Lee, and F. Giustino, Chem. Mater. **34**, 2107 (2022).

[5] R. Sarmiento-Pérez, T. F. T. Cerqueira, S. Körbel, S. Botti, and M. A. L. Marques, Chem. Mater. **27**, 5957 (2015).

[6] T. K. Ng, J. A. Holguin-Lerma, C. H. Kang, I. Ashry, H. Zhang, G. Bucci, and B. S. Ooi, J. Phys. D: Appl. Phys. **54**, 143001 (2021).

[7] M.-C. Jung, K.-W. Lee, and W. E. Pickett, Phys. Rev. B **97**, 121104 (2018).

[8] S. D. Kloß, M. L. Weidemann, and J. P. Attfield, Angew. Chem. Int. Ed. **60**, 22260 (2021).

[9] N. E. Brese and F. J. DiSalvo, J. Solid State Chem. **120**, 378 (1995).

[10] K. R. Talley, C. L. Perkins, D. R. Diercks, G. L. Brennecka, and A. Zakutayev, Science **374**, 1488 (2021).

[11] R. Sherbondy *et al.*, Chem. Mater. **34**, 6883 (2022).

[12] A. Jain *et al.*, APL Mater. **1**, 011002 (2013).

[13] J. Hu, S. Stefanov, Y. Song, S. S. Omee, S.-Y. Louis, E. M. D. Siriwardane, Y. Zhao, and L. Wei, npj Comput Mater **8**, 65 (2022).

[14] M. Gao, B. Cai, G. Liu, L. Xu, S. Zhang, and H. Zeng, Phys. Chem. Chem. Phys. **25**, 9123 (2023).

[15] Y. Zhuo, A. Mansouri Tehrani, and J. Brgoch, J. Phys. Chem. Lett. **9**, 1668 (2018).

[16] L. Ward, A. Agrawal, A. Choudhary, and C. Wolverton, npj Comput Mater **2**, 16028 (2016).

[17] K. Li, Y. Li, and D. Xue, Funct. Mater. Lett. **04**, 217 (2011).

[18] A.-S. Om Kumar, V. Shukla, and S. K. Srivastava, J SCI-ADV MATER DEV **4**, 158 (2019).

[19] K. Li, C. Kang, and D. Xue, Mater. Res. Bull. **47**, 2902 (2012).

[20] M. Rahm, P. Erhart, and R. Cammi, Chem. Sci. **12**, 2397 (2021).

[21] S. Bandyopadhyay and I. Dasgupta, Phys. Rev. B **103**, 014105 (2021).

[22] T. Ahmad, K. Jindal, M. Tomar, and P. K. Jha, Phys. Chem. Chem. Phys. **25**, 5857 (2023).

[23] J. Kangsabanik, M. K. Svendsen, A. Taghizadeh, A. Crovetto, and K. S. Thygesen, J. Am. Chem. Soc. **144**, 19872 (2022).

[24] S. Halder, R. A. Kumar, R. Maity, and T. P. Sinha, Ceram. Int. **49**, 8634 (2023).

[25] O. I. Malyi and C. M. Acosta, J. Phys. Chem. C **124**, 14432 (2020).

[26] R. Anbarasan, J. K. Sundar, M. Srinivasan, and P. Ramasamy, Comput. Condens. Matter **28**, e00581 (2021).

[27] Y. Kang, Y. Youn, S. Han, J. Park, and C.-S. Oh, Chem. Mater. **31**, 4072 (2019).

[28] A. J. Garza and G. E. Scuseria, J. Phys. Chem. Lett. **7**, 4165 (2016).

[29] S. Ghosh and J. Chowdhury, Mater Sci Eng B. **284**, 115903 (2022).

[30] S. Ghosh, S. Sarkar, and J. Chowdhury, Mater. Chem. Phys. **276**, 125379 (2022).

[31] R. R. Pela, M. Marques, and L. K. Teles, J. Phys.: Condens. Matter **27**, 505502 (2015).

[32] Y. Duan, L. Qin, L. Shi, and G. Tang, Comput. Mater. Sci. **101**, 56 (2015).

[33] P. Borlido, J. Schmidt, A. W. Huran, F. Tran, M. A. L. Marques, and S. Botti, npj Comput Mater **6**, 96 (2020).

[34] S. Matsuishi, D. Iwasaki, and H. Hosono, J. Solid State Chem. **315**, 123508 (2022).

[35] S. Ghosh and J. Chowdhury, Mod. Phys. Lett. B **38**, 2330003 (2023).

[36] P. Bhumla, D. Gill, S. Sheoran, and S. Bhattacharya, J. Phys. Chem. Lett. **12**, 9539 (2021).

[37] K. Demmouche and J. Coutinho, Int. J. Mod. Phys. B **32**, 1850328 (2018).

[38] Y. Kang, G. Kang, H.-H. Nahm, S.-H. Cho, Y. S. Park, and S. Han, Phys. Rev. B **89**, 165130 (2014).

[39] R. R. Banik, S. Ghosh, and J. Chowdhury, Phys. Scr. **98**, 105914 (2023).

[40] M. I. Naher and S. H. Naqib, Sci Rep **11**, 5592 (2021).

[41] R. Reisfeld, Opt. Mater. **32**, 850 (2010).

[42] L. Su, X. Fan, T. Yin, H. Wang, Y. Li, F. Liu, J. Li, H. Zhang, and H. Xie, Adv. Optical Mater. **8**, 1900978 (2020).

Chapter 8

Conclusions and future perspective

In summary, the dissertation reports the structural, electronic, and optical properties of technologically relevant materials from first-principle calculations. Chapter 1, which includes the overall introduction, highlights a brief historical timeline of different ages of materials and their uses for the welfare of mankind. Understanding of many-body theory, strongly correlated systems, and the machine learning approach in estimating the materials' properties have been discussed in Chapter 1. Recent works of renowned research groups working in the area of first-principle calculations have also been showcased in this chapter. In Chapter 2, the computational methodologies such as the first-principle DFT framework, calculations of phonon dispersion relations, Born-Oppenheimer molecular dynamics (BOMD) simulations, calculations of optical properties and machine learning methods, have been discussed. Chapter 3 focuses on understanding the structural and electronic properties of the Mercurous Chloride (Hg_2Cl_2) compound from first-principle DFT calculations. The charge-transfer insulating property of the Hg_2Cl_2 compound has been elaborately discussed in Chapter 3. In Chapter 4, the pressure-driven structural phase transitions of the Hg_2Cl_2 compound at room temperature (T = 300 K) have been deliberated. The structural phase transitions of Hg_2Cl_2 system from its body-centered tetragonal *I4/mmm* (D_{4h}^{17}) → base-centred orthorhombic *Cmcm* (D_{2h}^{17}) phase and from base-centred orthorhombic *Cmcm* (D_{2h}^{17}) → primitive orthorhombic *Pnma* (D_{2h}^{16}) phase at transition pressure 0.25 and 9 GPa respectively have been unveiled in Chapter 4. The key vibrational phonon modes linked with these structural phase transitions and the type of phase transition have also been discussed. Chapter 5 is devoted to understand the pressure-induced modulations of electronic and optoelectronic properties of the Hg_2Cl_2 system. The electronic band structures, anisotropic optoelectronic parameters such as complex dielectric function [$\varepsilon(\omega)$], absorption coefficient [$\alpha(\omega)$], optical conductivity [$\sigma(\omega)$], refractive indices (n_e, n_o), optical birefringence (Δn) of Hg_2Cl_2 at ambient conditions and under external pressures have been critically enlightened in Chapter 5. Chapter 6 is framed with the temperature-dependent structural phase transition and negative thermal expansion behaviour of the Hg_2Cl_2 compound. The structural phase transition of the system from *I4/mmm* (D_{4h}^{17}) → *Cmcm* (D_{2h}^{17}) phase at transition temperature T_c =186 K has been discussed here in detail. The associated order parameter, key phonon modes responsible for structural phase transition and negative thermal expansion behaviour have also been highlighted in Chapter 6. In Chapter 7, the band gaps of nitride perovskites, with general chemical formula ABN_3, have been predicted from machine learning and DFT calculations. Four machine learning models such as support vector regression (SVR), gradient boosted decision tree (GBDT), random forest regression (RFR) and multi-

layer perceptron (MLP) have been considered for predicting the band gaps of the ABN_3 – type compounds. The band gaps of two nitride perovskites $CeMoN_3$ and $CeWN_3$, so predicted from their electronic band structures, dielectric functions, absorption coefficients and machine learning models, have also been highlighted in Chapter 7. The overall dissertation report is expected to provide a wealth of information in understanding the structural, electronic and optical properties of technologically relevant materials from first-principle calculations.

Phonon dispersion relation and electronic band structure of a system are intrinsically linked with its lattice thermal conductivity and thermoelectric transport property respectively. Recently thermoelectric materials have drawn significant attention as they are one of the most viable options to convert waste heat into electricity and resolve the energy crisis of the environment [1-4]. The energy conversion efficiency of a thermoelectric system can be estimated from a dimensionless quantity, known as the thermoelectric figure of merit (ZT) and ZT can be obtained from the simple mathematical relation:

$$ZT = \frac{S^2 \sigma T}{k_l + k_e} \tag{8.1}$$

An ideal thermoelectric compound with high ZT demands a larger Seebeck coefficient (S), high electrical conductivity (σ) as well as low lattice (k_l) and electronic thermal conductivities (k_e) at a certain temperature (T). The future work is thus to explore the lattice thermal conductivities and thermoelectric properties of novel materials from first-principle calculations and molecular dynamics simulations. Special focus will be given to identify the contributions of particle and wave-like phonons in k_l. However, the estimation of k_l is computationally demanding and may alter according to the choice of third and fourth-order interatomic force constants (IFCs). Therefore, the future work also aims to unveil the k_l of the compounds from machine learning interatomic potentials under the moment tensor potentials and/ or neural network potentials framework [5,6].

Recently, spintronics has emerged as one of the most promising technologies in materials industries to resolve the key issues that exist in today's conventional electronic devices. Spintronic systems, which exhibit splitting of degenerate electronic energy bands into two spin-split states having opposite spin polarizations, are correlated with the Rashba-Dresselhaus (RD) effects [7-9]. In a simple picture, a spin-polarized relativistic electron with momentum **k** interacts with the local electric field of the crystal and results in the generation of an effective magnetic field. The effective magnetic field lifts the spin degeneracy in the

momentum space, showing the phenomena called RD effects. After the discovery of RD effects, the effects paved the way for the field of spintronics which is expected to bring a new revolution in discovering the next generation superfast energy-efficient computers and topological quantum computations. As a result, the involvement of researchers behind the RD effects has increased considerably in recent years. Large-size electronic equipment, which generates excessive heat, can be mapped into a single chip by combining the main functions of the semiconductors and magnetic storage devices through spintronics. Of late, the innovations of new materials like organic semiconductor spintronics, quantum dots spintronics, molecular and graphene spintronics open the possibilities of fabricating robust, cheap, and small-size devices that show faster operation, low power consumption, and high storage density [10-13]. Figure 8.1 shows a schematic representation of some exotic physical and transport properties that originated from spin-orbit interaction in conjunction with the broken inversion symmetry of a crystal. Thus, one of the future works also focuses on unveiling the Rashba and/ or Dresselhaus-type effect in novel materials from first-principle calculations by estimating the splitting of electronic band structures.

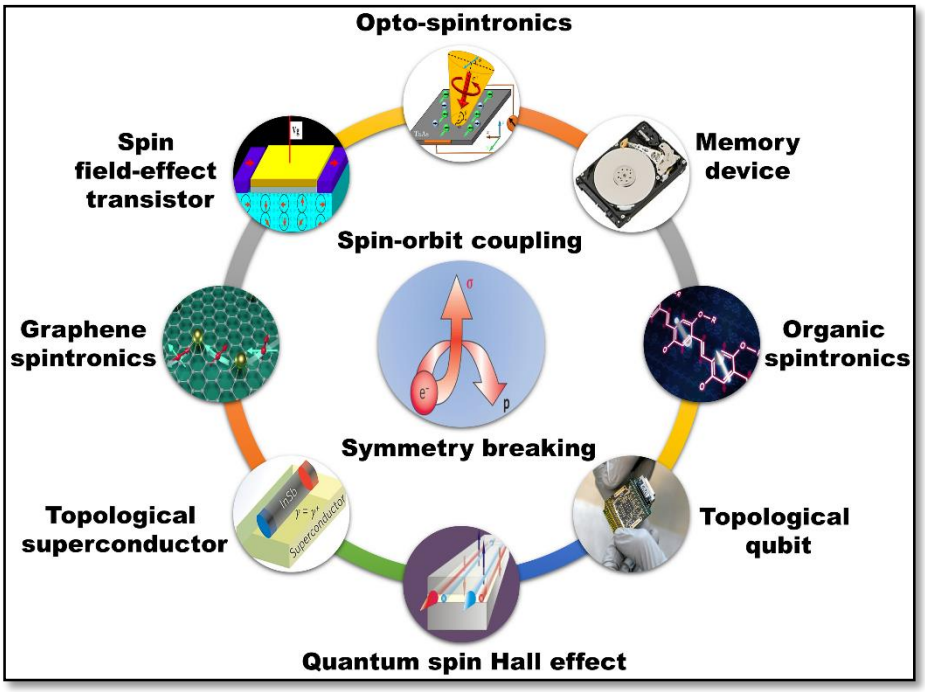

Figure 8.1. Schematic representation of some fascinating physical and transport properties originated from spin-orbit interaction in conjunction with broken inversion symmetry of a crystal. © World Scientific Publishing Company [14].

Bibliography

[1] A. K. Kushwaha, H. Kalita, S. Suman, A. Bhardwaj, and R. Ghosh, in *Thermoelectricity and Advanced Thermoelectric Materials*, edited by R. Kumar, and R. Singh (Woodhead Publishing, 2021), pp. 233.

[2] M. N. Hasan, H. Wahid, N. Nayan, and M. S. Mohamed Ali, Int. J. Energy Res. **44**, 6170 (2020).

[3] J. Wei, L. Yang, Z. Ma, P. Song, M. Zhang, J. Ma, F. Yang, and X. Wang, J. Mater. Sci. **55**, 12642 (2020).

[4] X.-L. Shi, J. Zou, and Z.-G. Chen, Chem. Rev. **120**, 7399 (2020).

[5] J. Behler and M. Parrinello, Phys. Rev. Lett. **98**, 146401 (2007).

[6] A. V. Shapeev, Multiscale Model. Simul. **14**, 1153 (2016).

[7] E. Rashba and V. Sheka, Fiz. Tverd. Tela: Collected Papers **2**, 162 (1959).

[8] E. Rashba, Sov. Phys.-Solid State **1**, 368 (1959).

[9] G. Dresselhaus, Phys. Rev. **100**, 580 (1955).

[10] P. Ghising, C. Biswas, and Y. H. Lee, Adv. Mater. **n/a**, 2209137 (2023).

[11] F. Z. Wang, arXiv preprint arXiv (2023).

[12] Y. Zhu, Q. Jiang, J. Zhang, and Y. Ma, Chem. Asian J. **18**, e202201125 (2023).

[13] S. M. Yakout, J Supercond Nov Magn **33**, 2557 (2020).

[14] S. Ghosh and J. Chowdhury, Mod. Phys. Lett. B **38**, 2330003 (2023).

Appendix

Paper presented at international/ national conferences/ seminars

1. **Oral presentation** on "**Machine Learning and Density Functional Theory Studies for Predicting Band Gaps of ABN_3 Perovskites**" in Fourth International Conference on Material Science- 2024 organized by the Department of Physics, Tripura University.
2. **Oral presentation** on "**Bulk Rashba and Anomalous Hall Effects in Rare – Earth Nitride Perovskites $CeAN_3$ (A = Mo, W): Insights from First-Principle Calculations**" in 6th Regional Science and Technology Congress 2023-24 organized by Department of Science and Technology and Biotechnology, Government of West Bengal.
3. **Poster presentation** on "**Predicting Band Gaps of Nitride Perovskites: A Combined Machine Learning and Density Functional Theory Study**" in Young Scientists Colloquium 2023 organized by Materials Research Society of India, Kolkata.
4. **Oral presentation** on "**Origin of Rashba-Dresselhaus Effects in Rare Earth Perovskites: Insights from First-Principle Calculations**" in 5th International Conference on Physics for Sustainable Development & Technology-2023, Chittagong, Bangladesh (***Awarded Best Oral Presentation***).
5. **Invited Lecture** on "**Structural Phase Transitions and Optoelectronic Properties of Mercurous Chloride: Insights from First-Principle Calculations**" in Department of Physics, Jadavpur University, Kolkata, India, 2023.
6. **Oral presentation** on "**Deciphering the Vibrational Phonon Modes Responsible for the Structural Phase Transitions of Mercurous Chloride: Insights from First-Principle DFT and Born-Oppenheimer On The Fly Molecular Dynamics Calculations**" in IX International Conference on Perspectives in Vibration Spectroscopy- 2022, Indore, India.
7. **Invited Lecture** on "**First-Principle Density functional theory and Machine Learning Approaches for the Prediction of Materials Properties**" in *A One Day Student Seminar* organized by Department of Physics, Sammilani Mahavidyalaya, Kolkata, India, 2022.
8. **Oral presentation** on "**Pressure Induced Structural Phase Transitions and Modulations of Optoelectronic Properties of Hg_2Cl_2 Compound: Insights from First-Principle Calculations**" in International Conference on Advanced Physics - 2022, Kolkata, India (***Awarded Best Paper Presentation***).
9. **Oral presentation** on "**Pressure Induced Structural Phase Transitions and Electronic Properties of Wide Band Gap Charge Transfer Insulator Mercurous Chloride: A First-Principle DFT Study**" in 3rd International Conference on Chemistry and Material Science- 2021, Jember, Indonesia.
10. **Oral presentation** on "**Soft-phonon driven structural phase transition and electronic properties of Hg_2Cl_2**" in International Conference on Advanced Physics - 2021, Kolkata, India (***Awarded Best Paper Presentation***).

Journal of Applied Physics ARTICLE scitation.org/journal/jap

Pressure induced structural phase transitions of technologically significant mercurous chloride at room temperature: An account from first-principle DFT and Born–Oppenheimer molecular dynamics studies

Cite as: J. Appl. Phys. **130**, 225103 (2021); doi: 10.1063/5.0068049
Submitted: 22 August 2021 · Accepted: 21 November 2021 ·
Published Online: 8 December 2021

Swarup Ghosh and Joydeep Chowdhury[a)]

AFFILIATIONS

Department of Physics, Jadavpur University, 188, Raja S.C. Mallick Road, Kolkata 700032, India

[a)]**Author to whom correspondence should be addressed:** joydeep72_c@rediffmail.com and joydeep.chowdhury@jadavpuruniversity.in

ABSTRACT

This paper reports for the first time an in-depth study based on first-principle calculations to unveil the underlying physics that governs the pressure induced structural phase transitions of Hg_2Cl_2 compound at room temperature. The phonon dispersion relations and phonon density of states have been critically explored for the tetragonal and orthorhombic phases of the compound to unveil the phonon modes associated with the phase transitions. The nature of the phase transition whether it is "displacive" or of "order–disorder" type has also been explored. We believe that the present study based on density functional theory and Born–Oppenheimer molecular dynamics calculations will help understand the underlying physics behind the above referred phase transitions and the anisotropic behavior of the compound, which in turn bears technologically significant relevance for its applications in optoelectronic devices, acousto-optic tunable filters, and in fiber-optic communication systems.

I. INTRODUCTION

Phase transition happens to be a fascinating physical phenomenon that engrossed the human minds over centuries. It is a process in which thermodynamic systems change from one state to the other with varying physical properties. The most common example of nature is the melting of ice into water in the liquid state, which on further heating turns to vapor. However, besides this, there exist many exotic examples involving the transformation of phases, which are not only interesting from physics points of view but are technologically very significant. Dramatic changes in the physical properties of materials upon changes in phases involve transitions from ferromagnetic to paramagnetic behaviors of materials at the Curie point, ordinary conducting to superconducting materials below the critical temperature (T_c), etc.[1–11] Moreover transitions from normal fluid helium (He-I) to the superfluid helium-II at the "lambda (λ)" point,[12–14] order–disorder transition in brass,[15] glass–liquid phase transition in polymer at glass transition temperature (T_g),[16] superconductor–insulator quantum phase transition,[17] and structural transitions from one solid phase to another with temperature and/or external pressure are also some prominent examples of phase transitions.[18–29]

Mercurous chloride (Hg_2Cl_2), commonly referred to as calomel, is a wide bandgap insulator and finds extensive applications as white pigment and electrode material.[30–32] This compound is reported to show strong birefringence, as a response to its anisotropic physical properties.[31–33] The anisotropic behavior of mercurous halide crystals not only makes them effective for designing polarizing prisms but also find their applications in acousto-optic tunable filters for the development of hyperspectral imagers covering wide UV–Vis–Long Wavelength Infrared (LWIR) spectral

window of the electromagnetic spectrum.[34] At room temperature and under ambient pressure (P = 0 GPa), Hg_2Cl_2 compound is known to exist in the tetragonal I4/mmm (D_{4h}^{17}) phase. The material is reported to undergo a temperature dependent structural phase transition from the body-centered tetragonal [I4/mmm (D_{4h}^{17})] phase to the base-centered orthorhombic [Cmcm (D_{2h}^{17})] phase at ~185 K.[35–39] Moreover, at room temperature, Hg_2Cl_2 also exhibits pressure induced structural phase transition from the I4/mmm (D_{4h}^{17}) → Cmcm (D_{2h}^{17}) phase at a pressure of 0.25 GPa.[40–42] Lately, the prevalence of another structural phase transition of the compound from the base-centered orthorhombic [Cmcm (D_{2h}^{17})] to the primitive orthorhombic [Pnma (D_{2h}^{16})] phase at relatively higher external pressure (P) = 8.95 GPa has been reported.[43]

Although the existences of pressure induced phase transitions of Hg_2Cl_2 have been reported, yet the underpinning physics behind these transitions are not being addressed in detail. Considering the above issue in mind, here we report a detailed study on the pressure induced structural phase transitions of the compound based on first-principle calculations. The nature of the phase transition whether it is "displacive" or of "order–disorder" type has also been investigated. We believe that the in-depth study on the pressure induced structural phase transitions of Hg_2Cl_2 at room temperature from the first-principle density functional theory(DFT) and Born–Oppenheimer molecular dynamics (BOMD) will help us to understand the underlying physics behind the above referred phase transitions and the anisotropic behavior of the compound, which in turn will be helpful for its applications in various optoelectronic devices, acousto-optic tunable filters, and in fiber-optic communications.

II. COMPUTATIONAL DETAILS

The crystal structure belonging to the tetragonal (I4/mmm) phase of Hg_2Cl_2 at room temperature (300 K) and at ambient pressure (P = 0 GPa) has been obtained from the experimentally determined x-ray diffraction data.[44] The experimentally determined crystallographic data of the compound are initially optimized within the static DFT (0 K) framework using hybrid generalized gradient approximations (GGA) plus Heyd–Scuseria–Ernzerhof (HSE)[45] exchange–correlation (XC) functional with the aid of Quantum ESPRESSO (QE) software.[46–48] The $5d^{10}6s^2$ and $3s^23p^5$ electrons for the Hg and Cl atoms, respectively, are considered valence electrons and are represented as plane wave with kinetic energy cutoff of 50 Ry. The interactions between the electrons and the ions have been incorporated through the pseudopotential using the projector augmented wave (PAW) method.[49] The systematic convergence criterion of total electronic energy in geometry optimization was primarily set to 10^{-8} Ry with threshold of the Hellman–Feynman force of 10^{-3} a.u. at a maximum cell pressure of 10^{-2} GPa. The unit cell comprising of eight atoms in the tetragonal structure of the Hg_2Cl_2 compound has been sampled with a gamma-centered k-point mesh of $9 \times 9 \times 9$ grid generated through the Monkhorst–Pack method. However, after optimization, the actual convergences of forces and energies have been achieved to be ~0.00026 a.u. and 2.5×10^{-10} Ry, respectively, for the pre-referred kinetic energy cutoff value of 50 Ry. Figures S1(a) and S1(b) in the supplementary material show the variations of the Hellman–Feynman force and total self-consistent field (SCF) energy for the body-centered tetragonal (I4/mmm) phase of the Hg_2Cl_2 compound under ambient condition as a function of plane wave kinetic energy cutoff. From Fig. S1 in the supplementary material, it is clearly seen that the kinetic energy cutoff for the plane wave at 50 Ry is fairly good to carry out the DFT calculations for the above referred phase of the compound.

The optimized geometry associated with the tetragonal phase of the Hg_2Cl_2 compound under ambient condition as attained from the static DFT calculations is further refined from the Born–Oppenheimer molecular dynamics (BOMD) simulation. The BOMD simulation has been performed within the same DFT framework with kinetic energy cutoff set at 50 Ry; threshold for total electronic energy and maximum Hellman–Feynman force were fixed at 10^{-8} Ry and 10^{-3} a.u., respectively, at a maximum cell pressure of 10^{-2} GPa. The electron–ion interactions in the BOMD simulation have been incorporated using the same PAW method as used for the static DFT calculations. The NPT ensemble was chosen for the simulation run, and the Andersen thermostat[50] was used to control the temperature of the ensemble. For the BOMD simulation, the tetragonal phase of the Hg_2Cl_2 compound at room temperature (300 K) has been initially equilibrated for 10 ps and then simulated further for another 48 ps with a chosen time step of 2 fs. Static DFT calculation followed by the BOMD simulation eventually result in the accomplishment of refined structural parameters for the tetragonal phase of the compound at room temperature and at ambient pressure (P = 0 GPa). This refined structure of the compound at room temperature and at ambient pressure is then further relaxed using the "variable cell molecular dynamics" (VC-MD) method. The cell pressure has been varied from 0 to 14 GPa at room temperature to achieve the BOMD simulated structural parameters and atomic positions of the base-centered [Cmcm ($\boldsymbol{D_{2h}^{17}}$)] and primitive [Pnma ($\boldsymbol{D_{2h}^{16}}$)] orthorhombic phases of the compound.

The refined structural parameters of the body-centered tetragonal and base-centered, primitive orthorhombic phases of the compound at room temperature (300 K) and under ambient/external pressures so accomplished from the BOMD simulations have been utilized to generate the phonon dispersion spectra and phonon density of states (PHDOS) within harmonic approximation and single point calculations using the linear response theory in the density functional perturbation theory (DFPT) framework from the unit cell geometry of the Hg_2Cl_2 compounds.[51–53] The phonon data have been estimated through the diagonalization and sampling of the dynamical matrix D(k) for any arbitrary wave vector k. The interatomic force constants on the real-space grid have been extracted from the backward Fourier transform approach of the calculated D(k). A denser Fourier re-interpolated grid of k-point mesh $19 \times 19 \times 19$ has been chosen for estimating the phonon dispersion spectra and PHDOS. The non-analytical term corrections have been applied in the phonon dispersion curves to isolate the LO–TO splitting in the phonon spectra.

III. RESULTS AND DISCUSSION

A. Structural analyses and pressure dependent phase transition of the Hg_2Cl_2 compound

At room temperature and ambient pressure, Hg_2Cl_2 crystallizes in the body-centered tetragonal phase with the I4/mmm

(space group no. 139) space group symmetry.[44] The unit cell of Hg_2Cl_2 comprises of one formula unit (Z = 2) with eight atoms, where Hg and Cl are in the respective 4e (0, 0, 0.11577) and 4e (0, 0, 0.3380) Wyckoff sites. The variations in the total energy (E) of the body-centered tetragonal [I4/mmm (D_{4h}^{17})] phase of Hg_2Cl_2 under ambient condition as a function of unit cell volume (V), as accomplished from the static DFT calculation, is shown in Fig. 1(a). The *E*–*V* plot has been fitted using fourth order Birch–Murnaghan equation of states.[54,55] From Fig. 1(a), it is observed that total energy for the I4/mmm (D_{4h}^{17}) phase of Hg_2Cl_2 attains the minimum energy at unit cell volume of 219.16 Å^3. The optimized structure of Hg_2Cl_2 at this unit cell volume is equilibrated for a time scale of 48 ps for further refinement. Fluctuations of the total energy of the system as a function of time are shown in Fig. 1(b). After primary flexing and relaxation, the energy of the system attains an equilibrium configuration after 10 ps time scale of the simulation run. To address the implications of finite size effects,[56,57] the convergences of energy and volume for the tetragonal [I4/mmm (D_{4h}^{17})] phase of the Hg_2Cl_2 system as a function of N-atom cell size (N = 8, 16, 32, 64) have been estimated. The representative plots are shown in Figs. S2(a) and S2(b) in the supplementary material, respectively. From Figs. S2(a) and S2(b) in the supplementary material, we can see clearly that both the energy and the volume of the system in its tetragonal (I4/mmm) phase remain almost constant for 8, 16, 32, and 64 atoms.

The refined optimized geometry of the compound as obtained from BOMD calculations in the tetragonal phase at room temperature (300 K) and at ambient pressure (P = 0 GPa) along with its structural parameters is shown in Fig. 2 and Table I, respectively. The lattice and structural parameters associated with the tetragonal (I4/mmm) phase of Hg_2Cl_2 are in close agreement with the experimental results as extracted from x-ray[44] and neutron powder diffraction data.[58] The optimized structure of Hg_2Cl_2 at room temperature and at ambient pressure as shown in Fig. 2(a) marks the presence of distorted octahedral domains with corner sharing Hg atoms. The zoomed-in-view of the distorted octahedron is shown in Fig. 2(c). From Fig. 2(c), it is clearly seen that the neighboring chlorine Cl(V) and apical mercury Hg(A) atoms at the vertices form the distorted octahedron Hg(C)Hg(A)[Cl (V)]$_5$ with Hg (C) at its center. Several distorted octahedra are spanned in three-dimensional space over the crystal lattice whose illustration is shown in Fig. 2(a). However, one of the neighboring Cl(V) atoms forms a Cl(V)–Hg(C)–Hg(A) linear chain with the associated angles of ~180°. To separate this chlorine Cl(V) atom involved in the linear chain from the rest, we designate it as Cl(L). The linear Cl(L)–Hg(C)–Hg(A)–Cl(L) chain of Hg_2Cl_2, as shown in Fig. 2(b), directed along the crystallographic *c* axis, is considered to be responsible for large anisotropy, birefringence, and low transverse acoustic (TA) wave velocity of Hg_2Cl_2.[34,59–61] The associated octahedron in the crystal structure of Hg_2Cl_2 is re-labeled as Hg(C)Hg(A)[Cl(V)]$_4$Cl(L) henceforth.

Figure 3(a) shows the variation in the ratio of the refined unit cell volume ratio (V/V_0) of the Hg_2Cl_2 compound as a function of external pressure.[54,55] Interestingly, with slight increase in P, the V/V_0 ratio shows a sharp rise with a peak at 0.25 GPa, beyond which the V/V_0 ratio falls monotonically until around P between 8 and 10 GPa, where a definite change in the gradient of the slope is observed. Significantly enough the pressure $P_T \sim 0.25$ GPa at which the V/V_0 ratio attains the maximum value corresponds to the first structural phase transition of Hg_2Cl_2 crystal from its tetragonal phase to the base-centered orthorhombic one [I4/mmm (D_{4h}^{17}) → Cmcm (D_{2h}^{17})] as reported elsewhere.[40–42] Our first-principle calculations further suggest nearly twofold increase in the unit cell volume at P = 0.25 GPa, mostly involving larger increments of the associated lattice parameters "a" and "b" in comparison to "c." Changes in the lattice parameters of the Hg_2Cl_2 crystal

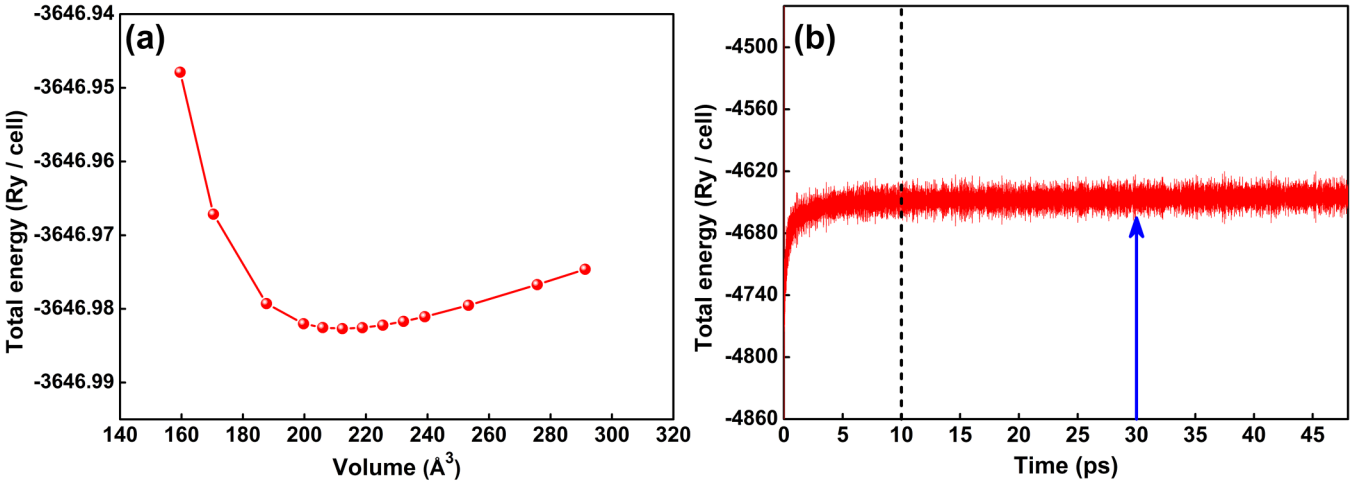

FIG. 1. (a) Total energy vs volume curve for the unit cell geometry for the body-centered tetragonal phase [I4/mmm (D_{4h}^{17})] of Hg_2Cl_2 as obtained from the static DFT calculations at the HSE level of theory. (b) Total energy of the body-centered tetragonal phase [I4/mmm (D_{4h}^{17})] of Hg_2Cl_2 as a function of time as estimated from the BOMD simulations. (Vertical blue arrow shows the time at which the refined geometry of the compound being extracted.)

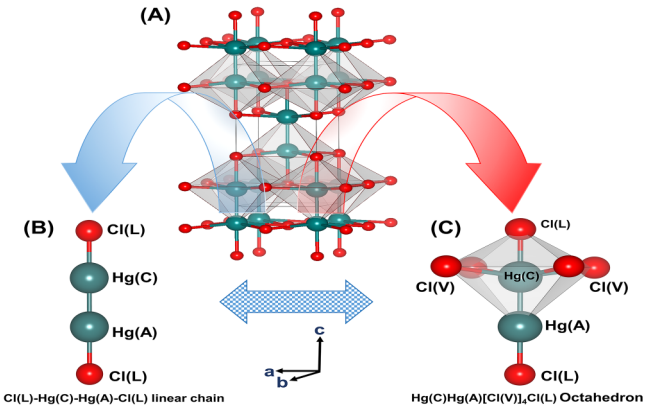

FIG. 2. (a) Refined optimized geometry for the tetragonal (I4/mmm) phase of Hg_2Cl_2 crystal at room temperature (300 K) and at ambient pressure (P = 0 GPa) as obtained from BOMD calculation. The zoomed-in-view of the structure showing (b) linear chain of the molecule containing of Cl(L)–Hg(C)–Hg (A)–Cl(L) atoms and (c) the distorted octahedron Hg(C)Hg(A)[Cl(V)]$_4$Cl(L). (Hg atoms are shown in emerald blue and Cl atoms are shown in red.)

as a function of P are shown in Fig. 3(b). Such doubling of the unit cell is also reported for the Hg_2Cl_2 crystal as it undergoes temperature driven structural phase transition from the tetragonal to base-centered orthorhombic [I4/mmm (D_{4h}^{17}) → Cmcm (D_{2h}^{17})] phase at 185 K.[60] With an increase in the external pressure P > 0.25 GPa, V/V_0 decreases smoothly until ∼8 GPa, while beyond that pressure, a distinct change in the slope is noticed at ∼ 9 GPa, primarily signifies the occurrence of the second phase transition for the crystal. The presence of second phase transition at ∼9 GPa has recently been estimated experimentally by Roginskii *et al.* from low-frequency Raman spectroscopic studies.[43] The associated lattice parameters ∼P = 9 GPa show overall small decrement in the "a," "b," and "c" values in comparison to that estimated between 0.5 and 8 GPa external pressure [Fig. 3(b)]. In fact, the external pressure ∼P = 9 GPa may mark the pressure driven second phase transition of the Hg_2Cl_2 crystal from the base-centered orthorhombic [Cmcm (D_{2h}^{17})] to the primitive orthorhombic [Pnma (D_{2h}^{16})] phase. The result as estimated from the BOMD calculations thus closely matches with the experimental observation. Representative plots, showing the temporal variations of energies for high pressure Cmcm (D_{2h}^{17}) and Pnma (D_{2h}^{16}) phases of the system, are depicted in Fig. S3 in the supplementary material. The variations in the total energy for Cmcm (D_{2h}^{17}) and Pnma (D_{2h}^{16}) phases of the Hg_2Cl_2 compound as a function of unit cell volume, as accomplished from BOMD simulations, are fitted using fourth order Birch–Murnaghan equation of states[54,55] and are shown in Fig. S4 in the supplementary material. As for the tetragonal [I4/mmm (D_{4h}^{17})] phase of Hg_2Cl_2, the consequences of the finite size effects for the orthorhombic [Cmcm (D_{2h}^{17}) and Pnma (D_{2h}^{16})] phases of the compound have also been considered. Figures S5(a) and S5(b) in the supplementary material show the convergences of energy and volume for the Cmcm (D_{2h}^{17}) and Pnma (D_{2h}^{16}) orthorhombic phases of the Hg_2Cl_2 system as a function of N-atom cell size (N = 8, 16, 32, 64). From Fig. S5 in the supplementary material, one can clearly see that both the energy and the volume of the Hg_2Cl_2 system in its orthorhombic [Cmcm (D_{2h}^{17}) and Pnma (D_{2h}^{16})] phases remain almost constant for 8, 16, 32, and 64 atoms.

The experimental observation further suggests that the base-centered orthorhombic phase of Hg_2Cl_2 remains stable within 0.25 < P < 9 GPa external pressure just before the onset of the second phase transition.[43] However, in general, both the phase transitions at ∼P = 0.25 and 9 GPa for the Hg_2Cl_2 compound are accompanied by the changes in volumes, thereby suggesting such transitions to be of first order type. The nature of such structural phase transitions from I4/mmm (D_{4h}^{17}) → Cmcm (D_{2h}^{17}) and from

TABLE I. Computed refined lattice and structural parameters for tetragonal I4/mmm, Cmcm, and Pnma phases of the Hg_2Cl_2 compound as obtained from BOMD simulations.

	Phases				
	I4/mmm		Cmcm		Pnma
Measured parameters	This study	Experiments[44,62]	This study	Experiments[60]	This study
Lattice parameters (Å)					
a	4.489	4.470, 4.480	6.299	6.290	5.752
b	4.489	4.470, 4.480	6.249	6.240	5.751
c	10.929	10.890, 10.910	10.857	10.860	10.677
Volume (Å^3)					
V	220.23 (V_0)	217.60, 218.97	427.36	426.25	342.14
Average bond length (Å)					
Hg(C)–Hg(A)	2.526	2.526	2.617	…	2.624
Hg(C)–Cl(L)	2.424	2.434	2.522	…	2.528
Average bond angle (deg)					
Hg(C)–Cl(V)	3.210	3.209	3.160	…	3.154
Cl(V)–Hg(C)–Cl(V)	161.920	162.240	169.290	…	171.120
Hg(A)–Hg(C)–Cl(V)	99.040	…	95.270	…	95.130
Cl(L)–Hg(C)–Hg(A)–Cl(L)	180.000	180.00	171.260	…	170.140

Cmcm (D_{2h}^{17}) → Pnma (D_{2h}^{16}), whether they are "displacive" or of "order–disorder" type, will be unveiled later.

Figure 4(a) shows the refined optimized geometries depicting the crystal structures of the Hg_2Cl_2 compound at 0.25, 6, and 9 GPa, representing the base-centered orthorhombic [Cmcm (D_{2h}^{17})] and primitive orthorhombic [Pnma ((D_{2h}^{16})] phases, respectively. The corresponding lattice and structural parameters associated with the above referred Cmcm (D_{2h}^{17}) and Pnma (D_{2h}^{16}) phases of the compound are also shown in Table I. The experimentally determined lattice parameters for the Pnma (D_{2h}^{16}) phase of the compound are not available in the literature; however, for the Cmcm (D_{2h}^{17}) phase, the available experimental results are depicted in Table I. The structural and lattice parameters associated with the base-centered orthorhombic Cmcm (D_{2h}^{17}) phase of Hg_2Cl_2, as estimated from the first-principle calculations, are in close harmony with the experimental result.[60] The refined structural parameters as reflected from Table I show alterations in Hg(C)–Hg(A), Hg(C)–Cl (L), and Hg(C)–Cl(V) bond lengths of the compound as they undergo structural phase changes from the body-centered tetragonal to base-centered orthorhombic [I4/mmm (D_{4h}^{17}) → Cmcm (D_{2h}^{17})] and primitive orthorhombic phases [Cmcm (D_{2h}^{17}) → Pnma (D_{2h}^{16})] at two different pressures. These structural phase changes also lead to variations in the Cl(V)–Hg(C)–Cl(V) and Hg(A)–Hg (C)–Cl(V) bond angles involving Hg(C and A) and neighboring Cl (V) of the compound, which in turn results in the distortion of the octahedral domains within the crystal lattice. Significantly enough, the average dihedral angle of Cl(L)–Hg(C)–Hg(A)–Cl(L) shows deviation from planarity and loses its linear form as the system undergoes pressure driven phase transition from the body-centered tetragonal to base-centered orthorhombic [I4/mmm (D_{4h}^{17}) → Cmcm (D_{2h}^{17})] and primitive orthorhombic phases [Cmcm (D_{2h}^{17}) → Pnma (D_{2h}^{16})]. The variation of the above referred dihedral angle with P is shown in Fig. 4(b). However, in this connection, it may be relevant to mention that the differences in the structural parameters associated with the compound at P = 0.25, 6, and 9 GPa [Fig. 4(a)] are indeed very minute, so it is not possible to capture these changes from their respective images.

To estimate precisely the transition pressure (P_T), the variation of enthalpy (H) with pressure for body-centered tetragonal [I4/mmm (D_{4h}^{17})] phase, base-centered orthorhombic [Cmcm (D_{2h}^{17})], and primitive orthorhombic [Pnma (D_{2h}^{16})] phases of Hg_2Cl_2 crystal at room temperature has been estimated using the following relation:

$$H = E + PV, \tag{1}$$

where E and V are the total energy and volume of the respective unit cells associated with I4/mmm (D_{4h}^{17}), Cmcm (D_{2h}^{17}), and Pnma (D_{2h}^{16}) phases of the Hg_2Cl_2 compound, respectively, and P is the applied external pressure on them. The respective variations of H for I4/mmm (D_{4h}^{17}), Cmcm (D_{2h}^{17}) and Cmcm (D_{2h}^{17}), and Pnma (D_{2h}^{16}) phases of Hg_2Cl_2 as a function P are shown in Fig. 5. The transition pressure (P_T) corresponds to the point on the H–P plots where the two enthalpy values for the above-mentioned phase pairs of the compound [ca. I4/mmm (D_{4h}^{17}), Cmcm (D_{2h}^{17}) and Cmcm (D_{2h}^{17}), and Pnma (D_{2h}^{16})] become equal. From Figs. 5(a) and 5(b), it is observed that the H–P plots of I4/mmm (D_{4h}^{17}), Cmcm (D_{2h}^{17}) and Cmcm (D_{2h}^{17}), and Pnma (D_{2h}^{16}) phases of Hg_2Cl_2 intersect at

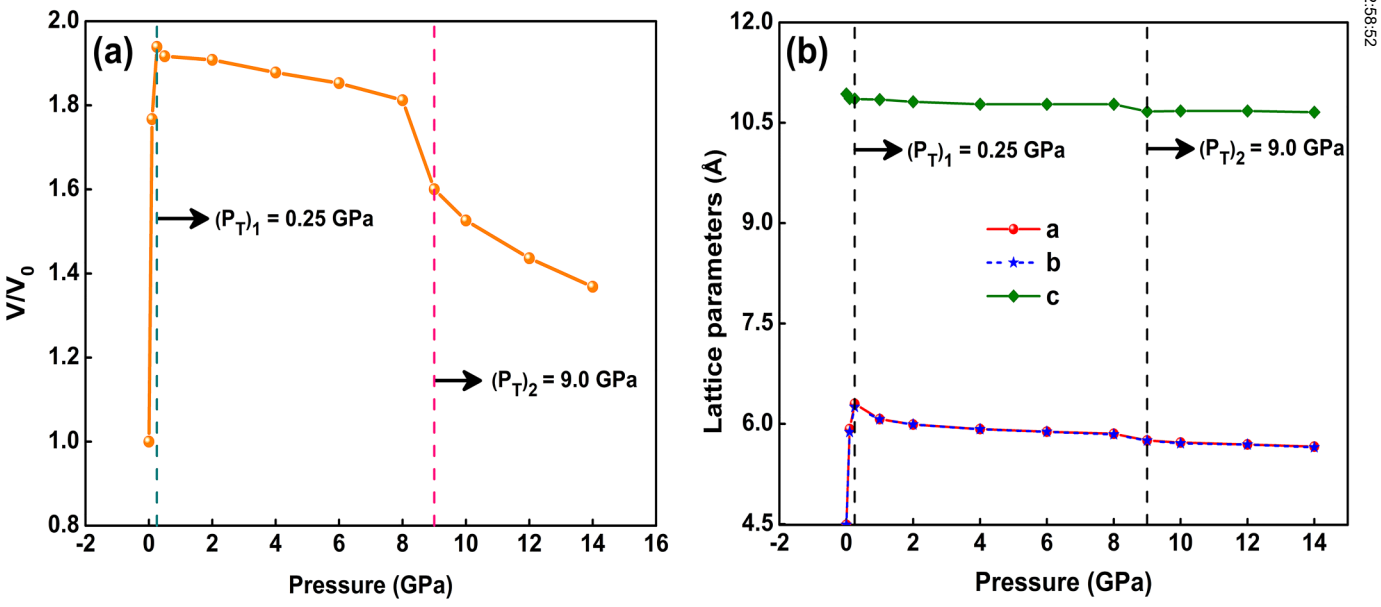

FIG. 3. (a) V/V_0 and (b) lattice parameters vs pressure plots under different external pressure ranging from 0 to 14 GPa. The transitions pressures $(P_T)_1$ and $(P_T)_2$ are marked in the figures as vertical dotted (—) lines.

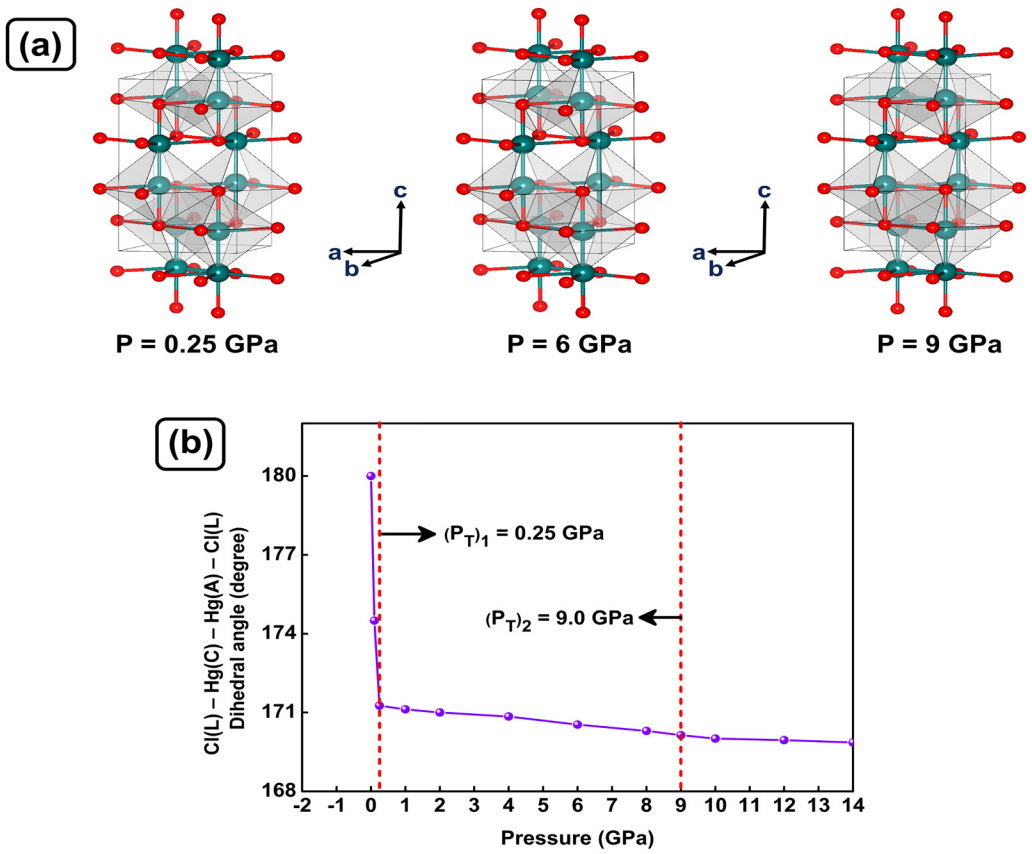

FIG. 4. (a) Refined structures of the I4/mmm phase at 0.25 GPa and the Cmcm phase at 6 and 9 GPa external pressure for the Hg_2Cl_2 compound calculated at room temperature (Hg atoms are shown in emerald blue and Cl atoms are shown in red). (b) Variation in Cl(L)–Hg(C)–Hg(A)–Cl(L) average dihedral angle as a function of pressure as calculated from the refined structures.

$P = (P_T)_1 = 0.25$ GPa and $P = (P_T)_2 = 9$ GPa. Thus, the external pressures $(P_T)_1$ and $(P_T)_2$ are related to the transition pressures that correspond to the first I4/mmm $(D_{4h}^{17}) \rightarrow$ Cmcm (D_{2h}^{17}) and second Cmcm $(D_{2h}^{17}) \rightarrow$ Pnma (D_{2h}^{16}) structural phase transitions of the system. The results are in concordance with the experimental observations that clearly predict the pressure induced phase transition of the Hg_2Cl_2 crystal at $P \sim 0.25$ and 9 GPa.[40–43]

B. The phonon dispersion relations and the phonon density of states of the Hg_2Cl_2 compound at various phases

The Hg_2Cl_2 crystal at ambient pressure crystallizes to I4/mmm (D_{4h}^{17}) space group symmetry. However, under different external pressures at P = 3 and 6 GPa, the compound belongs to the Cmcm (D_{2h}^{17}) phase while at 12 GPa, we observe the Pnma (D_{2h}^{16}) space group. The Hg_2Cl_2 crystal in each of the above referred phases contains eight atoms in their respective unit cells. Thus, 21 optical and 3 acoustic phonon branches are expected to appear in their phonon dispersion spectra. The left panels of Fig. 6 [Figs. 6(A) and 6(B)] and Fig. 7 [Fig. 7(A)] show the phonon dispersion curves of the Hg_2Cl_2 crystal representing body-centered tetragonal [I4/mmm (D_{4h}^{17})], base-centered orthorhombic [Cmcm (D_{2h}^{17})], and primitive orthorhombic [Pnma (D_{2h}^{16})] phases, respectively, along the high-symmetry directions $\Gamma \rightarrow M \rightarrow X \rightarrow \Gamma \rightarrow P$ and $\Gamma \rightarrow Z \rightarrow X \rightarrow \Gamma \rightarrow Y$ of the Brillouin zone. The total and atom resolved PHDOS related with the dispersion curves are also shown in the right panels of the Fig. 6 [Figs. 6(a) and 6(b)] and Fig. 7 [Fig. 7(a)]. The phonon dispersion curves for the crystal in general show the distinct presence of transverse acoustic (TA) and longitudinal acoustic (LA) phonon branches in the expected lower frequency window ranging from ~0 to 40 cm^{-1}. Among them, the TA branch is doubly degenerate along the $X \rightarrow \Gamma$ direction for the tetragonal and along $\Gamma \rightarrow Z$ for the orthorhombic phases of the crystal. From Fig. 6, nesting of the optical phonon branches for the body-centered tetragonal [I4/mmm (D_{4h}^{17})] phase of the compound at ambient pressure is seen in three distinct frequency regions spanning from ~27.9–54.1, 91.6–143.3, and 195–271.4 cm^{-1}. The dispersions of the phonon branches in the high frequency region are little more pronounced than for the low lying phonon branches at the ~27.9–54.1

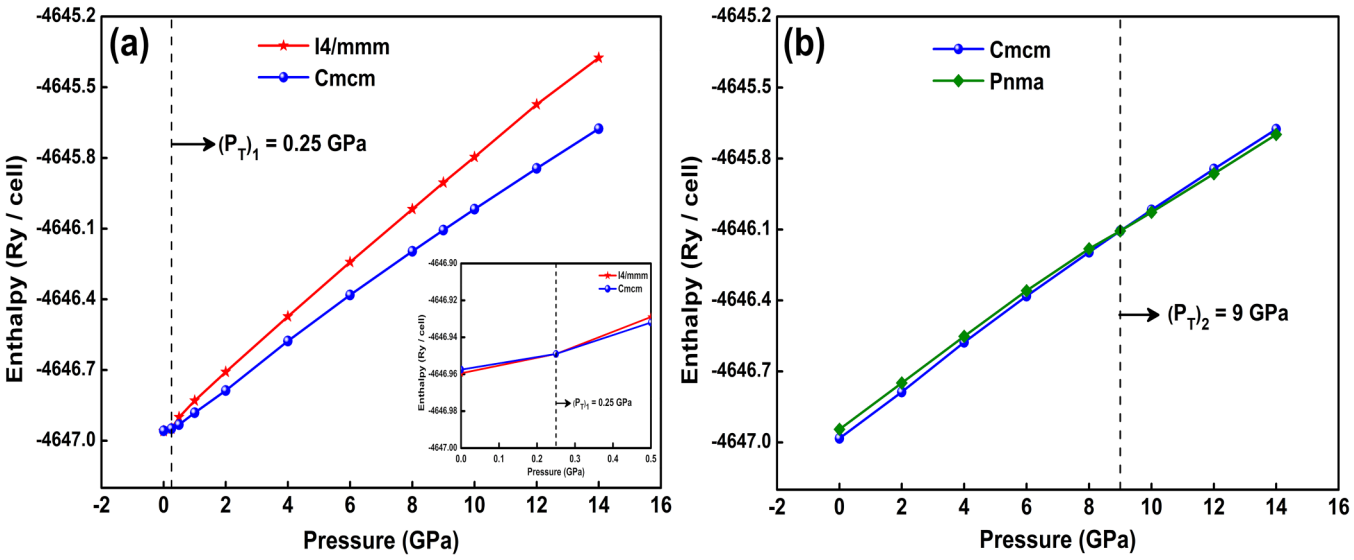

FIG. 5. The enthalpy–pressure plots for (a) I4/mmm and Cmcm phase and (b) Cmcm and Pnma phases of the refined structure of Hg_2Cl_2 compound. The inset of (a) shows the zoomed-in-view of the enthalpy–pressure plots for I4/mmm and Cmcm phases of the compound in the low-pressure domain ranging from pressure 0–0.5 GPa.

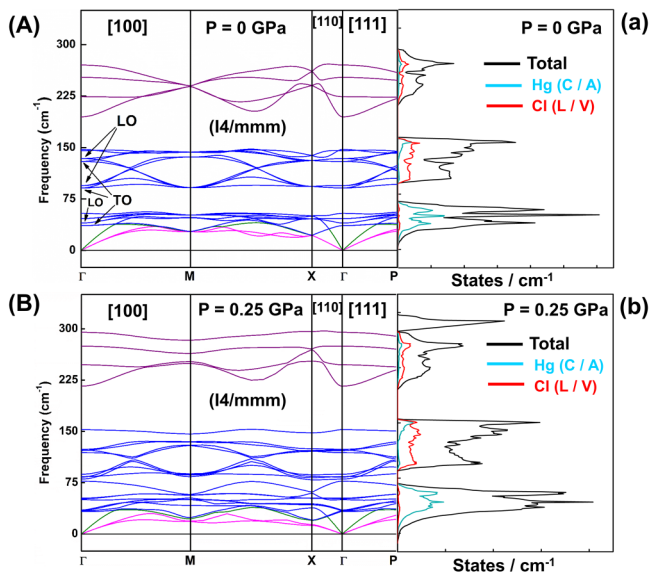

FIG. 6. Left panel shows the phonon dispersion curves along the high-symmetry points $\Gamma \rightarrow M \rightarrow X \rightarrow \Gamma \rightarrow P$ and the right panel depicts the total and partial PHDOS of the BOMD refined structure of Hg_2Cl_2 compound at P = 0 and P = 0.25 GPa as estimated from the HSE level of theory. (Blue and purple color traces indicate optical phonon modes in 27.9–143.3 and 195–271.4 cm^{-1} frequency windows, respectively, while those with magenta and green colors illustrate transverse and longitudinal acoustic phonon modes, respectively, in the phonon dispersion curve). LO–TO splittings are marked in (A).

and 91.6–143.3 cm^{-1} frequency regions. The corresponding total and atom resolved PHDOS [Fig. 6(a)] reveal that the phonon branches in the low frequency range (~27.9–54.1 cm^{-1}) are linked with vibrations involving Hg atoms, while in the high frequency region (91.6–143.3 and 195–271.4 cm^{-1}), larger weights on the PHDOS are owed to the vibrations of the Cl sublattices. However, the phonon branches for the Hg_2Cl_2 crystal with the space group I4/mmm (D_{4h}^{17}) at ambient pressure do not show any imaginary frequencies, signifying the structure to be dynamically stable. Interestingly, upon compression, the phonon dispersion spectrum of the compound at P = 0.25 GPa shows remarkable changes in their general features. It is marked by the decrease in frequencies of the optical Γ_{15}, M_{15}, X_{11}, P_{11} and slowest transverse acoustic (TA_1) X_1 phonon modes of vibrations at the respective high-symmetry points Γ, M, X, P, and X in the Brillouin zone. Among them, the decrease in the frequency of the TA_1 X_1 mode at the X high-symmetry point of the Brillouin zone boundary for the Hg_2Cl_2 crystal in the tetragonal I4/mmm (D_{4h}^{17}) phase at room temperature is reported to decrease with the increase in P from 0 to 0.25 GPa.[42] Moreover, hardening in the optical phonon frequencies of the Γ_{24}, M_{24}, X_{22}, and P_{24} modes is also observed. The corresponding PHDOS as shown in Fig. 6(b) exhibits broadening and shifts in the peak positions associated with Hg and Cl atoms in the frequency range of ~0–69.5 and ~84.6–155.6 cm^{-1}. Similar broadening of the PHDOS is also observed for hafnium when subjected to external pressure and has been reported elsewhere.[63] The reason behind the broadening of PHDOS spectra of Hg_2Cl_2 at an external pressure P = 0.25 GPa in contrast to that estimated for P = 0 GPa may be attributed to the increase of phonon energy states in the above referred frequency

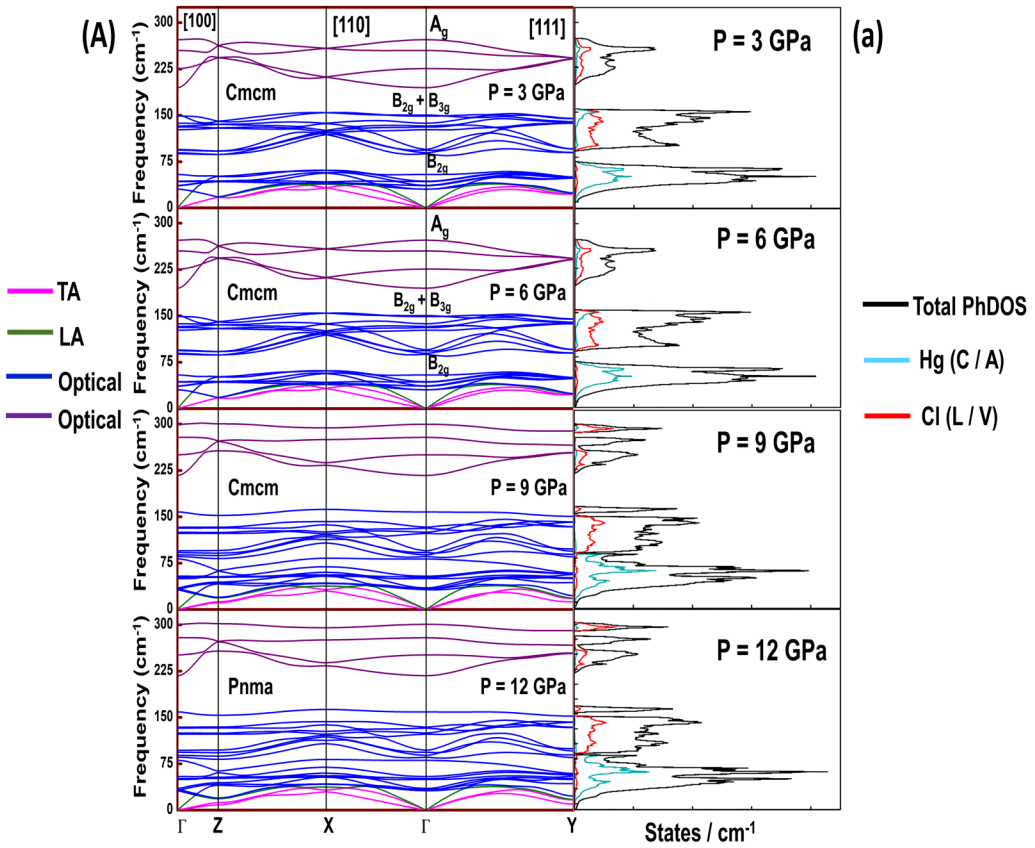

FIG. 7. (A) Phonon dispersion curves of the orthorhombic (Cmcm and Pnma) phases of Hg_2Cl_2 along the high-symmetry points Γ → Z → X → Γ → Y and the (a) total and partial PHDOS of the compound calculated at P = 3, 6, 9, and 12 GPa as estimated from the HSE level of theory.

range (~84.6–155.6 cm^{-1}). Incidentally, experimental results and our first-principle calculations (*vide ante*) suggest that external pressure P ~ 0.25 GPa happens to be the transition pressure $(P_T)_1$, which is explicitly linked with the first I4/mmm (D_{4h}^{17}) → Cmcm (D_{2h}^{17}) structural phase transition of the system.

Interestingly, after the first phase transition at $(P_T)_1$, at higher external P > 0.25 GPa, the Hg_2Cl_2 compound exits in the base-centered orthorhombic phase [Cmcm (D_{2h}^{17})]. The system is known to remain dynamically stable in the same phase over the external pressure range 0.25 < P < 9 GPa.[43] The phonon dispersion spectra of the Hg_2Cl_2 crystal and their related PHDOS at the external pressures P = 3 and 6 GPa, thus, show no significant alterations in the dispersion behavior of the phonon branches. These features are clearly apparent in Fig. 7(a). At pressure P = 9 GPa, appreciable changes in the dispersive features of the phonon branches are noticed. While decrement in frequencies of the phonons linked with $Γ_{15}$, Z_1, Z_{15}, X_{11}, and Y_{11} modes of vibrations are estimated from the first-principle calculations, concomitant up shifts of $Γ_{24}$, Z_{24}, X_{22}, and Y_{24} modes at the respective high-symmetry points Γ, Z, X, and Y in the Brillouin zone are also observed. Figure 7(a) shows the associated PHDOS of the compound at P = 9 GPa. The PHDOS shows remarkable changes in the features displaying significant shifts in the peak positions linked with Hg and Cl atoms of the compound together with the emergence of energy states particularly in the frequency window ~84–162 cm^{-1}. Significantly enough, the external pressure ~P = 9 GPa is the transition pressure $(P_T)_2$ that signifies the second phase transition of the Hg_2Cl_2 crystal leading to Cmcm (D_{2h}^{17}) → Pnma (D_{2h}^{16}) structural changes (*vide ante*). The condensations of Y_{11} and Z_1 phonons in the Cmcm (D_{2h}^{17}) → Pnma (D_{2h}^{16}) phase transition are in excellent agreement with the results of the earlier studies as reported by Roginskii *et al.*[43] At P > 9 GPa, Hg_2Cl_2 is dynamically stable and exists in the primitive orthorhombic phase with Pnma (D_{2h}^{16}) space group symmetry. A representative phonon dispersion spectrum along with its associated PHDOS for the Pnma (D_{2h}^{16}) phase of the compound at P = 12 GPa is shown in Fig. 7.

C. Pressure dependence on the phonon normal modes at high-symmetry points of the Hg_2Cl_2 compound and their corresponding eigenvectors

To gain more insights into the dependence of phonon frequencies as a function of external pressures leading to the first I4/

mmm (D_{4h}^{17}) → Cmcm (D_{2h}^{17}) and second Cmcm (D_{2h}^{17}) → Pnma (D_{2h}^{16}) structural phase transitions at $(P_T)_1 = 0.25$ and $(P_T)_2 = 9$ GPa, respectively, of the Hg_2Cl_2 compound, the variations of the phonon frequencies at different high-symmetry points in the Brillouin zone of the tetragonal [I4/mmm (D_{4h}^{17})] and orthorhombic [Cmcm (D_{2h}^{17})] phases of the system with pressure have been estimated. The variations are shown in Figs. 8(a) and 8(b). From Figs. 8(a) and 8(b), it is clearly seen that, in general, the low-frequency phonons in the frequency range of 27.9–143.3 cm^{-1} undergo noticeable downshifts while the high frequency ones in the ~195–271.4 cm^{-1} region are appreciably hardened. The other striking feature of the frequency vs P plots is the distinct changes in the slopes at P = 0.25 and 9 GPa, which incidentally correspond to the transition pressures $(P_T)_1$ and $(P_T)_2$ linked with the first and the second pressure driven phase transitions of the Hg_2Cl_2 compound. Strikingly enough, beyond $(P_T)_1 = 0.25$ and $(P_T)_2 = 9$ GPa, the phonon frequencies show no significant variations with P, suggesting the presence of base-centered orthorhombic [Cmcm (D_{2h}^{17})] and primitive orthorhombic [Pnma (D_{2h}^{16})] phases of the Hg_2Cl_2 compound over a wide range of external pressures ranging from ~0.5 to 8 and above 9 GPa, respectively. Figure 8(b) further entails about the variation in frequencies of the optical phonon branches associated with Γ_{15}, Z_1, Z_{15}, X_{11}, and Y_{11} and Γ_{24}, Z_{24}, X_{22}, and Y_{24} modes with pressure. The former phonon modes show gradual decrease in frequencies while the later reflect the opposite trend at the onset of the second phase transition pressure $(P_T)_2 = 9$ GPa. At P > 9 GPa, the phonon frequencies show no appreciable variations with P again suggesting the second structural phase transition from the base-centered orthorhombic [Cmcm (D_{2h}^{17})] to the primitive orthorhombic [Pnma (D_{2h}^{16})] phase of the compound at a pressure of 9 GPa.

In this connection, considerable attention may be drawn from the calculated low-frequency Raman active modes of the Cmcm and Pnma systems at the Γ point. The experimental observations of the low-frequency Raman mode ν_1' at ~59 cm^{-1} (calcd. 44 cm^{-1}) and the liberational mode ~137 cm^{-1} (calcd. 126.9 cm^{-1}) belonging to B_{2g} and $B_{2g} + B_{3g}$ irreducible representations, respectively, closely match with our calculated frequencies.[43] Among them, the B_{2g} mode at ~59 cm^{-1} had been experimentally reported to get softened and downshifted to ~ 56 cm^{-1} (calcd. 41.1 cm^{-1}) during the Cmcm (D_{2h}^{17}) → Pnma (D_{2h}^{16}) structural phase transition of the Hg_2Cl_2 compound at 9 GPa in concordance with our theoretical estimations. However, discrepancies in the assignment of the low-

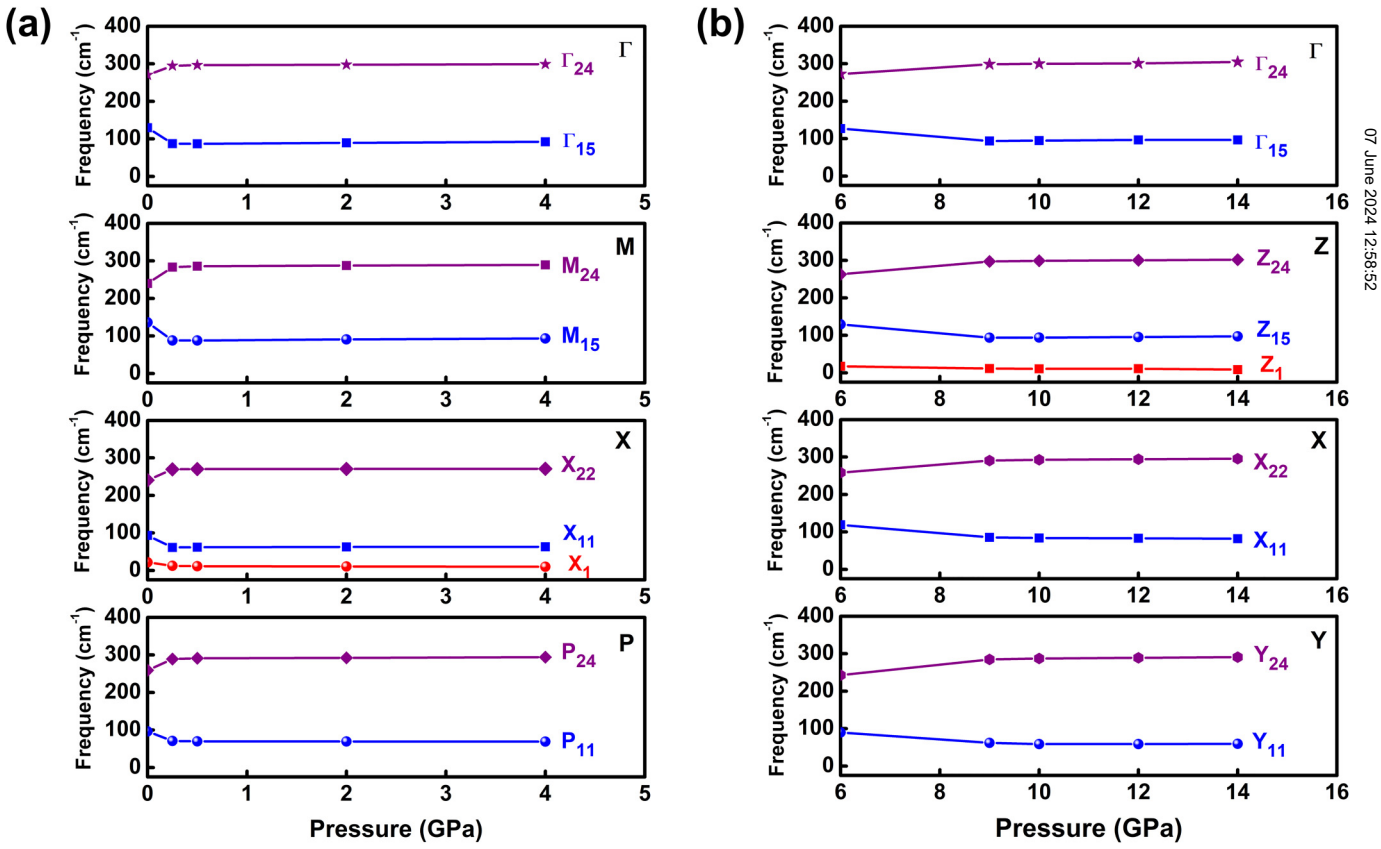

FIG. 8. Pressure dependent phonon frequencies at high-symmetry q points (a) Γ, M, X, and P for the tetragonal (I4/mmm) phase and (b) Γ, Z, X, and Y for the orthorhombic (Cmcm) phase of the Hg_2Cl_2 compound.

frequency Raman active mode belonging to the A_g irreducible representation have been noted. While this mode was experimentally observed to be at ~46 cm^{-1} by Roginskii *et al.*;[43] however, Kaplyanskii reported the same to be at much higher frequency of ~275 cm^{-1}.[64] Our theoretical calculations estimate the frequency of this mode to be at 272.5 cm^{-1} in close agreement with the report of Kaplyanskii. Although our estimated frequency does not match with the result of Roginskii *et al.*, yet subsequent hardening of this A_g mode (from 272.5 to 298.7 cm^{-1}) with an increase in pressure is still reflected from our first-principle calculations in harmony with that observed in the experimental observations.[43,64]

To understand the structural deformations associated with the decrement and hardening of the optical phonon frequencies of the Hg_2Cl_2 compound under external pressures leading to I4/mmm $(D_{4h}^{17}) \rightarrow$ Cmcm (D_{2h}^{17}) and Cmcm $(D_{2h}^{17}) \rightarrow$ Pnma (D_{2h}^{16}) structural phase transitions at $(P_T)_1 = 0.25$ GPa and $(P_T)_2 = 9$ GPa, respectively, the Cartesian displacements of atoms for some of the representative phonon modes are considered. They are shown in Fig. 9 and Fig. S6 in the supplementary material. From Fig. 9, it is clearly seen that the phonon modes Γ_{15} and X_{11} of the Hg_2Cl_2 compound involve displacements of the Cl atoms only along the basal ab plane, while the Hg atoms remain stationary. The phonon mode X_1 involves displacements of both Hg and Cl atoms in the ab plane. These modes of vibrations may not only result in the bending of linear Cl(L)–Hg(C)–Hg(A)–Cl(L) chain but also may promote increments in the lattice parameters "a" and "b" of the compound. Figure 9 also shows the atomic displacements of Γ_{24} and X_{22} phonon modes mostly involving stretching of the linear Cl(L)–Hg

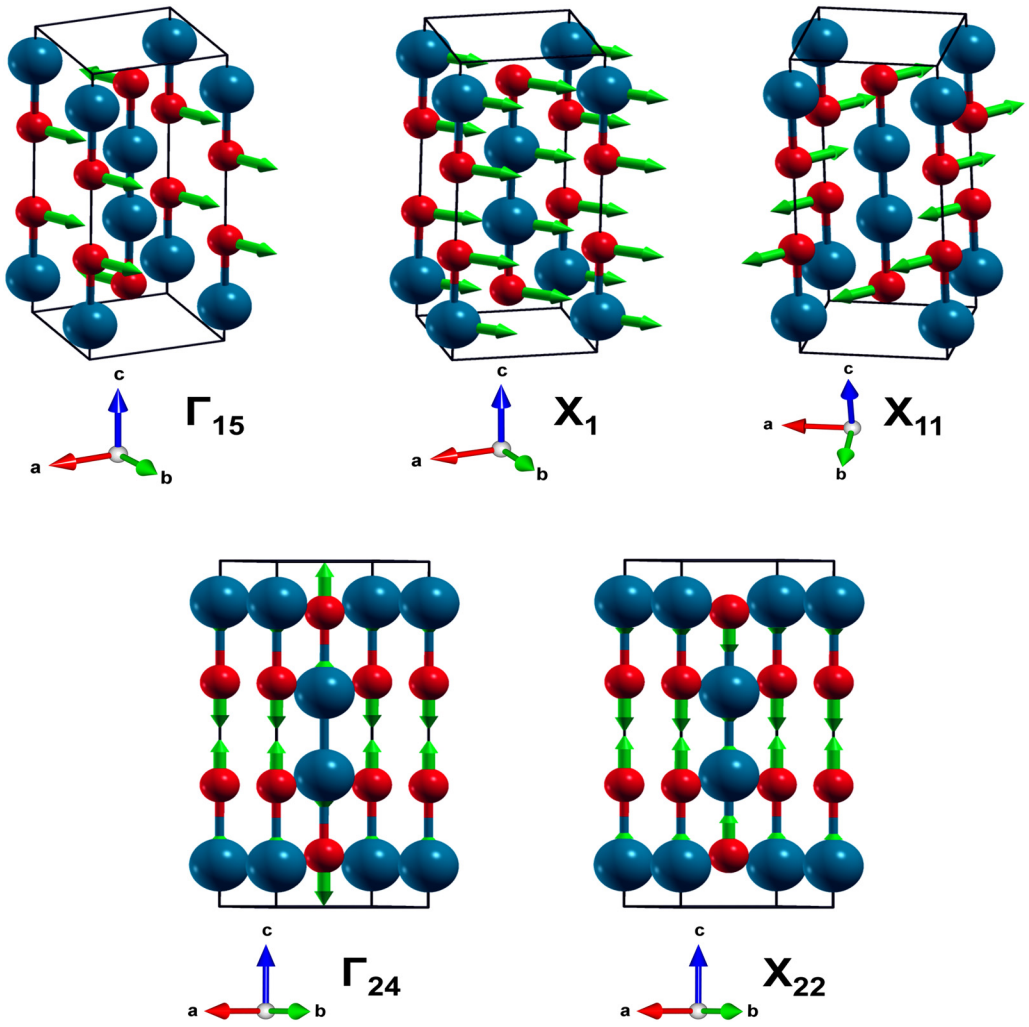

FIG. 9. Schematic representations of eigenvectors and atomic displacements for Γ_{15}, X_1, X_{11}, Γ_{24}, and X_{22} phonon modes of the tetragonal (I4/mmm) phase of Hg_2Cl_2 at 0.25 GPa. (Large Hg atoms are shown in emerald blue and small Cl atoms are shown in red. The green arrows signify the atomic displacements.)

TABLE II. Calculated non-zero components of on-site force constants for different phases of Hg_2Cl_2 compound.

	On-site force constants (N/m)					
Phases	K_{xx} (Hg)	K_{yy} (Hg)	K_{zz} (Hg)	K_{xx} (Cl)	K_{yy} (Cl)	K_{zz} (Cl)
I4/mmm (P = 0.25 GPa)	0.50	0.50	0.92	1.58	1.58	2.07
Cmcm (P = 9 GPa)	0.17	0.21	−0.07	0.17	1.07	−0.17

(C)–Hg(A)–Cl(L) chain Cl atoms in opposite directions along the crystallographic *c* axis. These results collectively signify some alterations in the lattice parameters of the Hg_2Cl_2 at P = 0.25 GPa, which in turn may result in the first phase transition of the compound from the body-centered tetragonal I4/mmm (D_{4h}^{17}) to the base-centered orthorhombic Cmcm (D_{2h}^{17}) phase.

Similar observations may be drawn from the representative Γ_{15}, Y_{11}, X_{11}, Γ_{24}, and X_{22} phonon modes linked with the orthorhombic (Cmcm) phase of Hg_2Cl_2 at 9 GPa. The Cartesian atomic displacements of the above referred modes are shown in Fig. S6 in the supplementary material. The atomic displacements of the phonon vibrational signatures, as shown in Fig. S4 in the supplementary material, in general suggest small variations in the lattice parameters of the compound that may lead to the second structural phase transition from the base-centered orthorhombic [Cmcm (D_{2h}^{17})] to the primitive orthorhombic [Pnma (D_{2h}^{16})] phase of the Hg_2Cl_2 crystal at P = 9 GPa.

D. Nature of the structural phase transitions of Hg_2Cl_2: Is it displacive or order–disorder type?

Two types of structural phase transitions, namely, displacive and order–disorder types driven by the soft phonon modes are known to exist.[65–69] For both displacive and/or order–disorder types of structural phase transitions, the high and the low symmetry phases are known to be disordered and ordered, respectively. In displacive-type phase transition, the potential energy hypersurface in the multidimensional configuration space of the collective displacements of atoms has a single global minimum at the equilibrium configuration. The atoms with varying kinetic and potential energies move to and fro about the equilibrium configuration of the potential energy hypersurface with frequencies that match with the order of the phonon frequencies. For order–disorder type phase transition, the potential energy hypersurface for the Cartesian displacements of atoms belonging to the system exhibits multiple wells of equal depths. Atoms jump over the finite barrier heights between the two adjacent local minima within much longer time intervals. To determine the nature of phase transition, on-site force constant value $K_{ij}(\mu)$ for an atom μ has been estimated from the first-principle calculations. This estimated force constant values together with their algebraic signs indicate the curvature and the nature of the potential energy surface. The negative values of $K_{ij}(\mu)$ signify the multiwell nature of the local potential energy surface, while the positive values correspond to a surface with single minimum. The positive and the negative values of the force constants thus decide the nature of the phase transition to be "displacive" or of "order–disorder" types, respectively.

The Hellmann–Feynman forces have been calculated separately from the independent displacements of Hg and Cl atoms of the Hg_2Cl_2 crystal along the *x*, *y*, and *z* directions for the tetragonal [I4/mmm (D_{4h}^{17})] and orthorhombic phases [Cmcm (D_{2h}^{17}), Pnma (D_{2h}^{16})] of the compound. To understand the nature of the pressure driven structural phase transitions, the on-site force constants K_{ij}(Hg) and K_{ij}(Cl) for the Hg_2Cl_2 system belonging to its [I4/mmm (D_{4h}^{17})] and [Cmcm (D_{2h}^{17})], [Pnma (D_{2h}^{16})] phases have been estimated from the DFPT calculations using the linear response theory. The DFPT calculations reveal force constants $K_{ij}(Hg) = K_{ij}(Cl) = 0$ for $i \neq j$, while K_{ii}(Hg) and K_{ii}(Cl) exhibit non-zero values. The non-zero values of the force constants K_{ii}(Hg) and K_{ii}(Cl) along the *xx*, *yy*, and *zz* directions are shown in Table II. Interestingly, the non-zero on-site force constants for Hg and Cl atoms are found to be positive in the first I4/mmm (D_{4h}^{17}) → Cmcm (D_{2h}^{17}) phase transition. These results signify the displacive nature of the first structural I4/mmm (D_{4h}^{17}) → Cmcm (D_{2h}^{17}) phase transition of the Hg_2Cl_2 compound at P = 0.25 GPa. Interestingly, the z-components of the non-zero value of force constant K_{zz} for Hg and Cl atoms show negative values for the second phase transition associated with Cmcm (D_{2h}^{17}) → Pnma (D_{2h}^{16}) transition at 9 GPa. This observation suggests that the second phase transition for the Hg_2Cl_2 compound at P = 9 GPa represents an order–disorder type.

IV. CONCLUSIONS

This paper reports for the first time a detailed study based on first-principle calculations that unveil the underpinning physics behind the pressure induced structural phase transitions of the Hg_2Cl_2 compound at room temperature. The phonon modes linked with the phase transitions of the compound have been critically explored for its tetragonal and orthorhombic phases from their corresponding phonon dispersion relations and PHDOS. The pressure dependence of the phonon modes at the respective high-symmetry points have also been investigated to get deeper insights on their role for the structural phase transitions of the compound. The nature of the phase transition, whether it is "displacive" or of "order–disorder" type, has been predicted. We believe that the present study based on DFT and BOMD calculations will unveil the underlying physics behind the phase transitions and the anisotropic behavior of the compound, which in turn bears technologically significant relevance for its applications in optoelectronic devices, acousto-optic tunable filters, polarized lasers, and in fiber-optic communication systems. The first-principle calculations to explore the temperature dependent phase transition of Hg_2Cl_2 are under way and will be focused in a separate publication.

SUPPLEMENTARY MATERIAL

The supplementary material includes the Hellman–Feynman force and total self-consistent field energy for the body-centered tetragonal (I4/mmm) phase of Hg_2Cl_2 compound as a function of plane wave kinetic energy cutoff as estimated from the static DFT calculations (Fig. S1), total energy and volume for the body-centered tetragonal (I4/mmm) phase of Hg_2Cl_2 compound as a function of N-atom cell (Fig. S2), the temporal variation of total energy of **the** Cmcm (D_{2h}^{17}) and Pnma (D_{2h}^{16}) phases of the Hg_2Cl_2 compound (Fig. S3), total energy vs volume curves for the Cmcm (D_{2h}^{17}) and Pnma (D_{2h}^{16}) phases of Hg_2Cl_2 as obtained from BOMD calculations (Fig. S4), total energy and volume for the base-centered (Cmcm) and primitive (Pnma) orthorhombic phases of Hg_2Cl_2 as a function of N-atom cell (Fig. S5), and the schematic diagrams of eigenvectors and atomic displacements for Γ_{15}, Γ_{24}, Y_{11}, X_{11}, and X_{22} phonon modes of the orthorhombic (Cmcm) phase of Hg_2Cl_2 at P = 9 GPa (Fig. S6).

ACKNOWLEDGMENTS

The authors acknowledge the Department of Physics, Jadavpur University, for availing the computational facility through the DST-FIST programme. S.G. sincerely acknowledges the University Grant Commission, Government of India, for providing the UGC-NET-JRF award in the form of a fellowship. The authors also thank Dr. Suman Chowdhury of the Indian Institute of Science, Bangalore, for his valuable suggestions regarding this work.

AUTHOR DECLARATIONS

Conflict of Interest

The authors have no conflicts to disclose.

DATA AVAILABILITY

The data that support the findings of this study are available in the supplementary material.

REFERENCES

[1]E. M. Landau and L. D. Lifshitz, *Statistical Physics* (Pergamon Press, Oxford, 1958).
[2]R. E. Kirby, E. Kisker, F. K. King, and E. L. Garwin, Solid State Commun. **56**, 425 (1985).
[3]D. Küpper, S. Easton, and J. A. C. Bland, J. Appl. Phys. **102**, 083902 (2007).
[4]V. Usov, S. Murphy, and I. V. Shvets, J. Magn. Magn. Mater. **290–291**, 764 (2005).
[5]B. Binaei Ghotbabadi, A. Sheykhi, and G. H. Bordbar, Phys. Lett. B **797**, 134896 (2019).
[6]A. K. Pramanik and A. Banerjee, Phys. Rev. B **79**, 214426 (2009).
[7]S. W. Biernacki, Phys. Rev. B **68**, 174417 (2003).
[8]Z.-Y. Song, L. Shang, Z. Hu, J. Chu, P.-P. Chen, A. Yamamoto, and T.-T. Kang, Sci. Rep. **9**, 12309 (2019).
[9]Z. Devizorova, A. V. Putilov, I. Chaykin, S. Mironov, and A. I. Buzdin, Phys. Rev. B **103**, 064504 (2021).
[10]X. Li, D. Chen, M. Jin, D. Ma, Y. Ge, J. Sun, W. Guo, H. Sun, J. Han, W. Xiao, J. Duan, Q. Wang, C.-C. Liu, R. Zou, J. Cheng, C. Jin, J. Zhou, J. B. Goodenough, J. Zhu, and Y. Yao, Proc. Natl. Acad. Sci. U.S.A. **116**, 17696 (2019).
[11]M. Marik, D. Jana, K. C. Majumder, and B. K. Chaudhuri, Mol. Cryst. Liq. Cryst. **606**, 111 (2015).
[12]J. F. Allen and A. D. Misener, Nature **141**, 75 (1938).
[13]J. F. Allen and A. D. Misener, Nature **142**, 643 (1938).
[14]J. K. Hoffer, W. R. Gardner, C. G. Waterfield, and N. E. Phillips, J. Low Temp. Phys. **23**, 63 (1976).
[15]A. Madsen, J. Als-Nielsen, J. Hallmann, T. Roth, and W. Lu, Phys. Rev. B **94**, 014111 (2016).
[16]J. C. Dyre, Rev. Mod. Phys. **78**, 953 (2006).
[17]V. F. Gantmakher and V. T. Dolgopolov, Phys. Usp. **53**, 1 (2010).
[18]E. S. Parrott, R. L. Milot, T. Stergiopoulos, H. J. Snaith, M. B. Johnston, and L. M. Herz, J. Phys. Chem. Lett. **7**, 1321 (2016).
[19]X. Z. Yan, Y. M. Chen, X. Y. Kuang, and S. K. Xiang, J. Appl. Phys. **116**, 083707 (2014).
[20]U. D. Wdowik, K. Parlinski, S. Rols, and T. Chatterji, Phys. Rev. B **89**, 224306 (2014).
[21]D. V. S. Muthu, P. Teredesai, S. Saha, U. V. Waghmare, A. K. Sood, and C. N. R. Rao, Phys. Rev. B **91**, 224308 (2015).
[22]K. A. Irshad, P. Anees, S. Sahoo, N. R. Sanjay Kumar, V. Srihari, S. Kalavathi, and N. V. Chandra Shekar, J. Appl. Phys. **124**, 155901 (2018).
[23]X. Yang, Q. Li, R. Liu, B. Liu, H. Zhang, S. Jiang, J. Liu, B. Zou, T. Cui, and B. Liu, J. Appl. Phys. **115**, 124907 (2014).
[24]V. Sivasubramanian, T. R. Ravindran, R. Nithya, and A. K. Arora, J. Appl. Phys. **96**, 387 (2004).
[25]M. Kurban, C. Kürkçü, Ç. Yamçıçıer, and F. Göktaş, J. Phys.: Condens. Matter **31**, 305401 (2019).
[26]B. D. Sahoo, K. D. Joshi, and T. C. Kaushik, J. Appl. Phys. **128**, 035902 (2020).
[27]Y.-K. Wei, N.-N. Ge, X.-R. Chen, G.-F. Ji, L.-C. Cai, and Z.-W. Gu, J. Appl. Phys. **115**, 124904 (2014).
[28]S. N. Guin, D. Sanyal, and K. Biswas, Chem. Sci. **7**, 534 (2016).
[29]S. N. Guin, S. Banerjee, D. Sanyal, S. K. Pati, and K. Biswas, Chem. Mater. **29**, 3769 (2017).
[30]V. V. Sobolev, V. V. Sobolev, and D. V. Anisimov, Semiconductors **50**, 29 (2016).
[31]M. Crippa, S. Legnaioli, C. Kimbriel, and P. Ricciardi, J Raman Spectrosc. **52**, 15 (2021).
[32]W. W. Ewing, J. Am. Chem. Soc. **47**, 301 (1925).
[33]T. Henningsen and N. B. Singh, J. Cryst. Growth **96**, 114 (1989).
[34]A. Pierson and C. Philippe, Proc. SPIE **11180**, 1118064 (2019).
[35]Č. Barta, A. A. Kaplyanskiĭ, V. V. Kulakov, and Y. F. Markov, J. Exp. Theor. Phys. **21**, 54 (1975).
[36]G. J. Rosasco, H. S. Parker, R. S. Roth, R. A. Forman, and W. S. Brower, J. Phys. C: Solid State Phys. **11**, 35 (1978).
[37]J. P. Benoit, C. X. An, Y. Luspin, J. P. Chappelle, and J. Lefebvre, J. Phys. C: Solid State Phys. **11**, L721 (1978).
[38]G. F. Dobrzhanskii, A. A. Kaplyanskii, M. F. Limonov, and Y. U. F. Markov, Ferroelectrics **48**, 69 (1983).
[39]M. E. Boiko, M. D. Sharkov, A. M. Boiko, and S. G. Konnikov, Crystallogr. Rep. **63**, 196 (2018).
[40]W. Dultz and E. Rehaber, J. Phys. C: Solid State Phys. **12**, L137 (1979).
[41]M. Midorikawa, Y. Ishibashi, S. Nakashima, and A. Mitsuishi, J. Phys. Soc. Jpn. **49**, 554 (1980).
[42]A. A. Kvasov, Y. F. Markov, E. M. Roginskii, and M. B. Smirnov, Ferroelectrics **397**, 81 (2010).
[43]E. M. Roginskii, A. S. Krylov, Y. F. Markov, and M. B. Smirnov, Bull. Russ. Acad. Sci. Phys. **80**, 1033 (2016).
[44]R. J. Havighurst, J. Am. Chem. Soc. **48**, 2113 (1926).
[45]J. Heyd, G. E. Scuseria, and M. Ernzerhof, J. Chem. Phys. **118**, 8207 (2003).
[46]P. Giannozzi, S. Baroni, N. Bonini, M. Calandra, R. Car, C. Cavazzoni, D. Ceresoli, G. L. Chiarotti, M. Cococcioni, I. Dabo, A. Dal Corso, S. de Gironcoli, S. Fabris, G. Fratesi, R. Gebauer, U. Gerstmann, C. Gougoussis, A. Kokalj, M. Lazzeri, L. Martin-Samos, N. Marzari, F. Mauri, R. Mazzarello, S. Paolini, A. Pasquarello, L. Paulatto, C. Sbraccia, S. Scandolo, G. Sclauzero,

A. P. Seitsonen, A. Smogunov, P. Umari, and R. M. Wentzcovitch, J. Phys.: Condens. Matter **21**, 395502 (2009).
[47]P. Giannozzi, O. Andreussi, T. Brumme, O. Bunau, M. Buongiorno Nardelli, M. Calandra, R. Car, C. Cavazzoni, D. Ceresoli, M. Cococcioni, N. Colonna, I. Carnimeo, A. Dal Corso, S. de Gironcoli, P. Delugas, R. A. DiStasio, A. Ferretti, A. Floris, G. Fratesi, G. Fugallo, R. Gebauer, U. Gerstmann, F. Giustino, T. Gorni, J. Jia, M. Kawamura, H.-Y. Ko, A. Kokalj, E. Küçükbenli, M. Lazzeri, M. Marsili, N. Marzari, F. Mauri, N. L. Nguyen, H.-V. Nguyen, A. Otero-de-la-Roza, L. Paulatto, S. Poncé, D. Rocca, R. Sabatini, B. Santra, M. Schlipf, A. P. Seitsonen, A. Smogunov, I. Timrov, T. Thonhauser, P. Umari, N. Vast, X. Wu, and S. Baroni, J. Phys.: Condens. Matter **29**, 465901 (2017).
[48]P. Giannozzi, O. Baseggio, P. Bonfà, D. Brunato, R. Car, I. Carnimeo, C. Cavazzoni, S. de Gironcoli, P. Delugas, F. Ferrari Ruffino, A. Ferretti, N. Marzari, I. Timrov, A. Urru, and S. Baroni, J. Chem. Phys. **152**, 154105 (2020).
[49]A. Dal Corso, Comput. Mater. Sci. **95**, 337 (2014).
[50]H. C. Andersen, J. Chem. Phys. **72**, 2384 (1980).
[51]X. Gonze and C. Lee, Phys. Rev. B **55**, 10355 (1997).
[52]S. Baroni, S. de Gironcoli, A. Dal Corso, and P. Giannozzi, Rev. Mod. Phys. **73**, 515 (2001).
[53]Y. Wang, S.-L. Shang, H. Fang, Z.-K. Liu, and L.-Q. Chen, NPJ Comput. Mater. **2**, 16006 (2016).
[54]F. Birch, Phys. Rev. **71**, 809 (1947).
[55]F. D. Murnaghan, Proc. Natl. Acad. Sci. U.S.A. **30**, 244 (1944).
[56]G. Makov and M. C. Payne, Phys. Rev. B **51**, 4014 (1995).
[57]G. Makov, R. Shah, and M. C. Payne, Phys. Rev. B **53**, 15513 (1996).
[58]N. J. Calos and C. H. L. Kennard, Z. Kristallogr. Cryst. Mater. **187**, 305 (1989).
[59]E. Ejder, J. Phys. Chem. Solids **31**, 453 (1970).
[60]I. Pelant, M. N. Popova, J. Hála, M. AmbroŽ, V. Lhotská, and K. Vacek, Czech J. Phys. **37**, 1183 (1987).
[61]X. Yin Jiang, T. Itoh, and T. Goto, J. Phys. Soc. Jpn. **53**, 3672 (1984).
[62]E. Dorm, J. Chem. Soc. D **1971**, 466.
[63]C.-B. Zhang, W.-D. Li, P. Zhang, and B.-T. Wang, Comput. Mater. Sci. **157**, 121 (2019).
[64]A. A. Kaplyanskii, in *Theory of Light Scattering in Condensed Matter*, edited by A. V. M. Bendow B and J. L. Birman (Springer, Boston, MA, 1976).
[65]T. Schneider and E. Stoll, Phys. Rev. B **13**, 1216 (1976).
[66]K. Parlinski, Z. Q. Li, and Y. Kawazoe, Phys. Rev. B **61**, 272 (2000).
[67]K. Parlinski and Y. Kawazoe, Eur. Phys. J. B **16**, 49 (2000).
[68]K. Parlinski, Y. Kawazoe, and Y. Waseda, J. Chem. Phys. **114**, 2395 (2001).
[69]A. I. Lebedev, Phys. Solid State **51**, 362 (2009).

Materials Chemistry and Physics 276 (2022) 125379

Contents lists available at ScienceDirect

Materials Chemistry and Physics

journal homepage: www.elsevier.com/locate/matchemphys

Structural and electronic properties of wide band gap charge transfer insulator Hg_2Cl_2: Insights from the first-principle calculations

Swarup Ghosh [a], Sougata Sarkar [b], Joydeep Chowdhury [a,*]

[a] Department of Physics, Jadavpur University, 188, Raja S.C. Mallick Road, Kolkata, 700032, India
[b] Department of Chemistry, Ramakrishna Mission Vivekananda Centenary College, Rahara, Kolkata, 700118, India

HIGHLIGHTS

- The structural and electronic properties of Hg_2Cl_2 have been investigated.
- The first-principles calculation was performed using GGA with hybrid functionals.
- The covalent and ionic interactions between Hg and Cl atoms have been studied.
- The NBO analyses have been performed to understand the CT interactions.
- The effect of Hubbard + U_{dd} and SOC have also been explored.

GRAPHICAL ABSTRACT

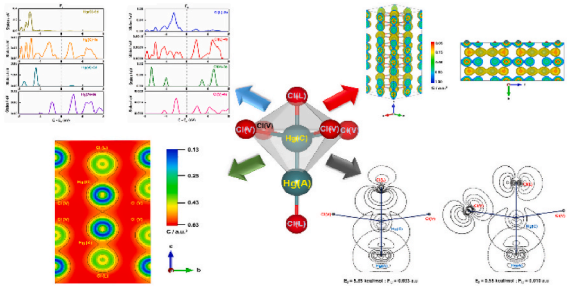

ARTICLE INFO

Keywords:
Density functional theory
Band gap
Charge transfer insulator
Covalent and ionic solid

ABSTRACT

The structural and electronic properties of Mercurous Chloride (Hg_2Cl_2) in its tetragonal (*I4/mmm*) phase at room temperature have been investigated from the first principle calculations. Detail calculations within the framework of density functional theory (DFT) upon incorporation of spin-orbit coupling (SOC) reveal that Hg_2Cl_2 is a wide band gap charge transfer (CT) insulator with band gap energy (E_g) ~ 3.96 eV. Despite being a CT insulator, the orbital resolved PDOS of Hg_2Cl_2 compound exhibit energy dispositions that do not obey the Zaanen – Sawatzky – Allen (ZSA) diagram. The effect of on-site Coulomb repulsion (Hubbard $+U_{dd}$) on the band gap of the compound has also been studied in detail. The Mulliken bond population, electronic charge density distribution and Bader charges analyses have been explored to unveil the covalent and ionic interactions between Hg and Cl atoms of the Hg_2Cl_2 compound. The Natural Bond Orbital (NBO) analyses have been performed to gain deeper insights on the CT interactions between Hg and Cl atoms of Hg_2Cl_2. The rationale behind the distortions of the octahedral domains within Hg_2Cl_2 crystal has also been elucidated in detail.

1. Introduction

One of the major challenges in the formalism of many body theory over the past two decades has been the correct interpretation of electronic properties of the transition metal oxides (TMOs) or heavy fermion systems (HFs) containing rare earth (RE) or actinide (Ac) elements [1–8]. The local density approximation (LDA) or generalized gradient approximation (GGA) within DFT formalism proved to be unexpectedly successful in predicting the electronic band structures as well as the ground state properties of some significant materials such as reduced

* Corresponding author.,
E-mail addresses: joydeep72_c@rediffmail.com, joydeep.chowdhury@jadavpuruniversity.in (J. Chowdhury).

https://doi.org/10.1016/j.matchemphys.2021.125379
Received 22 July 2021; Accepted 24 October 2021
Available online 26 October 2021

graphene oxide [9], aluminene [10], RuO_2 [11], LiX (X = F, Cl, Br and I) [12] in harmony with the experimental observations. However, for TMOs or HFs, both the formalisms struggle to reproduce any meaningful results and fail to explain the experimentally observed insulating behaviours of such materials. While both the LDA and GGA calculations suggest the metallic properties of the TMOs or HFs, in reality they turn out to be insulators [7,13–17]. The apparent disagreement between the theoretical predictions and experimental observations for these classes of materials was closely studied to understand the underlying physics behind them [6,13,14,18,19]. The root cause behind such anomaly was identified to be due to the presence of partially occupied d and f electrons in such systems of interest. In a simplified picture, the wavefunctions for the d or f orbitals of the transition metals (TMs) or RE/Ac elements are localized more closely to the nucleus in comparison to the wavefunctions associated with the s or p orbitals of similar energies [6,13,14,20,21]. Thus the relative motions of the electrons confined within these orbitals are statistically more correlated than for the electrons residing in the s or p orbitals. In defacto, both the LDA and the GGA formalisms do not explicitly take into account such electron correlation effect on such systems of interest and thus fail to establish the correct Hamiltonian that can reproduce closely with the experimental results. Thus the inclusion of on-site Coulomb repulsion ($+U_{dd}$) eventually splits the metallic bands as suggested from LDA or GGA calculations into two discrete sets of Hubbard bands [ca. Upper (UHB) and Lower Hubbard bands (LHB)] leaving behind a large band gap between them which is in close agreement with the experimental observations. Such systems are recognized as Mott – Hubbard (M − H) insulators [13,14,22–29]. However apart from M − H insulators there are other type of insulators known to be of charge transfer type [26,30–34]. The complete picture concerning the electronic properties of the compounds behaving as insulators in general can be accomplished by considering the p orbitals of the anions or the ligands surrounding the TM ions or rare earth elements. An electron from the p orbitals of the anion or the ligands can be transferred to the respective TM elements of the compound resulting in an energy cost of $\Delta_{CT,}$ known as CT energy. Interestingly, the characterization of the TM compounds exhibiting insulating behaviour can be explored from the Zaanen – Sawatzky – Allen diagram as depicted in the seminal work way back in 1985 [26]. The energy dispositions of the d orbitals for the TMs and p orbitals of the surrounding anions (or ligands) as estimated from first principle calculations and/or X-ray absorption – emission spectroscopic studies (XAS and XES) decide the nature of the insulator to be of M − H or of CT type [34,35].

Keeping the above things in mind the present paper reports an in-depth study on the electronic properties of Hg_2Cl_2 at room temperature (300 K), where the compound is known to exist in the tetragonal phase. Hg_2Cl_2, commonly referred to calomel, is an insulator and find extensive applications as white pigment and electrodes in electrochemistry [36,37]. Moreover the mercury (I) halide compounds are known to exhibit unique anisotropic behaviour with strong birefringence, effective for making polarizing prisms [38–40]. Of late these compounds show early promises to be used as acousto-optic tunable filters for the development of hyperspectral imagers covering the UV–Vis-LWIR region [41]. Recently temperature dependent X-Ray diffraction (XRD) studies of the tetragonal phase of Hg_2Cl_2 reveal negative thermal expansion coefficient of the compound over wide temperature domain ranging from 30° - 250 °C [42]. In fact the tetragonal phase of Hg_2Cl_2 at room temperature happens to be one of the most useful compounds that finds extensive applications as calomel electrodes, piezoelectric and birefringent materials and in acousto – optic tunable filters. This paper may thus be considered as the first comprehensive report where the band gap of Hg_2Cl_2 in its tetragonal phase has been suggested from the first principle calculations. The effects of $+U_{dd}$ and the spin – orbit coupling on the band gap of the compound have also been reported. Moreover, the nature of this insulator, whether it is M − H or of CT type in conjunction with covalent and/or ionic character is also explored in detail.

2. Computational details

The first principle calculations have been performed using generalized gradient approximations within the DFT frameworks implemented in Quantum ESPRESSO (QE) software [43–45]. Electron-ion interactions have been incorporated through the pseudopotentials using Projector Augmented Wave (PAW) method [46]. The GGA calculations within DFT framework have been performed in conjunction with non – hybrid PBE [47], PBEsol [48], BLYP [49] and hybrid B3LYP [50] and HSE [51] exchange-correlation (XC) functionals. Rationale behind the specific uses of hybrid functionals B3LYP and HSE in the first principle calculations is owed to the fact that both these functionals in conjunction with GGA can reproduce the experimentally determined band gaps of different materials with profound accuracies [52–57]. The convergence criterion of total electronic energy has been set to 10^{-8} a.u. with the threshold of maximum Hellman-Feynman force of 10^{-3} a.u. The maximum cell pressure and temperature have been fixed to 10^{-3} GPa and 300 K respectively throughout the optimization steps of the calculation. The plane wave kinetic energy (KE) cut-off for the first principle calculations was set at 50 Ry. The specific KE cut-off for the system under study has been estimated from total self-consistent field (SCF) energy versus kinetic energy cut-off plot for the associated charge density of ~ 400 Ry. A specific grid of 9 × 9 × 9 gamma-centred **k**-point mesh with Monkhorst-pack was set initially from the total SCF energy versus **k**-point mesh plots for optimization and SCF energy calculations. Later a dense **k** – point grid of 19 × 19 × 19 has been taken for further refined non-self-consistent field (nSCF) calculations involving density of states (DOS) and band structures of the compound.

Phonon dispersion spectrum and phonon density of states (PhDOS) have been estimated within harmonic approximation using the linear-response method through density functional perturbation theory (DFPT) [58,59]. The phonon data have been estimated through the diagonalization and sampling of dynamical matrix **D(k)** for any arbitrary wave vector **k**. To explore the effect of $+U_{dd}$ correction on the band gap of the Hg_2Cl_2 compound, the GGA + U calculations have been performed [22,26,28]. The rotationally invariant formalism of $+U_{dd}$ correction introduced by Dudarev *et al.* was used to implement the Coulomb repulsion term $+U_{dd}$ [60] for 5d orbital of Hg atom. To investigate the relativistic effects of the heavy Hg element on the band gap of the compound, the spin-orbit interaction [61] and non-collinear magnetism [62] has been taken into account in the above referred relativistic PAW pseudopotential.

The Bader charge analyses have been performed to estimate the differential charge distribution and the electron charge density localized in the valence band of the compound using BADER CHARGE ANALYSIS code developed by Henkelman Group [63–65]. The natural bond orbital analyses have been performed from the DFT calculation at HSEH1PBE/SDD level of theory using Gaussian 09 [66] and with GENNBO 5.0W suit of software. The 2D orbital contour diagrams are obtained from NBOView 6.0 [67] embedded in the GENNBO 5.0W suite of the software.

3. Results and discussions

3.1. Structure of Hg_2Cl_2 compound

Mercurous Chloride at room temperature crystallizes in the tetragonal phase and falls under *I4/mmm* (space group no. 139) space group symmetry. The crystal structure and the associated lattice parameters of Hg_2Cl_2 compound in the tetragonal phase are reported from the experimentally determined X-Ray [68] and neutron diffraction [69] data. The unit cell of Hg_2Cl_2 comprises of one formula unit (Z = 2) with 8 atoms, where Hg and Cl are at 4e (0, 0, 0.11577) and 4e (0, 0, 0.3380) Wyckoff sites. Starting from the experimentally determined lattice parameters a = b and c (a = b = 4.4795 Å, c = 10.9054 Å), the unit cell associated with the tetragonal (*I4/mmm*) phase of Hg_2Cl_2 has been optimized from

GGA calculations using PBE, PBEsol, BLYP, B3LYP and HSE exchange correlation functionals. Prior to optimizations, the plane wave kinetic energy cut-off for the valence electrons and the size of the **k** – point grid has been fixed. While the KE cut-off for the valence electrons of Hg_2Cl_2 compound has been estimated from the total SCF energy versus KE cut-off plots for different GGA-XC functionals; the mesh density of the grid has been accomplished from the variations of total energy as a function of **k** points for a fixed KE cut-off. The changes in the total SCF energies of Hg_2Cl_2 compound with plane wave KE cut-off plots and k-points are shown in Fig. 1 (a) and Fig. 1 (b) respectively. It is clearly seen from Fig. 1 (a) that the KE cut-off ~ 50 Ry is sufficient to carry out further calculations to estimate the size of the **k** – point grid. For a fixed energy cut-off at 50 Ry, Fig. 1 (b) shows successful convergences of total energies for the **k** – point mesh $\geq 5 \times 5 \times 5$. These results collectively suggest that the **k**-point mesh of $9 \times 9 \times 9$ and 50 Ry KE cut-off are sufficient to carry out the first principle calculations for predicting the optimized structure and the electronic properties of the Hg_2Cl_2 compound. However for nSCF calculations involving DOS and band structures of Hg_2Cl_2 more denser **k** – point grid $19 \times 19 \times 19$ have been considered.

The total SCF energies (E) for the unit cell of Hg_2Cl_2 as a function of unit cell volumes (V) have been estimated from the GGA – XC (XC = PBE, PBEsol, BLYP, B3LYP and HSE) calculations for the KE cut-off of the plane wave fixed at 50 Ry and mesh sizes each comprising of 9× 9× 9 **k**-points. The E versus V plots for different levels of theory are shown Fig. 2 (a, b). All the plots, so generated from the first principle calculations, are fitted using Birch-Murnaghan equation of state [70,71]. From Fig. 2 (b), it is clearly seen that the unit cell of Hg_2Cl_2 exhibits lowest SCF energy for the GGA - HSE calculations. The unit cell volume ~ 219.164 $Å^3$ corresponding to the minimum SCF energy ~ – 891.260 Ry closely matches with the experimental observations as reported from the neutron diffraction studies (~ 219 $Å^3$).

The optimized lattice parameters, the optimized volumes of the unit cell and their respective SCF energies, as obtained from different levels of theory, are shown in Table S1 (supplementary material). Table 1 further shows the optimized lattice and structural parameters of Hg_2Cl_2 compound as enumerated from GGA-HSE level of theory for direct comparison with the available experimental results. From Table 1, it is clearly seen that estimated parameters from GGA-HSE calculations are in excellent agreement with the experimental results in general and with the observations as reported by Dorm *et al.* [72].

The optimized geometrical structure of Hg_2Cl_2, as obtained from GGA-HSE level of theory is shown in Fig. 3. The crystal structure marks the presence of apparently distorted octahedral environments with corner sharing Hg(Cent) atoms. The magnified view of the quasi octahedral environment is shown in Fig. 3 (c). From Fig. 3 (c), it is clearly seen that the neighbouring chlorine [Cl(V)] and apical mercury [Hg (Ap)] atoms at the vertices form the distorted octahedron Hg(Cent)Hg (Ap)$[Cl(V)]_5$ with Hg(Cent) at its centre. Several distorted octahedra are dispensed in three dimensional space over the crystal lattice whose depiction is shown in Fig. 3 (a). Each of the apparently distorted corner sharing octahedron will now be designated as Hg(C)Hg(A)$[Cl(V)]_5$ henceforth just for the sake of simpler nomenclature. The distortion in the octahedron is manifested by the decrease in Cl(V)–Hg(C)–Cl(V) angle ~ 161.92^0 along the a-b plane [Fig. 3 (c)]. Interestingly, the Hg (C)–Cl(V) bond lengths for each of the Cl(V) pairs are equal and is ~ 3.21 Å. However, one of the neighbouring Cl(V) atom form a Cl(V)–Hg (C)–Hg(A) linear chain with the associated angles ~ 180^0. To isolate the chlorine atom [Cl(V)] involved in the linear chain from the rest, we designate it as Cl(L). The linear Cl(L)–Hg(C)–Hg(A)–Cl(L) chain of Hg_2Cl_2 in tetragonal (*I4/mmm*) phase is considered to be responsible for large anisotropy, birefringence and low transverse acoustic wave velocity of the compound [38–41,74]. In this new nomenclature, the associated octahedron in the crystal lattice of the Hg_2Cl_2 compound will be designated as Hg(C)Hg(A)$[Cl(V)]_4Cl(L)$ hereafter.

The Cl(L)–Hg(C), Hg(C)–Hg(A) bond lengths are not equal and estimated to be 2.424 Å, 2.526 Å respectively. The deviation in bond length of ~ 0.102 Å primarily signifies that Hg(C) is off-centered and

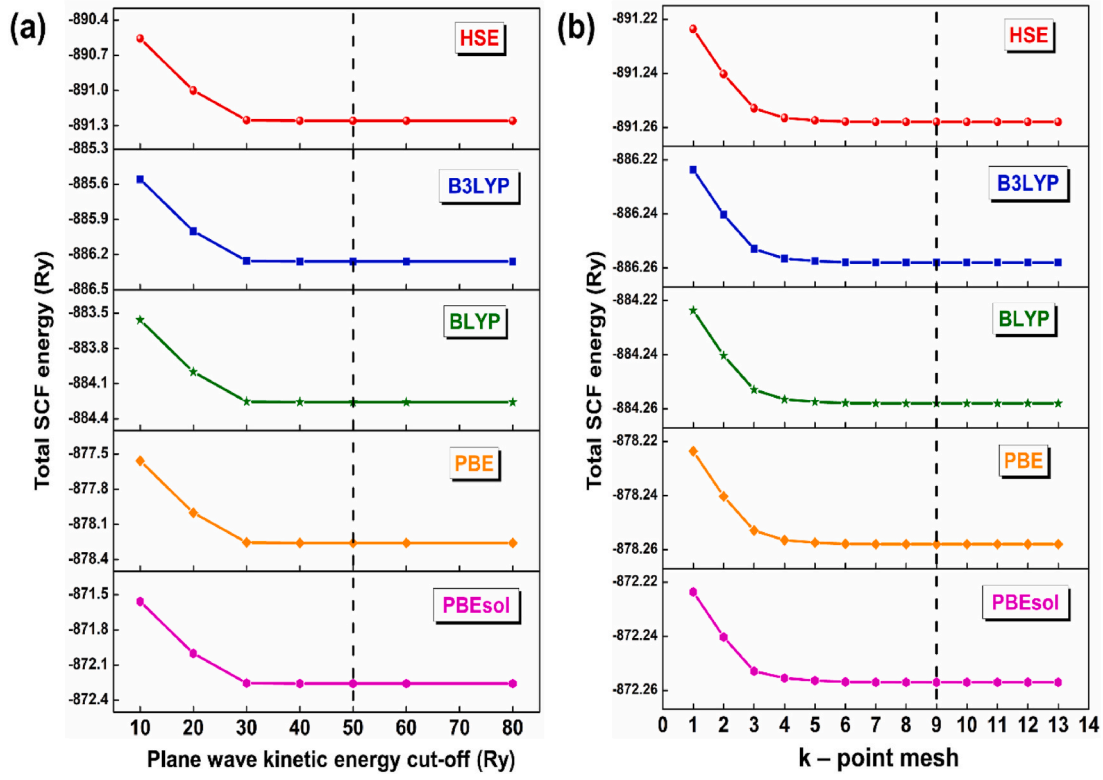

Fig. 1. Total SCF energy versus **(a)** plane wave kinetic energy cut-off and **(b)** **k** – point mesh plots for HSE, B3LYP, BLYP, PBE and PBEsol functionals within GGA method. The KE cut-off of 50 Ry and **k**-point mesh of $9 \times 9 \times 9$ are marked with black dashed vertical lines (-----).

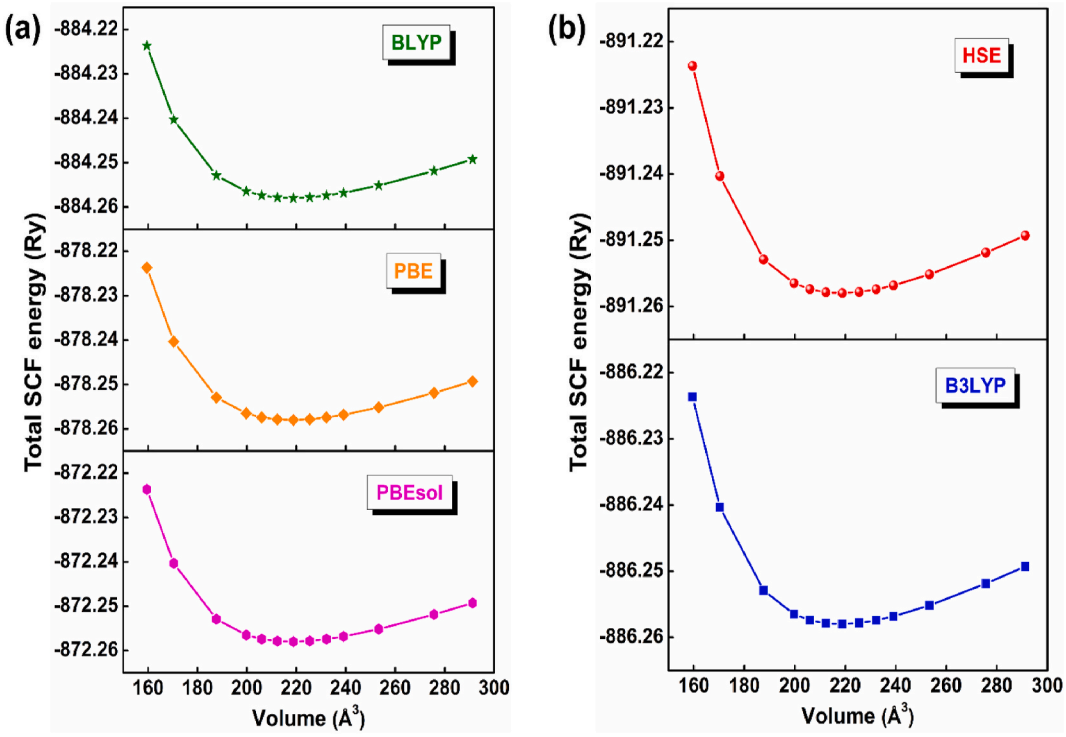

Fig. 2. The total SCF energy versus volume plots for the GGA calculations using **(a)** BLYP, PBE, PBEsol, **(b)** HSE and B3LYP functionals.

Table 1
Optimized lattice and structural parameters for the tetragonal (*I4/mmm*) phase of Hg_2Cl_2 compound.

Measured parameters	Havighurst (1926) [68]	Dorm *et al.* (1971) [72]	Kleier*et al.* (1980) [73]	Pelant*et al.* (1987) [40]	Nicholas *et al.* (1989) [69]	This Study
Lattice parameters (Å)						
a = b	4.470	4.482	–	4.478	4.479	4.482
c	10.890	10.910	–	10.910	10.905	10.910
Statistical average of bond lengths (Å)						
Hg(C)–Cl(L)	–	2.430	2.430	2.420	2.362	2.424
Hg(A)–Hg(C)	–	2.526	2.600	2.530	2.595	2.526
Hg(C)–Cl(V)	–	3.209	3.210	3.210	3.206	3.210
Statistical average of bond angles (degree)						
Hg(A)–Hg(C)–Cl(L)	–	180	180	180	180	180
Cl(V)–Hg(C)–Cl(V)	–	–	–	–	–	161.92
Hg(A)–Hg(C)–Cl(V)	–	–	–	–	–	99.04
Statistical average of dihedral angle (degree)						
Cl(L)–Hg(C)–Hg(A)–Cl(L)	180	180	180	180	180	180

shifted more towards the vertex, albeit lying undeviated on the local c - axis. Closer inspection of the supercell unveils another interesting feature concerning dispositions of the octahedral domains. The repetitive octahedra are connected through Cl(L)–Hg(C)–Hg(A)–Cl(L) linear chain with the corresponding dihedral angle ~ 180^0 (Fig. 3 (a)).

3.2. *Phonon dispersion and total phonon density of states of Hg_2Cl_2 in the tetragonal phase*

To ensure the dynamical stability of Hg_2Cl_2 compound, the phonon dispersion curve along the Γ→M→X→Γ→P high symmetry points has been estimated from GGA calculations in conjunction with HSE functional. The dispersion curve together with phonon density of states are shown in Fig. 4. From the dispersion plot, it is seen that all the twenty four phonon modes at any q points on the dispersion spectra (Fig. 4) show positive values thereby affirming the dynamical stability of the system. The phonon frequencies of the Hg_2Cl_2 crystal system spans a narrow wave number window ranging from 0 to 300 cm^{-1}. While the optical phonon modes at relatively higher frequencies ~85 – 300 cm^{-1} are emanated from Cl atoms, while those at ~85 – 150 cm^{-1} frequency window, both Cl and Hg atoms are seen to contribute. At comparatively lower frequency window (55 – 65 cm^{-1}), the optical phonons explicitly originate from the Hg atoms. The wide dispersions of optical phonon modes in three distinctively different wavenumber windows are owed to different atomic masses of the constituent Hg and Cl atoms of the Hg_2Cl_2 system. The acoustic phonon modes are also observed at lowest frequency window spanning in the range 0 – 45 cm^{-1}. The cross over regions between the optical and acoustical phonon vibrational modes is observed in the frequency range 35 – 45 cm^{-1}. Moreover this mixing of low - frequency optical phonons with transverse acoustic and longitudinal acoustic modes may suggest good thermal conductivity [75] in Hg_2Cl_2 compound.

Since Hg_2Cl_2 is an ionic solid the phonon dispersion calculations have been performed by considering the coupling between the macroscopic electric field and the atomic displacements. These calculations help to identify the Longitudinal Optical - Transverse Optical (LO - TO) splitting, resulting from loss of degeneracies of the optical phonon vibrations. The LO - TO splitting are observed near the Γ point at 84 cm^{-1}

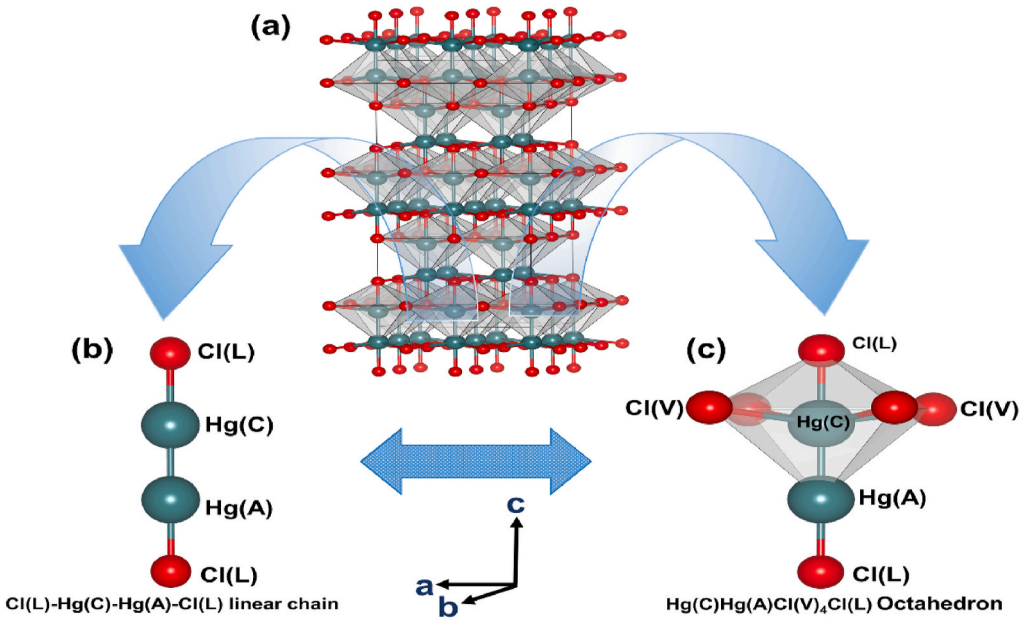

Fig. 3. (a) Supercell (2 x 2 x 2) of the tetragonal phase (*I4/mmm*) of Hg_2Cl_2compound. The magnified view of the supercell showing (b) linear chain comprising of Cl (L)–Hg(C)–Hg(A)–Cl(L) atoms **(c)** the octahedral environment. (Cl atoms are shown in red and the Hg atoms are shown in emerald blue). (For interpretation of the references to colour in this figure legend, the reader is referred to the Web version of this article.)

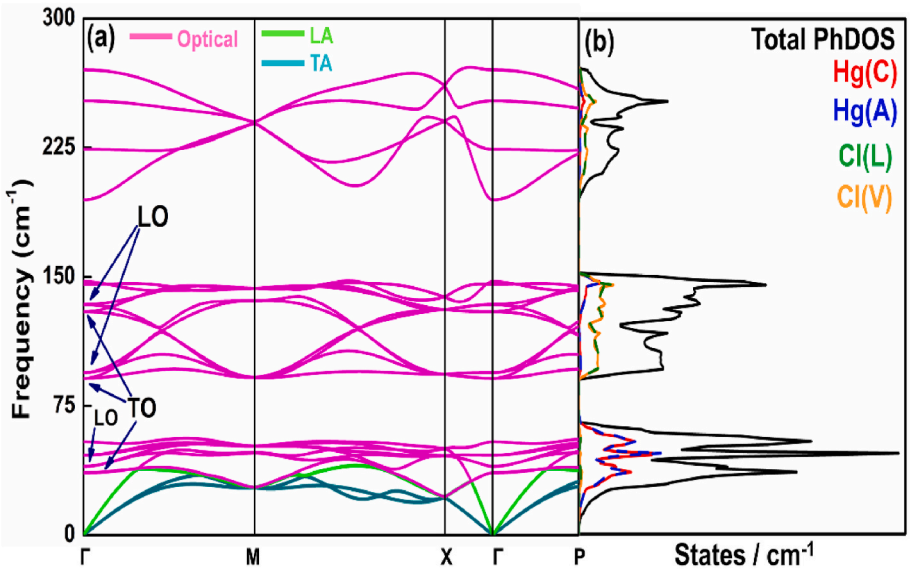

Fig. 4. (a) Phonon dispersion curve along the high-symmetry points Γ→M→X→Γ→P and **(b)** the total and partial PhDOS of the tetragonal phase of Hg_2Cl_2 compound calculated at ambient pressure in GGA – HSE level of theory. (Magenta colour traces indicate optical phonon modes, while those with cyan and light green colours illustrate transverse and longitudinal acoustic phonon modes respectively in the phonon dispersion curve. (Distinct LO – TO splittings are marked in the figure.). (For interpretation of the references to colour in this figure legend, the reader is referred to the Web version of this article.)

and 135 cm^{-1} in the phonon dispersion spectrum. The LO modes are estimated to have greater frequencies than the TO modes ($\omega_{LO} > \omega_{TO}$). The rationale behind it is due to the fact that the local field around the neighbouring atoms induce polarization in opposite direction for the LO modes, while the polarization is induced in the same direction for the TO modes. The Longitudinal Acoustic - Transverse Acoustic (LA – TA) splitting is also observed in the lowest phonon branches at ~ 14.723 cm^{-1} near the Brillouin zone boundary. The various LO - TO and LA - TA splitting of the phonon modes are marked in Fig. 4 (a).

3.3. Electronic properties of Hg_2Cl_2 compound in the tetragonal phase

The Hg^+ ion of the successive distorted octahedra prevalent in the supercell of Hg_2Cl_2 and the surrounding Cl^- ligands have electronic configurations of $[Xe]4f^{14}5d^{10}6s^1$ and $[Ne]3s^23p^6$ respectively. The probable band gap energy of the tetragonal (*I4/mmm*) phase of Hg_2Cl_2 at room temperature and ambient pressure has been estimated from the first principle study for GGA calculations with varied levels of theory using different exchange correlation functionals. The estimated values

Table 2
The estimated values of band gap of Hg_2Cl_2 in the tetragonal phase as obtained from GGA calculations in conjunction with different exchange functionals.

GGA with exchange functionals	Band Gap (eV)
HSE	3.93
B3LYP	3.78
BLYP	3.43
PBE	2.80
PBEsol	2.79

of E_g are shown in Table 2. From Table 2, it is clearly seen that the E_g values, as estimated from the first principle study with HSE, B3LYP and BLYP exchange functionals, predict a larger band gap (3.43eV - 3.93 eV), while for the functionals PBE and PBEsol the calculated E_g values are grossly underestimated. It is reported that GGA calculations with hybrid HSE functional has the capability to reproduce the experimental band gaps quite satisfactorily [54,76–78]. Thus we primarily believe that the predicted E_g value of the Hg_2Cl_2 compound at room temperature in its tetragonal (*I4/mmm*) phase to be ~ 3.93 eV, whose optical band gap at room temperature in this phase is experimentally reported to be ~ 4.0 eV [79].

Fig. 5 shows the E − **k** diagram of the tetragonal phase of Hg_2Cl_2 at room temperature and ambient pressure along the high symmetry points Γ→M→X→Γ→P in the reciprocal **k** space, as estimated from GGA – HSE calculations. Direct band gap ~ 3.93 eV is observed at the high symmetry point M. No trace of dispersive energy states are noted near the Fermi level (E_F) in the E-**k** diagram. These results signify that the tetragonal (*I4/mmm*) phase of Hg_2Cl_2 compound represent a wide band gap insulator.

Interestingly, Hg is a post transition metal whose "d" orbitals are completely filled. We are interested to see the effect of on-site Coulomb repulsion on the estimated E_g value of Hg_2Cl_2 compound. The strength of Hubbard "$+U_{dd}$" interaction has been varied over a wide range from 4 to 12 eV. Fig. S1 (supplementary material) shows the variation of E_g for different values of $+U_{dd}$ as obtained from the GGA calculations with hybrid HSE and non-hybrid BLYP functionals. No change in E_g value of Hg_2Cl_2 has been observed upon the inclusion of $+U_{dd}$ term for the GGA calculations with both the functionals HSE and BLYP. These observations indicate that the incorporation of the Hubbard $+U_{dd}$ term has no effect on the estimated band gap value of Hg_2Cl_2. The apparent inertness on the variation of band gap of Hg_2Cl_2 upon inclusion of the Hubbard $+U_{dd}$ parameter may be rationalised. The Hg atoms of Hg_2Cl_2 have completely filled $5d^{10}$ orbitals. This precludes the electrons to hop from any degenerate "d" orbitals to the other upon excitation, resulting in no energy cost $+U_{dd}$ associated with them ($d^n d^n \nrightarrow d^{n-1} d^{n+1}$). This result suggests that Hg_2Cl_2 is although an insulator but not of strongly correlated M − H type. However in this context it may be mentioned that electrons from the occupied 6s orbital of Hg are free to hop towards the vacant 3p orbital of Cl atoms, whose possibility will be explored later.

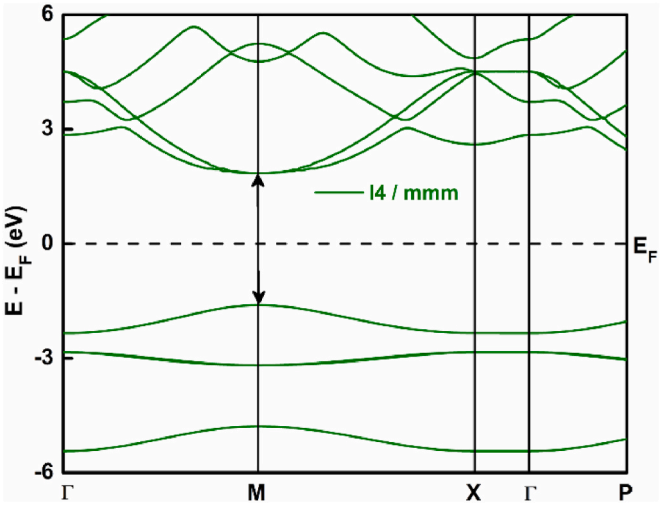

Fig. 5. Electronic band structure of the tetragonal phase of Hg_2Cl_2as calculated from GGA calculations in conjunction with HSE functional along the high-symmetry points Γ→M→X→Γ→P. The band gap and the Fermi energy (E_F) are shown in black arrow and black dashed line respectively.

3.4. Total electronic density of states (TDOS) and orbital resolved projected atomic density of states (PDOS) of Hg_2Cl_2 compound

To introspect the bonding configurations of Hg_2Cl_2 compound and to explore the possibility whether the compound falls under the class of charge transfer insulator or not, the TDOS and PDOS calculations have been performed within DFT framework for GGA – HSE level of theory. The results of the calculations are shown in Fig. 6. The TDOS calculations clearly show depletion of electronic energy states in the vicinity of the Fermi energy level, signifying the insulating behaviour of the compound. The orbital resolved PDOS for the atoms Hg(C), Hg(A) - 5d, 6s orbitals and Cl(L), Cl(V) - 3p and 4s orbitals have been estimated and are shown Fig. 6 (b) and 6 (c) respectively. The top of the valence bands of the compound, ranging between - 4 and 0 eV, are mainly dominated by Cl(L) - 3p, 4s; Cl(V) - 4s and Hg(C), Hg(A) - 6s orbitals. Partial overlap of the 6s orbitals of Hg(C) and Hg(A) may suggest weak to moderate s-s hybridization between two Hg atoms [80,81]. Significantly enough, substantial overlap between the 3p orbital of Cl(L) atom with Hg(C), Hg (A) - 6s orbitals have been noticed. These observations may signify strong covalent interactions resulting in the formation of directional σ bond between Hg(C), Hg(A) and Cl(L) atoms as a result of s-p hybridizations. The result is in accordance with the earlier report that depicted the molecular structure of Mercurous Halides [73].

Interestingly, Fig. 6 shows that the bottom of the conduction band is dominated by Hg(C), Hg(A) - 6s; Cl(L), Cl(V) – 4s orbitals with weak trace from the contributions of Cl(L) and Cl(V) - 3p orbitals. The relative weights from the contributions of Hg - 6s or Cl - 3p orbitals in the conduction band of the compound can be readily envisaged from the PDOS plots. While the 6s orbitals from both the Hg(C) and Hg(A) atoms show intense peaks around −4 to 4 eV, the peaks emanating from the 3p orbital of Cl(V) are comparatively weak and ill resolved. No prominent trace of bands originating from the 5d orbitals of either of Hg atoms is observed. These observations collectively suggest strong s-p and comparatively weak s-s hybridizations between Hg(C), Hg(A) - 6s with Cl(L) -3p and Hg(C) - 6s with Hg(A) - 6s atoms respectively. The strong s-p hybridizations may result in charge transfer (CT) interactions [82–85] between Hg(C and A) and the surrounding Cl(L) atoms forming the linear Cl(L)–Hg(C)–Hg(A)–Cl(L) chains of Hg_2Cl_2 compound. Moreover weak but definite overlap between Hg(C) - 6s and Cl(V) - 3p, 4s may also suggest remote possibility of CT interactions between Hg(C and A) and neighbouring Cl(V) atoms. In absence of on-site Coulomb repulsion $+U_{dd}$ (*vide ante*) resulting to upper and lower Hubbard bands, the transfer of electrons between Hg and Cl are associated with energy cost leading to CT interaction energy (Δ_{CT}). This in turn results in wide band gap opening and thereby identifying the compound to behave like a CT insulator. Significantly enough, the energy dispositions in the PDOS plots (Fig. 6) in case of Hg_2Cl_2 do not follow the nature of Zaanen – Sawatzky – Allen diagram [26], as frequently observed for CT insulators with p-d hybridizations. Above observations further indicate that the ZSA diagram which has been the hallmark of CT insulators for TM compounds is not necessary to be strictly obeyed in the case of CT insulators for the post transition metals like Hg. However, in this connection it may be relevant to mention that apart from being a CT insulator Hg and Cl atoms of the Hg_2Cl_2 compound can undergo long range ionic interactions between the Hg^+ cation and Cl^- anions as evinced from the LO - TO splitting of the phonon modes near the Γ point (*vide ante*).

3.5. Bond population analysis of Hg_2Cl_2 compound

To gain deeper insights concerning the covalent and/or ionic characters of bonding in Hg_2Cl_2, the Mulliken bond population analyses [86] have been carried out in terms of atomic, orbitals and effective valence charges of Hg and Cl atoms present in the compound. The results of the Mulliken bond population analysis have been illustrated in Table 3. From Table 3 it is observed that the atomic Mulliken charges for Hg(C),

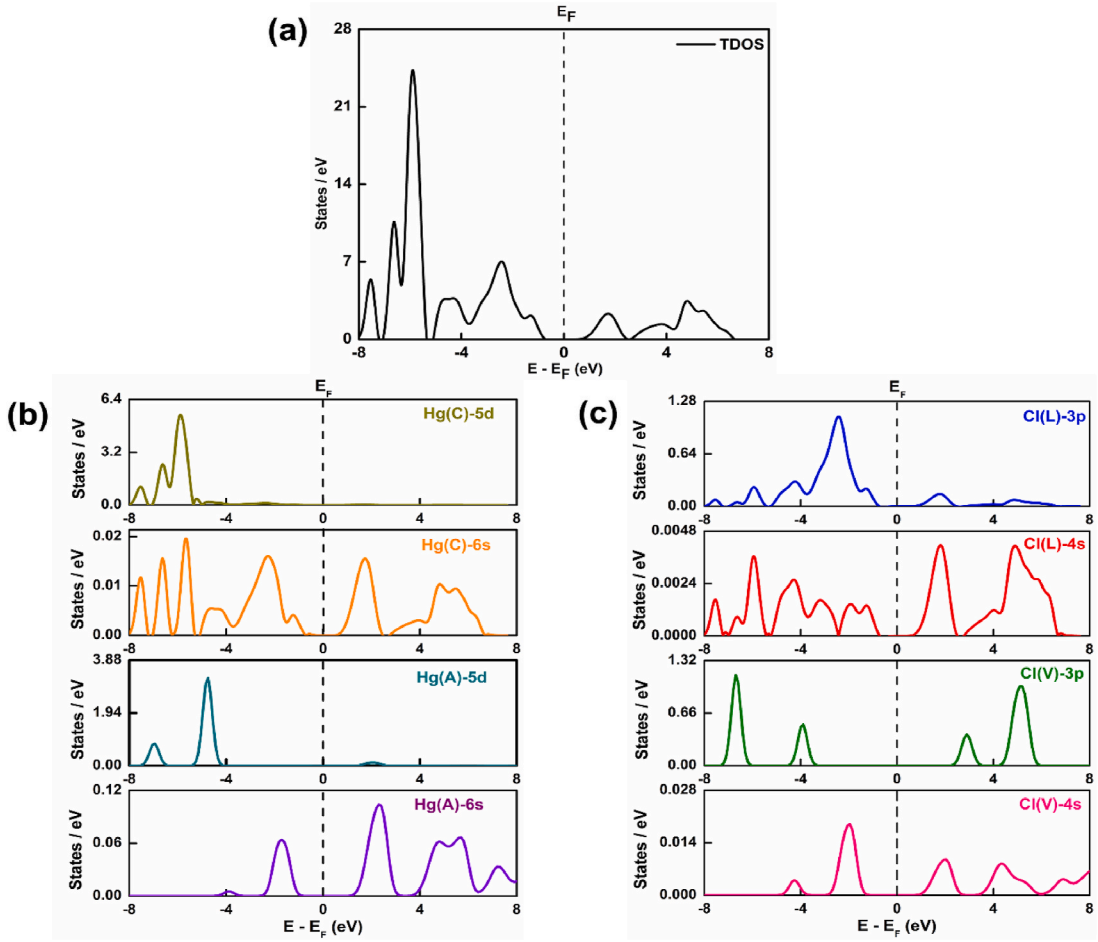

Fig. 6. **(a)** TDOS spectrum of the tetragonal phase of Hg_2Cl_2 as estimated from GGA level of theory in conjunction with HSE functional. **(b)** Orbital resolved PDOS plots of the 5d and 6s orbitals of Hg(C) and Hg(A) atoms. **(c)** PDOS spectra of the 3p and 4s orbitals of Cl(L) and Cl(V) atoms.

Table 3
Charge spilling parameter (%), individual Orbital, Mulliken and Effective Valance charges on Hg and Cl atoms in Hg_2Cl_2 compound.

Atoms	Charge spilling parameter (%)	s	p	d	Total charge	Mulliken charge	Effective Valance charge
Hg(C)	0.002	1.05	0.91	9.91	11.87	+ 0.13	+ 11.87
Hg(A)		1.01	0.91	9.93	11.85	+ 0.15	+ 11.85
Cl(L)		1.79	5.30	0.00	7.10	- 0.10	–
Cl(V)		1.99	5.19	0.00	7.18	- 0.18	–

Hg(A), Cl(L) and Cl(V) atoms are 0.13, 0.15, – 0.10 and – 0.18 respectively. In general the normal atomic charge values for pure ionic states of Hg and Cl atoms are +12 and – 7 respectively. The deviation of Mulliken charge values from pure ionic states of Hg and Cl atoms indicate the prevalence of covalent interactions between Hg and Cl atoms. The key contribution for the CT interaction between Hg(C/A) and Cl(L/V) atoms has been significantly noticed from the individual 6s and 3p orbital charges of Hg (+1.05 e, +1.01 e) and Cl (+5.30 e, + 5.19 e) atoms respectively. This implies CT interaction from 6s orbitals of Hg(C/A) to 3p orbitals of Cl(L/V) atoms. The estimated observations are in line with the PDOS as discussed earlier (*vide ante*). Moreover the effective valence charges on Hg(C)/Hg(A) atoms have been estimated to be +11.87 e/+ 11.85 e. The non – zero values of effective valence [87] signify the presence of both the covalent and ionic bonds in Hg_2Cl_2, albeit the covalent bond dominates in the compound [88].

3.6. *Electronic charge density distribution and the Bader charge analyses of Hg_2Cl_2*

To understand more closely the covalent and long range ionic interactions between Hg and Cl atoms and the CT mechanism (*vide ante*) of Hg_2Cl_2, the electron charge density in the valence band of the compound has been estimated and is shown in Fig. 7. From Fig. 7 it is clearly seen that the electronic charge density distributions around Hg(C/A) and Cl (L) atoms in the linear Cl(L)–Hg(C)–Hg(A)–Cl(L) chain of Hg_2Cl_2 compound are non – spherical, suggesting covalent interactions between them [88]. This is further substantiated by the considerable overlap of electron clouds between Hg(C), Cl(L) and Hg(A), Cl(L) atoms. All these observations are in close agreement with the orbital resolved PDOS and bond population analysis studies as discussed earlier (cf. 3.4 & 3.5).

The electron cloud density distribution as shown in Fig. 7 further unveils some interesting aspects. Depletion of electronic charge cloud density between Hg(C), Cl(V); Hg(A), Cl(V) and Hg(C), Hg(A) atoms have been noticed. While the depletion of electron cloud between the former pairs of Hg(C), Cl(V) and Hg(A), Cl(V) atoms may portend long

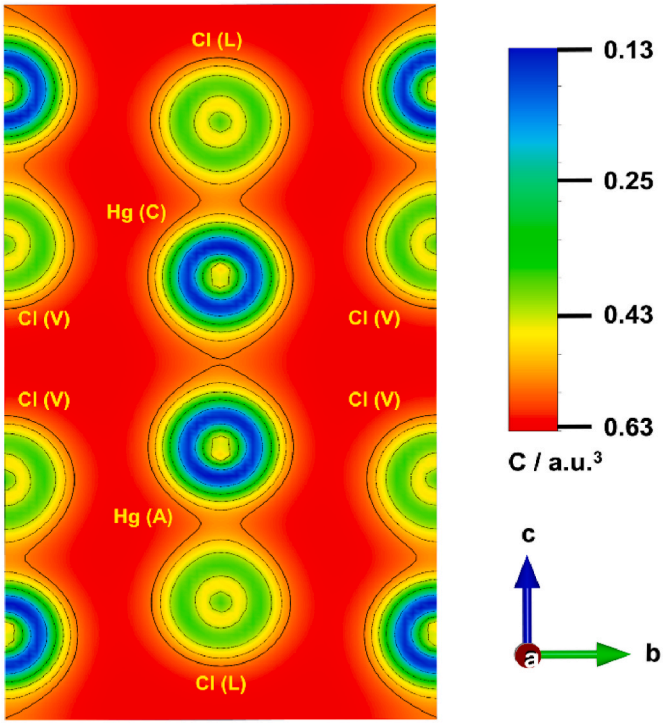

Fig. 7. The electronic charge density distribution map of Hg_2Cl_2 compound. (Isosurface value = 0.009).

range ionic interactions between them, however for the later pair [ca. Hg(C) and Hg (A) atoms] appreciable charge transfer from Hg(C/A) to the neighbouring Cl atoms may be presaged.

This result is further substantiated from the differential charge density distribution map as shown in Fig. 8. From Fig. 8, it is found that the differential Bader charge densities on Hg(C) and Hg(A) atoms are 0.14 e and 0.16 e respectively, while for Cl(L) it is − 0.09 e and for Cl(V) it is estimated to be − 0.20 e. Positive values of differential charge densities on Hg (+ 0.14 e, + 0.16 e) and negative values of the same in the Cl atoms (− 0.09 e, − 0.20 e) indicate charge transfer from Hg to Cl atoms [89,90].

3.7. Natural bond orbital analysis

To gather more information concerning the CT interactions between Hg and Cl atoms of the Hg_2Cl_2 compound, the Natural Bond orbital (NBO) analyses have been performed. The basic concept behind the NBO analyses was suggested by Löwdin in his seminal work and had been reported elsewhere [91]. NBO analyses generate molecular orbitals of the compound from the Lewis concept that depict localized and doubly occupied electron pair orbitals in one, two or three centred regions representing lone pairs (LPs) and chemical bonds (BD, 3C) respectively. Detail discussions and comprehensive reviews on the basic concept and applications of NBOs are depicted in several literatures reported elsewhere [92–100]. NBO calculations have been performed by considering the probable interactions between the donor (filled) and the acceptor (vacant) NBOs in terms of stabilization energy E_2, as estimated from the second order perturbation theory. The stabilization energy E_2 associated with the delocalization ($i \rightarrow j$) energy ΔE_{ij} is represented as:

$$E_2 = \Delta E_{ij} = q_i \frac{< \sigma_j \left| \widehat{F} \right| \sigma_i >}{\varepsilon_j - \varepsilon_i} \quad (1)$$

where q_i is the orbital occupancy of donor, $\widehat{F}$ is Fock or Kohn-Sham matrix and also known as effective orbital Hamiltonian. The diagonal elements ε_i ($\sim < \sigma_i \left| \widehat{F} \right| \sigma_i >$) and ε_j ($\sim < \sigma_j \left| \widehat{F} \right| \sigma_j >$) are the orbital energies of donor and acceptor respectively. The stabilization energies (E_2) of the relevant bond-bond Hg(C)–Hg(A) (σ)/Hg(C)–Cl(L) (σ) and bond-antibond Hg(C)–Hg(A) (σ)/Cl(L)–Cl(V) (σ*) interactions have been estimated and are shown in Table 4. From Table 4 it is clearly seen that the interaction between Hg(C)–Hg(A) (σ)/Hg(C)–Cl(L) (σ) shows strong stabilization accounting to the large E_2 value (5.85 kcal/mol) in comparison to the Hg(C)–Cl(V) (σ)/Cl(L)–Cl(V) (σ*) interaction. The large stabilization energy depicting bond-bond Hg(C)–Hg(A) (σ)/Hg(C)–Cl(L) (σ) interactions signifies considerable CT from Hg(C/A) to Cl(L) atoms in accordance to our earlier conjecture (*vide ante*).

Fig. 9 shows the 2D-contour plots depicting bond-bond Hg(C)–Hg(A) (σ)/Hg(C)–Cl(L) (σ) and bond-antibond Hg(C)–Cl(V) (σ)/Cl(L)–Cl(V) (σ*) interactions. The 2D contour plot for the Hg(C)–Hg(A) (σ)/Hg(C)–

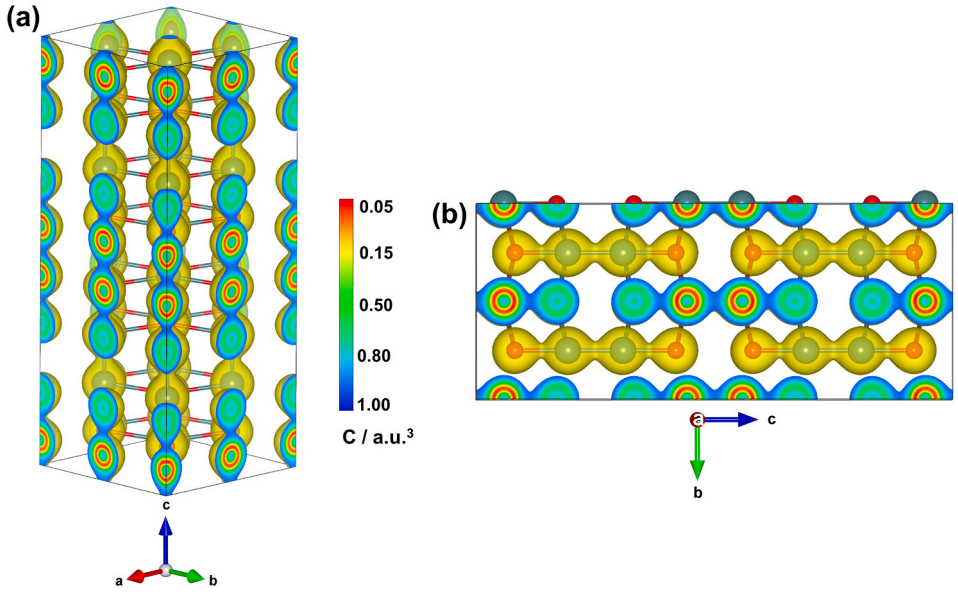

Fig. 8. Differential charge density distribution **(a)** side view and **(b)** planer view along bc - plane of the 2 x 2 x 2 supercell of Hg_2Cl_2 compound as estimated from the Bader charge analysis. [Emerald blue and the red colour balls in the ball and stick model of Hg_2Cl_2 compound indicate Hg and Cl atoms respectively. Isosurface level = 0.010]. (For interpretation of the references to colour in this figure legend, the reader is referred to the Web version of this article.)

Table 4
Bond – bond and bond – antibond interactions (in kcal/mol) for the Hg and Cl atoms of Hg_2Cl_2 compound as calculated from HSEH1PBE/SDD level of theory.

Bond – bond/antibond Interactions	Stabilization energy (E_2) (kcal/mol)	Fock matrix element (F_{ij}) (a.u.)
Hg(C)–Hg(A) (σ)/Hg(C)–Cl(L) (σ)	5.85	0.033
Hg(C)–Hg(A) (σ)/Cl(L)–Cl(V) (σ*)	0.58	0.010

Cl(L) (σ) bonding orbital reveals considerable overlap in the region of Hg(C)-Hg(A) and Hg(C)-Cl(L) bonds (F_{ij} = 0.033 a.u.) thereby promoting the CT interactions.

3.8. Distortions of the octahedral domains within the crystal lattice of Hg_2Cl_2

From the analyses of the PDOS, as discussed in the earlier section, we believe the self-consistent energy alignment through hybridization may primarily stands responsible in the formation of distorted octahedral domains of Hg(C)Hg(A)[Cl(V)]$_4$Cl(L) in the crystal structure of the Hg_2Cl_2 compound. In each octahedral domain (Fig. 3 (c)) one Hg(A) and five Cl [among them four are neighbouring Cl(V) and one is Cl(L)] atoms form the vertices of the octahedron with Hg(C) at the centre. We are interested to see how the presence of the neighbouring Cl [Cl(V) and/or Cl(L)] atoms influence the energy levels associated with the 5d orbitals of both Hg(C) and Hg(A) atoms despite of screening from their respective 6s orbitals. The orbital resolved PDOS of 5d orbital of Hg(C) and Hg (A) atoms are shown in Fig. 10. From Fig. 10 (A) (upper left panel) it is seen that near the valence band edge, loss of degeneracy of the 5d orbitals of Hg(C) has been observed. Similar observation is also noticed for different compounds and has been reported elsewhere [101–103]. Splitting of d orbitals in the PDOS spectrum appears as two distinct branches. While the former branch at higher energy is dominated by the overlapped $d_{x^2-y^2}$, d_{xy} and d_{zx} orbitals, the latter is mostly comprised of overlapped $d_{x^2-y^2}$, $d_{3z^2-r^2}$, $d_{xy,}$ d_{yz} and d_{zx} orbitals. Interestingly the 5d orbitals of Hg(A) atom around the valence band do not show any loss of degeneracy [Fig. 10 (A) (lower left panel)]. These results may suggest that the loss of degeneracy in the 5d orbitals of Hg(C) atom in the valence band may result in the structural distortion of the octahedral domains in the lattice of the Hg_2Cl_2 compound (*vide ante*) in pursuit for achieving the minimum energy configuration.

3.9. The effect of SOC on the band gap of the compound

Although the on-site Coulomb repulsion between the "d" electrons of Hg in Hg_2Cl_2 is suggested to play no role in the generation of band gap of the compound (*vide ante*), yet the effect of E_g upon inclusion of SOC has still been estimated. The SOC is primarily included in the calculations to account the relativistic effects of the heavy Hg atom. In presence of SOC, the GGA calculations with HSE functional suggest an overall increment in the band gap of the compound by 34 meV as shown in Fig. S2 (supplementary material).

Thus the "d" orbitals of Hg though have no apparent effect on the E_g of Hg_2Cl_2 due to the absence of on-site Coulomb repulsion, however these orbitals can perturb the band gap due to SOC. The SOC effect can further induce splitting of p orbitals associated with Cl atoms. The combined effect of SOC on the splitting of d orbitals of Hg atoms and p orbitals of Cl atoms may result in the increase in band gap of the compound by 34 meV. Thus the overall E_g for the tetragonal (*I4/mmm*) phase of Hg_2Cl_2 after considering the SOC effect has been finally predicted to be ~ 3.96 eV, whose experimental band gap has been reported as ~ 4.0 eV [79].

4. Conclusion

The structural and electronic properties of Hg_2Cl_2 at room temperature in its tetragonal phase have been investigated from density functional theory calculations. The SCF energies and the associated lattice parameters of the above referred compound have been estimated from the GGA calculations in conjunction with PBE, PBEsol, BLYP, B3LYP and HSE exchange-correlation functionals. Detail calculations using GGA-HSE level of theory suggest that Hg_2Cl_2 is a wide band gap CT insulator with band gap ~ 3.93 eV. Moreover the effects of on-site Coulomb repulsion $+U_{dd}$ and the SOC on the E_g of the compound have also been explored. Interestingly although the compound is suggested to be a CT insulator, however the corresponding energy dispositions in the orbital resolved PDOS plots do not obey the Zaanen-Sawatzky-Allen diagram. These observations suggest that the ZSA diagram, which being considered as the hallmark of CT insulators for transition metal compounds, is not seen to be followed in the case of CT insulators of the post transition metals like Hg. The PDOS spectra further revealed strong covalent as

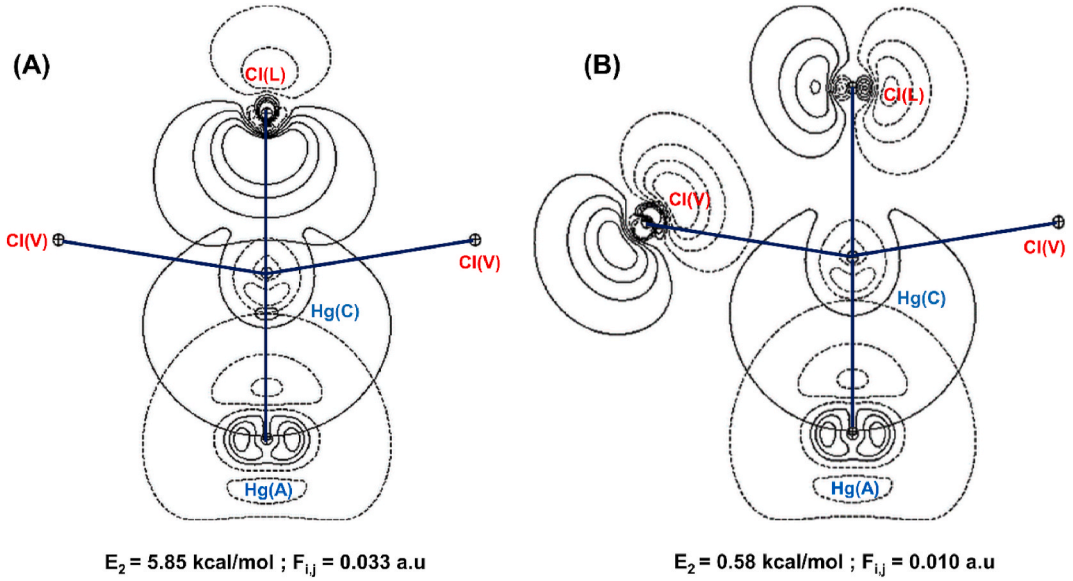

Fig. 9. 2D orbital contour diagram for **(A)** Hg(C) – Hg(A) (σ) bonding and Hg(C) – Cl(L) (σ) bonding, **(B)** Hg(C) – Cl(V) (σ) bonding and Cl(L) – Cl(V) (σ*) antibonding pre-NBO.

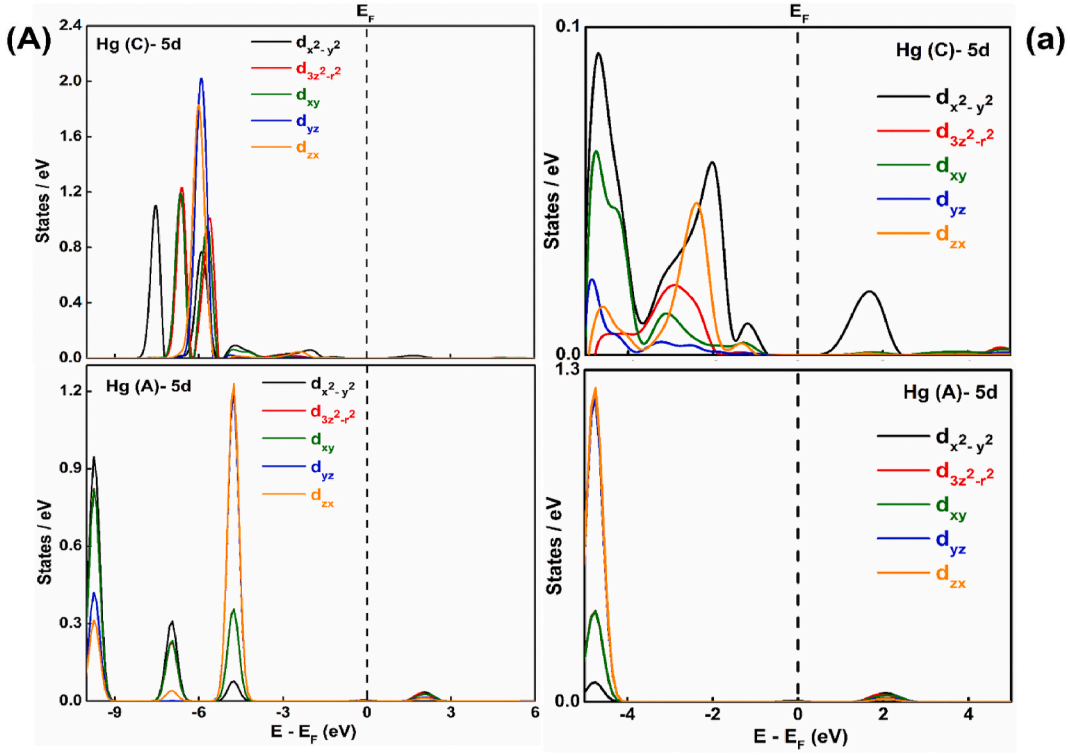

Fig. 10. **(A)** Splitting of 5d orbitals of Hg(C) and Hg(A) atoms in presence ligand Cl(L) and neighbouring Cl(V) atoms in the octahedral environment. **(a)** Right panel shows the magnified views of the splitting of 5d orbitals of Hg(C) and Hg(A) atoms near the Fermi energy.

well as CT interactions between Hg(C)/Hg(A) and Cl(L) atoms in the linear Cl(L)–Hg(C)–Hg(A)–Cl(L) chains of the compound. The Mulliken bond population analyses and the electronic charge density distributions unveiled the existence of weak ionic interactions (in addition to the covalent and CT interactions) mostly among the Hg(C/A) and Cl(V), that form the distorted octahedral domains in the crystal lattice of Hg_2Cl_2. The NBO analyses had also been carried out to gain deeper insights on the CT interactions between Hg and Cl atoms of the compound. Distortions of the octahedral domains within the crystal lattice of Hg_2Cl_2 have been deciphered from the loss of degeneracies in the 5d orbitals of Hg(C) atom in the valence band of the Hg_2Cl_2 compound. The predicted value of the band gap ~ 3.96 eV from the first principle calculations, close to experimentally reported optical band gap ~ 4.0 eV and the structural details of Hg_2Cl_2 at room temperature in the tetragonal phase is expected to provide a strong foundation for future applications of this material in acousto – optic tunable filters, thermoelectric conversion systems and fuel cells.

Declaration of competing interest

The authors declare that they have no known competing financial interests or personal relationships that could have appeared to influence the work reported in this paper.

Acknowledgements

Authors would like to thank the Department of Physics, Jadavpur University for availing the departmental computational facility through DST-FIST programme. Swarup Ghosh also likes to thank the University Grant Commission, Government of India for providing the financial support in form of NET- JRF Fellowship.

Supplementary material

Supplementary material comprises of Lattice parameters, unit cell volumes and SCF energies for different levels of theory (Table S1), the variation of band gap with inclusion of on-site Coulomb repulsion $+U_{dd}$ (Fig. S1) and the TDOS spectra for both SOC and without SOC calculations in GGA – HSE level of theory of Hg_2Cl_2 compound (Fig. S2).

Appendix A. Supplementary data

Supplementary data to this article can be found online at https://doi.org/10.1016/j.matchemphys.2021.125379.

References

[1] P. Hohenberg, W. Kohn, Inhomogeneous electron gas, Phys. Rev. 136 (1964) B864–B871, https://doi.org/10.1103/PhysRev.136.B864.
[2] M.S.S. Brooks, B. Johansson, Chapter 3 Density functional theory of the ground-state magnetic properties of rare earths and actinides, Handb. Magn. Mater. 7 (1993) 139–230, https://doi.org/10.1016/S1567-2719(05)80044-7.
[3] J.N. Harvey, On the accuracy of density functional theory in transition metal chemistry, Annu. Rep. Prog. Chem. Sect. C Phys. Chem. 102 (2006) 203–226, https://doi.org/10.1039/B419105F.
[4] C.J. Cramer, D.G. Truhlar, Density functional theory for transition metals and transition metal chemistry, Phys. Chem. Chem. Phys. 11 (2009) 10757–10816, https://doi.org/10.1039/B907148B.
[5] P. Söderlind, P.E.A. Turchi, A. Landa, V. Lordi, Ground-state properties of rare-earth metals: an evaluation of density-functional theory, J. Condens. Matter Phys. 26 (2014), 416001, https://doi.org/10.1088/0953-8984/26/41/416001.
[6] V.I. Anisimov, Electronic structure of strongly correlated materials, AIP Conf. Proc. 1297 (2010) 3–134, https://doi.org/10.1063/1.3518902.
[7] M.K. Aydinol, A.F. Kohan, G. Ceder, K. Cho, J. Joannopoulos, Ab initio study of lithium intercalation in metal oxides and metal dichalcogenides, Phys. Rev. B 56 (1997) 1354–1365, https://doi.org/10.1103/PhysRevB.56.1354.
[8] G. Colò, Heavy nuclei: introduction to density functional theory and variations on the theme, Eur. Phys. J. Plus. 133 (2018) 553, https://doi.org/10.1140/epjp/i2018-12391-4.
[9] M. Lundie, Ž. Šljivančanin, S. Tomić, Electronic and optical properties of reduced graphene oxide, J. Mater. Chem. C. 3 (2015) 7632–7641, https://doi.org/10.1039/C5TC00437C.
[10] C. Kamal, A. Chakrabarti, M. Ezawa, Aluminene as highly hole-doped graphene, New J. Phys. 17 (2015), 83014, https://doi.org/10.1088/1367-2630/17/8/083014.

[11] G.L. Zhao, D. Bagayoko, T.D. Williams, Local-density-approximation prediction of electronic properties of GaN, Si, C, and RuO_2, Phys. Rev. B 60 (1999) 1563–1572, https://doi.org/10.1103/PhysRevB.60.1563.

[12] J. Wang, M. Deng, Y. Chen, X. Liu, W. Ke, D. Li, W. Dai, K. He, Structural, elastic, electronic and optical properties of lithium halides (LiF, LiCl, LiBr, and LiI): first-principle calculations, Mater. Chem. Phys. 244 (2020), 122733. https://doi.org/10.1016/j.matchemphys.2020.122733.

[13] A. Georges, Strongly correlated electron materials: dynamical mean-field theory and electronic structure, AIP Conf. Proc. 715 (2004) 3–74. https://doi.org/10.1063/1.1800733.

[14] K. Held, Electronic structure calculations using dynamical mean field theory, Adv. Phys. 56 (2007) 829–926, https://doi.org/10.1080/00018730701619647.

[15] M. Imada, T. Miyake, Electronic structure calculation by first principles for strongly correlated electron systems, J. Phys. Soc. Jpn. 79 (2010), 112001, https://doi.org/10.1143/JPSJ.79.112001.

[16] V.N. Antonov, L. V Bekenov, A.N. Yaresko, Electronic structure of strongly correlated systems, Adv. Condens. Matter Phys. 2011 (2011), 298928, https://doi.org/10.1155/2011/298928.

[17] S. Kumari, A.K. Sahu, S. Paul, S. Raj, Investigation of correlation effects on the electronic structure of 3d1 perovskites, J. Phys. Chem. Solid. 124 (2019) 157–162. https://doi.org/10.1016/j.jpcs.2018.09.023.

[18] C.N.R. Rao, Transition metal oxides, Annu. Rev. Phys. Chem. 40 (1989) 291–326, https://doi.org/10.1146/annurev.pc.40.100189.001451.

[19] A. Munoz-Paez, Transition metal oxides: geometric and electronic structures: introducing solid state topics in inorganic chemistry courses, J. Chem. Educ. 71 (1994) 381, https://doi.org/10.1021/ed071p381.

[20] S.A. Cotton, The actinides, Annu. Rep. Prog. Chem. Sect. A Inorg. Chem. 107 (2011) 264–273, https://doi.org/10.1039/C1IC90009A.

[21] F. Saraci, V. Quezada-Novoa, P.R. Donnarumma, A.J. Howarth, Rare-earth metal–organic frameworks: from structure to applications, Chem. Soc. Rev. 49 (2020) 7949–7977, https://doi.org/10.1039/D0CS00292E.

[22] V.I. Anisimov, J. Zaanen, O.K. Andersen, Band theory and Mott insulators: hubbard U instead of stoner I, Phys. Rev. B 44 (1991) 943–954, https://doi.org/10.1103/PhysRevB.44.943.

[23] V.I. Anisimov, F. Aryasetiawan, A.I. Lichtenstein, First-principles calculations of the electronic structure and spectra of strongly correlated systems: the LDA+U method, J. Phys. Condens. Matter 9 (1997) 767–808, https://doi.org/10.1088/0953-8984/9/4/002.

[24] B. Himmetoglu, R.M. Wentzcovitch, M. Cococcioni, First-principles study of electronic and structural properties of CuO, Phys. Rev. B 84 (2011), 115108, https://doi.org/10.1103/PhysRevB.84.115108.

[25] A.G. Petukhov, I.I. Mazin, L. Chioncel, A.I. Lichtenstein, Correlated metals and the LDA+U method, Phys. Rev. B 67 (2003), 153106, https://doi.org/10.1103/PhysRevB.67.153106.

[26] J. Zaanen, G.A. Sawatzky, J.W. Allen, Band gaps and electronic structure of transition-metal compounds, Phys. Rev. Lett. 55 (1985) 418–421, https://doi.org/10.1103/PhysRevLett.55.418.

[27] The Hubbard model at half a century, Nat. Phys. 9 (2013) 523, https://doi.org/10.1038/nphys2759.

[28] A.I. Liechtenstein, V.I. Anisimov, J. Zaanen, Density-functional theory and strong interactions: orbital ordering in Mott-Hubbard insulators, Phys. Rev. B 52 (1995) R5467–R5470, https://doi.org/10.1103/PhysRevB.52.R5467.

[29] M. Cococcioni, S. de Gironcoli, Linear response approach to the calculation of the effective interaction parameters in the LDA+U method, Phys. Rev. B 71 (2005), 35105, https://doi.org/10.1103/PhysRevB.71.035105.

[30] R. Avci, C.P. Flynn, Charge-transfer insulators, Phys. Rev. Lett. 41 (1978) 428–431, https://doi.org/10.1103/PhysRevLett.41.428.

[31] T.M. Schuler, D.L. Ederer, S. Itza-Ortiz, G.T. Woods, T.A. Callcott, J.C. Woicik, Character of the insulating state in NiO: a mixture of charge-transfer and Mott-Hubbard character, Phys. Rev. B 71 (2005), 115113, https://doi.org/10.1103/PhysRevB.71.115113.

[32] J. Kuneš, V.I. Anisimov, S.L. Skornyakov, A. V Lukoyanov, D. Vollhardt, NiO: correlated band structure of a charge-transfer insulator, Phys. Rev. Lett. 99 (2007), 156404, https://doi.org/10.1103/PhysRevLett.99.156404.

[33] M. Gatti, I. V Tokatly, A. Rubio, Sodium: a charge-transfer insulator at high pressures, Phys. Rev. Lett. 104 (2010), 216404, https://doi.org/10.1103/PhysRevLett.104.216404.

[34] P. Olalde-Velasco, J. Jiménez-Mier, J.D. Denlinger, Z. Hussain, W.L. Yang, Direct probe of Mott-Hubbard to charge-transfer insulator transition and electronic structure evolution in transition-metal systems, Phys. Rev. B 83 (2011), 241102, https://doi.org/10.1103/PhysRevB.83.241102.

[35] J. Jiménez-Mier, P. Olalde-Velasco, G. Herrera-Pérez, G. Carabalí -Sandoval, E. Chavira, W.-L. Yang, J. Denlinger, Strongly correlated transition metal compounds investigated by soft X-ray spectroscopies and multiplet calculations, J. Electron. Spectrosc. Relat. Phenom. 196 (2014) 136–141. https://doi.org/10.1016/j.elspec.2014.07.002.

[36] W.W. Ewing, The preparation of electrolytic mercurous chloride in saturated potassium chloride for use in the calomel electrode, J. Am. Chem. Soc. 47 (1925) 301–305, https://doi.org/10.1021/ja01679a002.

[37] M. Crippa, S. Legnaioli, C. Kimbriel, P. Ricciardi, New evidence for the intentional use of calomel as a white pigment, J. Raman Spectrosc. 52 (2021) 15–22. https://doi.org/10.1002/jrs.5876.

[38] X. Yin Jiang, T. Itoh, T. Goto, Reflection and absorption edge spectra in mercurous halide single crystals, J. Phys. Soc. Jpn. 53 (1984) 3672–3675, https://doi.org/10.1143/JPSJ.53.3672.

[39] T. Henningsen, N.B. Singh, Crystal characterization by use of birefringence interferometry, J. Cryst. Growth 96 (1989) 114–118. https://doi.org/10.1016/0022-0248(89)90281-9.

[40] I. Pelant, M.N. Popova, J. Hála, M. AmbroŽ, V. Lhotská, K. Vacek, Two-photon absorption and energy band structure of orthorhombic Hg_2Cl_2 crystals, Czech. J. Phys. 37 (1987) 1183–1197, https://doi.org/10.1007/BF01597034.

[41] A. Pierson, C. Philippe, Acousto-optic interaction model with mercury halides (Hg2Cl2 and Hg2Br2) as AOTF cristals, in: Z. Sodnik, N. Karafolas, B. Cugny (Eds.), Proc. SPIE 11180, Int. Conf. Sp. Opt. — ICSO 2018, SPIE, 2019, pp. 2196–2206, https://doi.org/10.1117/12.2536139.

[42] P.M. Amarasinghe, J.-S. Kim, S. Trivedi, S.B. Qadri, E.P. Gorzkowski, G. Imler, J. Soos, N. Gupta, J. Jensen, Negative thermal expansion of mercurous halides, J. Electron. Mater. 48 (2019) 7063–7067, https://doi.org/10.1007/s11664-019-07518-7.

[43] P. Giannozzi, S. Baroni, N. Bonini, M. Calandra, R. Car, C. Cavazzoni, D. Ceresoli, G.L. Chiarotti, M. Cococcioni, I. Dabo, A. Dal Corso, S. de Gironcoli, S. Fabris, G. Fratesi, R. Gebauer, U. Gerstmann, C. Gougoussis, A. Kokalj, M. Lazzeri, L. Martin-Samos, N. Marzari, F. Mauri, R. Mazzarello, S. Paolini, A. Pasquarello, L. Paulatto, C. Sbraccia, S. Scandolo, G. Sclauzero, A.P. Seitsonen, A. Smogunov, P. Umari, R.M. Wentzcovitch, Quantum espresso: a modular and open-source software project for quantum simulations of materials, J. Phys. Condens. Matter 21 (2009), 395502, https://doi.org/10.1088/0953-8984/21/39/395502.

[44] P. Giannozzi, O. Andreussi, T. Brumme, O. Bunau, M. Buongiorno Nardelli, M. Calandra, R. Car, C. Cavazzoni, D. Ceresoli, M. Cococcioni, N. Colonna, I. Carnimeo, A. Dal Corso, S. de Gironcoli, P. Delugas, R.A. DiStasio, A. Ferretti, A. Floris, G. Fratesi, G. Fugallo, R. Gebauer, U. Gerstmann, F. Giustino, T. Gorni, J. Jia, M. Kawamura, H.-Y. Ko, A. Kokalj, E. Küçükbenli, M. Lazzeri, M. Marsili, N. Marzari, F. Mauri, N.L. Nguyen, H.-V. Nguyen, A. Otero-de-la-Roza, L. Paulatto, S. Poncé, D. Rocca, R. Sabatini, B. Santra, M. Schlipf, A.P. Seitsonen, A. Smogunov, I. Timrov, T. Thonhauser, P. Umari, N. Vast, X. Wu, S. Baroni, Advanced capabilities for materials modelling with Quantum ESPRESSO, J. Phys. Condens. Matter 29 (2017), 465901, https://doi.org/10.1088/1361-648x/aa8f79.

[45] P. Giannozzi, O. Baseggio, P. Bonfà, D. Brunato, R. Car, I. Carnimeo, C. Cavazzoni, S. de Gironcoli, P. Delugas, F. Ferrari Ruffino, A. Ferretti, N. Marzari, I. Timrov, A. Urru, S. Baroni, Quantum ESPRESSO toward the exascale, J. Chem. Phys. 152 (2020), 154105, https://doi.org/10.1063/5.0005082.

[46] P.E. Blöchl, Projector augmented-wave method, Phys. Rev. B 50 (1994) 17953–17979, https://doi.org/10.1103/PhysRevB.50.17953.

[47] J.P. Perdew, K. Burke, M. Ernzerhof, Generalized gradient approximation made simple, Phys. Rev. Lett. 77 (1996) 3865–3868, https://doi.org/10.1103/PhysRevLett.77.3865.

[48] J.P. Perdew, A. Ruzsinszky, G.I. Csonka, O.A. Vydrov, G.E. Scuseria, L. A. Constantin, X. Zhou, K. Burke, Restoring the density-gradient expansion for exchange in solids and surfaces, Phys. Rev. Lett. 100 (2008) 136406, https://doi.org/10.1103/PhysRevLett.100.136406.

[49] A.D. Becke, Density-functional exchange-energy approximation with correct asymptotic behavior, Phys. Rev. 38 (1988) 3098–3100, https://doi.org/10.1103/PhysRevA.38.3098.

[50] A.D. Becke, Density-functional thermochemistry. III. The role of exact exchange, J. Chem. Phys. 98 (1993) 5648–5652, https://doi.org/10.1063/1.464913.

[51] J. Heyd, G.E. Scuseria, M. Ernzerhof, Hybrid functionals based on a screened Coulomb potential, J. Chem. Phys. 118 (2003) 8207–8215, https://doi.org/10.1063/1.1564060.

[52] S. Śmiga, L.A. Constantin, Unveiling the physics behind hybrid functionals, J. Phys. Chem. 124 (2020) 5606–5614, https://doi.org/10.1021/acs.jpca.0c04156.

[53] H. Xiao, J. Tahir-Kheli, W.A. Goddard, Accurate band gaps for semiconductors from density functional theory, J. Phys. Chem. Lett. 2 (2011) 212–217, https://doi.org/10.1021/jz101565j.

[54] A.J. Garza, G.E. Scuseria, Predicting band gaps with hybrid density functionals, J. Phys. Chem. Lett. 7 (2016) 4165–4170, https://doi.org/10.1021/acs.jpclett.6b01807.

[55] F. Viñes, O. Lamiel-García, K. Chul Ko, J. Yong Lee, F. Illas, Systematic study of the effect of HSE functional internal parameters on the electronic structure and band gap of a representative set of metal oxides, J. Comput. Chem. 38 (2017) 781–789. https://doi.org/10.1002/jcc.24744.

[56] C. Peng, Y. Liu, J. Cui, K. Luo, Y. Shen, X. Li, First-principle calculation of the electronic structure of α-Ag3VO4 using two different exchange correlation functionals, Mater. Chem. Phys. 262 (2021), 124307. https://doi.org/10.1016/j.matchemphys.2021.124307.

[57] M. Marsman, J. Paier, A. Stroppa, G. Kresse, Hybrid functionals applied to extended systems, J. Phys. Condens. Matter 20 (2008), 64201, https://doi.org/10.1088/0953-8984/20/6/064201.

[58] X. Gonze, C. Lee, Dynamical matrices, Born effective charges, dielectric permittivity tensors, and interatomic force constants from density-functional perturbation theory, Phys. Rev. B 55 (1997) 10355–10368, https://doi.org/10.1103/PhysRevB.55.10355.

[59] S. Baroni, S. de Gironcoli, A. Dal Corso, P. Giannozzi, Phonons and related crystal properties from density-functional perturbation theory, Rev. Mod. Phys. 73 (2001) 515–562, https://doi.org/10.1103/RevModPhys.73.515.

[60] S.L. Dudarev, A.I. Liechtenstein, M.R. Castell, G.A.D. Briggs, A.P. Sutton, Surface states on NiO (100) and the origin of the contrast reversal in atomically resolved scanning tunneling microscope images, Phys. Rev. B 56 (1997) 4900–4908, https://doi.org/10.1103/PhysRevB.56.4900.

[61] R.J. Elliott, Theory of the effect of spin-orbit coupling on magnetic resonance in some semiconductors, Phys. Rev. 96 (1954) 266–279, https://doi.org/10.1103/PhysRev.96.266.
[62] D. Hobbs, G. Kresse, J. Hafner, Fully unconstrained noncollinear magnetism within the projector augmented-wave method, Phys. Rev. B 62 (2000) 11556–11570, https://doi.org/10.1103/PhysRevB.62.11556.
[63] W. Tang, E. Sanville, G. Henkelman, A grid-based Bader analysis algorithm without lattice bias, J. Phys. Condens. Matter 21 (2009), 84204, https://doi.org/10.1088/0953-8984/21/8/084204.
[64] E. Sanville, S.D. Kenny, R. Smith, G. Henkelman, Improved grid-based algorithm for Bader charge allocation, J. Comput. Chem. 28 (2007) 899–908. https://doi.org/10.1002/jcc.20575.
[65] G. Henkelman, A. Arnaldsson, H. Jónsson, A fast and robust algorithm for Bader decomposition of charge density, Comput. Mater. Sci. 36 (2006) 354–360. https://doi.org/10.1016/j.commatsci.2005.04.010.
[66] G.E. S, , et al.G.W.T. M, J. Frisch, H.B. Schlegel, Gaussian 09 Citation, Gaussian 09, Revis. E.01, Gaussian, Inc., Wallingford CT, 2009. https://gaussian.com/g09citation/.
[67] E.D. Glendening, C.R. Landis, F. Weinhold, NBO 6.0: natural bond orbital analysis program, J. Comput. Chem. 34 (2013) 1429–1437. https://doi.org/10.1002/jcc.23266.
[68] R.J. Havighurst, Parameters IN crystal structure. The mercurous halides, J. Am. Chem. Soc. 48 (1926) 2113–2125, https://doi.org/10.1021/ja01419a016.
[69] NicholasJ. Calos, ColinH.L. Kennard, The structure of calomel, Hg_2Cl_2, derived from neutron powder data, Z. Krist. Cryst. Mater. 187 (1989) 305–307. https://doi.org/10.1524/zkri.1989.187.3-4.305.
[70] F. Birch, Finite elastic strain of cubic crystals, Phys. Rev. 71 (1947) 809–824, https://doi.org/10.1103/PhysRev.71.809.
[71] F.D. Murnaghan, The compressibility of media under extreme pressures, Proc. Natl. Acad. Sci. Unit. States Am. 30 (1944) 244, https://doi.org/10.1073/pnas.30.9.244. LP – 247.
[72] E. Dorm, Intermetallic distances in mercury(I) halides Hg_2F_2, Hg_2Cl_2, and Hg_2Br_2, J. Chem. Soc. D (1971) 466–467, https://doi.org/10.1039/C29710000466.
[73] D.A. Kleier, W.R. Wadt, Molecular structure of mercurous halides: mercurous fluoride and mercurous chloride, J. Am. Chem. Soc. 102 (1980) 6909–6913, https://doi.org/10.1021/ja00543a001.
[74] A.A. Kvasov, Y.F. Markov, E.M. Roginskii, M.B. Smirnov, Phonon dispersion and pressure behavior of Hg2Cl2 crystals, Ferroelectrics 397 (2010) 81–89, https://doi.org/10.1080/00150193.2010.484732.
[75] Y. Luo, J. Wang, Y. Li, J. Wang, Giant phonon anharmonicity and anomalous pressure dependence of lattice thermal conductivity in Y2Si2O7 silicate, Sci. Rep. 6 (2016) 29801, https://doi.org/10.1038/srep29801.
[76] Z. Zhu, B. Dong, H. Guo, T. Yang, Z. Zhang, Fundamental band gap and alignment of two-dimensional semiconductors explored by machine learning, Chin. Phys. B 29 (2020), 46101, https://doi.org/10.1088/1674-1056/ab75d5.
[77] L. Sun, Y. Liu, P. Wu, W. Zhou, Band structure and optical properties of MoS2/SnO2 hetero-bilayer from hybrid functional calculations, Mater. Chem. Phys. 239 (2020), 122071. https://doi.org/10.1016/j.matchemphys.2019.122071.
[78] J. Kaczkowski, Electronic structure and lattice dynamics of rhombohedral BiAlO3 from first-principles, Mater. Chem. Phys. 177 (2016) 405–412. https://doi.org/10.1016/j.matchemphys.2016.04.045.
[79] V. V Sobolev, V.V. Sobolev, D. V Anisimov, On the complex structure of the optical spectra of a tetragonal calomel single crystal in a wide energy range, Semiconductors 50 (2016) 29–33, https://doi.org/10.1134/S1063782616010206.
[80] H.M. Tütüncü, H.Y. Uzunok, E. Karaca, S. Bağcı, G.P. Srivastava, Ab initio investigation of spin orbit coupling effect on the physical properties of IrGe superconductor, Intermetallics 106 (2019) 107–114. https://doi.org/10.1016/j.intermet.2018.12.017.
[81] Y. Liu, N. Zhang, Y. Jia, Q. Sun, M. Chao, Phonon softening induced cubic-to-tetragonal phase transition in ReO3, Phys. Lett. 379 (2015) 2756–2760. https://doi.org/10.1016/j.physleta.2015.07.030.
[82] Y.K. Chang, K.P. Lin, W.F. Pong, M.-H. Tsai, H.H. Hseih, J.Y. Pieh, P.K. Tseng, J. F. Lee, L.S. Hsu, Charge transfer and hybridization effects in Ni3Al and Ni3Ga studies by x-ray-absorption spectroscopy and theoretical calculations, J. Appl. Phys. 87 (2000) 1312–1317, https://doi.org/10.1063/1.372015.
[83] T. Abtew, B.-C. Shih, S. Banerjee, P. Zhang, Graphene–ferromagnet interfaces: hybridization, magnetization and charge transfer, Nanoscale 5 (2013) 1902–1909, https://doi.org/10.1039/C2NR32972G.
[84] M.N. Grisolia, J. Varignon, G. Sanchez-Santolino, A. Arora, S. Valencia, M. Varela, R. Abrudan, E. Weschke, E. Schierle, J.E. Rault, J.-P. Rueff, A. Barthélémy, J. Santamaria, M. Bibes, Hybridization-controlled charge transfer and induced magnetism at correlated oxide interfaces, Nat. Phys. 12 (2016) 484–492, https://doi.org/10.1038/nphys3627.
[85] S. Sahu, M.R. Sahoo, A.K. Kushwaha, G.C. Rout, S.K. Nayak, Charge transfer and hybridization effect at the graphene-nickel interface: a tight binding model study, Carbon N. Y. 142 (2019) 685–696. https://doi.org/10.1016/j.carbon.2018.10.078.
[86] R.C.D. Richardson, The wear of metals by hard abrasives, Wear 10 (1967) 291–309. https://doi.org/10.1016/0043-1648(67)90093-2.
[87] M.D. Segall, R. Shah, C.J. Pickard, M.C. Payne, Population analysis of plane-wave electronic structure calculations of bulk materials, Phys. Rev. B 54 (1996) 16317–16320, https://doi.org/10.1103/PhysRevB.54.16317.
[88] M.I. Naher, S.H. Naqib, An ab-initio study on structural, elastic, electronic, bonding, thermal, and optical properties of topological Weyl semimetal TaX (X = P, As), Sci. Rep. 11 (2021) 5592, https://doi.org/10.1038/s41598-021-85074-z.
[89] S. Moshat, H. Luitel, D. Sanyal, Half-metallic ferromagnetism in molybdenum doped methylammonium lead halides (MAPbX3, X = Cl, Br, I) system: first-principles study, J. Magn. Magn Mater. 519 (2021), 167463. https://doi.org/10.1016/j.jmmm.2020.167463.
[90] S. Roy, H. Luitel, D. Sanyal, First-principles analysis of ferromagnetic properties of molybdenum-doped wide-band-gap oxides, Phil. Mag. Lett. 99 (2019) 326–337, https://doi.org/10.1080/09500839.2019.1692155.
[91] P.-O. Löwdin, Quantum theory of many-particle systems. I. Physical interpretations by means of density matrices, natural spin-orbitals, and convergence problems in the method of configurational interaction, Phys. Rev. 97 (1955) 1474–1489, https://doi.org/10.1103/PhysRev.97.1474.
[92] J.P. Foster, F. Weinhold, Natural hybrid orbitals, J. Am. Chem. Soc. 102 (1980) 7211–7218, https://doi.org/10.1021/ja00544a007.
[93] A.E. Reed, F. Weinhold, Natural localized molecular orbitals, J. Chem. Phys. 83 (1985) 1736–1740, https://doi.org/10.1063/1.449360.
[94] A.E. Reed, L.A. Curtiss, F. Weinhold, Intermolecular interactions from a natural bond orbital, donor-acceptor viewpoint, Chem. Rev. 88 (1988) 899–926, https://doi.org/10.1021/cr00088a005.
[95] F. Weinhold, C.R. Landis, Natural bond orbitals and extensions of localized bonding concepts, Chem. Educ. Res. Pract. 2 (2001) 91–104, https://doi.org/10.1039/B1RP90011K.
[96] B.D. Dunnington, J.R. Schmidt, Generalization of natural bond orbital analysis to periodic systems: applications to solids and surfaces via plane-wave density functional theory, J. Chem. Theor. Comput. 8 (2012) 1902–1911, https://doi.org/10.1021/ct300002t.
[97] D. Guo, L. Goodman, Nature of barrier forces in acetaldehyde, J. Phys. Chem. 100 (1996) 12540–12545, https://doi.org/10.1021/jp960182c.
[98] B. Dutta, R. De, C. Pal, J. Chowdhury, Vibrational analysis of the conformers and understanding the genesis of the internal rotational barriers of Isobutyl Cyanide molecule, Spectrochim. Acta A 96 (2012) 837–847. https://doi.org/10.1016/j.saa.2012.07.106.
[99] B. Dutta, B. Bhattacharjee, J. Chowdhury, Physics behind the barrier to internal rotation of an acetyl chloride molecule: a combined approach from density functional theory, car–parrinello molecular dynamics, and time-resolved wavelet transform theory, ACS Omega 3 (2018) 6794–6803, https://doi.org/10.1021/acsomega.8b00316.
[100] S.P. Veccham, J. Lee, Y. Mao, P.R. Horn, M. Head-Gordon, A non-perturbative pairwise-additive analysis of charge transfer contributions to intermolecular interaction energies, Phys. Chem. Chem. Phys. 23 (2021) 928–943, https://doi.org/10.1039/D0CP05852A.
[101] R.F. Zhang, X.D. Wen, D. Legut, Z.H. Fu, S. Veprek, E. Zurek, H.K. Mao, Crystal field splitting is limiting the stability and strength of ultra-incompressible orthorhombic transition metal tetraborides, Sci. Rep. 6 (2016) 23088, https://doi.org/10.1038/srep23088.
[102] I.R. Reddy, P.M. Oppeneer, K. Tarafder, Interfacial spin manipulation of nickel-quinonoid complex adsorbed on Co(001) substrate, Magnetochemistry 5 (2019), https://doi.org/10.3390/magnetochemistry5010002.
[103] L. Craco, S. Leoni, All-t2g electronic orbital reconstruction of monoclinic MoO2 battery material, Appl. Sci. 10 (2020), https://doi.org/10.3390/app10175730.

Materials Science and Engineering B 284 (2022) 115903

Contents lists available at ScienceDirect

Materials Science & Engineering B

journal homepage: www.elsevier.com/locate/mseb

Pressure induced modulations in the optoelectronic properties of Hg_2Cl_2 compound: Insights from the first-principle calculations

Swarup Ghosh, Joydeep Chowdhury *

Department of Physics, Jadavpur University, 188, Raja S.C. Mallick Road, Kolkata 700032, India

ARTICLE INFO

Keywords:
Structural phase transitions
Band gap
Anisotropy
Optical properties
Birefringence

ABSTRACT

Optical properties linked with various phases of Hg_2Cl_2 crystal under ambient and different external pressures have been explored in detail from the first-principle calculations for the first time. Crystal structures and pressure driven structural phase transitions of the compound have been critically explored. Electronic and the associated anisotropic optical properties of the Hg_2Cl_2 crystal that prevails in its various phases under ambient and external pressures have been elucidated in terms of complex dielectric functions, absorption coefficients, optical conductivities, refractive indices and optical birefringences. We believe that the present in-depth study on the optical properties of Hg_2Cl_2 compound will not only decipher the underlying physics behind the anisotropy of the crystal but will help to design improved optoelectronic devices in the future endeavours.

1. Introduction

Understanding the optical properties of 2D or 3D materials from first-principle calculations have drawn significant attentions in recent years [1–22]. Recently, the first-principle calculations had been reported for the analyses of metal halides of ABX_3-type super-alkali perovskites in estimating their stable dynamics performance and high efficiency first obtained by introducing H_5O_2 cation [23]. Two-dimensional lead-free hybrid halide perovskite using superatom anions with tunable electronic properties had also been reported from the first-principal calculations [24]. Moreover, tunable electronic structures and high efficiency obtained by introducing superalkali and superhalogen into AMX_3-type perovskites had also been estimated from the first-principle calculations [25]. Thus the results of the first-principle calculations alone or in unison with the experimental observations not only provide strong foundations for the futuristic applications of these materials in optoelectronic devices but also help to explore the underlying physics that drive their optical responses [26–41].

Mercurous chloride (Hg_2Cl_2), commonly known as calomel, is a wide band gap charge-transfer insulator and finds extensive applications as white pigment and electrode material [42–45]. Recently, we reported structural and electronic properties of the compound from first-principle calculations [45]. Under ambient pressure (P = 0 GPa) and at room temperature, Hg_2Cl_2 crystallizes in the body-centered tetragonal [I4/mmm (D_{4h}^{17})] phase [46], shows anisotropic physical properties and exhibits strong birefringence [43,44,47]. The ingrained anisotropic behaviour of the compound makes it effective for designing polarizing prisms and provides a leeway towards it applications in acousto-optic tuneable filters for the fabrications of hyperspectral imagers [48]. Interestingly, at low temperature ~185 K, the material is known to exhibit structural phase transition from body-centred tetragonal [I4/mmm (D_{4h}^{17})] to the base-centred orthorhombic [Cmcm (D_{2h}^{17})] phase [49–53]. Apart from thermally driven phase changes, the Hg_2Cl_2 compound also shows pressure (P) induced structural phase transition from I4/mmm (D_{4h}^{17}) → Cmcm (D_{2h}^{17}) phase at the transition pressure $(P_T)_1$ ~ 0.25 GPa [54–57]. Of late, at higher external pressure (P) > 8.95 GPa, the existence of yet another orthorhombic phase (primitive orthorhombic [Pnma (D_{2h}^{16})]) of the compound had been reported [57,58]. The existence of this primitive orthorhombic phase appears as a consequence of the structural phase transition from Cmcm (D_{2h}^{17}) → Pnma (D_{2h}^{16}) phase at the second transition pressure $(P_T)_2$ ~ 8.95 GPa. The above referred temperature and pressure driven phase transitions of Hg_2Cl_2 may lead to the changes in the electronic properties of the compound which in turn can modulate their respective optical responses. The alterations in the optical properties of the compound, that exists in various phases, may provide the fundamental inklings towards their possible applications in optoelectronics and in hyperspectral imagers.

Keeping the above issues in mind, this paper reports for the first time an in-depth study based on first-principle calculations that portrays the

* Corresponding author.
E-mail address: joydeep.chowdhury@jadavpuruniversity.in (J. Chowdhury).

https://doi.org/10.1016/j.mseb.2022.115903
Received 18 November 2021; Received in revised form 26 May 2022; Accepted 23 July 2022
Available online 30 July 2022

optical properties linked with the various phases of Hg_2Cl_2 crystal under ambient and external pressures. The entire article is organized in the following manner. While Section 2 discusses about the computational details, Section 3.1 is devoted on the crystal structures and pressure driven structural phase transitions of Hg_2Cl_2 compound. Electronic and optical properties of the Hg_2Cl_2 crystal in terms of complex dielectric function $[\varepsilon(\omega)]$, absorption coefficient $[\alpha(\omega)]$, optical conductivity $[\sigma(\omega)]$, refractive indices (n_e, n_o), optical birefringence (Δn) etc. under different pressures are focussed in Section 3.2 and 3.3 respectively. Finally, the overall summary of the work is represented under the "Conclusions" section.

2. Computational details

The crystal structure belonging to the body-centered tetragonal [I4/mmm (D_{4h}^{17})] phase of Hg_2Cl_2 compound under ambient condition (P = 0 GPa) has been optimized within the framework of Density Functional Theory (DFT). The DFT calculations have been accomplished from generalized gradient approximations (GGA) in conjunction with Heyd–Scuseria–Ernzerhof (HSE) [59] exchange–correlation (XC) functional with the aid of Quantum ESPRESSO (QE) software [60–62]. Valance electrons of Hg_2Cl_2 compound that comprise the plane wave for the DFT calculations, have electronic configurations of $5d^{10}6s^2$ and $3s^23p^5$ for Hg and Cl atoms respectively. The plane wave kinetic energy cut-off has been taken to 50 Ry with a gamma-centred k-point mesh of 9 × 9 × 9 grid generated through Monkhorst-Pack. The electron–ion interactions between the above referred valence electrons and the ions have been accomplished through the pseudopotential using Projector Augmented Wave (PAW) method [63,64]. The systematic convergence criteria for the estimation of total electronic energy of Hg_2Cl_2 compound in its tetragonal [I4/mmm (D_{4h}^{17})] phase has been set to 10^{-8} Ry with the threshold of maximum Hellman-Feynman force and cell pressure fixed at 10^{-3} a.u. and 10^{-2} GPa respectively. The optimized structure, so generated for the tetragonal phase of Hg_2Cl_2 at ambient pressure, has been further relaxed using the "variable cell relaxation" (VC-relax) method by varying the cell pressure from 0.1 to 14 GPa to attain the lattice and structural parameters for the base-centered [Cmcm (D_{2h}^{17})] and primitive [Pnma (D_{2h}^{16})] orthorhombic phases of the compound. The variations of the total energy as a function of plane wave kinetic energy cut-off and k-mesh grid for the orthorhombic (Cmcm and Pnma) phases of Hg_2Cl_2 compound are depicted in Fig. S1 (a) and S1 (b) (Electronic Supplementary Material) respectively. From Fig. S1, it is clearly seen that the plane wave kinetic energy cut-off of 50 Ry with k-mesh of 9 × 9 × 9 grid is sufficient enough to carry out the first-principle calculations for the above referred phases of the system.

To estimate the electronic band structures and the optical properties for the tetragonal and orthorhombic phases of Hg_2Cl_2 compound, a denser k-point mesh of 19 × 19 × 19 Monkhorst-Pack grid has been used. The optoelectronic parameters like complex dielectric functions, absorption coefficients, optical conductivities and refractive indices have been accomplished from a post-processing code *epsilon.x* [65] implemented in QE software with optical broadening of 0.14 eV.

3. Results and discussion

3.1. Crystal structures and pressure driven structural phase transitions of Hg_2Cl_2

Hg_2Cl_2 at room temperature crystallizes to I4/mmm space group symmetry and represents a body-centred tetragonal phase under ambient pressure (P = 0 GPa). The unit cell of the compound is composed of one formula unit (Z = 2) with 8 atoms, where Hg and Cl atoms are placed at 4e (0, 0, 0.11577) and 4e (0, 0, 0.3380) Wyckoff sites respectively. The variation in total energy (E) as a function of the unit cell volume (V) of the Hg_2Cl_2 crystal in its tetragonal phase [I4/mmm (D_{4h}^{17})], so obtained from the first-principle calculations, has been fitted using fourth order Birch-Murnaghan equation of states [66,67] and the result is shown in Fig. 1. From Fig. 1 it is seen that E primarily decreases with increase in V, attains a minimum value at ~ 219.16 Å^3 and increases again with further increase in the unit cell volume.

The optimized crystal structure of the compound at the minimum value of E is shown in Fig. 2 (a). The crystal structure of Hg_2Cl_2 compound in its tetragonal phase [I4/mmm (D_{4h}^{17})], as shown in Fig. 2, is marked by the presence of parallel Cl(L)–Hg(C)–Hg(A)–Cl(L) linear chains aligned parallel to the crystallographic c - axis along [0 0 1] direction. The enlarged view of Cl(L)–Hg(C)–Hg(A)–Cl(L) linear chain is shown in Fig. 2 (b). The linear chain arrangements of the Cl and Hg atoms in Hg_2Cl_2 directed along the crystallographic c - axis are known to promote strong anisotropy in the physical properties of the crystal [48,68–70], which in turn result in its remarkably large birefringence value (Δn) ~ +0.65 [71]. However, closer look at the crystal structure further displays the existence of distorted octahedral domains formed through the coordination of Hg atoms in the unit cell. The zoomed-in-view of one such distorted octahedron is shown in Fig. 2 (c). The apical mercury Hg(A) and the neighbouring chlorine Cl(V) atoms form the skeleton of the distorted octahedron Hg(C)Hg(A)$[Cl(V)]_5$ with Hg(C) at its centre. The lattice along with the relevant structural parameters of the Hg_2Cl_2 compound in the tetragonal (I4/mmm) phase, as obtained from DFT calculations, are shown in Table 1. The estimated values are in close agreement with the available experimental results so predicted from X-Ray [46] and neutron powder diffraction studies [71].

Fig. 3 shows the effect of external pressure on the normalized lattice parameters a/a_0, b/b_0 and c/c_0 of the Hg_2Cl_2 crystal. Normalizations have been done with respect to the optimized lattice parameters a_0, b_0, and c_0 of the compound in its body-centred tetragonal [I4/mmm (D_{4h}^{17})] phase at ambient pressure (P = 0 GPa). Interestingly, with slight increase in P from 0 GPa to 0.25 GPa, sudden rise in both a/a_0 and b/b_0 ratios have been noticed, while in the same pressure range the other normalized lattice parameter c/c_0 ratio shows small decrement in its absolute value. Incidentally at P ~ 0.25 GPa, where such variations in the ratios of the normalized lattice parameters are perceived, have been reported to be the transition pressure $(P_T)_1$ that leads to the pressure driven first structural phase transition of the compound from body-centered tetragonal [I4/mmm (D_{4h}^{17})] to the base-centered orthorhombic [Cmcm (D_{2h}^{17})] phase [54–57]. However, at P > 2 GPa, both a/a_0 and b/b_0 ratios exhibit small decrements in their respective absolute values until around 8 GPa, where sudden changes in the slopes are observed. For P > 8 GPa, a/a_0 and b/b_0 ratios further depict gradual

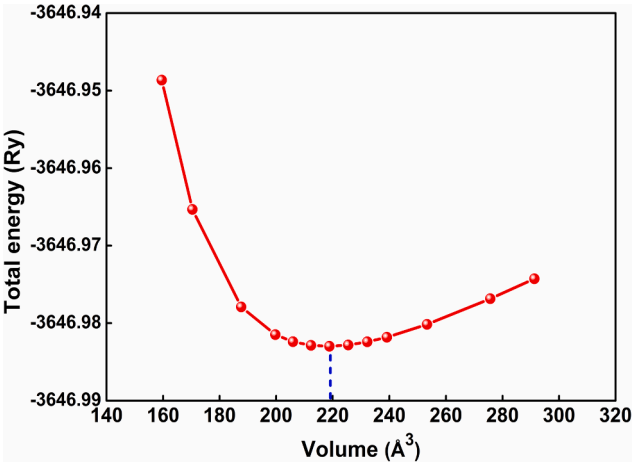

Fig. 1. Energy versus volume plot for the I4/mmm phase of Hg_2Cl_2 crystal under ambient pressure (P = 0 GPa) as estimated from GGA – HSE level of theory. The minimum energy and corresponding unit cell volume are marked with blue dashed line.

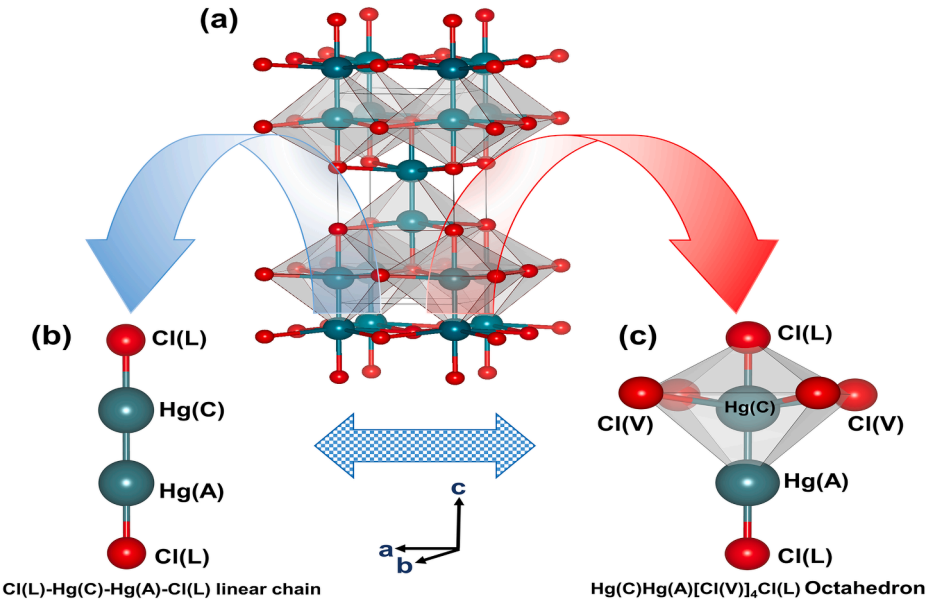

Fig. 2. **(a)** Optimized geometry for the tetragonal (I4/mmm) phase of Hg_2Cl_2 crystal at ambient pressure (P = 0 GPa). The zoomed-in-view of the structure showing **(b)** linear Cl(L)–Hg(C)–Hg(A)–Cl(L) chain and **(c)** the distorted octahedron Hg(C)Hg(A)[Cl(V)]$_4$Cl(L). (Large Hg atoms are shown in emerald blue and small Cl atoms are shown in red).

Table 1
The optimized lattice and structural parameters for I4/mmm, Cmcm and Pnma phases of Hg_2Cl_2 compound as estimated from GGA-HSE level of theory.

Parameters	Phases				
	I4/mmm		Cmcm		Pnma
	This study	Experiments [46,72]	This study	Experiments [69]	This study
a (Å)	4.482	4.470, 4.480	6.299	6.290	5.752
b (Å)	4.482	4.470, 4.480	6.249	6.240	5.751
c (Å)	10.910	10.890, 10.910	10.857	10.860	10.677
Hg(C)–Hg (A) (Å)	2.526	2.526	2.617	–	2.624
Hg(C)–Cl (L) (Å)	2.424	2.434	2.522	–	2.528
Hg(C)–Cl (V) (Å)	3.210	3.209	3.160	–	3.154
Cl(V)–Hg (C)–Cl (V)	161.920°	162.240°	169.290°	–	171.120°
Hg(A)–Hg (C)–Cl (V)	99.040°		95.270°	–	95.130°
Cl(L)–Hg (C)–Hg (A)–Cl(L)	180.000°	180.000°	171.260°	–	170.140°

decrement in their values. The c/c_0 ratio of the compound on the other hand in the range 2 GPa < P < 8 GPa shows a flat trace followed by the change in slope at P = 9 GPa, beyond which the said ratio again almost remains parallel to the abscissa. Significantly enough P = 9 GPa is known to correspond with the transition pressure $(P_T)_2$ that marks the pressure driven second phase transition of the Hg_2Cl_2 crystal from base-centered orthorhombic to the primitive orthorhombic [Cmcm (D_{2h}^{17}) → Pnma (D_{2h}^{16})] phase [57,58]. The overall results as a whole signify increments in the lattice parameters a and b with contraction of c at the onset of the first pressure driven phase transition I4/mmm (D_{4h}^{17}) → Cmcm (D_{2h}^{17}) at $(P_T)_1$ = 0.25 GPa. The second phase transition from Cmcm (D_{2h}^{17}) → Pnma (D_{2h}^{16}) phase at $(P_T)_2$ = 9 GPa is characterized by the contractions of the lattice parameters a and b, while the length of c remains almost unaltered. Interestingly from Fig. 3 it is clearly seen that sudden changes in the slopes of the normalized lattice parameters at the external pressures P = 0.25 GPa and 9 GPa incidentally coincide with the respective (P_T)s that are known to promote pressure induced structural phase transitions of the Hg_2Cl_2 crystal at room temperature [54–56,58]. Furthermore, the structural phase transitions at $(P_T)_1$ = 0.25 GPa and $(P_T)_2$ = 9 GPa for Hg_2Cl_2 compound is accompanied by the changes in lattice parameters (a, b, c) and volume of the crystal with external pressures, suggesting the phase transitions to be of first order type due to breaking of the associated translational symmetry. Such structural phase transition driven by the breaking of translational symmetry is a well-known physical process and has been observed for different exotic materials reported elsewhere [73–78].

To enumerate the transition pressures (P_T) precisely from the first-principle calculations, the variations in enthalpy (H) with induction of P for I4/mmm (D_{4h}^{17}), Cmcm (D_{2h}^{17}) and Pnma (D_{2h}^{16}) phases of the compound at room temperature have been estimated using the following relation:

$$H = E + PV \quad (1)$$

where E, V are the total energy and volume of the unit cells associated with I4/mmm (D_{4h}^{17}), Cmcm (D_{2h}^{17}) and Pnma (D_{2h}^{16}) phases of the Hg_2Cl_2 and P represents the respective external pressures subjected on them. The variations in H with P for Hg_2Cl_2 crystal belonging to I4/mmm (D_{4h}^{17}), Cmcm (D_{2h}^{17}) and Cmcm (D_{2h}^{17}), Pnma (D_{2h}^{16}) phases are shown in Fig. 4 (a) and 4 (b) respectively.

The transition pressure refers to the point on the abscissa of the H-P plots where the enthalpy values for I4/mmm (D_{4h}^{17}), Cmcm (D_{2h}^{17}) and Cmcm (D_{2h}^{17}), Pnma (D_{2h}^{16}) phases of the system become identical. From Fig. 4 (a) and (b), it is seen that the enthalpies for the I4/mmm (D_{4h}^{17}), Cmcm (D_{2h}^{17}) and Cmcm (D_{2h}^{17}), Pnma (D_{2h}^{16}) phases of the Hg_2Cl_2 crystal become equal at the respective points of intersection at pressure $(P_T)_1$ = 0.25 GPa and $(P_T)_2$ = 9 GPa. These $(P_T)_1$ and $(P_T)_2$ signify the transition pressures associated with the first I4/mmm (D_{4h}^{17}) → Cmcm (D_{2h}^{17}) and second Cmcm (D_{2h}^{17}) → Pnma (D_{2h}^{16}) structural phase transitions of the system at room temperature. The evolutions of above referred structures of the compound under external pressures are also shown in Fig. 4 (a) and (b). These results, so obtained from first-principle calculations, are

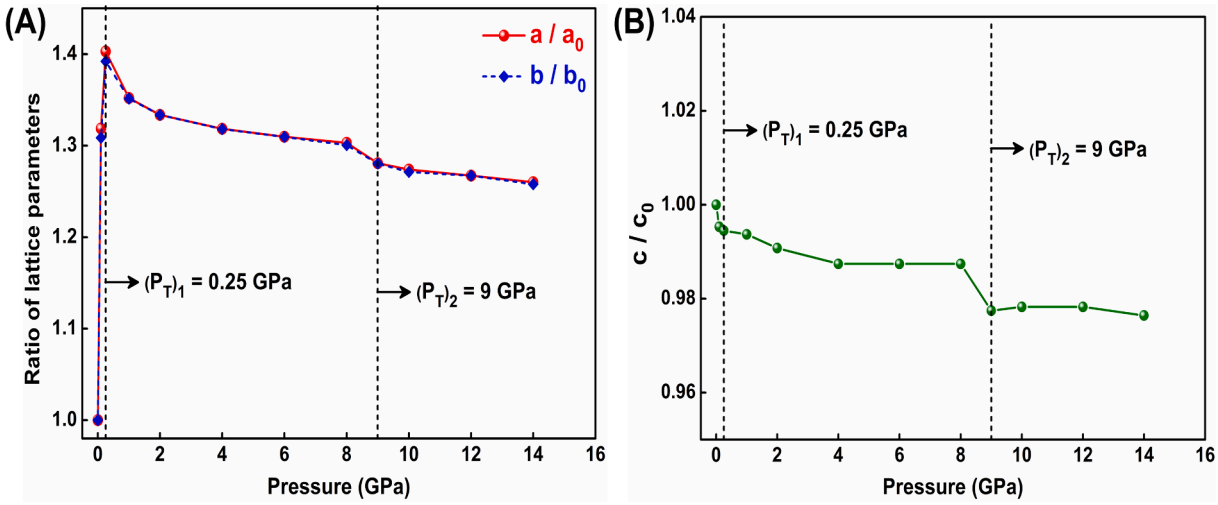

Fig. 3. Lattice parameters **(A)** a/a_0, b/b_0 and **(B)** c/c_0 ratios versus pressure curves for the Hg_2Cl_2 crystal. The transitions pressures are marked in the figures as vertical dotted lines.

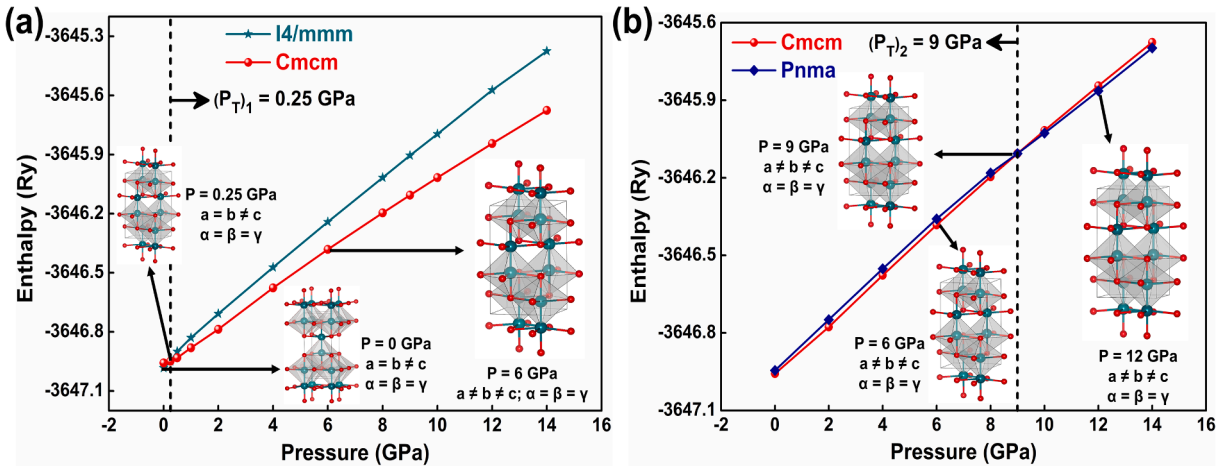

Fig. 4. The enthalpy (H) – pressure (P) plots and associated structural evolutions for **(a)** I4/mmm, Cmcm phases and **(b)** Cmcm, Pnma phases of the Hg_2Cl_2 compound. The transitions pressures are marked in the figures as vertical dotted lines.

in excellent agreement with the experimental observations that suggest pressure induced structural phase transitions of the Hg_2Cl_2 crystal at P = 0.25 GPa [54–56] and 8.95 GPa [58]. The H-P plots, as shown in Fig. 4 (a) and (b), further show that the body-centered tetragonal [I4/mmm (D_{4h}^{17})] phase of Hg_2Cl_2 crystal is thermodynamically more stable than base-centered [Cmcm (D_{2h}^{17})] and primitive [Pnma (D_{2h}^{16})] orthorhombic phases of the compound. The fitted [66,67] E vs V plots for the Cmcm (D_{2h}^{17}) and Pnma (D_{2h}^{16}) phases of the system, as shown in Fig. S2 (Electronic Supplementary Material), further substantiate our conjecture along with the E vs V plot for I4/mmm (D_{4h}^{17}) phase in Fig. 1. The optimized crystal structures for Cmcm (D_{2h}^{17}) and Pnma (D_{2h}^{16}) phases of Hg_2Cl_2 compound along with the associated lattice and structural parameters are shown in Fig. 5 and Table 1. From Table 1, it is clearly seen that apart from changes in lattice parameters, the average Cl(L)–Hg(C)–Hg(A)–Cl(L) dihedral angle of the compound also undergoes deviation from planarity and becomes distorted as the system undergoes pressure induced I4/mmm (D_{4h}^{17}) → Cmcm (D_{2h}^{17}) and Cmcm (D_{2h}^{17}) → Pnma (D_{2h}^{16}) structural phase transitions at $(P_T)_1$ = 0.25 GPa and $(P_T)_2$ = 9 GPa respectively.

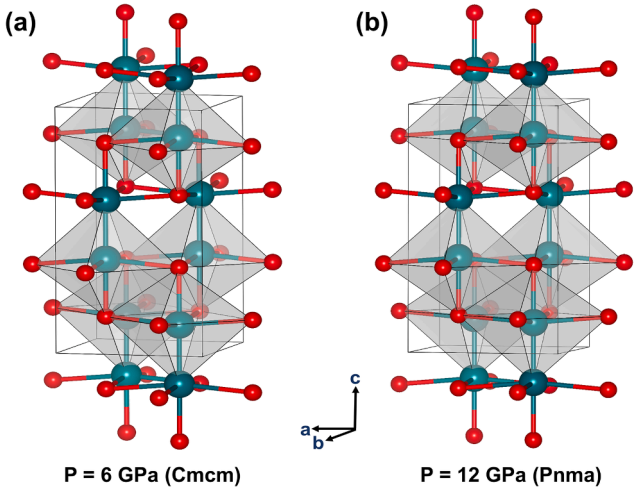

Fig. 5. The optimized geometries for the orthorhombic **(a)** Cmcm and **(b)** Pnma phases of Hg_2Cl_2 compound as estimated from the GGA-HSE level of theory. (Large Hg atoms are shown in emerald blue and small Cl atoms are shown in red).

3.2. Electronic band structures of Hg_2Cl_2 crystal under ambient and external pressures

Fig. 6 shows the theoretically simulated electronic band structures of the tetragonal (I4/mmm) and orthorhombic (Cmcm, Pnma) phases of the Hg_2Cl_2 crystal under ambient and external pressures respectively. From Fig. 6 it is apparent that at ambient pressure (ca. P = 0 GPa), where Hg_2Cl_2 crystallizes to I4/mmm phase, shows a direct gap opening with electronic band gap energy (E_g) ~ 3.93 eV, where both the valence band maximum (VBM) and the conduction band minimum (CBM) are located at the same high-symmetry point M. The estimated value of E_g ~ 3.93 eV is in close harmony with the experimentally determined optical band gap (~ 4.0–4.1 eV) for I4/mmm phase of the compound at room temperature [42]. Small deviation (~ +0.07 eV) in the recorded optical band gap energy from the estimated E_g value may be due to the contribution from the excitonic effects [79,80] which are not considered in the band structure calculations.

With the application of pressure in the range of 0.25 – 14 GPa, small increment in the E_g values of the compound have been noticed, although both the VBM and CBM are now shifted from M to Γ, the Brillouin zone centre. The shift in the direct band gap position from M to Γ high-symmetry points may be identified with the pressure dependent structural phase transition of the Hg_2Cl_2 crystal, which eventually leads to the overall reduction in symmetry from tetragonal [I4/mmm (D_{4h}^{17})] to the orthorhombic [Cmcm (D_{2h}^{17}), Pnma (D_{2h}^{16})] phases of the compound. The reduction in symmetry due to phase transition is not only limited to the obvious changes in the high symmetric points (Γ → M → X → Γ → P in tetragonal [I4/mmm] as compared to X → Γ → Z → Y → Γ for base-centred [Cmcm (D_{2h}^{17})] and primitive [Pnma (D_{2h}^{16})] orthorhombic phases) in the E-**k** diagrams but also depicts distinguishable variations in the dispersion relations of the energy bands, as evinced in Fig. 6. The alterations in the electronic band structures linked with different phases of the compound at P = 0, 6 and 12 GPa in turn may modulate their corresponding optical properties, whose detail discussions are presented in the next section of the manuscript. However, the E_g values, as estimated from the DFT calculations, for all the three phases (ca. P = 0, 6 and 12 GPa) of Hg_2Cl_2 crystal, further recognize them as wide band gap insulators where electronic transitions from valence to the conduction bands account for their respective optical absorptions.

3.3. Optical properties of Hg_2Cl_2 crystal under ambient and external pressures

The linear response and the optical properties of a crystal under electromagnetic radiation can be readily envisaged from the frequency dependent complex dielectric function $\varepsilon(\omega)$ [81,82]. The complex function $\varepsilon(\omega)$ is mathematically expressed as:

$$\varepsilon(\omega) = \varepsilon_1(\omega) + i\varepsilon_2(\omega) \tag{2}$$

where $\varepsilon_1(\omega)$ and $\varepsilon_2(\omega)$ are the real and imaginary parts of $\varepsilon(\omega)$ respectively.

While $\varepsilon_1(\omega)$ depicts the linear polarization and dispersion of the incident light passing through the crystal, $\varepsilon_2(\omega)$ on the other hand may be directly correlated with the electronic band structure and absorption of incident radiation by the crystals. The imaginary part of the dielectric function $\varepsilon_2(\omega)$ is estimated from the first-order time dependent perturbation theory following the simple dipole approximation. In the long wavelength (q → 0) limit, $\varepsilon_2(\omega)$ is represented as [83]:

$$\varepsilon_2(\omega) = \frac{8\pi^2 e^2}{\omega^2 m^2 V} \sum_{i\in c, f\in v} \sum | < \boldsymbol{k}, i|\boldsymbol{u}.\boldsymbol{r}|\boldsymbol{k}, f > |^2 \times \delta[E_i(\boldsymbol{k}) - E_f(\boldsymbol{k}) - \hbar\omega] \tag{3}$$

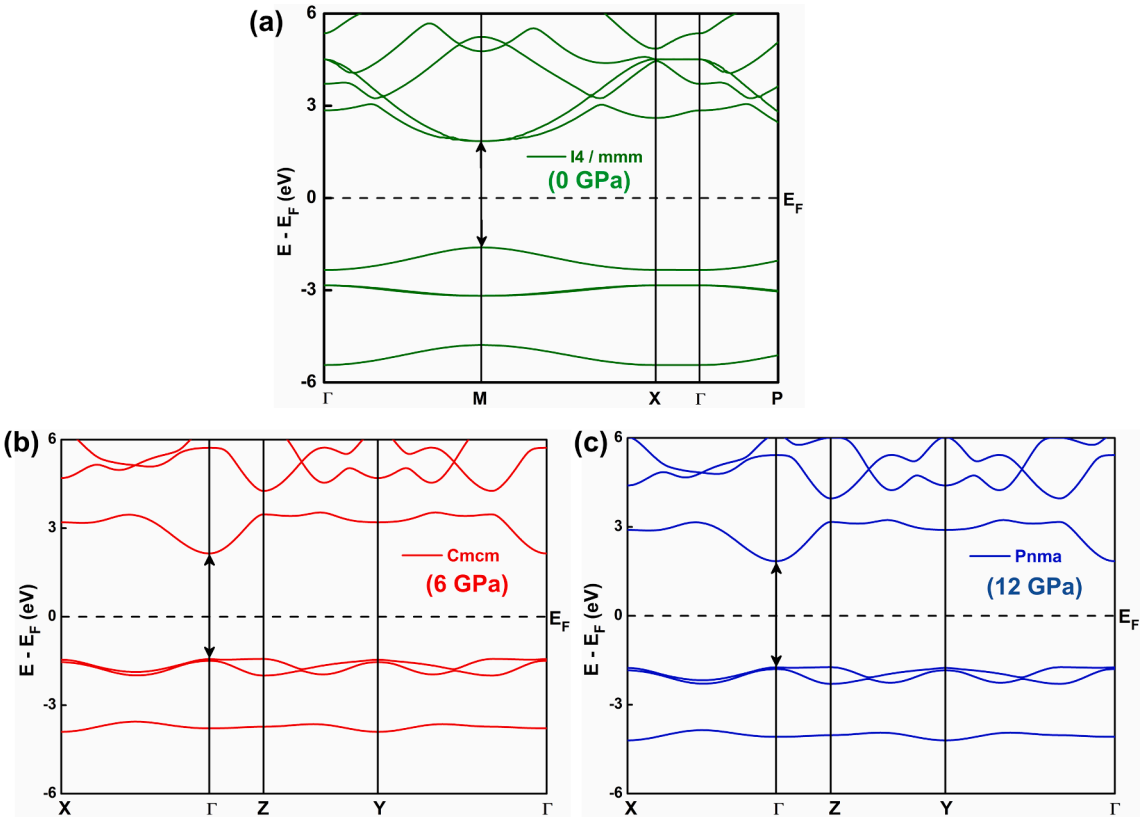

Fig. 6. Electronic band structures for **(a)** tetragonal (I4/mmm) and orthorhombic **(b)** Cmcm and **(c)** Pnma phases of the Hg_2Cl_2 compound along the high symmetry points Γ → M → X → Γ → P and X → Γ → Z → Y → Γ respectively. The band gaps and the Fermi energies (E_F) are shown as black vertical arrows and black horizontal dashed lines respectively.

where V is the volume of unit cell. $|\boldsymbol{k}, i>$ and $|\boldsymbol{k}, f>$ represent the valance and conduction band states respectively over the wave vector $\boldsymbol{k}$, $\boldsymbol{u}$ and $\boldsymbol{r}$ are the polarization and position vectors of the electromagnetic wave respectively. The real part $\varepsilon_1(\omega)$ can be accomplished from $\varepsilon_2(\omega)$ using the Kramers – Kronig relation [84,85] and is depicted as follows:

$$\varepsilon_1(\omega) = \frac{1}{\pi} P \int_{-\infty}^{\infty} \frac{\varepsilon_2(\omega')}{\omega' - \omega} d\omega' \tag{4}$$

where P is the Cauchy principal value.

The frequency dependent complex dielectric function of any dispersive materials carries wealth of information relating to their optical properties. For example, the complex refractive index $\mathrm{N}(\omega)$ is related with $\varepsilon(\omega)$ through the following simple relation:

$$\mathrm{N}(\omega) = \sqrt{\varepsilon(\omega)} = n(\omega) + ik(\omega) \tag{5}$$

where the real part of the complex refractive index is expressed as

$$n(\omega) = \left(\frac{\sqrt{\varepsilon_1^2 + \varepsilon_2^2} + \varepsilon_1}{2} \right)^{\frac{1}{2}} \tag{6}$$

and the corresponding imaginary part, known as the extinction coefficient (k), is expressed by the following equation:

$$k(\omega) = \left(\frac{\sqrt{\varepsilon_1^2 + \varepsilon_2^2} - \varepsilon_1}{2} \right)^{\frac{1}{2}} \tag{7}$$

The absorption coefficient $\alpha(\omega)$ is referred to the attenuation of incident radiation in percentage as it propagates per unit distance through the materials. It is closely associated with the extinction coefficient of the material and also with $\varepsilon_2(\omega)$ through the following relation

$$\alpha(\omega) = \frac{2k\omega}{c\hbar} = \frac{\omega}{nc}\varepsilon_2(\omega) \tag{8}$$

where c is the speed of light in vacuum.

The imaginary part of the dielectric function $\varepsilon_2(\omega)$ is closely related with the optical conductivity $\sigma(\omega)$, which provides valuable information pertaining to the conduction of free charge carriers over a defined range of energies of incident photons. The optical conductivity $\sigma(\omega)$ is mathematically expressed as:

$$\sigma(\omega) = \frac{\omega\varepsilon_2}{4\pi} \tag{9}$$

3.3.1. *Linear response of the complex dielectric function for the Hg_2Cl_2 crystal*

Hg_2Cl_2 crystal is known to possess large elastic and structural anisotropies at room temperature and under ambient pressure [86]. The anisotropies in the physical properties of the compound are mainly attributed to the presence of parallel Cl(L)–Hg(C)–Hg(A)–Cl(L) linear chains directed along the crystallographic c - axis representing [0 0 1] direction. The ingrained anisotropies associated with the elastic and physical properties of the compound may presage similar direction dependence behaviour in the optical properties as well. The optical properties of the Hg_2Cl_2 crystal are thus initially investigated for all the three [1 0 0], [0 1 0] and [0 0 1] polarization directions of the incident electric field. However, the optical properties of the compound are found to be identical in both [1 0 0] and [0 1 0] polarization directions, but are substantially altered along the [0 0 1] direction. The electric field components along [1 0 0]/[0 1 0] and [0 0 1] directions are owed to $E_\perp$ and $E\|$ respectively.

3.3.2. *The dielectric function $\varepsilon_1(\omega)$*

Fig. 7 (a) shows the variation of the real part of the complex dielectric function $[\varepsilon_1(\omega)]$ as a function of the incident electromagnetic field energy (E_{EM}) for Hg_2Cl_2 crystal under ambient pressure P = 0 GPa and at P = 6, 12 GPa, where the compound exists in tetragonal [I4/mmm (D_{4h}^{17})] and orthorhombic [Cmcm (D_{2h}^{17}), Pnma (D_{2h}^{16})] phases respectively. The static dielectric constant $\varepsilon_1(0)$ of the compound at P = 0 GPa has been estimated to be ~ 4.9 for [0 0 1]/ $E\|$ while it is close to zero along [1 0 0] and [0 1 0]/$E_\perp$ polarization directions of the electric field. The estimated value of $\varepsilon_1(0) \sim 4.9$ for Hg_2Cl_2 crystal under ambient pressure P is in close agreement with the calculated value ~ 4.6 reported by Sobolev *et al.* [42]. Distinct anisotropies in the $\varepsilon_1(\omega)$ values are also noted for two different polarization directions of the incident

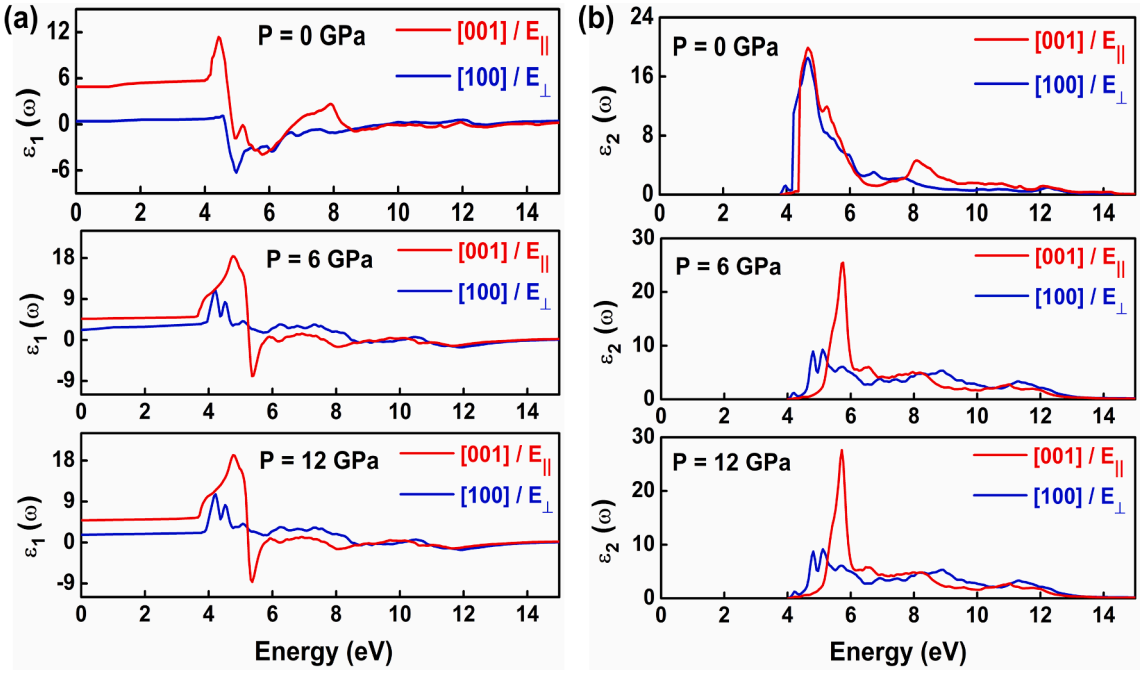

Fig. 7. The **(a)** real and **(b)** imaginary part of the complex dielectric function of Hg_2Cl_2 compound as a function of energy under ambient pressure P = 0 GPa and under external pressures P = 6 GPa, 12 GPa along [0 0 1]/ $E\|$ and [1 0 0]/ $E_\perp$ directions of polarization as estimated from GGA – HSE level of theory.

electromagnetic wave. For $E\|$ polarization of electric field, $\varepsilon_1(\omega)$ shows maximum positive value at ~ 4.5 eV, beyond which it gradually decreases and becomes negative over the energy range ~ 5 – 7 eV. The real part of the dielectric function $\varepsilon_1(\omega)$ is linked with the dispersion and linear polarization of light as it propagates through the material medium [28,34,37,38,87–92]. The maximum dispersion is achieved at the resonance frequency that corresponds to E_{EM} value at ~ 4.5 eV for $E\|$ polarization. However, for $E_{EM} > 9$ eV, $\varepsilon_1(\omega)$ becomes nearly zero. Interestingly, the dispersive nature of $\varepsilon_1(\omega)$ for $E_\perp$ is markedly different from that estimated for the $E\|$ polarization. Over a wide energy range from 0 – 4 eV, $\varepsilon_1(\omega)$ remains nearly zero and is consistent with the static value of the dielectric constant $\varepsilon_1(0)$. However, within ~ 4.6 – 7.5 eV, it becomes negative, beyond which $\varepsilon_1(\omega)$ increases and becomes zero in the high energy limit. The negative values of $\varepsilon_1(\omega)$ for the Hg_2Cl_2 crystal under ambient pressure at room temperature in the 5.12 – 6.97 eV and 4.6 – 7.5 eV energy windows for $E\|$ and $E_\perp$ polarization directions of the electric field respectively signify the metallic Drude like features of the compound. The positive values of $\varepsilon_1(\omega)$ spanned in 0 – 5.12 eV for $E\|$ and 0 – 4.6 eV for $E_\perp$ polarizations are intrinsically related with the interband transitions linked with the optical features of the crystal [93–95].

Interestingly, under the application of external pressures (ca. P = 6 and 12 GPa), the variations in $\varepsilon_1(\omega)$ for Hg_2Cl_2 as a function of incident E_{EM} for both $E\|$ and $E_\perp$ polarizations show remarkable differences in their features in comparison to that recorded under ambient condition at P = 0 GPa. The static dielectric constant $\varepsilon_1(0)$ of the compound at P = 6 and 12 GPa have been estimated to be ~ 4.86 and 4.65 respectively for [0 0 1]/ $E\|$ polarization directions of the electric field, while both the values of $\varepsilon_1(0)$ are 2.2 and 1.68 along [1 0 0]/[0 1 0]/ $E_\perp$ polarization directions respectively. The variations in $\varepsilon_1(\omega)$ of Hg_2Cl_2 compound at P = 6, 12 GPa with change in incident E_{EM} for $E\|$ and $E_\perp$ polarizations follow similar traces, although clear anisotropies in the values of $\varepsilon_1(\omega)$ are noted for two different polarization states of the incident radiation. However, both the traces show resonance peak maximum ~ 4.8 eV, which are slightly shifted towards higher frequency in comparison to that estimated under ambient pressure (~ 4.5 eV, P = 0 GPa). The slight change in the resonance frequency may be attributed to the variation in electronic band energy states as reflected from the corresponding E-**k** diagram in the first Brillouin zone (*vide supra, cf.* Section 3.2) [37]. Significantly enough, the $\varepsilon_1(\omega)$ vs energy plots for the Hg_2Cl_2 crystal at P = 0 and 6, 12 GPa, as shown in Fig. 7 (a), show unique characteristic features that can be directly correlated with the tetragonal and orthorhombic phases of the compound under study. At room temperature the tetragonal phase of Hg_2Cl_2 crystal is known to exist under ambient pressure P = 0 GPa while under external pressure the system undergoes structural phase transitions from tetragonal [I4/mmm (D_{4h}^{17})] to orthorhombic [Cmcm (D_{2h}^{17}), Pnma (D_{2h}^{16})] phases at transition pressures $(P_T)_1$ = 0.25 GPa [54–57] and $(P_T)_2$ = 9 GPa [57,58]. The other striking observation has been the small decrements in the $\varepsilon_1(0)$ values of the compound with increase in P. This is an expected observation as $\varepsilon_1(0)$ scales inversely with E_g following Penn's model [96]. Small increments in the E_g values with increase in P have indeed being estimated from the first-principle calculations and are depicted in the preceding section (*vide supra*).

3.3.3. *The dielectric function* $\boldsymbol{\varepsilon_2(\omega)}$

The variations of the imaginary part of the complex dielectric function [$\varepsilon_2(\omega)$] with energy for Hg_2Cl_2 crystal under ambient (P = 0 GPa) and external pressures P = 6 and 12 GPa are shown in Fig. 7 (b). The dielectric function $\varepsilon_2(\omega)$ signifies the interband transitions and identifies frequency dependent attenuation of incident electromagnetic field energy (E_{EM}) by the materials [28,34,37,38,87–92]. The take-off or critical value of $\varepsilon_2(\omega)$ is intrinsically related with the E_g of the compound [37,38,90,97,98]. Interestingly, the critical values of $\varepsilon_2(\omega)$ for both $E\|$ and $E_\perp$ polarization directions of the electric field have been estimated to be ~3.92, 4.00 and 4.05 eV when the crystal is subjected to external pressures P = 0, 6 and 12 GPa respectively. These results are in accordance with the estimated E_g values of the compound under similar perturbations (*cf.* Section 3.2). The critical value of $\varepsilon_2(\omega)$ of the compound at room temperature and under ambient pressure is in close agreement with the result as suggested by Sobolev *et al.* [42]. The structured bands are visible in $\varepsilon_2(\omega)$ versus energy plots [Fig. 7 (b)] whose peaks are owed to the interband transitions of the compound [34,38,87,99–101]. The peak positions of these bands at ~ 4.67 and ~ 5.71 eV under ambient and external pressures P = 6, 12 GPa respectively have unique characteristics of their kind that allow one to identify the tetragonal and orthorhombic phases of the compound under investigation. Furthermore, the anisotropies in the $\varepsilon_2(\omega)$ values of compound under natural conditions and under external pressures are distinctly identified for both the polarization directions of the incident electric field. However, large to moderate positive values of $\varepsilon_2(\omega)$ in the energy range 4.5 – 12 eV for both $E\|$ and $E_\perp$ polarizations [Fig. 7 (b)] may signify strong absorption of the incident electromagnetic wave by this compound in this energy window. This is clearly reflected in $\alpha(\omega)$ and $\sigma(\omega)$ plots as shown in Fig. 8, where both the absorption coefficient and the optical conductivity exhibit appreciable values in 4.5 – 12 eV energy window of the electromagnetic spectrum.

Closer inspections of $\alpha(\omega)$ and $\sigma(\omega)$ plots (Fig. 8) reveal certain interesting features. Both these plots show the appearance of a well resolved band peaked at ~ 5.80 eV for $E\|$ polarization (along [0 0 1] direction) of the incident electric field. This band appears in $\alpha(\omega)$ and $\sigma(\omega)$ plots for the Hg_2Cl_2 under external pressures P = 6 and 12 GPa, where the crystal exists in the orthorhombic phase at room temperature. This peak eventually disappears when the system crystallizes to the tetragonal phase under ambient pressure. The physical origin of the peak at ~ 5.80 eV in the absorption coefficient $\alpha(\omega)$ and optical conductivity $\sigma(\omega)$ for $E\|$ [0 0 1] polarization of the incident electromagnetic field energy (E_{EM}) at P = 6 and 12 GPa [Fig. 8 (a)] may be rationalised from the corresponding crystal structures of the compound. Interestingly, the crystallographic c - axes representing [0 0 1] direction of the compound under elevated pressures (ca. P = 6 and 12 GPa) are marked by the presence of parallel Cl(L)–Hg(C)–Hg(A)–Cl(L) distorted chains in contrast to parallel linear chains of the same under ambient pressure (*vide supra, cf.* Table 1) [69]. The distortions of the linear Cl(L)–Hg(C)–Hg(A)–Cl(L) chains at P = 6 and 12 GPa result in the alterations of electronic arrangements which in turn may promote excitonic transitions leading to large increase in the absorption coefficients [$\alpha(\omega)$] and associated optical conductivities [$\sigma(\omega)$] for $E\|$ polarization of the incident electric field at ~ 5.80 eV [102]. The variations in electronic arrangements of the Hg_2Cl_2 compound under ambient (P = 0 GPa) and elevated pressures (P = 6 and 12 GPa) are clearly reflected from their corresponding E-**k** diagrams as depicted in Fig. 6 (*vide supra, cf.* Section 3.2). The appearance of this characteristic peak at ~ 5.80 eV thus may be intrinsically related with the orthorhombic phase of Hg_2Cl_2 crystal at room temperature. The appearance and disappearance of the band peaked at ~ 5.80 eV in $\alpha(\omega)$, $\sigma(\omega)$ plots as a function of energy, akin ~ 4.67 and ~ 5.71 eV peaks in the $\varepsilon_2(\omega)$ plots (*vide supra*) may be considered as a signature band that carries the latent information regarding the crystal system (tetragonal or orthorhombic) of the compound not only under ambient condition but also when subjected to external pressures.

Interestingly both $\alpha(\omega)$ and $\sigma(\omega)$ plots at ambient and under external pressures (P = 6 and 12 Pa) for $E\|$ and $E_\perp$ polarizations begin at ~ 3.92, 4.00 and 4.05 eV respectively which corresponds to the take-off or critical values $\varepsilon_2(\omega)$ of the compound under study. The critical values $\varepsilon_2(\omega)$ of the compound in turn is linked with E_g, as discussed earlier (*vide supra*). These calculations thus help us to cross-check the E_g values of the compounds from their corresponding optical properties. It may be relevant to mention that although in strict sense $\alpha(\omega)$ signifies the optical band gap of a compound, but for wide band gap insulators as in the case of Hg_2Cl_2, this energy gap value closely resembles with E_g where

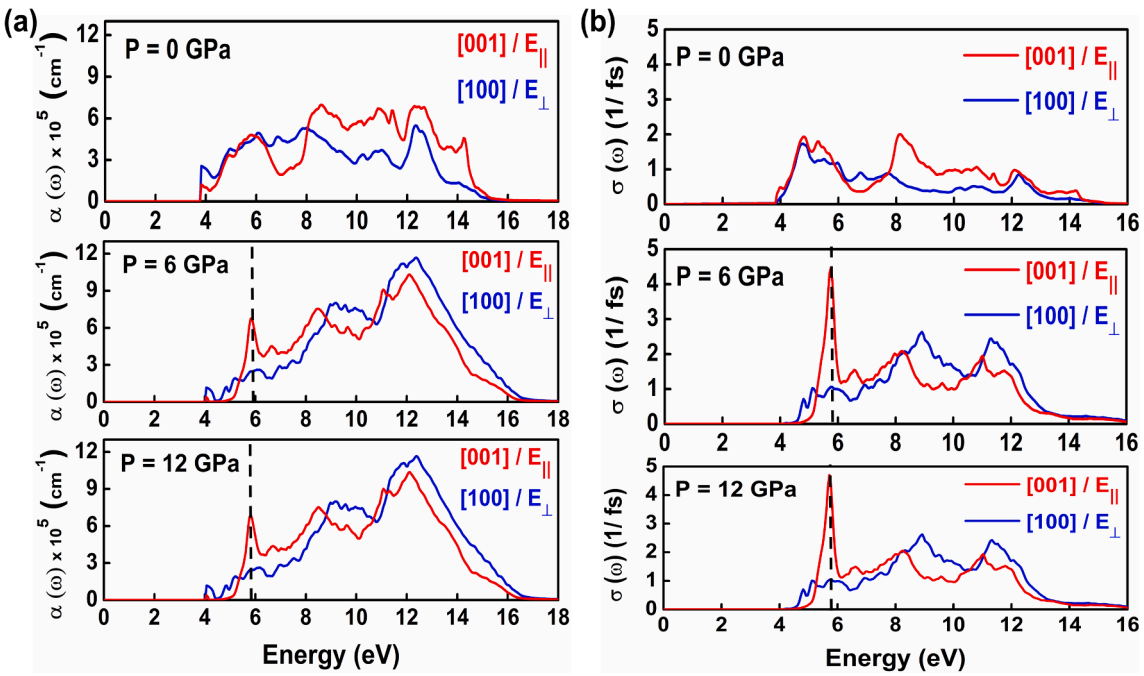

Fig. 8. **(a)** Optical absorption coefficient and **(b)** optical conductivity of Hg_2Cl_2 compound as a function of energy under ambient (P = 0 GPa) and external pressures (P = 6 GPa and 12 GPa) along [0 0 1]/ $E\|$ and [1 0 0]/ $E_\perp$ directions of polarization as obtained from GGA – HSE level of theory. The characteristic peaks in the orthorhombic phases of the Hg_2Cl_2 compound are marked with dotted arrows.

interband transitions only account for the optical absorption. Moreover, in the energy windows ~ 0 – 3.9 eV, and beyond ~ 15 eV, the $\alpha(\omega)$ values of the compound under external pressures P = 0 and 6, 12 GPa for both $E\|$ and $E_\perp$ polarizations of the incident electric field show zero or almost negligible values. These results suggest that Hg_2Cl_2 crystal remains highly transparent in the energy windows ~ 0 – 4 eV, and above 15 eV under wide range of external pressures spanning between 0 and 14 GPa regardless of the structural phase transitions at $(P_T)_1$ = 0.25 GPa and $(P_T)_2$ = 9 GPa. The wide spectral range of transparency covering UV–Vis-LWIR and extreme UV regions of the electromagnetic spectrum together with pronounce optical properties make Hg_2Cl_2 a promising material for various applications in acousto-optic devices.

3.3.4. Refractive indices (n_e, n_o) and the optical birefringence (Δn) of the Hg_2Cl_2 crystal

Anisotropic crystals are composed of complex atomic lattice orientations with varying electrical, optical and mechanical properties depending upon the polarization direction of the incident electromagnetic field energy (E_{EM}). As a result, the refractive indices of the anisotropic crystals also vary with the polarization direction of the electromagnetic wave, giving rise to direction dependence trajectories and velocities of the emergent ray. This phenomenon is designated as double refraction and the emergent rays whose velocity is independent (dependent) of propagation direction is termed as ordinary (extraordinary) rays. The corresponding refractive indices for the ordinary (O-) ray are designated as n_o while that for the extraordinary (E-) ray as n_e. The difference in refractive indices ($\Delta n = n_e - n_o$) between the extraordinary and ordinary rays is termed as optical birefringence of the doubly refracting crystal [103]. In the present context, the directions of the O- and E- rays after double refraction through the Hg_2Cl_2 crystal have been identified with $E_\perp$ and $E\|$ polarizations of the electric field along [1 0 0]/ [0 1 0] and [0 0 1] directions respectively. The anisotropic response of the complex dielectric functions $\varepsilon_1(\omega)$ and $\varepsilon_2(\omega)$ for the uniaxial Hg_2Cl_2 crystal under ambient (P = 0 GPa) and external pressures P = 6, 12 GPa for both $E_\perp$ and $E\|$ polarizations of the incident electric field invoke us to study in details the real part of the complex refractive index [$n(\omega)$] and the corresponding birefringence (Δn) value of the material.

Fig. 9 (a) shows the variations of refractive indices n_o and n_e as a function of incident E_{EM} for the Hg_2Cl_2 crystal under ambient and external pressures P = 6 and 12 GPa. From Fig. 9 (a), it is observed that n_o and n_e values of the compound under ambient (ca. P = 0 GPa) and external pressures (ca. P = 6 and 12 GPa) are nearly independent of incident E_{EM} in the energy window ~ 0 to 4.1 eV. However, beyond this energy window both n_o,n_e values of Hg_2Cl_2 under ambient condition/ under external pressures (P = 6, 12 GPa) increase, attain maximum values at ~ 4.62, 4.52 eV/ 4.71, 5.35 eV and then decrease again with increase in E_{EM} within the energy window ~ 4.70 – 6.50 eV/ 5.73 – 6.05 eV. The increase in the values of refractive indices with E_{EM} in the above referred energy window may be related to large opacity and low phase velocities of the propagating electromagnetic rays inside the compound [34,37]. The shifts in the peak values of n_o and n_e for the compound are intrinsically related with the corresponding complex dielectric functions [$\varepsilon(\omega)$] which in turn are linked with the electronic band structures of the compound under ambient (P = 0 GPa) and external pressures (P = 6, 12 GPa). Interestingly, the characteristic peaks in $n(\omega)$ versus energy plots for n_o, (n_e) at ~ 4.62, (4.52) eV owed to Hg_2Cl_2 crystal in ambient condition (ca. P = 0 GPa) and ~ 4.71 (5.35) eV under external pressures P = 6, 12 GPa may be directly related with the respective tetragonal and orthorhombic phases of the system under study. The Hg_2Cl_2 crystal at room temperature, under ambient condition and under external pressures at P = 6, 12 GPa is indeed known to exist in body-centered tetragonal (I4/mmm) and orthorhombic (Cmcm, Pnma) phases respectively (*vide supra*).

Moreover, Fig. 9 (a) also shows marked differences between the values of n_o and n_e not only for the crystal under ambient condition but also under high external pressures. The difference (Δn) between the values of n_o and n_e makes Hg_2Cl_2 crystal optically birefringent and is expected to show birefringence phenomenon. The calculated birefringence value Δn = 0.64 at ~ 2 eV for the studied compound under ambient condition is in excellent agreement with the reported value ~ 0.65 – 0.66, as depicted in the available literatures [48,70]. This result further justifies the level of theory used in the first-principle calculations which has the unique power to reproduce the experimentally determined optical band gap, imaginary part of the complex dielectric

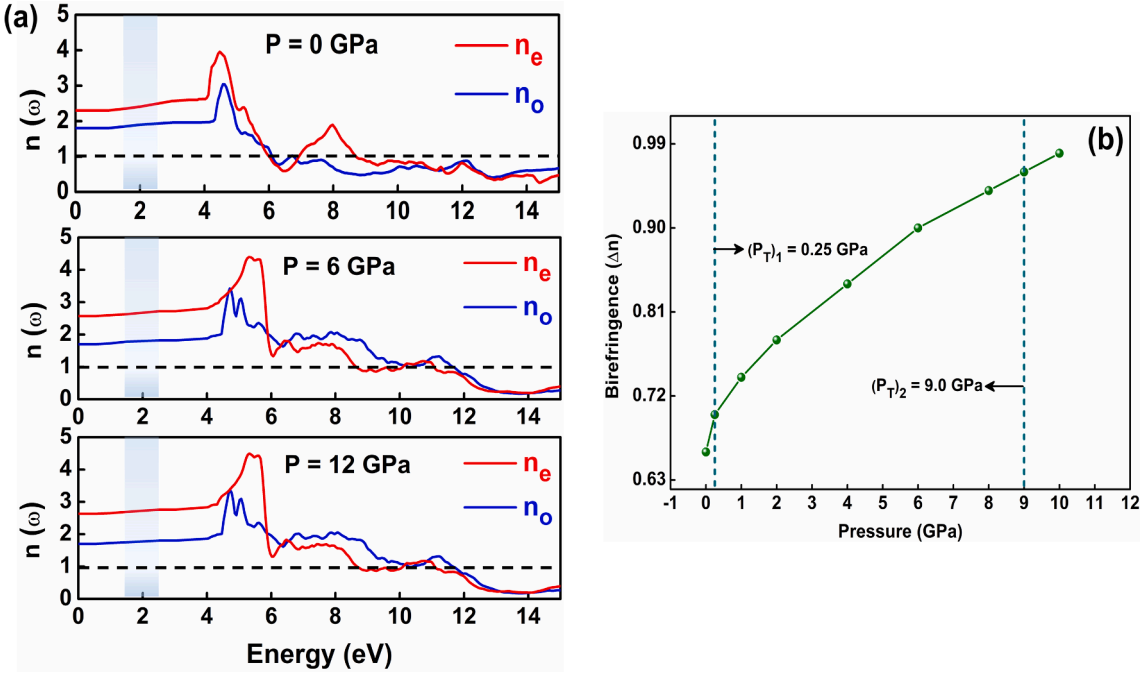

Fig. 9. **(a)** Real part of the refractive index $n(\omega)$ of Hg_2Cl_2 compound computed as a function of energy under ambient (P = 0 GPa) and external pressures (P = 6 GPa and 12 GPa) along [001]/ $E\|$ and [100]/ $E_\perp$ directions of polarization. The visible region (~ 1.5 eV to 3 eV) is shaded with blue in each plot. **(b)** The birefringence (Δn) as a function of external pressure for Hg_2Cl_2 compound as estimated from GGA – HSE level of theory. The transitions pressures are marked in the figures as vertical dotted lines.

function, refractive indices and optical birefringence of the compound [42,48,70]. In this connection it may be worth to mention that the first-principle calculations with GGA-HSE level of theory are known to reproduce the experimentally determined band gaps and optical properties of different materials with profound accuracies and have been reported elsewhere [104–110].

Fig. 9 (a) further reveals that both the values of the refractive indices (n_o, n_e) of the compound in ambient condition and under external pressures P = 6, 12 GPa are less than 1 for the incident energies above 9 and 12 eV respectively. These results signify that the group velocity (v_g) of the incoming wave within the crystal exceeds the velocity of light "c" in the energy windows above 9 eV for the tetragonal (I4/mmm) phase and above 12 eV for the orthorhombic (Cmcm, Pnma) phases of the compound. Beyond the above referred energy windows (ca. P = 0 and 6, 12 GPa) the Hg_2Cl_2 crystal is thus turned to exotic metamaterials or left-handed materials and is expected to show non-linear optical properties and superluminal characteristic features [37,90,111–116].

The variation in Δn for Hg_2Cl_2 crystal as a function of external pressure P is shown in Fig. 9 (b). From Fig. 9 (b) it is clearly seen that Δn increases with increase in P. However, deeper inspection further reveals distinct changes in the slopes of the curve at P ~ 0.25 and 9 GPa which incidentally correspond to the transition pressures $(P_T)_1$ and $(P_T)_2$ associated with I4/mmm (D_{4h}^{17}) → Cmcm (D_{2h}^{17}) and Cmcm (D_{2h}^{17}) → Pnma (D_{2h}^{16}) structural phase transitions of the compound (*vide supra*). Appreciable increments in the optical birefringence with pressure are associated with increase in anisotropic behaviour of the crystal as it undergoes two consecutive phase transitions from tetragonal to the orthorhombic phases of the compound at P = 0.25 and 9 GPa. We believe that such changes in the optical birefringence with P will be helpful in designing improved optoelectronic devices such as polarized lasers, waveguides and fiber-optic communication systems in future endeavours [117–120].

4. Conclusions

Pressure induced modulations in the optoelectronic properties of Hg_2Cl_2 compound have been explored in detail for the first time from first-principle calculations. Crystal structures and the pressure driven structural phase transitions from the tetragonal [I4/mmm (D_{4h}^{17})] to orthorhombic [Cmcm (D_{2h}^{17}) and Pnma (D_{2h}^{16})] phases of the compound have been critically explored. Variations in the optoelectronic properties of the material in ambient condition and under external pressures have been explored in terms of complex dielectric functions, absorption coefficients, optical conductivities, refractive indices and optical birefringences. We believe that the present study will help to unfold the anisotropic properties of the crystal which in turn may be helpful in designing improved optoelectronic devices such as polarized lasers, waveguides and fiber-optic communication systems.

Declaration of Competing Interest

The authors declare that they have no known competing financial interests or personal relationships that could have appeared to influence the work reported in this paper.

Acknowledgements

Authors acknowledge the Department of Physics, Jadavpur University for availing the computational facility through DST-FIST programme. Swarup Ghosh also thanks to the University Grants Commission, Government of India for providing the UGC-NET-JRF award in form of fellowship.

Data availability statement

Data are available on valid request from the corresponding author.

Appendix A. Supplementary data

Electronic supplementary material includes the variations of the total energy as a function of plane wave kinetic energy cut-off and k-mesh grid for the orthorhombic (Cmcm and Pnma) phases of Hg_2Cl_2 compound (Fig. S1) and the E vs V plots for the Cmcm (D_{2h}^{17}) and Pnma (D_{2h}^{16}) phases of the system (Fig. S2).

Supplementary data to this article can be found online at https://doi.org/10.1016/j.mseb.2022.115903.

References

[1] Y.K. Yap, Z. Zhou, Two-Dimensional Electronics and Optoelectronics, MDPI AG, 2017.

[2] L.A. Burton, T.J. Whittles, D. Hesp, W.M. Linhart, J.M. Skelton, B.o. Hou, R. F. Webster, G. O'Dowd, C. Reece, D. Cherns, D.J. Fermin, T.D. Veal, V.R. Dhanak, A. Walsh, Electronic and optical properties of single crystal SnS2: an earth-abundant disulfide photocatalyst, J. Mater. Chem. A. 4 (4) (2016) 1312–1318, https://doi.org/10.1039/C5TA08214E.

[3] A.M.A. Leguy, P. Azarhoosh, M.I. Alonso, M. Campoy-Quiles, O.J. Weber, J. Yao, D. Bryant, M.T. Weller, J. Nelson, A. Walsh, M. van Schilfgaarde, P.R.F. Barnes, Experimental and theoretical optical properties of methylammonium lead halide perovskites, Nanoscale. 8 (12) (2016) 6317–6327, https://doi.org/10.1039/C5NR05435D.

[4] C.-W. Chen, S.-Y. Hsiao, C.-Y. Chen, H.-W. Kang, Z.-Y. Huang, H.-W. Lin, Optical properties of organometal halide perovskite thin films and general device structure design rules for perovskite single and tandem solar cells, J. Mater. Chem. A. 3 (17) (2015) 9152–9159, https://doi.org/10.1039/C4TA05237D.

[5] W. Zhu, G. Xin, Y. Wang, X. Min, T. Yao, W. Xu, M. Fang, S. Shi, J. Shi, J. Lian, Tunable optical properties and stability of lead free all inorganic perovskites (Cs2SnIxCl6−x), J. Mater. Chem. A. 6 (6) (2018) 2577–2584, https://doi.org/10.1039/C7TA10040J.

[6] H.-C. Chung, C.-P. Chang, C.-Y. Lin, M.-F. Lin, Electronic and optical properties of graphene nanoribbons in external fields, Phys. Chem. Chem. Phys. 18 (11) (2016) 7573–7616, https://doi.org/10.1039/C5CP06533J.

[7] M.R. Bryce, A review of functional linear carbon chains (oligoynes, polyynes, cumulenes) and their applications as molecular wires in molecular electronics and optoelectronics, J. Mater. Chem. C. 9 (33) (2021) 10524–10546, https://doi.org/10.1039/D1TC01406D.

[8] J. Liu, J. Qu, T. Kirchartz, J. Song, Optoelectronic devices based on the integration of halide perovskites with silicon-based materials, J. Mater. Chem. A. (2021), https://doi.org/10.1039/D1TA04527J.

[9] E. Drueke, J. Yang, L. Zhao, Observation of strong and anisotropic nonlinear optical effects through polarization-resolved optical spectroscopy in the type-II Weyl semimetal Td-WTe2, Phys. Rev. B. 104 (2021) 64304, https://doi.org/10.1103/PhysRevB.104.064304.

[10] Y.K. Chembo, D. Brunner, M. Jacquot, L. Larger, Optoelectronic oscillators with time-delayed feedback, Rev. Mod. Phys. 91 (2019) 35006, https://doi.org/10.1103/RevModPhys.91.035006.

[11] L. Chouhan, S. Ghimire, C. Subrahmanyam, T. Miyasaka, V. Biju, Synthesis, optoelectronic properties and applications of halide perovskites, Chem. Soc. Rev. 49 (10) (2020) 2869–2885, https://doi.org/10.1039/C9CS00848A.

[12] T. Kocabaş, D. Çakır, C. Sevik, First-principles discovery of stable two-dimensional materials with high-level piezoelectric response, J. Phys.: Condens. Matter. 33 (11) (2021) 115705, https://doi.org/10.1088/1361-648X/abd3da.

[13] Y. Li, Y. Xu, First-principles discovery of novel quantum physics and materials: From theory to experiment, Comput. Mater. Sci. 190 (2021) 110262, https://doi.org/10.1016/j.commatsci.2020.110262.

[14] K. Chen, R. Dronskowski, First-Principles Study of Divalent 3d Transition-Metal Carbodiimides, J. Phys. Chem. A. 123 (43) (2019) 9328–9335, https://doi.org/10.1021/acs.jpca.9b05799.

[15] R. Santosh, V. Kumar, The pressure effect on stability, electronic and optical properties of fluorine passivated graphene (CF)n: A first-principle study, Mater. Sci. Eng. B. 269 (2021) 115163, https://doi.org/10.1016/j.mseb.2021.115163.

[16] R. Santosh, A. Sinha, V. Kumar, Structural, stability, electronic, optical and thermodynamic properties of hydrogenated germanene using first-principle calculations, Mater. Sci. Eng. B. 259 (2020), 114584, https://doi.org/10.1016/j.mseb.2020.114584.

[17] M.I. Naher, S.H. Naqib, Structural, elastic, electronic, bonding, and optical properties of topological CaSn3 semimetal, J. Alloys Compd. 829 (2020), 154509, https://doi.org/10.1016/j.jallcom.2020.154509.

[18] M.A. Kamboh, H. Wang, L. Wang, L. Hao, Y. Su, L. Chen, Q. Wang, Ab initio study of the thermodynamic, electronic and optical properties of WC (Bh) phase ZnO under pressure, Mater. Sci. Eng. B. 265 (2021), 115008, https://doi.org/10.1016/j.mseb.2020.115008.

[19] V.V. Kulish, W. Huang, Single-layer metal halides MX2 (X = Cl, Br, I): stability and tunable magnetism from first principles and Monte Carlo simulations, J. Mater. Chem. C. 5 (2017) 8734–8741. 10.1039/C7TC02664A.

[20] W. Kaiser, M. Carignano, A.A. Alothman, E. Mosconi, A. Kachmar, W.A. Goddard, F. de Angelis, First-Principles Molecular Dynamics in Metal-Halide Perovskites: Contrasting Generalized Gradient Approximation and Hybrid Functionals, J. Phys. Chem. Lett. 12 (2021) 11886–11893, https://doi.org/10.1021/acs.jpclett.1c03428.

[21] H. Xue, G. Brocks, S. Tao, First-principles calculations of defects in metal halide perovskites: A performance comparison of density functionals, Phys. Rev. Materials. 5 (2021), 125408, https://doi.org/10.1103/PhysRevMaterials.5.125408.

[22] Y. Yu, Z. Wang, G. Shao, Formulation of Li-metal-halide (LMX) solid state electrolytes through extensive first principles modelling, J. Mater. Chem. A. 9 (45) (2021) 25585–25594, https://doi.org/10.1039/D1TA05849E.

[23] T. Zhou, M. Wang, Z. Zang, L. Fang, Stable Dynamics Performance and High Efficiency of ABX3-Type Super-Alkali Perovskites First Obtained by Introducing H5O2 Cation, Adv. Energy Mater. 9 (2019) 1900664, https://doi.org/10.1002/aenm.201900664.

[24] T. Zhou, M. Wang, Z. Zang, X. Tang, L. Fang, Two-dimensional lead-free hybrid halide perovskite using superatom anions with tunable electronic properties, Sol. Energy Mater. Sol. Cells. 191 (2019) 33–38, https://doi.org/10.1016/j.solmat.2018.10.021.

[25] T. Zhou, Y. Zhang, M. Wang, Z. Zang, X. Tang, Tunable electronic structures and high efficiency obtained by introducing superalkali and superhalogen into AMX3-type perovskites, J. Power Sources. 429 (2019) 120–126, https://doi.org/10.1016/j.jpowsour.2019.04.111.

[26] H. Huang, J. Peng, H. Dong, L. Huang, M. Wen, F. Wu, First-principles study of p-type doping in Two Dimensional GaN, Phys. Chem. Chem. Phys. (2021), https://doi.org/10.1039/D1CP02904E.

[27] Z. Tong, T. Dumitrică, T. Frauenheim, First-principles prediction of infrared phonon and dielectric function in biaxial hyperbolic van der Waals crystal α-MoO3, Phys. Chem. Chem. Phys. (2021), https://doi.org/10.1039/D1CP00682G.

[28] S. Ghosal, A. Bandyopadhyay, D. Jana, Electric field induced band tuning, optical and thermoelectric responses in tetragonal germanene: a theoretical approach, Phys. Chem. Chem. Phys. 22 (35) (2020) 19957–19968, https://doi.org/10.1039/D0CP03892J.

[29] S. Ghosal, A. Bandyopadhyay, D. Jana, Correction: Electric field induced band tuning, optical and thermoelectric responses in tetragonal germanene: a theoretical approach, Phys. Chem. Chem. Phys. 22 (2020) 27458, https://doi.org/10.1039/D0CP90246B.

[30] D. Karmakar, S. Datta, D. Jana, Combined theoretical and experimental study of the electronic and optical property of Sb2WO6, J. Alloys Compd. 881 (2021), 160586, https://doi.org/10.1016/j.jallcom.2021.160586.

[31] S. Sinha, S. Ghosal, D. Jana, Electronic and optical properties of PTCDI adsorbed graphene heterostructure: A first principles study, J. Phys. Chem. Solids. 155 (2021) 110109, https://doi.org/10.1016/j.jpcs.2021.110109.

[32] S. Nath, A. Bandyopadhyay, S. Sen, D. Jana, First principles investigation of structural, electronic and optical properties of synthesized radiaannulene oligomers for 6,6,12-graphyne, J. Phys. Chem. Solids. 153 (2021), 109990, https://doi.org/10.1016/j.jpcs.2021.109990.

[33] S. Ghosal, H. Luitel, S.K. Mandal, D. Sanyal, D. Jana, Half metallic ferromagnetic and optical properties of ruthenium-doped zincblende ZnS: A first principles study, J. Phys. Chem. Solids. 136 (2020) 109175, https://doi.org/10.1016/j.jpcs.2019.109175.

[34] M.I. Naher, S.H. Naqib, An ab-initio study on structural, elastic, electronic, bonding, thermal, and optical properties of topological Weyl semimetal TaX (X = P, As), Sci Rep. 11 (2021) 5592, https://doi.org/10.1038/s41598-021-85074-z.

[35] T. Kashyap, P.J. Boruah, H. Bailung, D. Sanyal, B. Choudhury, Simultaneous layer exfoliation and defect activation in g-C3N4 nanosheets with air–water interfacial plasma: spectroscopic defect probing with tailored optical properties, Nanoscale Adv. 3 (2021) 3260–3271, https://doi.org/10.1039/D1NA00098E.

[36] P. Nath, D. Sanyal, D. Jana, Ab-initio calculation of optical properties of AA-stacked bilayer graphene with tunable layer separation, Curr. Appl. Phys. 15 (6) (2015) 691–697, https://doi.org/10.1016/j.cap.2015.03.011.

[37] N.A. Noor, Q. Mahmood, M. Rashid, B. Ul Haq, A. Laref, The pressure-induced mechanical and optoelectronic behavior of cubic perovskite PbSnO3 via ab-initio investigations, Ceram. Int. 44 (12) (2018) 13750–13756, https://doi.org/10.1016/j.ceramint.2018.04.217.

[38] M. Kaur, G. Sharma, M. Rérat, K.B. Joshi, Computational analysis of strain-induced electronic and optical properties of Zn3As2, J. Mater. Sci. 55 (12) (2020) 5099–5110, https://doi.org/10.1007/s10853-019-04331-9.

[39] R.O. Balogun, M.A. Olopade, O.O. Oyebola, A.D. Adewoyin, First-principle calculations to investigate structural, electronic and optical properties of MgHfS3, Mater. Sci. Eng. B. 273 (2021), 115405, https://doi.org/10.1016/j.mseb.2021.115405.

[40] H.A. Rahnamaye Aliabad, M. Mousavi, A. Abareshi, First-principles calculations of optoelectronic and thermoelectric properties of HgGa2S4 chalcopyrite under pressure effect, Mater. Sci. Eng. B. 272 (2021), 115336, https://doi.org/10.1016/j.mseb.2021.115336.

[41] R. Rani, M. Sharma, R. Sharma, Optical anisotropy in bare and janus tellurene allotropes from ultraviolet to visible region: A first principle study, Mater. Sci. Eng. B. 265 (2021) 115014, https://doi.org/10.1016/j.mseb.2020.115014.

[42] V.V. Sobolev, V.V. Sobolev, D.V. Anisimov, On the complex structure of the optical spectra of a tetragonal calomel single crystal in a wide energy range, Semiconductors. 50 (1) (2016) 29–33, https://doi.org/10.1134/S1063782616010206.

[43] M. Crippa, S. Legnaioli, C. Kimbriel, P. Ricciardi, New evidence for the intentional use of calomel as a white pigment, J. Raman Spectrosc. 52 (1) (2021) 15–22, https://doi.org/10.1002/jrs.5876.

[44] W.W. Ewing, The preparation of electrolytic mercurous chloride in saturated potassium chloride for use in the calomel electrode, J. Am. Chem. Soc. 47 (2) (1925) 301–305, https://doi.org/10.1021/ja01679a002.

[45] S. Ghosh, S. Sarkar, J. Chowdhury, Structural and electronic properties of wide band gap charge transfer insulator Hg2Cl2: Insights from the first-principle calculations, Mater. Chem. Phys. (2021), 125379, https://doi.org/10.1016/j.matchemphys.2021.125379.

[46] R.J. Havighurst, Parameters in crystal structure. The mercurous halides, J. Am. Chem. Soc. 48 (1926) 2113–2125. 10.1021/ja01419a016.

[47] T. Henningsen, N.B. Singh, Crystal characterization by use of birefringence interferometry, J. Cryst. Growth. 96 (1) (1989) 114–118, https://doi.org/10.1016/0022-0248(89)90281-9.

[48] A. Pierson, C. Philippe, Acousto-optic interaction model with mercury halides (Hg2Cl2 and Hg2Br2) as AOTF cristals, in: Z. Sodnik, N. Karafolas, B. Cugny (Eds.), Proc. SPIE 11180, International Conference on Space Optics — ICSO 2018, SPIE, 2019: pp. 2196–2206. 10.1117/12.2536139.

[49] Ċ. Barta, A.A. Kaplyanskiĭ, V. v Kulakov, Yu.F. Markov, Soft mode at the boundary of the Brillouin zone and nature of the phase transition in monovalent mercury-halide crystals, J. Exp. Theor. Phys. 21 (1975) 54. https://ui.adsabs.harvard.edu/abs/1975JETPL..21...54B.

[50] G.J. Rosasco, H.S. Parker, R.S. Roth, R.A. Forman, W.S. Brower, Study of the low-temperature phase transition in Hg2Cl2, J. Phys. C: Solid State Phys. 11 (1) (1978) 35–44, https://doi.org/10.1088/0022-3719/11/1/015.

[51] J.P. Benoit, C.X. An, Y. Luspin, J.P. Chappelle, J. Lefebvre, Study of inelastic neutron scattering and by the Raman effect, of the soft mode in the prototype phase of Hg2Cl2, J. Phys. C: Solid State Phys. 11 (17) (1978) L721–L723, https://doi.org/10.1088/0022-3719/11/17/003.

[52] G.F. Dobrzhanskii, A.A. Kaplyanskii, M.F. Limonov, YU.F. Markov, A ferroelastic phase transition in Hg2(ClxBr 1–x)2 crystals, Ferroelectrics. 48 (1) (1983) 69–80, https://doi.org/10.1080/00150198308227840.

[53] M.E. Boiko, M.D. Sharkov, A.M. Boiko, S.G. Konnikov, Study of the Phase Transition in Hg2Cl2 Crystals Using Anomalous X-Ray Transmission, Crystallogr. Rep. 63 (2) (2018) 196–199, https://doi.org/10.1134/S1063774518020037.

[54] W. Dultz, E. Rehaber, A pressure-dependent optical soft mode in calomel (Hg2Cl2), J. Phys. C: Solid State Phys. 12 (4) (1979) L137–L139, https://doi.org/10.1088/0022-3719/12/4/001.

[55] M. Midorikawa, Y. Ishibashi, S.-I. Nakashima, A. Mitsuishi, Effect of Pressure on Phase Transition in Hg2Cl2 Crystals, J. Phys. Soc. Jpn. 49 (2) (1980) 554–556, https://doi.org/10.1143/JPSJ.49.554.

[56] A.A. Kvasov, Y.F. Markov, E.M. Roginskii, M.B. Smirnov, Phonon Dispersion and Pressure Behavior of Hg2Cl2 Crystals, Ferroelectrics. 397 (1) (2010) 81–89, https://doi.org/10.1080/00150193.2010.484732.

[57] S. Ghosh, J. Chowdhury, Pressure induced structural phase transitions of technologically significant mercurous chloride at room temperature: An account from first-principle DFT and Born-Oppenheimer molecular dynamics studies, J. Appl. Phys. 130 (2021), 225103, https://doi.org/10.1063/5.0068049.

[58] E.M. Roginskii, A.S. Krylov, Y.F. Markov, M.B. Smirnov, Lattice dynamics and baric behavior of phonons in Hg2Cl2 crystals at high hydrostatic pressures, Bull. Russ. Acad. Sci. Phys. 80 (9) (2016) 1033–1037, https://doi.org/10.3103/S1062873816090409.

[59] J. Heyd, G.E. Scuseria, M. Ernzerhof, Hybrid functionals based on a screened Coulomb potential, J. Chem. Phys. 118 (18) (2003) 8207–8215, https://doi.org/10.1063/1.1564060.

[60] P. Giannozzi, O. Baseggio, P. Bonfà, D. Brunato, R. Car, I. Carnimeo, C. Cavazzoni, S. de Gironcoli, P. Delugas, F. Ferrari Ruffino, A. Ferretti, N. Marzari, I. Timrov, A. Urru, S. Baroni, Quantum ESPRESSO toward the exascale, J. Chem. Phys. 152 (2020), 154105, https://doi.org/10.1063/5.0005082.

[61] P. Giannozzi, O. Andreussi, T. Brumme, O. Bunau, M. Buongiorno Nardelli, M. Calandra, R. Car, C. Cavazzoni, D. Ceresoli, M. Cococcioni, N. Colonna, I. Carnimeo, A. Dal Corso, S. de Gironcoli, P. Delugas, R.A. DiStasio, A. Ferretti, A. Floris, G. Fratesi, G. Fugallo, R. Gebauer, U. Gerstmann, F. Giustino, T. Gorni, J. Jia, M. Kawamura, H.-Y. Ko, A. Kokalj, E. Küçükbenli, M. Lazzeri, M. Marsili, N. Marzari, F. Mauri, N.L. Nguyen, H.-V. Nguyen, A. Otero-de-la-Roza, L. Paulatto, S. Poncé, D. Rocca, R. Sabatini, B. Santra, M. Schlipf, A.P. Seitsonen, A. Smogunov, I. Timrov, T. Thonhauser, P. Umari, N. Vast, X. Wu, S. Baroni, Advanced capabilities for materials modelling with Quantum ESPRESSO, J. Phys.: Condens. Matter. 29 (46) (2017) 465901, https://doi.org/10.1088/1361-648X/aa8f79.

[62] P. Giannozzi, S. Baroni, N. Bonini, M. Calandra, R. Car, C. Cavazzoni, D. Ceresoli, G.L. Chiarotti, M. Cococcioni, I. Dabo, A. Dal Corso, S. de Gironcoli, S. Fabris, G. Fratesi, R. Gebauer, U. Gerstmann, C. Gougoussis, A. Kokalj, M. Lazzeri, L. Martin-Samos, N. Marzari, F. Mauri, R. Mazzarello, S. Paolini, A. Pasquarello, L. Paulatto, C. Sbraccia, S. Scandolo, G. Sclauzero, A.P. Seitsonen, A. Smogunov, P. Umari, R.M. Wentzcovitch, QUANTUM ESPRESSO: a modular and open-source software project for quantum simulations of materials, J. Phys.: Condens. Matter. 21 (2009), 395502, https://doi.org/10.1088/0953-8984/21/39/395502.

[63] P.E. Blöchl, Projector augmented-wave method, Phys. Rev. B. 50 (24) (1994) 17953–17979, https://doi.org/10.1103/PhysRevB.50.17953.

[64] A. Dal Corso, Pseudopotentials periodic table: From H to Pu, Comput. Mater. Sci. 95 (2014) 337–350, https://doi.org/10.1016/j.commatsci.2014.07.043.

[65] A. Benassi, PWSCF 's epsilon.x user's manual, (2008). https://ir.library.dc-uoit.ca/bitstream/10155/159/3/McNelles_Phillip_appendixA.pdf.

[66] F.D. Murnaghan, The Compressibility of Media under Extreme Pressures, PNAS. 30 (1944) 244 LP – 247. 10.1073/pnas.30.9.244.

[67] F. Birch, Finite Elastic Strain of Cubic Crystals, Phys. Rev. 71 (11) (1947) 809–824, https://doi.org/10.1103/PhysRev.71.809.

[68] E. Ejder, Some optical properties of Hg2Cl2, J. Phys. Chem. Solids. 31 (3) (1970) 453–462, https://doi.org/10.1016/0022-3697(70)90085-5.

[69] I. Pelant, M.N. Popova, J. Hála, M. AmbroŽ, V. Lhotská, K. Vacek, Two-photon absorption and energy band structure of orthorhombic Hg2Cl2 crystals, Czech, J Phys. 37 (10) (1987) 1183–1197, https://doi.org/10.1007/BF01597034.

[70] X. Yin Jiang, T. Itoh, T. Goto, Reflection and Absorption Edge Spectra in Mercurous Halide Single Crystals, J. Phys. Soc. Jpn. 53 (10) (1984) 3672–3675, https://doi.org/10.1143/JPSJ.53.3672.

[71] N.J. Calos, C.H.L. Kennard, R.L. Davis, The structure of calomel, Hg2Cl2, derived from neutron powder data, Z, Kristallogr. Cryst. Mater. 187 (3-4) (1989) 305–307, https://doi.org/10.1524/zkri.1989.187.3-4.305.

[72] E. Dorm, Intermetallic distances in mercury(I) halides Hg2F2, Hg2Cl2, and Hg2Br2, J. Chem. Soc. D. (1971) 466–467, https://doi.org/10.1039/C29710000466.

[73] A. Majumdar, R. Ahuja, Pressure induced structural phase transition and piezochromism in photovoltaic sillen compounds PbBiO2X (X = Cl, Br & I), Appl. Mater. Today. 26 (2022), 101372, https://doi.org/10.1016/j.apmt.2022.101372.

[74] Y. Liu, H. Du, L. Fang, F. Sun, H. Su, Z. Ge, W. Guo, J. Zhu, Pressure-driven electronic phase transition in the high-pressure phase of nitrogen-rich 1H-tetrazoles, RSC Adv. 11 (35) (2021) 21507–21513, https://doi.org/10.1039/D1RA00522G.

[75] K.A. Irshad, V. Srihari, S. Kalavathi, N.V.C. Shekar, Structural phase transition, equation of state and phase diagram of functional rare earth sesquioxide ceramics (Eu1−xLax)2O3, Sci Rep. 10 (2020) 11829, https://doi.org/10.1038/s41598-020-68400-9.

[76] J.M. Perez-Mato, M.I. Aroyo, D. Orobengoa, Symmetry considerations in structural phase transitions, EPJ Web Conf. 22 (2012), https://doi.org/10.1051/epjconf/20122200008.

[77] S. Banerjee, A.B. Garg, H.K. Poswal, Pressure driven structural phase transition in EuTaO4: experimental and first principles investigations, J. Phys.: Condens. Matter. 34 (2022), 135401, https://doi.org/10.1088/1361-648x/ac484f.

[78] K. Mencel, P. Starynowicz, M. Siczek, A. Piecha-Bisiorek, R. Jakubas, W. Medycki, Symmetry breaking structural phase transitions, dielectric properties and molecular motions of formamidinium cations in 1D and 2D hybrid compounds: (NH2CHNH2)3[Bi2Cl9] and (NH2CHNH2)3[Bi2Br 9], Dalton Trans. 48 (39) (2019) 14829–14838, https://doi.org/10.1039/C9DT02916H.

[79] O.D.D. Couto, J. Puebla, E.A. Chekhovich, I.J. Luxmoore, C.J. Elliott, N. Babazadeh, M.S. Skolnick, A.I. Tartakovskii, A.B. Krysa, Charge control in InP/(Ga, In)P single quantum dots embedded in Schottky diodes, Phys. Rev. B. 84 (2011), 125301, https://doi.org/10.1103/PhysRevB.84.125301.

[80] N.T. Han, V.K. Dien, M.-F. Lin, Excitonic effects in the optical spectra of Li2SiO3 compound, Sci Rep. 11 (2021) 7683, https://doi.org/10.1038/s41598-021-87269-w.

[81] J.H. Daniel, P. Howsmon, IEEE Standard Definitions of Terms for Radio Wave Propagation, IEEE Std 211-1997. (1997) 1–44. 10.1109/IEEESTD.1997.8638365.

[82] S.E. Braslavsky, Glossary of terms used in photochemistry, 3rd edition (IUPAC Recommendations 2006):, Pure Appl. Chem. 79 (2007) 293–465. doi:10.1351/pac200779030293.

[83] P.O. Nilsson, Solid State Physics, Volume 29, in: D.T. Henry Ehrenreich, Frederick Seitz (Ed.), 1st Editio, Academic Press, New York, 1974: p. 387. https://www.elsevier.com/books/solid-state-physics/ehrenreich/978-0-12-607729-2.

[84] R. de L. Kronig, On the Theory of Dispersion of X-Rays, J. Opt. Soc. Am. 12 (1926) 547–557. 10.1364/JOSA.12.000547.

[85] H.A. Kramers, La diffusion de la lumière par les atomes, Atti Del Congresso Internationale Dei Fisici, Como. (1927) 545–557. https://www.lorentz.leidenuniv.nl/IL-publications/sources/Kramers_27.pdf.

[86] A.A. Kaplyanskii, Raman Spectra and Structural Phase Transitions in Improper Ferroelastics Hg2Cl2 and Hg2Br2, in: A.V.M. Bendow B., Birman J.L. (Ed.), Theory of Light Scattering in Condensed Matter, Springer, Boston, MA, 1976. 10.1007/978-1-4613-4301-1_4.

[87] R. Das, S. Chowdhury, A. Majumdar, D. Jana, Optical properties of P and Al doped silicene: a first principles study, RSC Adv. 5 (2015) 41–50, https://doi.org/10.1039/C4RA07976K.

[88] P. Nath, D. Sanyal, D. Jana, Optical properties of transition metal atom adsorbed graphene: A density functional theoretical calculation, Phys. E: Low-Dimens. Syst. Nanostructures. 69 (2015) 306–315, https://doi.org/10.1016/j.physe.2015.02.004.

[89] R. Saniz, L.-H. Ye, T. Shishidou, A.J. Freeman, Structural, electronic, and optical properties of NiAl3: First-principles calculations, Phys. Rev. B. 74 (2006) 14209, https://doi.org/10.1103/PhysRevB.74.014209.

[90] M. Saeed, M.A. Ali, S. Murad, R. Ullah, T. Alshahrani, A. Laref, G. Murtaza, Pressure induced structural, electronic, optical and thermal properties of CsYbBr 3, a theoretical investigation, J. Mater. Res. Technol. 10 (2021) 687–696, https://doi.org/10.1016/j.jmrt.2020.12.052.

[91] M.Ya. Rudysh, M.G. Brik, O.Y. Khyzhun, A.O. Fedorchuk, I. v Kityk, P.A. Shchepanskyi, V.Yo. Stadnyk, G. Lakshminarayana, R.S. Brezvin, Z. Bak, M. Piasecki, Ionicity and birefringence of α-LiNH4SO4 crystals: ab initio DFT study, X-ray spectroscopy measurements, RSC Adv. 7 (2017) 6889–6901. 10.1039/C6RA27386F.

[92] Y. Huang, W. Jie, G. Zha, Band gap, electronic and optical properties of Zn1−xCrxS: An ab initio study, J. Alloys Compd. 555 (2013) 117–122, https://doi.org/10.1016/j.jallcom.2012.11.201.
[93] J. Toudert, R. Serna, Interband transitions in semi-metals, semiconductors, and topological insulators: a new driving force for plasmonics and nanophotonics [Invited], Opt. Mater. Express. 7 (2017) 2299–2325, https://doi.org/10.1364/OME.7.002299.
[94] J. Yin, H.N.S. Krishnamoorthy, G. Adamo, A.M. Dubrovkin, Y. Chong, N.I. Zheludev, C. Soci, Plasmonics of topological insulators at optical frequencies, NPG Asia Mater. 9 (2017) e425–e425. 10.1038/am.2017.149.
[95] S. v. Cai W., Optical Properties of Metal-Dielectric Composites, in: Optical Metamaterials, Springer, New York, NY, 2010. 10.1007/978-1-4419-1151-3_2.
[96] D.R. Penn, Wave-Number-Dependent Dielectric Function of Semiconductors, Phys. Rev. 128 (5) (1962) 2093–2097, https://doi.org/10.1103/PhysRev.128.2093.
[97] H. Lu, X. Meng, Correlation between band gap, dielectric constant, Young's modulus and melting temperature of GaN nanocrystals and their size and shape dependences, Sci. Rep. 5 (2015) 16939, https://doi.org/10.1038/srep16939.
[98] G. Suchaneck, D. Chvostová, J. Kousal, V. Železný, A. Lynnyk, L. Jastrabík, G. Gerlach, A. Dejneka, Vacuum-ultraviolet ellipsometry spectra and structural properties of Pb(Zr, Ti)O3 films, Thin Solid Films. 519 (9) (2011) 2885–2888, https://doi.org/10.1016/j.tsf.2010.11.076.
[99] K. Jiang, R. Zhao, P. Zhang, Q. Deng, J. Zhang, W. Li, Z. Hu, H. Yang, J. Chu, Strain and temperature dependent absorption spectra studies for identifying the phase structure and band gap of EuTiO3 perovskite films, Phys. Chem. Chem. Phys. 17 (47) (2015) 31618–31623, https://doi.org/10.1039/C5CP06318C.
[100] P.D. Khang, M. Davoudiniya, L.T.T. Phuong, T.C. Phong, M. Yarmohammadi, Optical interband transitions in strained phosphorene, Phys. Chem. Chem. Phys. 21 (27) (2019) 15133–15141, https://doi.org/10.1039/C9CP01833F.
[101] W. Li, K. Jiang, J. Zhang, X. Chen, Z. Hu, S. Chen, L. Sun, J. Chu, Temperature dependence of phonon modes, dielectric functions, and interband electronic transitions in Cu2ZnSnS4 semiconductor films, Phys. Chem. Chem. Phys. 14 (2012) 9936–9941, https://doi.org/10.1039/C2CP41209H.
[102] M.W. Kim, P. Murugavel, S. Parashar, J.S. Lee, T.W. Noh, Origin of the 2 eV peak in optical absorption spectra of LaMnO3: an explanation based on the orbitally degenerate Hubbard model, New J. Phys. 6 (2004) 156–156. 10.1088/1367-2630/6/1/156.
[103] F.A. Jenkins, H.E. White, Fundamentals of Optics, McGraw-Hill, 2018. https://books.google.co.in/books?id=4SPCJ0wtFSUC.
[104] H. ben Abdallah, W. Ouerghui, Hybrid functional calculations of electro-optical properties of novel Ga1−xInxTe ternary chalcogenides, Appl. Phys. A. 126 (2020) 387. 10.1007/s00339-020-03581-8.
[105] M. Ramzan, Y. Li, R. Chimata, R. Ahuja, Electronic, mechanical and optical properties of Y2O3 with hybrid density functional (HSE06), Comput. Mater. Sci. 71 (2013) 19–24, https://doi.org/10.1016/j.commatsci.2012.12.026.
[106] M. Nishiwaki, H. Fujiwara, Highly accurate prediction of material optical properties based on density functional theory, Comput. Mater. Sci. 172 (2020), 109315, https://doi.org/10.1016/j.commatsci.2019.109315.
[107] S.S.A. Shah, N. Muhammad, G. Murtaza, A. Khan, M.W. Ashraf, S. Khan, Hybrid functional calculations of optoelectronic properties of ultra-wide bandgap LiSmO2: A first-principle study, Solid State Commun. 342 (2022) 114619, https://doi.org/10.1016/j.ssc.2021.114619.
[108] S. Hussain, L. Guo, T. He, Hybrid Density Functional Theory Study on Structural and Optoelectronic Properties of ZnSe1–xTex for the Photocatalytic Applications, J. Phys. Chem. C. 125 (29) (2021) 16235–16245, https://doi.org/10.1021/acs.jpcc.1c0367010.1021/acs.jpcc.1c03670.s001.
[109] M. Gerosa, C.E. Bottani, C. di Valentin, G. Onida, G. Pacchioni, Accuracy of dielectric-dependent hybrid functionals in the prediction of optoelectronic properties of metal oxide semiconductors: a comprehensive comparison with many-body GW and experiments, J. Phys.: Condens. Matter. 30 (2017), 044003, https://doi.org/10.1088/1361-648x/aa9725.
[110] G. Tse, Evaluation of the structural, electronic, optical, elastic, mechanical, and vibrational properties of graphene-like g-GaN using density functional theory, AIP Adv. 11 (2021), 115211, https://doi.org/10.1063/5.0063765.
[111] Q. Mahmood, M. Hassan, N.A. Noor, Systematic study of room-temperature ferromagnetism and the optical response of Zn1−xTMxS/Se (TM = Mn, Fe Co, Ni) ferromagnets: first-principle approach, J. Phys.: Condens. Matter. 28 (2016), 506001, https://doi.org/10.1088/0953-8984/28/50/506001.
[112] S.S. D. R. Smith, W. J. Padilla, D. C. Vier, R. Shelby, S. C. Nemat-Nasser, N. Kroll, Left-Handed Metamaterials, in: Photonic Crystals and Light Localization in the 21st Century, NATO Scien, Springer, Dordrecht, 2001. 10.1007/978-94-010-0738-2_25.
[113] D.R. Smith, W.J. Padilla, D.C. Vier, S.C. Nemat-Nasser, S. Schultz, Composite Medium with Simultaneously Negative Permeability and Permittivity, Phys. Rev. Lett. 84 (18) (2000) 4184–4187, https://doi.org/10.1103/PhysRevLett.84.4184.
[114] V.G. Veselago, The electrodynamics of substances with simultaneously negative values of ε and μ, Sov. Phys. Usp. 10 (1968) 509–514, https://doi.org/10.1070/pu1968v010n04abeh003699.
[115] L.J. Wang, A. Kuzmich, A. Dogariu, Gain-assisted superluminal light propagation, Nature. 406 (6793) (2000) 277–279, https://doi.org/10.1038/35018520.
[116] D. Mugnai, A. Ranfagni, R. Ruggeri, Observation of Superluminal Behaviors in Wave Propagation, Phys. Rev. Lett. 84 (21) (2000) 4830–4833, https://doi.org/10.1103/PhysRevLett.84.4830.
[117] J. Guo, A. Tudi, S. Han, Z. Yang, S. Pan, α-SnF2: A UV Birefringent Material with Large Birefringence and Easy Crystal Growth, Angew. Chem. Int. Ed. 60 (2021) 3540–3544, https://doi.org/10.1002/anie.202014279.
[118] Z. Zhang, Y. Wang, B. Zhang, Z. Yang, S. Pan, Designing Deep-UV Birefringent Crystals by Cation Regulation, Chem. Eur. J. 24 (44) (2018) 11267–11272, https://doi.org/10.1002/chem.201802866.
[119] C.-S. Lin, A.-Y. Zhou, W.-D. Cheng, N. Ye, G.-L. Chai, Atom-Resolved Analysis of Birefringence of Nonlinear Optical Crystals by Bader Charge Integration, J. Phys. Chem. C. 123 (2019) 31183–31189. 10.1021/acs.jpcc.9b08762.
[120] Y. Li, F. Liang, S. Zhao, L. Li, Z. Wu, Q. Ding, S. Liu, Z. Lin, M. Hong, J. Luo, Two Non-π-Conjugated Deep-UV Nonlinear Optical Sulfates, J. Am. Chem. Soc. 141 (2019) 3833–3837. 10.1021/jacs.9b00138.

PHASE TRANSITIONS
2023, VOL. 96, NO. 6, 446–463
https://doi.org/10.1080/01411594.2023.2209258

Taylor & Francis
Taylor & Francis Group

Temperature dependent phase transition and negative thermal expansion of Hg_2Cl_2 compound: insights from first-principle DFT and Born-Oppenheimer on the fly molecular dynamics calculations

Swarup Ghosh and Joydeep Chowdhury

Department of Physics, Jadavpur University, Kolkata, India

ABSTRACT

The paper is aimed to understand the key phonon modes that are responsible for the temperature dependent structural phase transition and negative thermal expansion of Hg_2Cl_2 compound for the first time with the aid of density functional theory and Born-Oppenheimer on the fly molecular dynamics calculations. The phonon dispersion spectra, phonon density of states and Grüneisen parameters for the body-centered tetragonal and base-centered orthorhombic phases of the compound have been explored in detail. The order parameter associated with the phase transition and its nature has also been reported herewith. We believe that the present study will not only help for futuristic designs of improved functionalized systems with Hg_2Cl_2 compound but also can augment their applications in thermoelectric conversion systems, fibre-optic communications, thermal expansion compensators and in fuel cells.

ARTICLE HISTORY
Received 1 November 2022
Accepted 24 April 2023

KEYWORDS
Structural phase transition; ferroelastic; phonon modes; negative thermal expansion; fuel cells

1. Introduction

Phase transitions are considered as one of the fundamental physical processes that have drawn significant attentions over the years among the physicists and chemists. During phase transition, physical and thermodynamic parameters of a system can alter significantly, as it undergoes transformation from one physical state to another. The most familiar examples of phase transitions in nature is the conversion of ice to water and then into vapour with the rise in temperature [1–3]. However, in de facto there exists many exotic examples of phase transitions in physics that include conversions of ferromagnetic/ antiferromagnetic materials into paramagnetic at the Curie point (T_{Curie})/Neel temperature (T_{N}) [4–11], transformation of conducting materials into superconductors at the critical temperature [12,13], conversion of the normal fluid Helium-I to the superfluid Helium-II at the lambda point [14–16], order–disorder phase transition in brass [17], the temperature and/or pressure driven structural phase transitions in the crystals [18–38], to name a few.

Mercurous chloride (Hg_2Cl_2) aka calomel is reckoned as a charge transfer insulator [39] and is extensively used as electrode material, white pigment and polarizing prisms [40–42]. The material is known to show strong birefringence, befitting its use in acousto-optic tuneable filters for the development of hyperspectral imagery over large UV-Vis-LWIR window of the electromagnetic spectrum [43,44]. Hg_2Cl_2 also exhibits the negative thermal expansion (NTE) behaviour at high temperature [45,46]. At room temperature ($T = 300$ K) and under ambient pressure ($P = 0$ GPa)

CONTACT Joydeep Chowdhury joydeep72_c@rediffmail.com; joydeep.chowdhury@jadavpuruniversity.in
Supplemental data for this article can be accessed online at https://doi.org/10.1080/01411594.2023.2209258.

Hg_2Cl_2 is known to possess in the body-centered tetragonal [*I4/mmm* (D_{4h}^{17})] phase and undergoes pressure-driven structural phase transitions where the successive transformations from the body-centered tetragonal [*I4/mmm* (D_{4h}^{17})] → base-centered orthorhombic [*Cmcm* (D_{2h}^{17})] and from the base-centered orthorhombic [*Cmcm* (D_{2h}^{17})] → primitive orthorhombic [*Pnma* (D_{2h}^{16})] phases of the compound at transition pressures (P_T) 0.25 and 9 GPa, respectively have been reported experimentally and from the first-principle calculations [22,47–50]. Experimental observations also suggest that Hg_2Cl_2 compound at low temperature (ca. $T \sim 186$ K) encounters *I4/mmm* (D_{4h}^{17}) → *Cmcm* (D_{2h}^{17}) structural phase transition and finally end up in the base-centered orthorhombic [*Cmcm* (D_{2h}^{17})] phase [51–55]. Though the existence of two different phases of the Hg_2Cl_2 compound with temperature has been reported experimentally from anomalous X-ray transmission, inelastic neutron and Raman scattering studies [51–54], the underlying cause that drives this transition has not been addressed so far. Understanding the physics behind the above referred phase transition and NTE behaviour will not only help for the sensible futuristic designs of improved functionalized systems or the prototypes but also can augment their applications surpassing the existing real-world technologies.

Considering the above issues in mind, the present paper reports for the first time a detail study on the temperature dependent *I4/mmm* (D_{4h}^{17}) → *Cmcm* (D_{2h}^{17}) structural phase transition of the compound from the first-principle density functional theory (DFT) and Born-Oppenheimer on the fly molecular dynamics (BOMD) simulations. The order parameter, nature of the phase transition and the Grüneisen parameters have also been unveiled. The present study will help to identify the key phonon modes that stand responsible for the above referred phase transition and NTE behaviour of the compound. We believe that this in-depth study may be helpful for its applications in fibre-optic communications, thermomechanical actuators and in fuel cells.

2. Computational methodology

The first-principle density functional theory (DFT) calculations have been accomplished from generalized gradient approximation (GGA) with the Heyd–Scuseria–Ernzerhof (HSE) exchange–correlation functional [56] using Quantum ESPRESSO (QE) software [57–59]. The crystal structure of the body-centered tetragonal [*I4/mmm* (D_{4h}^{17})] phase of Hg_2Cl_2 compound at room temperature ($T = 300$ K) has been primarily noted from the experimentally determined X-ray diffraction data [60]. The experimentally determined structural parameters of the compound have been initially optimized through the variable cell relaxation scheme following Broyden-Fletcher-Goldfarb-Shanno (BFGS) method [61–64] at pressure (P) = 0 GPa using the DFT method. The electron-ion interactions have been taken into account from the pseudopotential approach using the projector augmented wave (PAW) method [65]. Valance electrons $5d^{10}6s^2$ and $3s^23p^5$ associated with the respective Hg and Cl atoms of the compound are represented as plane wave with kinetic energy cut-off at 80 Ry. The unitcell of Hg_2Cl_2 crystal system is allowed to relax until the Hellmann–Feynman (H–F) force reaches a value less than 10^{-4} Ry/Bohr for the maximum cell pressure of 10^{-2} GPa and the total electronic energy difference $<10^{-14}$ Ry. A gamma-centered k-point mesh of $10\times10\times10$ Monkhorst–Pack grid has been fixed for the optimization of the crystal structure. To precisely estimate the relativistic effect of heavy Hg atom, the spin–orbit coupling (SOC) correction and relativistic pseudopotentials have been incorporated in the calculations.

Using optimized geometry of the unitcell, a $2\times2\times2$ supercell with 64 atoms for the tetragonal (*I4/mmm*) phase of Hg_2Cl_2 compound has been constructed. Born-Oppenheimer on the fly molecular dynamics (BOMD) simulations for the *I4/mmm* phase of Hg_2Cl_2 compound have been accomplished at room temperature ($T = 300$ K) on the supercell. The BOMD simulations have been accomplished using HSE + SOC level of theory keeping the convergence criteria for H–F force, cell pressure and total electronic energy similar to that used for the static DFT calculations. On the fly molecular dynamics simulations have been performed using 'variable-cell molecular dynamics' method as implemented in QE software [57–59]. Total energy of the supercell ($\tilde{E}$), so

obtained from the simulation run at the optimized volume (V) are then estimated by changing V of the systems. The $\tilde{E}$–V plots are finally fitted using fourth-order Birch–Murnaghan (B–M) equation of states [66,67]. All the simulations were performed within the chosen NPT ensemble whose temperature is controlled by the Nose–Hoover thermostat [68–70]. In the BOMD simulation, the supercell for the *I4/mmm* phase of Hg_2Cl_2 system at room temperature has been equilibrated initially for 10 ps followed by further simulations for 48 ps with the time step of 1 fs. The refined structure of Hg_2Cl_2 at room temperature ($T = 300$ K), as obtained from the BOMD calculations, is then relaxed again by decreasing the temperature of the ensemble spanning in the range from 275 to 80 K to attain the BOMD simulated supercell geometry for the low temperature base-centred orthorhombic [*Cmcm* (D_{2h}^{17})] phase of the Hg_2Cl_2 compound. The output files, so generated after running the BOMD simulations, consist of the atomic positions, Bravais-lattice indices, lattice parameters and their corresponding angles of the refined optimized structures of the compounds. The symmetries of those structures have been systematically determined by extracting the BOMD simulated output files in the visualization software packages XCrySDen [71] and VESTA [72]. In this connection it may be relevant to mention that in the present report, we started our calculation from experimentally determined X-ray diffraction data for the *I4/mmm* phase of Hg_2Cl_2 compound at $T =$ 300 K, hence, we subsequently estimate the temperature-dependent phase transition of the compound at lower temperature where the system is shown to undergo structural phase transition from *I4/mmm* to *Cmcm* phase.

The temperature dependent phonon dispersion spectra, phonon density of states (PhDOS) and Grüneisen parameters for the *I4/mmm* and *Cmcm* phases of the Hg_2Cl_2 system have been estimated by calculating second (harmonic) and third-order (anharmonic) interatomic force constants (IFCs) $K_{ij}(\lambda)$ following the supercell approach using Phono3py suite of software [73]. The $K_{ij}(\lambda)$ for atom λ has been estimated by introducing a set of finite atomic displacements with the amplitude of ± 0.03 Å to the supercells along x, y and z directions in three – dimensional Euclidean space. The magnitude of $K_{ij}(\lambda)$ determines the curvature, while its sign signifies the nature of the potential energy hypersurface. A denser grid of 30×30×30 k-point mesh has been used for calculating the phonon dispersion spectra, PhDOS and Grüneisen parameters. The transverse optical (TO) and longitudinal optical (LO) phonon modes have been isolated from the non-analytic term correction at long-wavelength ($k \rightarrow 0$) limit.

3. Results and discussions

3.1. Crystal structures and temperature dependent structural phase transition of Hg_2Cl_2 compound

The Hg_2Cl_2 compound, at room temperature ($T = 300$ K) and at $P = 0$ GPa, crystallizes in the body-centered tetragonal phase with *I4/mmm* (D_{4h}^{17}) space group symmetry (space group no. 139) [60]. The chosen unitcell of the crystal contains one formula unit ($Z = 2$) with the Wyckoff sites at 4*e* (0, 0, 0.1157) and 4*e* (0, 0, 0.3380) are occupied by Hg and Cl atoms, respectively. Total energy of the unitcell (E) versus unitcell volume (V) for the *I4/mmm* (D_{4h}^{17}) phase of Hg_2Cl_2 system, as obtained from the static DFT calculations at HSE + SOC level of theory, is shown in Figure 1(a). The discrete points in the E versus V plot has been fitted using fourth order B–M equation of states [66,67]. From Figure 1(a), it is seen that E attains minimum value in the E–V curve at ∼ −455.873 Ry/atom for $V \sim 219.16$ Å^3. The optimized unitcell structure for *I4/mmm* phase of the compound is shown in Figure 1(b).

The nomenclature of the unitcell, as shown in Figure 1(b), has been adopted from our earlier report that depicted the structural and electronic properties of the compound under ambient condition [39]. Apical and the central mercury atoms are denoted as Hg(A) and Hg(C), respectively, while the linear and the neighbouring chlorine atoms for the compound are represented as Cl(L) and Cl(V), respectively, much in the same way as reported in our earlier publication [39]. The

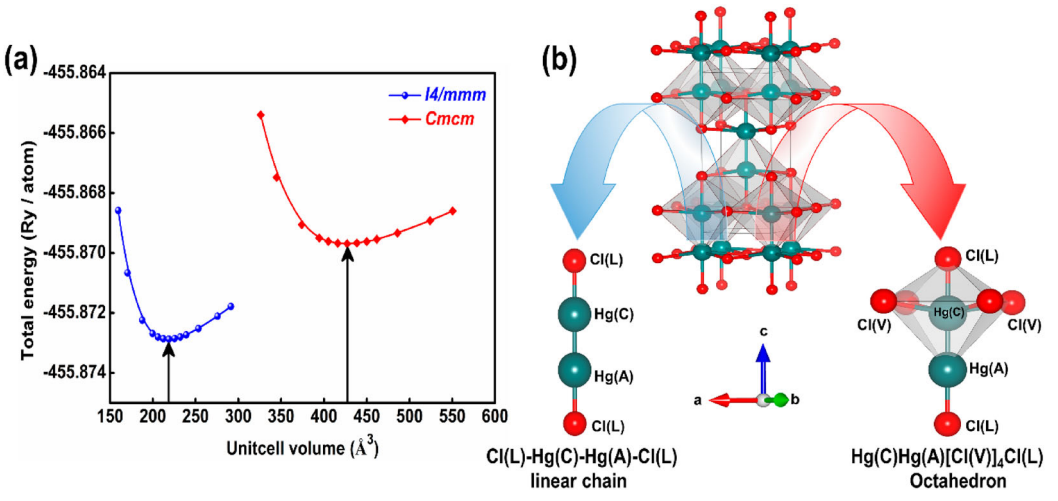

Figure 1. (a) Total energy of the unitcell versus unitcell volume plots for *I4/mmm* (blue trace), *Cmcm* (red trace) phases of Hg_2Cl_2 compound and (b) optimized geometry of the unitcell for *I4/mmm* phase of the compound as obtained from the static DFT calculations using HSE + SOC level of theory. [Vertical black arrows show the unitcell volume at minimum energy configuration on Figure (a). Emerald blue and red colours represent Hg and Cl atoms, respectively on Figure (b)].

crystal structure of the Hg_2Cl_2 compound in *I4/mmm* (D_{4h}^{17}) phase (Figure 1(b)) harbours successive distorted octahedral domains comprising of Hg(C), Hg(A) and Cl(L), Cl(V) atoms dispensed in the three-dimensional space. The associated lattice and structural parameters of the compound are shown in Table 1.

The variations in the supercell energy ($\tilde{E}$) of the Hg_2Cl_2 compound in its *I4/mmm* phase at room temperature ($T = 300$ K) with time is shown in Figure 2(a). After primary relaxations marked by concomitant rise in energy with time, the system attains equilibrium energy value after a lapse of ~ 10 ps. The refined supercell geometry of the system, so extracted from the from the BOMD simulation run at 30 ps time scale, is depicted in Figure 2(b).

The variation in the supercell volume (V) of Hg_2Cl_2 crystal in its *I4/mmm* phase as a function of temperature is shown in Figure 3(a). Interestingly, with decrease in temperature from 300 K, slight increase in V has been noticed until the temperature (T) attains 188 K, where distinct discontinuity in V–T curve has been observed. Before this discontinuity, the system remains in the *I4/mmm* phase. The sharp discontinuity in the V–T curve is followed by appreciable rise in the supercell volume from ~ 1779.89 to 3420.44 Å^3. Supercell volume ~ 3420.44 Å^3 corresponds to the base-centered orthorhombic [*Cmcm* (D_{2h}^{17})] phase of the compound. Such doubling of volume is also reported for the Hg_2Cl_2 crystal as it undergoes temperature dependent structural phase transition from *I4/mmm* (D_{4h}^{17}) $\rightarrow$ *Cmcm* (D_{2h}^{17}) phase at $T = 185$ K [76]. However, with further decrease in temperature from $T = 188$ K, the supercell volume of the system increases monotonically. The prominent discontinuity in the V–T curve at $T = 188$ K indicates structural phase transition of the

Table 1. The lattice and structural parameters for the I4/mmm phase of Hg_2Cl_2 compound as accomplished from the DFT calculation with HSE + SOC level of theory.

Parameters	This Study	Experiments [74,75]
a = b (Å)	4.482	4.479, 4.480
c (Å)	10.910	10.905, 10.910
V (Å^3)	219.16	218.77, 218.97
Hg(C)-Hg(A) (Å)	2.526	2.595, 2.526
Hg(C)-Cl(L) (Å)	2.424	2.362, 2.430
Cl(L)-Hg(C)-Hg(A)-Cl(L) (degree)	180	180

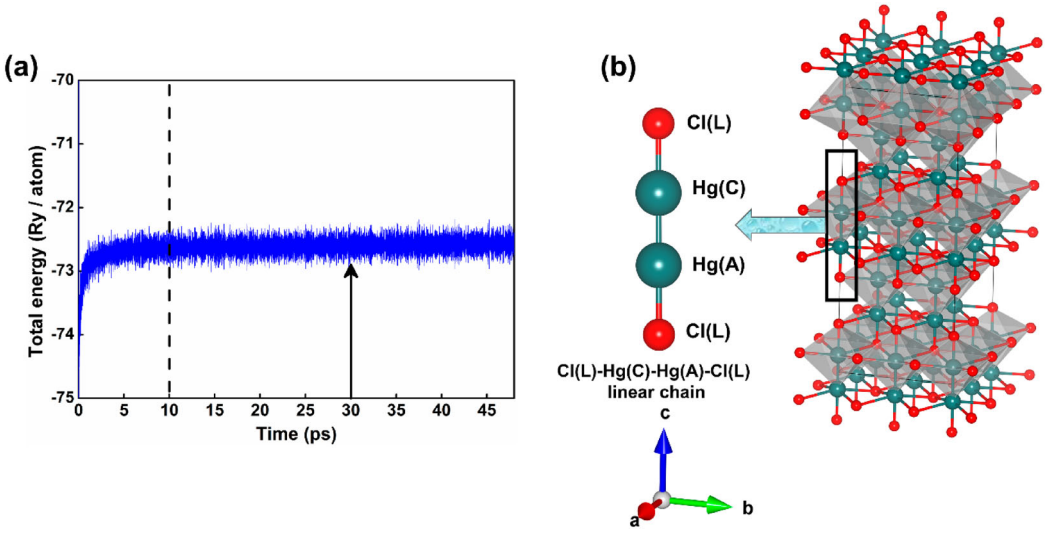

Figure 2. (a) Temporal variations of total energy and (b) the optimized geometry of 2×2×2 supercell for the *I4/mmm* phase of Hg_2Cl_2 crystal at room temperature (T = 300 K) as accomplished from the BOMD simulations. (Emarald blue and red colours show Hg and Cl atoms, respectively).

Hg_2Cl_2 compound from body-centered tetragonal [*I4/mmm* (D_{4h}^{17})] to base-centered orthorhombic [*Cmcm* (D_{2h}^{17})] phase. Strikingly enough this temperature T = 188 K closely corresponds to the transition temperature (T_c) ~ 186 K where the compound is experimentally reported to undergo temperature dependent *I4/mmm* (D_{4h}^{17}) → *Cmcm* (D_{2h}^{17}) structural phase transition [51]. Furthermore, the structural phase transition at T_c = 188 K for Hg_2Cl_2 system is associated with the discrete changes in supercell volume with temperature. This result indicates first-order phase transition of the system due to breaking of the translational symmetry. The alterations in the lattice parameters (a, b, c) of Hg_2Cl_2 compound as a function of temperature are shown in Figure 3(b). Akin to the V–T plot, the variations in the lattice parameters of the compound with temperature (Figure 3(b)) are marked by noticeable discontinuities at T = 188 K, which further corresponds to T_c that leads to the *I4/mmm* (D_{4h}^{17}) → *Cmcm* (D_{2h}^{17}) structural phase transition of the system under study.

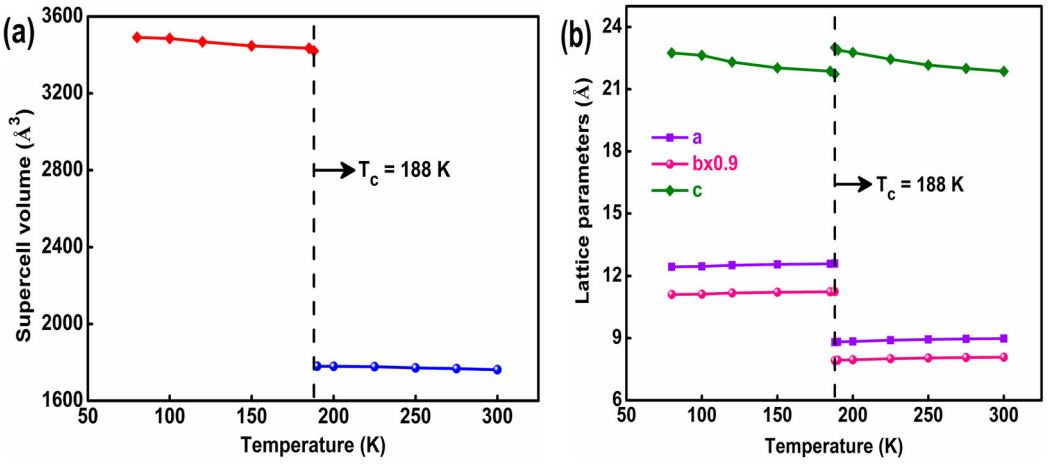

Figure 3. (a) Supercell volume and (b) lattice parameters versus temperature plots as obtained from the BOMD simulations. The transition temperature T_c has been marked with vertical dotted (------) line.

In this connection it is pertinent to mention that the decrease in supercell volume with temperature (Figure 3(a)) promotes the negative thermal expansion (NTE) behaviour of the compound in the temperature window ranging between 300 and 80 K. To understand the NTE of the system, the volumetric coefficient of thermal expansion (α) has been estimated using the following relation.

$$\alpha = \frac{1}{v}\frac{\partial v}{\partial T}. \tag{1}$$

The α values for the *I4/mmm* and *Cmcm* phases of the Hg_2Cl_2 compound at $T = 300$ and 185 K are found to be -1.34×10^{-4} K^{-1} and -7.62×10^{-4} K^{-1} respectively. The α value for the *I4/mmm* phase of the compound at $T = 300$ K closely resembles to the experimental observations as reported elsewhere [45,46]. Moreover, the NTE of the system may be linked with the variation of the crystallographic c-axis which is found to be significantly decreased with increase in T (Figure 3(b)). The detail discussion on NTE of Hg_2Cl_2 compound will be unveiled in the later section.

The total energy for the base-centered orthorhombic [*Cmcm* (D_{2h}^{17})] phase of Hg_2Cl_2 compound (that is experimentally known to remain stable at $T < 186$ K [51]) as a function BOMD simulation time and supercell volume are shown in Figure S1 (Supplementary Information). The $E - V$ plot for the *Cmcm* phase of the compound, as estimated from the DFT calculation, is also depicted in Figure 1(a). The optimized crystal structure for the *Cmcm* (D_{2h}^{17}) phase of Hg_2Cl_2 at temperature $T = 185$ K, so accomplished from the BOMD simulations is shown in Figure 4(a). The unitcell for the *Cmcm* phase of the crystal also contains one formula unit ($Z = 2$) and eight atoms in its unitcell (64 atoms in the $2\times2\times2$ supercell). The corresponding lattice and the structural parameters are shown in Table S1 (Supplementary Information). The lattice and structural parameters belonging to the supercell for *Cmcm* (D_{2h}^{17}) phase of the compound, as estimated from the BOMD calculations, are in close agreement with the available experimental results reported elsewhere [76]. From Tables 1 and S1, it is clearly seen that the structural parameters of the Hg_2Cl_2 system show distinct changes in the average value of Cl(L)–Hg(C)–Hg

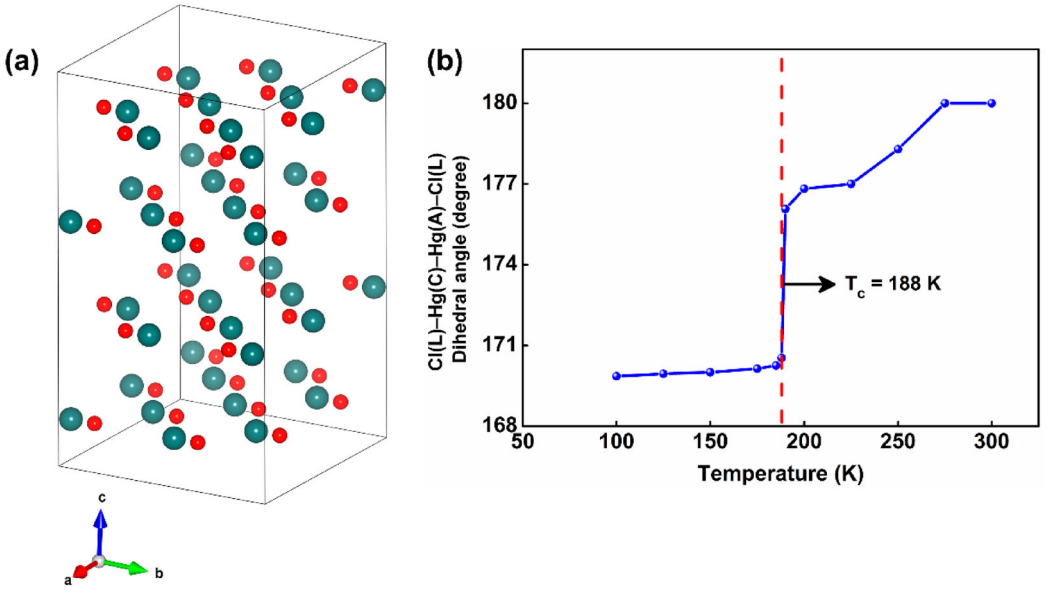

Figure 4. (a) Optimized $2\times2\times2$ supercell for the *Cmcm* phase of Hg_2Cl_2 at $T = 185$ K (Hg atoms are shown in emerald blue, while Cl atoms are in red colours). (b) Average Cl(L)–Hg(C)–Hg(A)–Cl(L) dihedral angle as a function of temperature as obtained from the BOMD simulations.

(A)–Cl(L) dihedral angle and Hg(C)–Hg(A), Hg(C)–Cl(L) bond lengths as it undergoes structural phase transitions from $I4/mmm$ (D_{4h}^{17}) → $Cmcm$ (D_{2h}^{17}) phase at $T_c = 188$ K. The variation of the average Cl(L)–Hg(C)–Hg(A)–Cl(L) dihedral angle as a function of temperature is shown in Figure 4(b). From Figure 4(b) it is seen that the average value of Cl(L)–Hg(C)–Hg(A)–Cl(L) dihedral angle deviates from planar dispositions (from 180° to 170.54°) of the associated atoms as the compound undergoes temperature dependent structural phase transition from the body-centered tetragonal to base-centered orthorhombic [$I4/mmm$ → $Cmcm$ (D_{2h}^{17})] phase at $T = 188$ K. Deviation from planarity of the Cl(L)–Hg(C)–Hg(A)–Cl(L) chain in the Hg_2Cl_2 system, in turn, can alter its anisotropic behaviour and this anisotropy may become more prominent as the compound undergoes phase transition at the specified T_c.

3.2. Order parameter linked with the paraelastic to ferroelastic phase transition of Hg_2Cl_2 compound

The order parameter associated with $I4/mmm$ (D_{4h}^{17}) → $Cmcm$ (D_{2h}^{17}) structural phase transition of the Hg_2Cl_2 compound at $T_c = 188$ K has been estimated from the second rank strain tensor function (e_{ij}) [77–79]. Hg_2Cl_2 is known to undergo paraelastic to ferroelastic phase transition with temperature [51,80,81]. While spontaneous strain is harboured in the ferroelastic phase of the compound, the paraelastic phase on the other hand does not show any such behaviour. In this temperature dependent paraelastic to ferroelastic phase transition of Hg_2Cl_2 compound, the strain tensor function e_{ij} is thus considered as the order parameter. Strain tensor $e_{ij} = 0$ represents the paraelastic phase of the compound with no spontaneous strain. However, $e_{ij} \neq 0$ suggests the ferroelastic behaviour of the system with spontaneous strain.

The tensor function is represented as

$$e_{ij} = \frac{1}{\sqrt{2}}(e_{xx} - e_{yy}), \tag{2}$$

where

$$e_{xx} = \frac{(c_o - c)}{a}, \tag{3}$$

and

$$e_{yy} = \frac{\left(\frac{a_0}{\sqrt{2}} - a\right)}{a}, \tag{4}$$

where 'a', 'c' and 'a_0', 'c_0' are the lattice parameter of the body-centered tetragonal ($I4/mmm$) structure and base-centered orthorhombic ($Cmcm$) phases of the compound respectively. Figure 5 shows the variation of e_{ij} (here the order parameter) as a function of temperature. Interestingly while e_{ij} shows near zero value for $T > 188$ K, however, for $T < 188$ K non-zero value of e_{ij} has been estimated. Zero and non-zero values of e_{ij} indicate that the Hg_2Cl_2 system belongs to the respective paraelastic $I4/mmm$ and ferroelastic $Cmcm$ phases above and below $T = 188$ K. Furthermore, the marked changes in the order parameters for the Hg_2Cl_2 compound at $T = 188$ K, not only corroborates $I4/mmm$ (D_{4h}^{17}) → $Cmcm$ (D_{2h}^{17}) structural phase transition at the pre referred temperature but also unveil $T_c = 188$ K for such transition.

3.3. Helmholtz free energy and transition temperature

To precisely determine the transition temperature (T_c) associated with $I4/mmm$ (D_{4h}^{17}) → $Cmcm$ (D_{2h}^{17}) structural phase transition of Hg_2Cl_2 compound, the Helmholtz free energies (F) of the

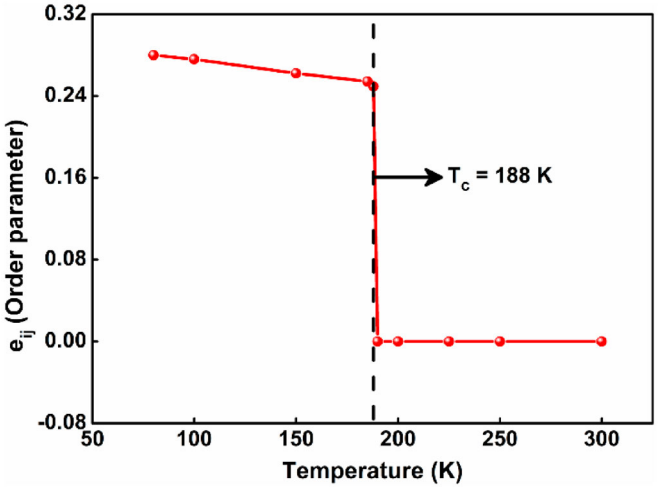

Figure 5. Variations of e_{ij} (order parameter) as a function of temperature as obtained from BOMD simulations.

systems have been estimated using the following relation:

$$F(T, \upsilon) = E(\upsilon) + F_{el}(T, \upsilon) + F_{ph}(T, \upsilon), \tag{5}$$

where E is the total ground state energy of the respective supercells, V signifies the supercell volume at temperature T, $F_{el}(T, \upsilon)$ and $F_{ph}(T, \upsilon)$ are the Helmholtz free energies of the electrons and phonons, respectively. $F_{el}(T, \upsilon)$ can be estimated using the following relation [82,83]:

$$F_{el}(T, \upsilon) \approx k_B T \int d\upsilon\, N_{el}(\upsilon)\, [n \ln n + (1 - n) \ln (1 - n)], \tag{5a}$$

where $N_{el}(\upsilon)$ is the electronic density of states and n is the Fermi occupation number.

$F_{ph}(T, \upsilon)$ has been calculated within the thermodynamic integration approach [83,84] and is expressed as

$$F_{ph}(T, \upsilon) = \int_0^1 d\upsilon\, F_{el}(\{R_I\}) - F_{el}(\{R_I^0\}) - \sum_{i,j} \frac{m}{2}\, u_i u_j\, D_{ij}(T, \upsilon)_\upsilon, \tag{5b}$$

where $F_{el}(\{R_I\}) - F_{el}(\{R_I^0\})$ corresponds to the change in electronic free energy at a certain fixed point of ionic coordinates $(\{R_I\})$. $u_i = \{R_i\} - \{R_i^0\}$, m is the atomic mass and D represents the dynamical matrix of the system. The thermodynamic average $(\langle \ldots\ldots \rangle_\upsilon)$ has been estimated using the BOMD simulations.

The variations of Helmholtz free energy difference (ΔF) as a function of temperature for the *I4/mmm* and *Cmcm* phases of the compound are shown in Figure 6. From Figure 6, it is clearly seen that the ΔF–T plots for the *I4/mmm* and *Cmcm* phases of the system intersect at temperature T = 186 K. The point of intersection at T = 186 K not only signifies the isoenergetic point where both the phases of Hg_2Cl_2 share the common Helmholtz free energy but also marks the transition temperature (T_c) that is linked with *I4/mmm* (D_{4h}^{17}) → *Cmcm* (D_{2h}^{17}) structural phase transition of the compound. Fortuitously, the result is in complete agreement with the experimental observation as reported elsewhere who reported T_c = 186 K associated with *I4/mmm* (D_{4h}^{17}) → *Cmcm* (D_{2h}^{17}) structural phase transition of the system [51]. The ΔF–T plots further divulge that body-centered tetragonal (*I4/mmm*) phase of the compound is thermodynamically more stable above T_c = 186 K, while below T_c ($T < T_c$) it is the base-centered orthorhombic (*Cmcm*) phase that is estimated to be thermodynamically stable. In this connection it may be relevant to mention that the same

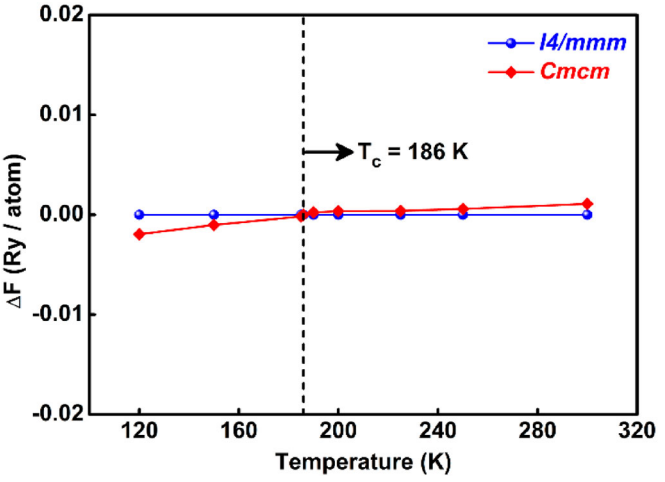

Figure 6. The Helmholtz free energy difference versus temperature plots for *I4/mmm* and *Cmcm* phases of the Hg_2Cl_2 compound.

Cmcm phase of Hg_2Cl_2 compound has been observed when the system is subjected to external pressure $P = 0.25$ GPa [22,48–50] as the one that is estimated at $P = 0$ GPa and $T = 186$ K [51]. However, at room temperature and $P = 9$ GPa the same compound is known to exist in the primitive orthorhombic (*Pnma*) phase [22,47].

3.4. Phonon dispersion relations at various temperatures

Hg_2Cl_2 compound belongs to the body-centered tetragonal [*I4/mmm* (D_{4h}^{17})] phase at room temperature. However, below the transition temperature $T_c = 186$ K, the system crystallizes to the base-centered orthorhombic [*Cmcm* (D_{2h}^{17})] phase (*vide supra*). Figures 7(A) and 8(A) show the phonon dispersion spectra for the *I4/mmm* and *Cmcm* phases of Hg_2Cl_2 compound along the high symmetry directions $\Gamma \rightarrow M \rightarrow X \rightarrow \Gamma \rightarrow P$ and $\Gamma \rightarrow Z \rightarrow X \rightarrow \Gamma \rightarrow Y$, respectively. The total and partial phonon density of states (PhDOS) for the *I4/mmm* phase of system at $T = 300$ K is shown in Figure 7(a) while that for the *Cmcm* phase at $T = 185$ K is depicted in Figure 8(a). The transverse acoustic (TA), longitudinal acoustic (LA) phonon modes are observed in the low-frequency window of the phonon dispersion spectra ranging between ~ 0–1 THz and 0–0.95 THz for the *I4/mmm* and *Cmcm* phases of Hg_2Cl_2 compound, respectively. The TA phonon branches are found to be doubly degenerate between $\Gamma \rightarrow M$, $X \rightarrow \Gamma$ and $\Gamma \rightarrow P$ directions for the *I4/mmm* phase of the compound, while the same is observed along $\Gamma \rightarrow Z$, $Z \rightarrow X$ and $\Gamma \rightarrow Y$ directions for the *Cmcm* phase. The optical phonon branches for both the *I4/mmm* and *Cmcm* phases of the Hg_2Cl_2 compound at $T = 300$ and 185 K, respectively, are localized in two disparate frequency regions ranging from ~ 0.69 to 4.41 THz, 7.07 to 8.85 THz and 0.64 to 4.56 THz, 6.76 to 8.76 THz. The corresponding PhDOS plots for the *I4/mmm*, *Cmcm* phases of the system (Figures 7(a) and 8(a)) indicate that the low- and high-frequency phonons are dominated by twisting/wagging/scissoring and stretching modes of the compound respectively. Interestingly, no imaginary or negative frequency has been noticed in the phonon dispersion curves. This result signifies that *I4/mmm* and *Cmcm* phases of the Hg_2Cl_2 compound at $T = 300$ and 185 K are dynamically stable.

Surprisingly, at $T = 186$ K, the phonon dispersion spectra (Figure 7(B)) exhibit prominent changes in the dispersions of the phonon branches, of which the slowest transverse acoustic X_1, low-lying optical X_8, Γ_6, Γ_{10}, M_{15} and P_{11} phonon modes undergo remarkable softening by decreasing their frequencies at the respective high symmetry points, X, Γ, M and P. Besides, at $T = 186$ K, hardening of the optical Γ_{23}, X_{24} and M_{24} phonon modes have also been noticed at the high-

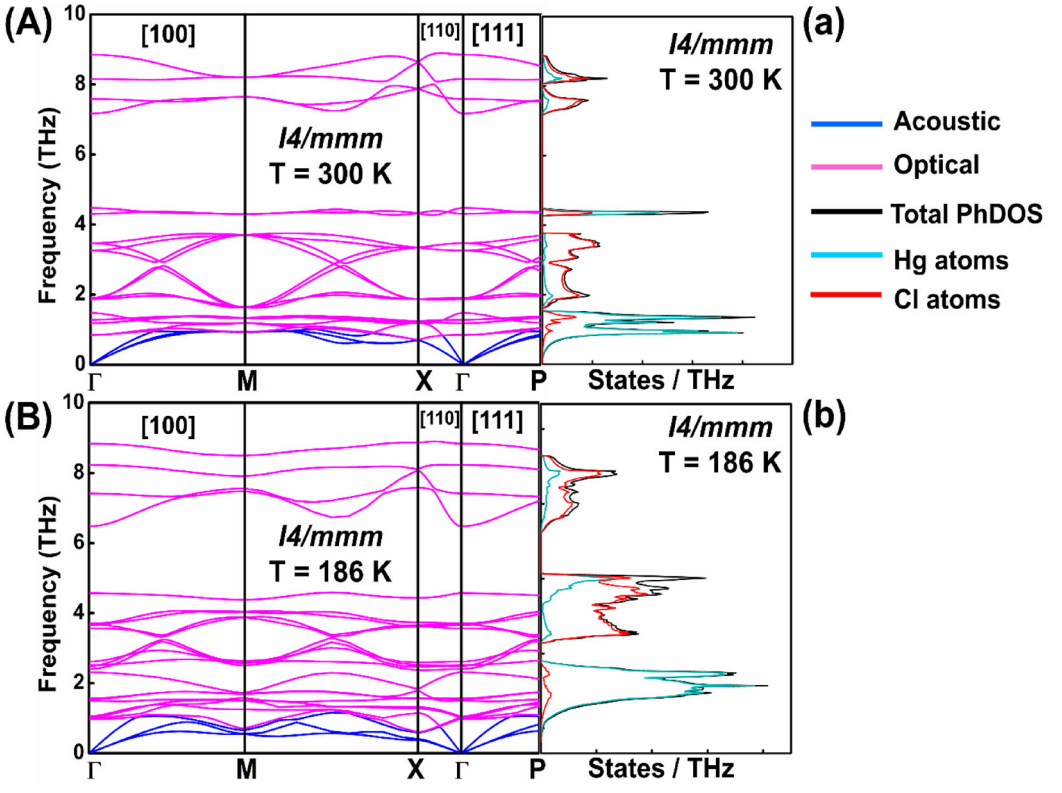

Figure 7. The phonon dispersion spectra along the high-symmetry points Γ→M→X→Γ→P for the *I4/mmm* phase of Hg_2Cl_2 at *T* = (A) 300 K and (B) 186 K. The total and atom resolved PhDOS for *I4/mmm* phase of the compound for temperature (a) 300 K and (b) 186 K.

symmetry points Γ, X and M, respectively, in the Brillouin zone. The alterations in phonon frequencies of Γ_6 and Γ_{23} modes with temperature are in close agreement with the temperature dependent ν_1 (E_g) and ν_4 (A_{1g}) Raman active vibrations respectively as the compound suffers *I4/mmm* → *Cmcm* structural phase transition at T ~ 186 K [52,54,55].

Surprisingly, below T_c = 186 K, the base-centered orthorhombic [*Cmcm* (D_{2h}^{17})] phase of the compound is again found to be dynamical stable as it is evident from the corresponding phonon dispersion spectra (Figure 8(A)). The phonon dispersion spectra at T = 185 K show noticeable changes in their spectral features with respect to the phonon modes as estimated at T = 186 K and are marked by hardening of X_1 and Γ_{10} phonons and softening of Γ_{23} and X_{24} phonon modes. The hardening and softening of these phonon modes in phonon dispersion spectra at T = 185 K thereby allow the system to achieve dynamical stability. In this connection, it is relevant to mention that similar softening of X_1, X_8, Γ_6, Γ_{10} and Γ_{15} phonon modes and hardening of Γ_{23} and X_{24} phonons have also been observed in the phonon dispersion spectra for the *Cmcm* phase of the system at T = 186 K. The corresponding phonon dispersion spectra and PhDOS for the *Cmcm* phase of the compound at T = 186 K are shown in Figure 8(B) and 8(b), respectively.

3.5. Identifying the phonon modes responsible for phase transition

To identify the key phonon mode/ modes responsible for the temperature dependent phase transition of the Hg_2Cl_2 compound, the variations in vibrational frequencies for some of the representative X_1, X_8, X_{24}, Γ_6, Γ_{10} and Γ_{23} phonon modes with temperature have been estimated. The results

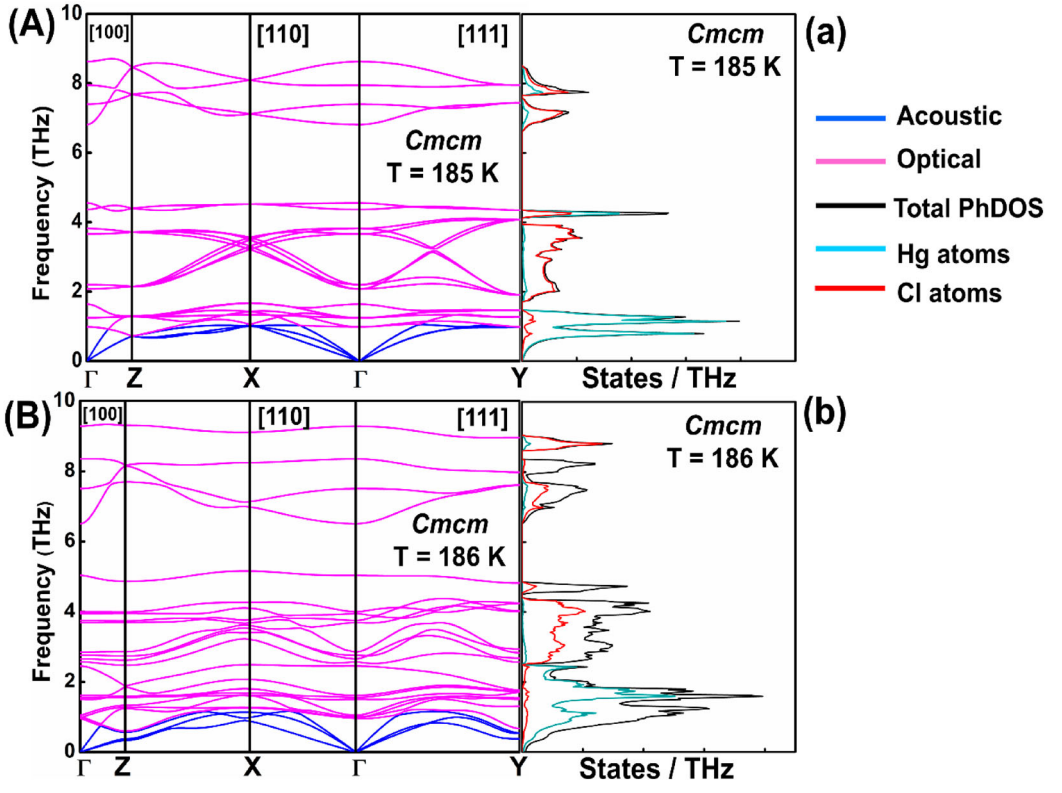

Figure 8. (A) The phonon dispersion curves along the high-symmetry points Γ→Z→X→Γ→Y for the *Cmcm* phase of Hg_2Cl_2 compound at T = (A) 185 K and (B) 186 K. The total and atom resolved PhDOS for *Cmcm* phase of the compound estimated at temperature (a) 185 K and (b) 186 K.

are shown in Figure 9. From Figure 9, it is observed that the frequencies of the acoustic X_1 and low-lying optical phonon modes X_8, Γ_6, Γ_{10} at 186 < T ≤ 300 K are almost independent of temperature. However, at T = 186 K, these modes undergo sharp drop in frequencies portending the transition temperature (T_c) associated with temperature dependent structural phase transition of the system. Furthermore, the high-frequency X_{24} and Γ_{23} optical phonon modes, like the acoustic phonons, remain independent with temperature except at T = 186 K, where instead of softening exhibit appreciable hardening of the vibrational frequencies. All these observations collectively suggest that acoustic X_1 and optical X_8, X_{24}, Γ_6, Γ_{10}, Γ_{23} phonon vibrations may be responsible for the temperature dependent $I4/mmm$ (D_{4h}^{17}) → $Cmcm$ (D_{2h}^{17}) structural phase transition of the Hg_2Cl_2 compound at the transition temperature ($T = T_c$ = 186 K).

The cartesian displacements of the relevant X_1, X_8, X_{24}, Γ_{10}, Γ_{23}, and M_{24} phonon modes, as estimated from the first-principle calculations are shown in Figure 10. From Figure 10, it is observed that the high frequency optical X_{24} and Γ_{23} phonon modes are strongly linked with the vibrations of Hg atoms along the crystallographic c – axis. While the acoustic X_1 and optical X_8, M_{24} phonon modes are involved with the atomic displacements of both Hg and Cl atoms, the Γ_{10} phonon is associated with the vibrations of Cl atoms of the compound. Visual inspections of the cartesian displacements linked with the pre referred phonon modes of the compound not only suggest perturbations in the lattice parameters (a, b, c) of the system but also signify considerable alterations of the linear Cl(L)–Hg(C)–Hg(A)–Cl(L) chain from its planar dispositions as the compound undergoes structural phase transition from the body-centered tetragonal to base-centered orthorhombic [$I4/mmm$ (D_{4h}^{17}) → $Cmcm$ (D_{2h}^{17})] phase at T_c = 186 K.

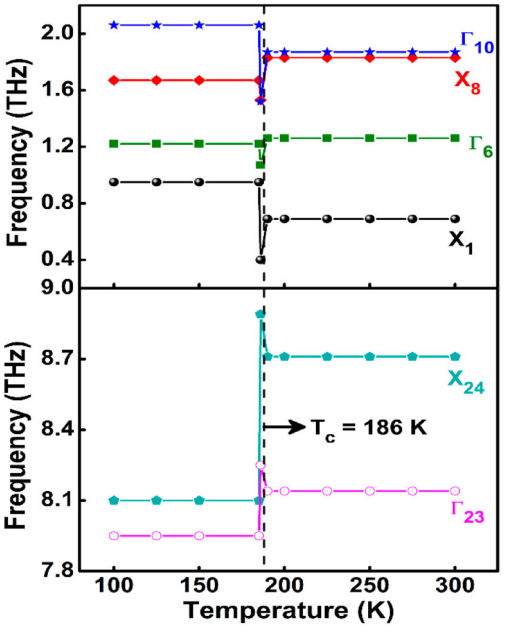

Figure 9. Variations of phonon frequencies as a function of temperature for the phonon normal modes X_1, X_8, X_{24} and Γ_6, Γ_{10}, Γ_{23} along the respective high-symmetry points X and Γ.

3.6. Displacive or order–disorder type phase transition

To understand the nature of the structural phase transition whether it is 'displacive' or of 'order-disorder' type, the on-site interatomic force constants $[K_{ij}(\lambda)]$ for an atom λ have been calculated from the respective supercells of the compound. In order–disorder type structural phase transition the potential energy hypersurface for the collective atomic displacements shows multiple potential wells of equal depths. Atoms jump over the finite potential barrier between the two nearest local potential minima within longer interval of time. However, for displacive type structural phase transition, the potential energy hypersurface of the cartesian displacements of atoms exhibits a single global minimum at equilibrium. The atoms move to and fro about the equilibrium of the potential energy hypersurface with frequencies which link with the order of the phonon frequencies. The magnitude of $K_{ij}(\lambda)$ determines the curvature, while its sign signifies the nature of the potential energy hypersurface. Positive values of $K_{ij}(\lambda)$ suggest the single minimum on the local potential energy hypersurface signifying 'displacive' type structural phase transition. The negative values of $K_{ij}(\lambda)$ on the other hand correspond to the multiwell nature of the potential energy hypersurface and linked the phase transition to be of 'order – disorder' type [22,85–90].

The on-site interatomic forces have been calculated by displacing the Hg and Cl atoms with an amplitude of ± 0.03 Å from their respective equilibrium positions along the crystallographic *x*, *y* and *z* directions for the *I*4/*mmm* (D_{4h}^{17}) and *Cmcm* (D_{2h}^{17}) phases of the Hg_2Cl_2 compound. The off-diagonal ($i \neq j$) IFCs K_{ij}(Hg) and K_{ij}(Cl) for the *I*4/*mmm* phase of the compound are found to be zero, however, the diagonal components ($i = j$) of the IFCs K_{ii}(Hg) and K_{ii}(Cl) are estimated to be have non-zero values at transition temperature $T_c = 186$ K. The non-zero positive values of force constants along *xx*, *yy* and *zz* directions [K_{xx}(Hg) = K_{yy}(Hg) = 0.18 N/m, K_{zz}(Hg) = 0.61 N/m, K_{xx}(Cl) = K_{yy}(Cl) = 0.33 N/m, K_{zz}(Cl) = 1.39 N/m] thereby suggest the nature of *I*4/*mmm* (D_{4h}^{17}) → *Cmcm* (D_{2h}^{17}) structural phase transition is of 'displacive' type in harmony with the available experimental observations [51].

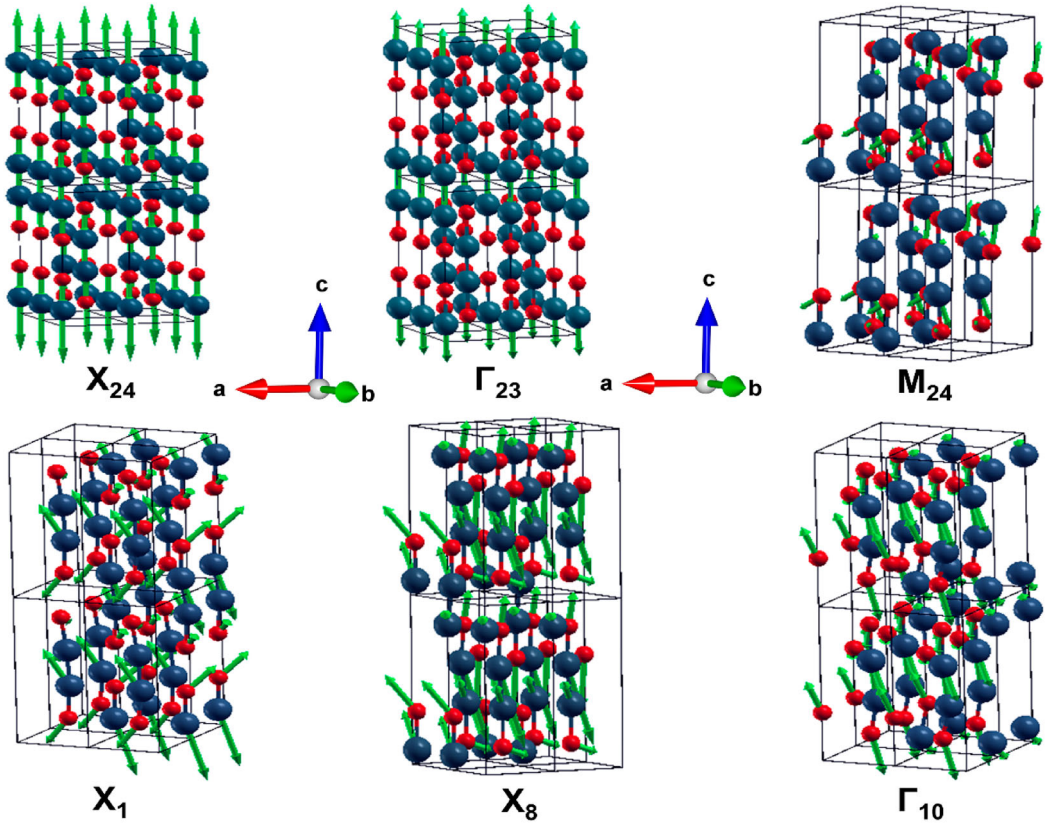

Figure 10. Schematic diagrams of eigenvectors and cartesian displacements of X_1, X_8, X_{24}, Γ_{10}, Γ_{23}, and M_{24} phonon modes for the *I4/mmm* phase of Hg_2Cl_2 compound at $T = 186$ K. (Emarald blue and red colours represent Hg and Cl atoms respectively. The green arrows illustrate the directions of cartesian displacements).

3.7. Grüneisen parameter and negative thermal expansion of Hg_2Cl_2 compound

To precisely understand the negative thermal expansion (NTE) of Hg_2Cl_2 compound, the mode Grüneisen parameters for the phonon modes have been estimated. The volume dependent mode Grüneisen parameter $\gamma_j(\boldsymbol{k})$ is defined as [91]

$$\gamma_j(\boldsymbol{k}) = \frac{\partial\,[\ln \omega_j(\boldsymbol{k})]}{\partial(\ln \boldsymbol{V})}, \tag{6}$$

where $\omega_j(\boldsymbol{k})$ is the phonon frequency of the j-th phonon mode with wave vector $\boldsymbol{k}$ while V is the volume of the unitcell of the compound. The weighted average Grüneisen parameter γ_{avg} can be expressed as

$$\gamma_{\text{avg}} = \frac{\sum_{\boldsymbol{k}} \gamma_j(\boldsymbol{k})\; C_j(\boldsymbol{k})}{\sum_{\boldsymbol{k}} C_j(\boldsymbol{k})}. \tag{7}$$

The specific heat $[C_j(\boldsymbol{k})]$ of the j-th phonon mode for the wave-vector $\boldsymbol{k}$ is calculated using the following relations [73]

$$C_j(\boldsymbol{k}) = k_B \left[\frac{\hbar\,\omega_j(\boldsymbol{k})}{k_B T}\right]^2 \frac{\exp[\hbar\,\omega_j(\boldsymbol{k})\;/\;k_B T]}{[\exp\,[\hbar\,\omega_j(\boldsymbol{k})\;/\;k_B T]\;-1]^2}, \tag{8}$$

where k_B and $\hbar$ are the Boltzmann and reduced Planck's constants respectively.

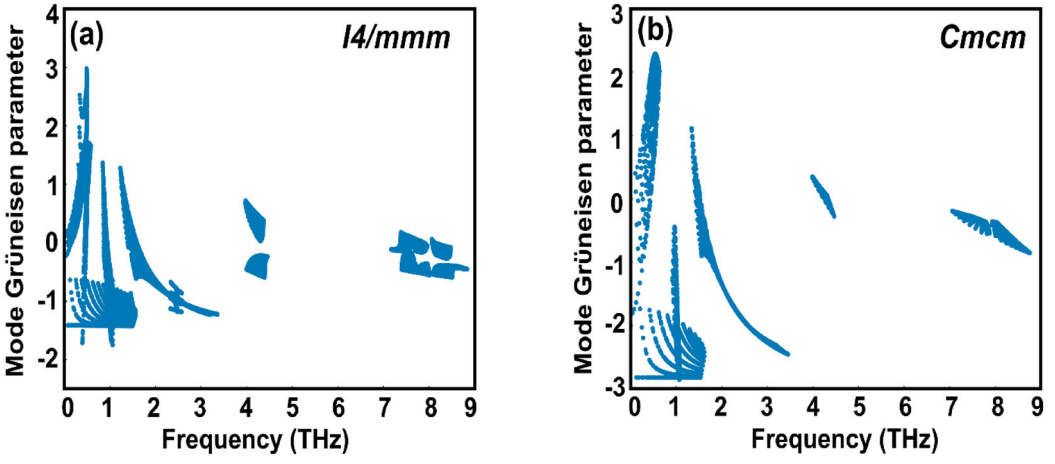

Figure 11. Mode Grüneisen parameters as a function of frequency for the (a) *I4/mmm* and (b) *Cmcm* phases of Hg_2Cl_2 compound.

The variation of mode Grüneisen parameter as a function of frequency for the body-centered tetragonal (*I4/mmm*) and base-centered orthorhombic (*Cmcm*) phases of the Hg_2Cl_2 compound are shown in Figure 11(a,b) respectively. Interestingly, from Figure 11(a,b), the average values of Grüneisen parameter are found to be −0.56 and −0.64, respectively for *I4/mmm* and *Cmcm* phases of the compound. The negative values of γ_{avg} of Hg_2Cl_2 in its high and low-temperature phases (*I4/mmm* and *Cmcm*), however represent an unconventional phenomenon called NTE. The low temperature *Cmcm* phase shows stronger NTE behaviour ($\gamma_{avg} = -0.64$) than that of its high temperature counterpart ($\gamma_{avg} = -0.56$). This result is in harmony with the inference so predicted from the corresponding thermal expansion (α) values [*vide supra*, Section 3.1]. Figure 11(a,b) further depict that, the acoustic phonon modes (TA and LA) in the low frequency window ranging from ∼ 0 to 1 THz and the low-lying optical phonons in the frequency region ranging between ∼ 0 and 4 THz show significant negative values of mode Grüneisen parameters, while small negative values of mode Grüneisen parameters come from the high-frequency optical phonon modes localized in the frequency window ranging from ∼ 7 to 8.85 THz. The larger negative Grüneisen parameters, as observed for the LA, TA and low-lying optical phonon modes, are the key candidates for the generation of soft phonon modes which further promote the structural instability and the phase transition of the compound [92,93]. The NTE materials are known to subtle for their wide applications in developing high precision optical equipment, fibre-optic communication systems, and in fuel cells [93,94]. Besides, both the room temperature *I4/mmm* and low-temperature *Cmcm* phases of Hg_2Cl_2 compound can be used as a composite with other positive thermal expansion materials to form a zero thermal expansion coefficient compound which in turn may be useful in seismographs, thermomechanical actuators and in aerospace components [95–98].

4. Conclusions

Temperature dependent structural phase transition of Hg_2Cl_2 compound has been studied from the first-principle DFT and Born-Oppenheimer on the fly molecular dynamics calculations. At transition temperature $T_c = 186$ K, the system is found to transform from the body-centered tetragonal (*I4/mmm*) to the base-centered orthorhombic (*Cmcm*) phase. The structural deformation of Hg_2Cl_2 compound with temperature has been primarily predicted from the alterations of structural parameters and Helmholtz free energy difference. The phonon dispersion relations have been estimated to explore the key phonon modes associated with the phase transition of the compound. While the order parameter e_{ij} suggests its paraelastic to ferroelastic phase transition at T_c, the

on-site force constants $K_{ij}(\lambda)$ indicate the phase transition to be of 'displacive' in nature. The negative values of mode Grüneisen parameters reveal the negative thermal expansion of Hg_2Cl_2 compound. We believe that this paper will not only provide a wealth information to study the temperature dependent structural phase transition from first-principle calculations, but may promote Hg_2Cl_2 for its future applications in low-temperature physics, thermomechanical actuators, fibre-optic communication systems and in fuel cells.

Acknowledgements

Authors would like to thank the Department of Physics, Jadavpur University for availing the computational facility through DST-FIST programme. Swarup Ghosh truly acknowledges the University Grants Commission (UGC), Government of India for providing the senior research fellowship (NET) award.

Disclosure statement

No potential conflict of interest was reported by the author(s).

Data availability statement

Data are available on valid request from the corresponding author.

References

[1] Lifshitz EM, Pitaevskii LP. Statistical physics: theory of the condensed state. Oxford, UK: Elsevier Science; 2013.
[2] Hobbs PV. Ice physics. Oxford: OUP; 2010.
[3] Marcellini M, Fernandes FM, Dedovets D, et al. Water/ice phase transition: the role of zirconium acetate, a compound with ice-shaping properties. J Chem Phys. 2017;146(14):144504.
[4] Kirby RE, Kisker E, King FK, et al. The ferromagnetic to paramagnetic phase transition of Fe studied by x-ray photoelectron spectroscopy. Solid State Commun. 1985;56(5):425–429.
[5] Küpper D, Easton S, Bland JAC. Paramagnetic-ferromagnetic phase transition and magnetic properties of ultrathin CoFe/Cu(110) films. J Appl Phys. 2007;102(8):0083902.
[6] Usov V, Murphy S, Shvets IV. Study of ferromagnetic–paramagnetic phase transition in two-dimensional Fe/Mo(110) epitaxial films. J Magn Magn Mater. 2005;290–291:764–767.
[7] Binaei Ghotbabadi B, Sheykhi A, Bordbar GH. Holographic paramagnetic-ferromagnetic phase transition with Power-Maxwell electrodynamics. Phys Lett B. 2019;797:134896.
[8] Pramanik AK, Banerjee A. Critical behavior at paramagnetic to ferromagnetic phase transition in $Pr_{0.5}Sr_{0.5}MnO_3$: a bulk magnetization study. Phys Rev B. 2009;79(21):214426.
[9] Biernacki SW. Ferromagnetic-paramagnetic phase transition in manganite perovskites: thermal hysteresis. Phys Rev B. 2003;68(17):174417.
[10] Zu L, Lin S, Liu Y, et al. A first-order antiferromagnetic-paramagnetic transition induced by structural transition in $GeNCr_3$. Appl Phys Lett. 2016;108(3):0031906.
[11] He Z, Taniyama T, Itoh M. Antiferromagnetic-paramagnetic transitions in longitudinal and transverse magnetic fields in a $SrCo_2V_2O_8$ crystal. Phys Rev B. 2006;73(21):212406.
[12] Marik M, Jana D, Majumder KC, et al. Dielectric behavior in B1 and B2 phases composed of unsymmetrical bent shaped liquid crystal molecules. Mol Cryst Liq Cryst. 2015;606(1):111–125.
[13] Li X, Chen D, Jin M, et al. Pressure-induced phase transitions and superconductivity in a quasi–1-dimensional topological crystalline insulator α-Bi_4Br_4. PNAS. 2019;116(36):17696–17700.
[14] Hoffer JK, Gardner WR, Waterfield CG, et al. Thermodynamic properties of4He. II. The bcc phase and the P-T and V-T phase diagrams below 2 K. J Low Temp Phys. 1976;23(1):63–102.
[15] Allen JF, Misener AD. Flow phenomena in liquid helium II. Nature. 1938;142(3597):643–644.
[16] Allen JF, Misener AD. Flow of liquid helium II. Nature. 1938;141(3558):75–75.
[17] Madsen A, Als-Nielsen J, Hallmann J, et al. Critical behavior of the order-disorder phase transition inβ-brass investigated by x-ray scattering. Phys Rev B. 2016;94(1):014111.
[18] Sahoo BD, Joshi KD, Kaushik TC. Structural, elastic, vibrational, thermophysical properties and pressure-induced phase transitions of ThN_2, Th_2N_3, and Th_3N_4: an ab initio investigation. J Appl Phys. 2020;128(3):0035902.

[19] Kurban M, Kürkçü C, Yamçıçıer Ç, et al. A study of structural phase transitions and optoelectronic properties of perovskite-type hydride $MgFeH_3$: ab initio calculations. J Phys: Condens Matter. 2019;31(30):305401.
[20] Irshad KA, Anees P, Sahoo S, et al. Pressure induced structural phase transition in rare earth sesquioxide Tm_2O_3: experiment and ab initio calculations. J Appl Phys. 2018;124(15):155901.
[21] Tao Y, Xie S, Lu T, et al. Pressure-induced evolution of structure and electronic property of GeP. J Appl Phys. 2022;131(16):165901.
[22] Ghosh S, Chowdhury J. Pressure induced structural phase transitions of technologically significant mercurous chloride at room temperature: an account from first-principle DFT and Born–Oppenheimer molecular dynamics studies. J Appl Phys. 2021;130(22):225103.
[23] Zakharov BA, Michalchuk AAL, Morrison CA, et al. Anisotropic lattice softening near the structural phase transition in the thermosalient crystal 1,2,4,5-tetrabromobenzene. Phys Chem Chem Phys. 2018;20(13):8523–8532. doi:10.1039/C7CP08609A
[24] Krylov A, Yushina I, Slyusareva E, et al. Structural phase transitions in flexible DUT-8(Ni) under high hydrostatic pressure. Phys Chem Chem Phys. 2022;24(6):3788–3798.
[25] Pushkarev GV, Mazurenko VG, Mazurenko VV, et al. Structural phase transitions in VSe_2: energetics, electronic structure and magnetism. Phys Chem Chem Phys. 2019;21(40):22647–22653.
[26] Chen H-W, Huang C-Y, Shu G-J, et al. Temperature-dependent optical properties of $CuFeO_2$ through the structural phase transition. RSC Adv. 2021;11(63):40173–40181.
[27] Duan Y, Li J, Li T, et al. Density dependent structural phase transition for confined copper: origin of the layering. Phys Chem Chem Phys. 2018;20(14):9337–9342.
[28] Dudka A, Nesterenko S, Tursina A. Multi-temperature X-ray diffraction study of a reversible structural phase transition in the high-temperature polymorph of Ce_2Rh_2Ga compound. J Alloys Compd. 2022;890:161759.
[29] Yang X, Jiang S-Q, Zhang H-C, et al. Pressure-induced structural phase transition and electrical properties of Cu_2S. J Alloys Compd. 2018;766:813–817.
[30] Nonato A, Lima PHM, Ferreira WC, et al. Pressure-induced structural phase transition in multiferroic $KBiFe_2O_5$. J Alloys Compd. 2019;787:1195–1203.
[31] Shrivastava D, Sanyal SP. Structural phase transition, electronic and lattice dynamical properties of half-Heusler compound CaAuBi. J Alloys Compd. 2018;745:240–246.
[32] Nag A, Kumari A, Kumar J. Pressure dependent structural phase transition and observation of Dirac-like dispersions in CaTe and SrTe. J Solid State Chem. 2021;304:122600.
[33] Peng Y, Wei X, Jin C, et al. Strain induced structural phase transition in TM6X6 (TM = Mo, W; X = S, Se, Te) nanowires (TM = Mo, W; X = S, Se, Te) nanowires. J Solid State Chem. 2021;300:122194.
[34] Sharma S, Nandan R, Shah J, et al. Phase evolution and enhanced electrical properties in $Ba_{0.85}Ca_{0.15}Zr_{0.10}Ti_{0.90}O_3$ lead-free ceramics prepared at different sintering temperatures. Phase Transit. 2022;95(8–9):609–625.
[35] Kapustianyk V, Semak S, Chornii Y, et al. Manifestation of ferroelastoelectric phase transition in temperature changes of the optical absorption edge in $(NH_4)_2CuCl_4{\cdot}2H_2O$ crystal. Phase Transit. 2022;95(8-9):626–633.
[36] de Armas Figueroa Y, Portelles J, López-Noda R, et al. Study of a polymorphic phase transition in $KNNLiTaLa_{0.01}$ by Raman spectroscopy. Phase Transit. 2022;95(6):466–473.
[37] Bejaoui Ouni I, Aroui H, Fontana MD. Sub-THz Raman response and soft phonon in tetragonal $BaTiO_3$. Phase Transit. 2022;95(11):749–757.
[38] Chen RH, Chen SC, Chen TM. High-temperature structural phase transition in $Na_3H(SO_4)_2$crystal. Phase Transit. 1995;53(1):15–22.
[39] Ghosh S, Sarkar S, Chowdhury J. Structural and electronic properties of wide band gap charge transfer insulator Hg_2Cl_2: insights from the first-principle calculations. Mater Chem Phys. 2022;276:125379.
[40] Henningsen T, Singh NB. Crystal characterization by use of birefringence interferometry. J Cryst Growth. 1989;96(1):114–118.
[41] Ewing WW. The preparation of electrolytic mercurous chloride in saturated potassium chloride for use in the calomel electrode. J Am Chem Soc. 1925;47(2):301–305.
[42] Crippa M, Legnaioli S, Kimbriel C, et al. New evidence for the intentional use of calomel as a white pigment]. J Raman Spectrosc. 2021;52(1):15–22. doi:10.1002/jrs.5876
[43] Pierson A, Philippe C. Acousto-optic interaction model with mercury halides (Hg_2Cl_2 and Hg_2Br_2) as AOTF cristals. Vol. 11180. SPIE; 2019. International Conference on Space Optics –ICSO 2018.
[44] Ghosh S, Chowdhury J. Pressure induced modulations in the optoelectronic properties of Hg_2Cl_2 compound: insights from the first-principle calculations. Mater Sci Eng B. 2022;284:115903.
[45] Amarasinghe PM, Kim J-S, Trivedi S, et al. Negative thermal expansion of mercurous halides. J Electron Mater. 2019;48(11):7063–7067.
[46] Venudhar YC, Iyengar L, Rao KVK. Unusual thermal behaviour of mercurous chloride. Cryst Res Technol. 1986;21(1):151–156. doi:10.1002/crat.2170210136
[47] Roginskii EM, Krylov AS, Markov YF, et al. Lattice dynamics and baric behavior of phonons in Hg_2Cl_2 crystals at high hydrostatic pressures. Bull Russ Acad Sci Phys. 2016;80(9):1033–1037.

[48] Kvasov AA, Markov YF, Roginskii EM, et al. Phonon dispersion and pressure behavior of Hg_2Cl_2 crystals. Ferroelectrics. 2010;397(1):81–89.
[49] Midorikawa M, Ishibashi Y, Nakashima S-i, et al. Effect of pressure on phase transition in Hg_2Cl_2 crystals. J Phys Soc Jpn. 1980;49(2):554–556.
[50] Dultz W, Rehaber E. A pressure-dependent optical soft mode in calomel (Hg_2Cl_2). J Phys C: Solid State Phys. 1979;12(4):L137–L139.
[51] Boiko ME, Sharkov MD, Boiko AM, et al. Study of the phase transition in Hg_2Cl_2 crystals using anomalous X-ray transmission. Crystallogr Rep. 2018;63(2):196–199.
[52] Dobrzhanskii GF, Kaplyanskii AA, Limonov MF, et al. A ferroelastic phase transition in Hg_2 $(Cl_xBr_{1-x})_2$ crystals. Ferroelectrics. 1983;48(1):69–80.
[53] Benoit JP, An CX, Luspin Y, et al. Study of inelastic neutron scattering and by the Raman effect, of the soft mode in the prototype phase of Hg_2Cl_2. J Phys C: Solid State Phys. 1978;11(17):L721–L723.
[54] Barta C, Kaplyanskiĭ A, Kulakov V, et al. Soft mode at the boundary of the Brillouin zone and nature of the phase transition in monovalent mercury-halide crystals. JETP Lett. 1974;21:121.
[55] Kaplyanskii AA. Raman spectra and structural phase transitions in improper ferroelastics Hg_2Cl_2 and Hg_2Br_2. In: Bendow B, Birman JL, Agranovich VM, editor. Theory of light scattering in condensed matter. Boston, MA: Springer US; 1976. p. 31–52.
[56] Heyd J, Scuseria GE, Ernzerhof M. Hybrid functionals based on a screened Coulomb potential. J Chem Phys. 2003;118(18):8207–8215.
[57] Giannozzi P, Baseggio O, Bonfà P, et al. Quantum ESPRESSO toward the exascale. J Chem Phys. 2020;152 (15):154105.
[58] Giannozzi P, Andreussi O, Brumme T, et al. Advanced capabilities for materials modelling with quantum ESPRESSO. J Phys: Condens Matter. 2017;29(46):465901.
[59] Giannozzi P, Baroni S, Bonini N, et al. QUANTUM ESPRESSO: a modular and open-source software project for quantum simulations of materials. J Phys: Condens Matter. 2009;21(39):395502.
[60] Havighurst RJ. Parameters in crystal structure: the mercurous halides. J Am Chem Soc. 1926;48 (8):2113–2125.
[61] Broyden CG. The convergence of a class of double-rank minimization algorithms 1: general considerations. IMA J Appl Math. 1970;6(1):76–90.
[62] Fletcher R. A new approach to variable metric algorithms. Comput J. 1970;13(3):317–322.
[63] Goldfarb D. A family of variable-metric methods derived by variational means. Math Comp. 1970;24 (109):23–26.
[64] Shanno DF. Conditioning of quasi-newton methods for function minimization. Math Comp. 1970;24 (111):647–656.
[65] Dal Corso A. Pseudopotentials periodic table: from H to Pu. Comput Mater Sci. 2014;95:337–350.
[66] Murnaghan FD. The compressibility of media under extreme pressures. PNAS. 1944;30(9):244–247.
[67] Birch F. Finite elastic strain of cubic crystals. Phys Rev. 1947;71(11):809–824.
[68] Hoover WG. Canonical dynamics: equilibrium phase-space distributions. Phys Rev A. 1985;31(3):1695–1697.
[69] Nosé S. A molecular dynamics method for simulations in the canonical ensemble. Mol Phys. 1984;52 (2):255–268.
[70] Nosé S. A unified formulation of the constant temperature molecular dynamics methods. J Chem Phys. 1984;81 (1):511–519.
[71] Kokalj A. XCrySDen – a new program for displaying crystalline structures and electron densities. J Mol Graph Model. 1999;17(3):176–179.
[72] Momma K, Izumi F. *VESTA*: a three-dimensional visualization system for electronic and structural analysis. J Appl Cryst. 2008;41(3):653–658.
[73] Togo A, Chaput L, Tanaka I. Distributions of phonon lifetimes in Brillouin zones. Phys Rev B. 2015;91 (9):094306.
[74] Nicholas J, Calos CLK. The structure of calomel, Hg_2Cl_2, derived from neutron powder data. Z Krist Cryst Mater. 1989;187(3–4):305–307.
[75] Dorm E. Intermetallic distances in mercury(I) halides Hg_2F_2, Hg_2Cl_2, and Hg_2Br_2. J Chem Soc D. 1971;9:466–467.
[76] Pelant I, Popova MN, Hála J, et al. Two-photon absorption and energy band structure of orthorhombic Hg_2Cl_2 crystals. Czech J Phys. 1987;37(10):1183–1197.
[77] Grzechnik A, Friese K, Dmitriev V, et al. Pressure-induced tricritical phase transition from the scheelite structure to the fergusonite structure in $LiLuF_4$. J Phys: Condens Matter. 2005;17(4):763–770.
[78] Wadhawan VK. Ferroelasticity. Bull Mater Sci. 1984;6(4):733–753.
[79] Salje E, Bismayer U, Jansen M. Temperature evolution of the ferroelastic order parameter of As_2O_5 as determined from optical birefringence. J Phys C: Solid State Phys. 1987;20(24):3613.
[80] Petrova AV, Nedopekin OV, Minisini B, et al. Pressure-induced ferroelastic phase transition in $LuLiF_4$ compound. Phase Transit. 2015;88(5):534–539.

[81] Tsunekawa S, Kamiyama T, Sasaki K, et al. Precise structure analysis by neutron diffraction for $R\mathrm{NbO_4}$ and distortion of $\mathrm{NbO_4}$ tetrahedra. Acta Cryst. 1993;49(4):595–600.
[82] Phillips R. Crystals, defects and microstructures: modeling across scales. Cambridge: Cambridge University Press; 2001.
[83] Grabowski B, Söderlind P, Hickel T, et al. Temperature-driven phase transitions from first principles including all relevant excitations: the fcc-to-bcc transition in Ca. Phys Rev B. 2011;84(21):214107.
[84] Grabowski B, Hickel T, Neugebauer J. Formation energies of point defects at finite temperatures]. Phys Status Solidi B. 2011;248(6):1295–1308. doi:10.1002/pssb.201046302
[85] Lebedev AI. Ab initio calculations of phonon spectra in $\mathrm{AT_iO_3}$ perovskite crystals (A = Ca, Sr, Ba, Ra, Cd, Zn, Mg, Ge, Sn, Pb). Phys Solid State. 2009;51(2):362–372.
[86] Parlinski K, Kawazoe Y, Waseda Y. Ab initio studies of phonons in $\mathrm{CaTiO_3}$. J Chem Phys. 2001;114(5):2395–2400.
[87] Parlinski K, Kawazoe Y. Ab initio study of phonons and structural stabilities of the perovskite-type. Eur Phys J B. 2000;16(1):49–58.
[88] Parlinski K, Li ZQ, Kawazoe Y. Ab initio calculations of phonons in $\mathrm{L_iNbO_3}$. Phys Rev B. 2000;61(1):272–278.
[89] Schneider T, Stoll E. Molecular-dynamics study of structural-phase transitions. I. One-component displacement models. Phys Rev B. 1976;13(3):1216–1237.
[90] Wdowik UD, Parlinski K, Rols S, et al. Soft-phonon mediated structural phase transition in GeTe. Phys Rev B. 2014;89(22):224306.
[91] Grüneisen E. Theorie des festen Zustandes einatomiger Elemente]. Ann Phys. 1912;344(12):257–306. doi:10.1002/andp.19123441202
[92] Wei L, Wang XP, Liu B, et al. The role of acoustic phonon anharmonicity in determining thermal conductivity of $\mathrm{CdSiP_2}$and $\mathrm{AgGaS_2}$: first principles calculations. AIP Adv. 2015;5(12):127236.
[93] Gupta MK, Mittal R, Chaplot SL. Negative thermal expansion in cubic $\mathrm{ZrW_2O_8}$: role of phonons in the entire Brillouin zone from *ab initio* calculations. Phys Rev B. 2013;88(1):014303.
[94] Takenaka K. Progress of research in negative thermal expansion materials: paradigm shift in the control of. thermal expansion [review]. Front Chem. 2018;6:7–19.
[95] Mohn P. A century of zero expansion. Nature. 1999;400(6739):18–19.
[96] Chen J, Hu L, Deng J, et al. Negative thermal expansion in functional materials: controllable thermal expansion by chemical modifications. Chem Soc Rev. 2015;44(11):3522–3567.
[97] Sleight A. Zero-expansion plan. Nature. 2003;425(6959):674–676.
[98] Liu J, Maynard-Casely HE, Brand HEA, et al. $\mathrm{Sc_{1.5}Al_{0.5}W_3O_{12}}$ exhibits zero thermal expansion between 4 and 1400 K. Chem Mater. 2021;33(10):3823–3831.

RSC Advances

PAPER

View Article Online
View Journal | View Issue

Cite this: *RSC Adv.*, 2024, **14**, 6385

Predicting band gaps of ABN_3 perovskites: an account from machine learning and first-principle DFT studies†

Swarup Ghosh and Joydeep Chowdhury *

The present paper is primarily focused on predicting the band gaps of nitride perovskites from machine learning (ML) models. The ML models have been framed from the feature descriptors and band gap values of 1563 inorganic nitride perovskites having formation energies <−0.026 eV and band gaps ranging from ∼1.0 to 3.1 eV. Four supervised ML models such as multi-layer perceptron (MLP), gradient boosted decision tree (GBDT), support vector regression (SVR) and random forest regression (RFR) have been considered to predict the band gaps of the said systems. The accuracy of each model has been tested from mean absolute error, root-mean-square error and determination coefficient R^2 values. The bivariate plots between the predicted and input band gaps of the compounds for both the training and test datasets have also been estimated. Additionally, two ABN_3-type nitride perovskites $CeBN_3$ (B = Mo, W) have been selected and their electronic band structures and optoelectronic properties have been studied from density functional theory (DFT) calculations. The band gap values of the said compounds have been estimated from DFT calculations at PBE, HSE06, G_0W_0@PBE, G_0W_0@HSE06 level of theories. The present study will be helpful in exploring the ML models in predicting the band gaps of nitride perovskites which in turn may bear potential applications in photovoltaic cells and optical luminescent devices.

Received 15th January 2024
Accepted 14th February 2024

DOI: 10.1039/d4ra00402g

rsc.li/rsc-advances

1. Introduction

Perovskites are ternary compounds with general chemical formula ABX_3 where "A" and "B" are cationic elements and "X" can be either oxygen or halogens in anionic forms. While "A" atoms are located in the cuboctahedral cavities of the crystal, "X" atoms on the other hand form corner sharing BX_6 octahedra. These compounds are known to show fascinating physical and chemical properties and find extensive applications in the fabrications of solar, fuel cells, energy conversion and optoelectronic devices.[1–10] Moreover, perovskites containing heavy fermionic elements, that show Rashba splittings, find promising applications in spintronics.[11–14]

Despite considerable successes of oxide and halide perovskites, recently much attention has been focused on the synthesis and first-principle calculations of nitride perovskites having general formula ABN_3.[15–19] Of late, ABN_3 find potential applications as topological insulators, photovoltaic cells and are being successfully used as optical luminescent materials.[18,20,21] The primary driving force behind the realization of ABN_3 stems from their extraordinary electronic, optical and magnetic properties of nitride compounds. For example, 2D hexagonal boron nitride is used in 5G wireless technology.[22] Vanadium nitride (VN), niobium nitride (NbN) and tantalum nitride (TaN) compounds are commonly employed in the fabrications of high – T_c superconductors, supercapacitors and batteries.[23–27]

Barring several attributes, syntheses of nitride perovskites are experimentally challenging as their synthetic protocols demand oxygen free environment.[28] Despite this limitation, successful preparations of $ThTaN_3$, $LaWN_3$, $LaReN_3$, $LaMoN_3$, $CeMoN_3$, $CeWN_3$, $YMoN_3$ and YWN_3 systems have so far been reported.[28–31] Readers who are interested in their synthesis procedures are referred to the literature[28–31] as depicted under reference section. Interestingly, these nitride perovskites find wide applications as topological insulators, spintronics and microelectromechanical devices.[21,30,32]

Considering the enormous applications of nitride perovskites, *in silico* approaches alone or in conjunction with experiments have been successfully applied to predict the structure–function relationships of these compounds. A combined minima hopping method and density functional theory (DFT) calculations have been performed to predict the crystal structures and band gaps (E_g) of twenty-one ABN_3 perovskites such as $LaBN_3$ (B = Re, W, Mo, Tc, Os, Cr, Mn, Co), $SrBN_3$ (B = Re, W, Tc), $CaBN_3$ (B = Re, W, Mo, Tc), $BaBN_3$ (B = Re, W) and YBN_3 (B = Re, W, Mo, Tc).[19] Those systems were observed to be thermodynamically stable

Department of Physics, Jadavpur University, 188, Raja S.C. Mallick Road, Kolkata 700032, India. E-mail: joydeep72_c@rediffmail.com; joydeep.chowdhury@jadavpuruniversity.in

† Electronic supplementary information (ESI) available. See DOI: https://doi.org/10.1039/d4ra00402g

and proposed to have excellent chances of being experimentally accessible.[19] Recently, the first-principle DFT calculations have been carried out to calculate the magnetic moments and thermodynamic stabilities of some rare-earth nitride perovskites ABN_3 (A = La, Ce, Pr, Nd, Pm, Sm, Eu, Gd, Tb, Dy, Ho, Er, Tm, Yb, Lu and B = Re, W) and suggested their numerous technological applications in the domain of nitride materials.[16] In this regard DFT is now recognized to be an elegant approach to estimate the electronic and optoelectronic properties of the materials under study. Both the electronic as well the optoelectronic properties are primarily guided by the band gaps of the materials. While DFT calculations with local density approximation (LDA) and generalized gradient approximation (GGA) underestimate E_g values,[33–36] the unscreened hybrid and Perdew–Burke–Ernzerhof–Hartree–Fock exchange (PBE0) functionals overestimate band gap energies of the compounds relative to their experimental counterparts.[37–39] In this regard DFT calculations, as accomplished from single-shot GW (G_0W_0) approximation using hybrid exchange-correlation (XC) functionals such as Heyd–Scuseria–Ernzerhof (HSE), Becke-3-parameter-Lee-Yang-Parr (B3LYP) and B3PW91 are known to predict the E_g values of the compounds close to the experimental results.[14,33,40–48] The major pitfalls of such calculations are that they are computationally demanding and need high end servers to run them. In this context, the machine learning (ML) is now considered as an effective alternative route to avoid the inherent computational costs linked with DFT calculations and helps in establishing a simple model between the characteristics features of materials and the target variable (here E_g).[49–60] Although ML approach is successfully implemented recently to predict the band gaps of oxide, halide perovskites and double perovskite compounds,[61–66] no such report is found in predicting the band gaps of nitride perovskites.

Considering the above issues in mind, the present paper is aimed to predict the band gaps of ABN_3 perovskites from ML models. The DFT studies have been performed to estimate the electronic band structures, E_g values and optoelectronic properties of two new nitride perovskites $CeBN_3$ (B = Mo, W). The manuscript has been organized in the following manner. In Section 2, the computational methodology, which includes ML methods and first-principle DFT calculations, has been discussed. Cleaning and preprocessing of data for ABN_3 perovskites have been shared in Section 3.1. In section 3.2, the training and validation of ML models have been deliberated. Section 3.3 is devoted to understand the structural properties and stabilities of two newly discovered nitride perovskite compounds $CeBN_3$ (B = Mo, W). Section 3.4 is framed with the calculations of electronic band structures and band gaps of $CeBN_3$ compounds using different level of theories in DFT calculations. The corresponding optoelectronic properties have also been highlighted in the Section 3.5. Overall conclusions of this work have been discussed under Section 4.

2. Computational methodology

2.1. Machine learning models

To predict the band gaps of nitride perovskite compounds, the ML models such as support vector regression (SVR), gradient boosted decision tree (GBDT), random forest regression (RFR) and multi-layer perceptron (MLP) algorithms have been considered. The input data consist of material descriptors of nitride perovskites and their corresponding target variables E_g. The algorithms have been realized using the Scikit-learn software package within the Python 3.9 framework.[67] The parameters of the algorithms have been optimized and the model performances have been estimated using the grid search of the average root-mean-square error (RMSE) of each model validation set. The E_g values have been predicted from SVR model using the following mathematical relation:[53]

$$f_{SVR}(y) = \sum_{i=1}^{N}(a_i - a_i^*)K(y_i, y) + b \quad (1)$$

where a_i and a_i^* are non-negative multipliers for each observation y_i. K is the kernel or radial basis function which is used to calculate the difference between training (y_i) and predicted (y) values of band gaps. "b" can be estimated from the Lagrange function.

The E_g values, so predicted from the GBDT algorithm, are represented using the following expression:[53]

$$f_{GBDT}(y) = f_0(y) + \sum_{m=1}^{M}\sum_{j=1}^{J}\Theta_{m,j}I\left(y \in R_{m,j}\right) \quad (2)$$

where $f_0(y)$ is the initial single decision tree. M,J and $\Theta_{m,j}$ are the number of regression trees, number of leaf nodes of the trees and the best fitting value respectively for each set of leaf nodes $R_{m,j}$.

Using RFR model the predicted E_g can be represented as:[53]

$$f_{RFR}(y) = \sum_{t=1}^{T}\sum_{n=1}^{N}C_n I(y \in D_n)/t \quad (3)$$

where t runs from 1 to T and T represents the number of formed classification or regression trees. C_n signifies the mean value of dataset D_n for randomly selecting N training samples from the said dataset.

The E_g values, so predicted from neural network based MLP framework, can be expressed using the following mathematical function:[53]

$$f_{MLP}(y) = \sum_{j=1}^{N} W_0{}^{ij}\theta\left(W_1{}^{ij}y_j + b_1\right) + b_0 \quad (4)$$

where $W_0{}^{ij}$ and $W_l{}^{ij}$ are the weights of ith neurons in the output and lth layers respectively. b_0 and b_1 represent the respective output layer and hidden biases respectively.

The characteristics of each model have been estimated from the Pearson correlation coefficient (p) which is expressed as:[68]

$$p = \frac{\sum_{i=1}^{N}(x_i - \bar{x})(y_i - \bar{y})}{\sqrt{\sum_{i=1}^{N}(x_i - \bar{x})^2}\sqrt{\sum_{i=1}^{N}(y_i - \bar{y})^2}} \quad (5)$$

where x_i and y_i are the comparative features of x and y respectively, $\bar{x}$ and $\bar{y}$ are their respective average values. N represent total number of samples in the training set. The accuracy of each ML model has been determined from RMSE, mean absolute error

(MAE) and evaluation coefficient (R^2) values. RMSE, MAE and R^2 have been calculated using the following relations:

$$\mathrm{RMSE} = \sqrt{\frac{1}{N}\sum_{i=1}^{N}(y_i - y)^2} \quad (6)$$

$$\mathrm{MAE} = \frac{1}{N}\sum_{i=1}^{N}|y_i - y| \quad (7)$$

$$R^2 = 1 - \frac{\sum_{i=1}^{N}(y_i - y)^2}{\sum_{i=1}^{N}(y_i - \bar{y})^2} \quad (8)$$

respectively. Where y_i and y are the respective input and predicted values of the dataset.

2.2. First-principle DFT calculations

The first-principle calculations have been carried out under the DFT framework within Quantum ESPRESSO (QE) software.[69–71] The crystal structures of $CeBN_3$ (B = Mo, W) compounds have been primarily optimized using "variable-cell relaxation" method followed by Broyden–Fletcher–Goldfarb–Shanno scheme.[72–75] The Born Oppenheimer molecular dynamics (BOMD) simulations have then been performed at $T = 300$ K on the supercell structures ($2 \times 2 \times 2$) of the compounds, so obtained from the optimized unitcell geometries of the said systems. BOMD simulations have been accomplished from the NPT ensemble whose temperature is controlled by the Nose–Hoover thermostat. The projector augmented wave (PAW) pseudopotentials[76] have been included to consider the electron–ion interactions and the exchange-correlation (XC) term of the pseudopotential has been implemented from Perdew–Burke–Ernzerhof (PBE) XC functional[77] which is known as a parameterization form of GGA. The valence electrons of Ce, B (B = Mo, W) and *N* atoms have been considered as plane wave with kinetic energy cut-off of 80 Ry. Each crystal structure is allowed to optimize until the Hellmann–Feynman force attains a value $<10^{-3}$ Ry Bohr^{-1} for total electronic energy difference $<10^{-8}$ Ry at $P = 0$ GPa. A gamma-centered *k*-point mesh of $10 \times 10 \times 10$ grid under Monkhorst–Pack scheme has been set for geometry optimization and self-consistent-field (SCF) calculations.

The electronic band structures of $CeBN_3$ crystal systems have been estimated from different level of theories such as PBE, HSE06, G_0W_0@PBE and G_0W_0@HSE06 in the DFT calculations. The optoelectronic properties of the said compounds have been calculated from SCF method as employed in QE software.[78] The optical broadening of 0.15 eV has been considered for estimating the optoelectronic parameters which include complex dielectric function [$\varepsilon(\omega)$], absorption coefficient [$\alpha(\omega)$] and optical conductivity [$\sigma(\omega)$].

3. Results and discussions

3.1. Data cleaning and pre-processing for machine learning

The raw data of inorganic ABN_3-type perovskite compounds have been obtained from the available literature.[15–19,21,28–31,79,80] By selecting all possible combinations of cations as "A" and "B", a set of 5566 inorganic ABN_3-type perovskites have been initially selected for model evaluation. Lead (Pb) containing perovskites in all combinations, due their inherent toxic characters, are not considered in the above mentioned dataset. In the next step, the samples have been primarily identified according to their respective formation energies (E_f). Using support vector classification (SVC), the samples are then categorized by eliminating those candidates which show $E_f >$ thermal excitation energy ($E_{Th} \sim -0.026$ eV) at room temperature ($T = 300$ K).[57] To implement SVC, initially 5566 samples have been randomly divided into 4866 (~87%) and 700 (~13%) samples as training and test set, respectively. Fig. 1(a) shows the E_f as a function of sample number of the test dataset as obtained from SVC algorithm. From Fig. 1(a), it is observed that the samples are segregated into $E_f < E_{Th}$ and $E_f > E_{Th}$ classes. The merit of this SVC algorithm is then tested from confusion matrix and receiver operating characteristics (ROC) curve.[55] The results are shown in Fig. 1(b) and (c) respectively. From Fig. 1(b), the correctly identified compounds with $E_f < E_{Th}$ and $E_f > E_{Th}$ classes are observed to be 482 [true positive (TP)] and 181 [true negative (TP)], respectively. However, the number of incorrectly identified samples under $E_f < E_{Th}$ and $E_f > E_{Th}$ classes are found to be 18 [false positive (FP)] and 19 [false negative (FN)], respectively. Out of 700 test dataset, it is found that only 5% samples (37 out of 700) have been misclassified, which in turn suggests the reliability of the SVC model to segregate the samples into their respective classes. The F1 score of the model, as attained from confusion matrix, is mathematically expressed as:

$$\text{F1 score} = \frac{2 \times \text{recall} \times \text{precision}}{\text{recall} + \text{precision}} \quad (9)$$

$$\text{where precision} = \frac{\mathrm{TP}}{\mathrm{TP} + \mathrm{FP}} \quad (10)$$

$$\text{and recall} = \frac{\mathrm{TP}}{\mathrm{TP} + \mathrm{FN}} \quad (11)$$

The F1 score is calculated to be 96.2% which also suggests the better performance of the said model. The ROC curve, as depicted in Fig. 1(c), represents the relation between the TP rate (sensitivity) and FP rate (1 – specificity). From Fig. 1(c), the area under curve (AUC) is estimated to be 0.98. The AUC closer to 1 further signifies the excellent segregation between the $E_f < E_{Th}$ and $E_f > E_{Th}$ classes.

Here we primarily focused on ABN_3 compounds which bear potential applications as photovoltaic and optical luminescent materials, the selection space has thus been further narrowed down to 1563 samples which exhibit E_g values spanning in the range from 1.0 to 3.1 eV. The E_g of the compounds in general are linked with the proposed 145 feature descriptors which include electronegativity, atomic weight, covalent radius, d valence electrons *etc.*[57,81] Out of 145 feature descriptors, 117 feature attributes of ABN_3 perovskites have been initially framed for the target variable E_g. The list of 117 features such as Mendeleev number, electronegativity, covalent radius, d valence electrons

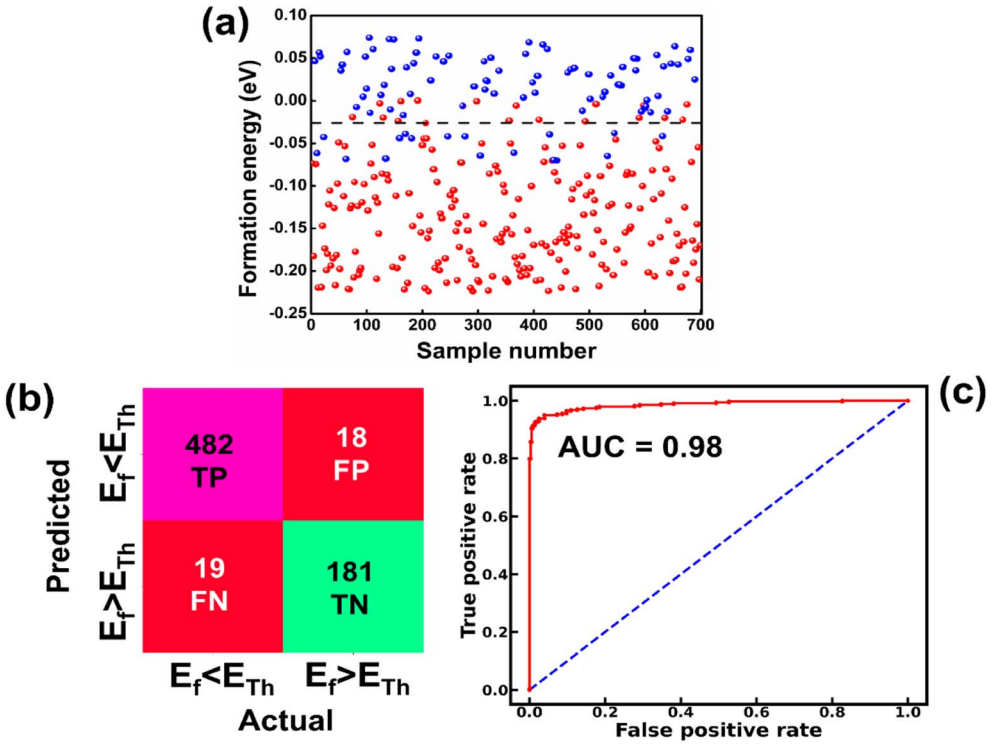

Fig. 1 (a) Formation energy as a function of sample number for 700 test sets as estimated from SVC model. [The horizontal dashed line represents formation energy (E_f) = −0.026 eV]. (b) Confusion matrix representing the correlation between predicted and actual values in form of true positive (TP), false negative (FN), false positive (FP) and true negative (TN) values for the tested samples. [$E_f < E_{Th}$ and $E_f > E_{Th}$ symbolize the formation energies below and above E_{Th} (=−0.026 eV), respectively]. (c) The ROC curve illustrating the TP and FP rates of the test datasets.

etc. are shown in Table S1 (ESI).† With these 117 features, the Pearson correlation heatmap is constructed and the result is shown in Fig. 2(a). The features having absolute correlation values <0.89 and with multiple collinearities between them have been eliminated. The final top 10 feature descriptors which include electronegativity, d valence electrons, formation energy, p valence electrons, Mendeleev number, specific volume of ground state, mean covalent radius, space group number, melting temperature and atomic weight, have been selected using the de-correlation method for further model evaluation. The heatmap portraying the evaluated top 10 feature descriptors and their order of importance are shown in Fig. 2(b) and (c), respectively. From Fig. 2(c), it is clearly seen that the electronegativity, d valence electrons and mean covalent radius show predominant contributions in predicting E_g values of the ABN_3 compounds.

The correlations between E_g and electronegativity, mean covalent radius and d valence electrons can be rationalized. Electronegativity is a measure of ability to attract electrons of two bonded atoms towards their valence electrons. This ability results the delocalized distribution of valence electrons, which in turn influences the nature of the bonding as well as the E_g values of the compounds.[82–84] The mean covalent radii of the constituent atoms are intrinsically linked with the electronegativity of the system. Systems with constituent atoms having larger mean covalent radii thus result in decrease in electronegativity of the compounds in general.[85] Hence, the mean covalent radius is considered as an important feature descriptor in modulating the E_g values of the systems. The d valence electrons play major roles in the formation of energy bands in the electronic band structure and has direct impact on the E_g of the materials. Larger number of d valence electrons can realign the Fermi energy level (E_F) through p-d and s-d hybridizations, which in turn may alter the E_g values of the compounds.[57]

3.2. Machine learning model training and validation

To precisely predict the band gaps of ABN_3-ype perovskite compounds, four ML models such as SVR, MLP, GBDT and RFR have been considered. The accuracy of each model has been tested by selecting their respective hyperparameters. The list of hyperparameters of each model are shown in Table 1. From the dataset of 1563 ABN_3 perovskites and their top 10 feature descriptors (*vide supra*), 1363 (∼87%) samples have been randomly selected for training and the rest 200 (∼13%) samples have been set for testing of each model. The random selection has been considered two times for each model to confirm the statistical validity of the results. The performance of ML model has been estimated by calculating the RMSE, MAE and R^2 values. The RMSE, MAE and R^2 values of each model for the test dataset, so attained from the 10-dimensional feature space, are illustrated in Table 1.

From Table 1, it is observed that while RFR predicts the E_g values of the compound with 3% MAE; SVR, GBDT and MLP

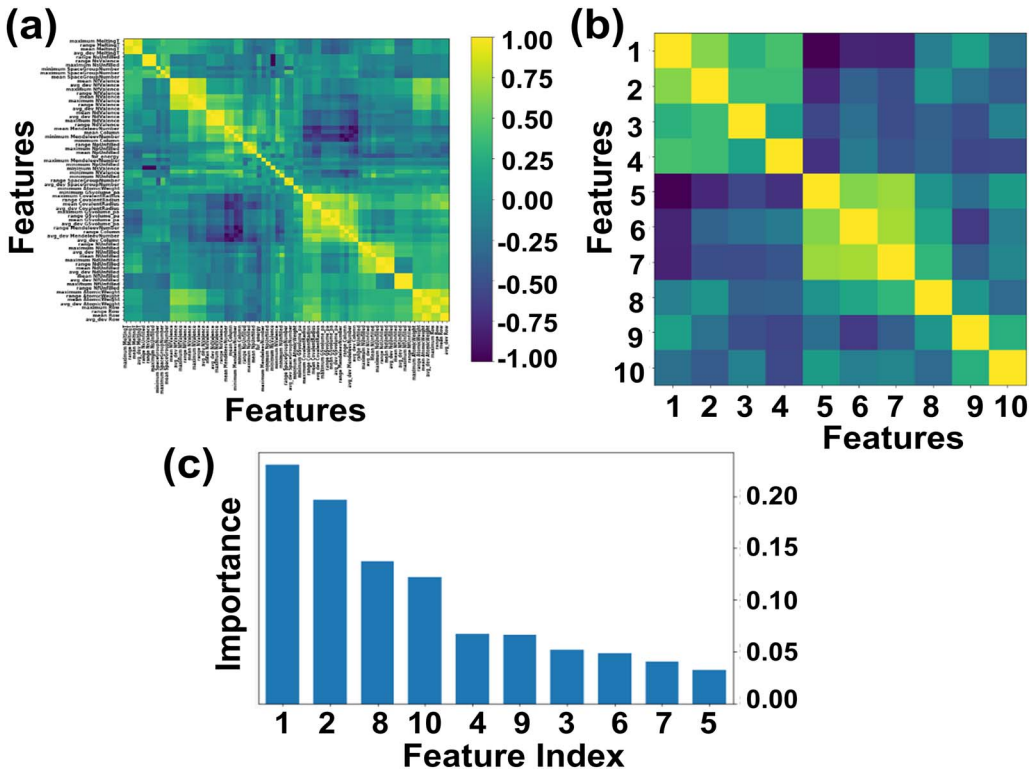

Fig. 2 (a and b) Heatmap representing the initial 117 and final top 10 features respectively of ABN_3 perovskites [yellow and dark blue colors in the heatmap represent the respective strong and weak correlations among the features]. (c) The relative importance of top 10 features of the compounds. [Feature indices (in the order of importance): 1-electronegativity, 2-d valence electrons, 3-formation energy, 4-p valence electrons, 5-Mendeleev number, 6-specific volume of ground state, 7-atomic weight, 8-mean covalent radius, 9-melting temperature and 10-space group number].

predict the same E_g within MAEs of 8%, 10% and 16% respectively. From Table 1, the RFR algorithm shows lowest RMSE (=0.11 eV) and highest R^2 (=0.94) values in contrast to other models. R^2 (RMSE) values of GBDT, SVR and MLP models are estimated to be 0.90 (0.15 eV), 0.91 (0.13 eV) and 0.74 (0.22 eV) respectively. These results collectively suggest the reliability of the RFR model in predicting the band gaps of ABN_3-type perovskite compounds. The bivariate plots from the RFR model showing both the predicted, input band gap values for the training and testing datasets are illustrated in Fig. 3(a). From Fig. 3(a), strong linear correlation [with $R^2 = 0.98$ (training set) and 0.94 (test set)] between the predicted and input E_g values have been observed in both the training and test datasets. This result further justifies the accuracy of RFR model in predicting the band gaps of ABN_3 perovskites. The corresponding bivariate plots between the predicted and input values of E_g, as accomplished from SVR, GBDT and MLP ML models, are also shown in Fig. 3(b–d) respectively. From Fig. 3(b–d), moderate to weak linear correlations between the predicted and input E_g values have been observed as the model goes from SVR, GBDT to MLP algorithms. The above results as a whole suggest the superiority of the RFR algorithm as an effective ML model is predicting the band gaps of ABN_3 compounds in contrast to SVR, GBDT and MLP algorithms.

Besides, two newly synthesized nitride perovskites $CeMoN_3$ and $CeWN_3$, as reported elsewhere[28] and whose band gaps are yet to be explored, have been selected for first-principle DFT calculations. Their electronic band structures, E_g values and optoelectronic properties have been studied from DFT calculations. The E_g values of the said systems have been predicted from both the DFT as well as RFR ML model to verify the

Table 1 Statistics of different ML models and their corresponding hyperparameters for predicting bandgaps of ABN_3 perovskites

Models	Hyperparameters	MAE	RMSE	R^2
MLP	Solver = adam, alpha = 1×10^{-8}, tol = 1×10^{-6}, max_iter = 5000, random_state = 0	0.16	0.22	0.74
GBDT	n_estimators = 2000, max_depth = 30, min_samples_split = 2	0.10	0.15	0.90
SVR	C = 50, gamma = 10, epsilon = 0.05, kernel = 'rbf'	0.08	0.13	0.91
RFR	max_depth = 30, min_samples_split = 2, n_estimators = 2000, min_samples_leaf = 1, random_state = 0	0.03	0.11	0.94

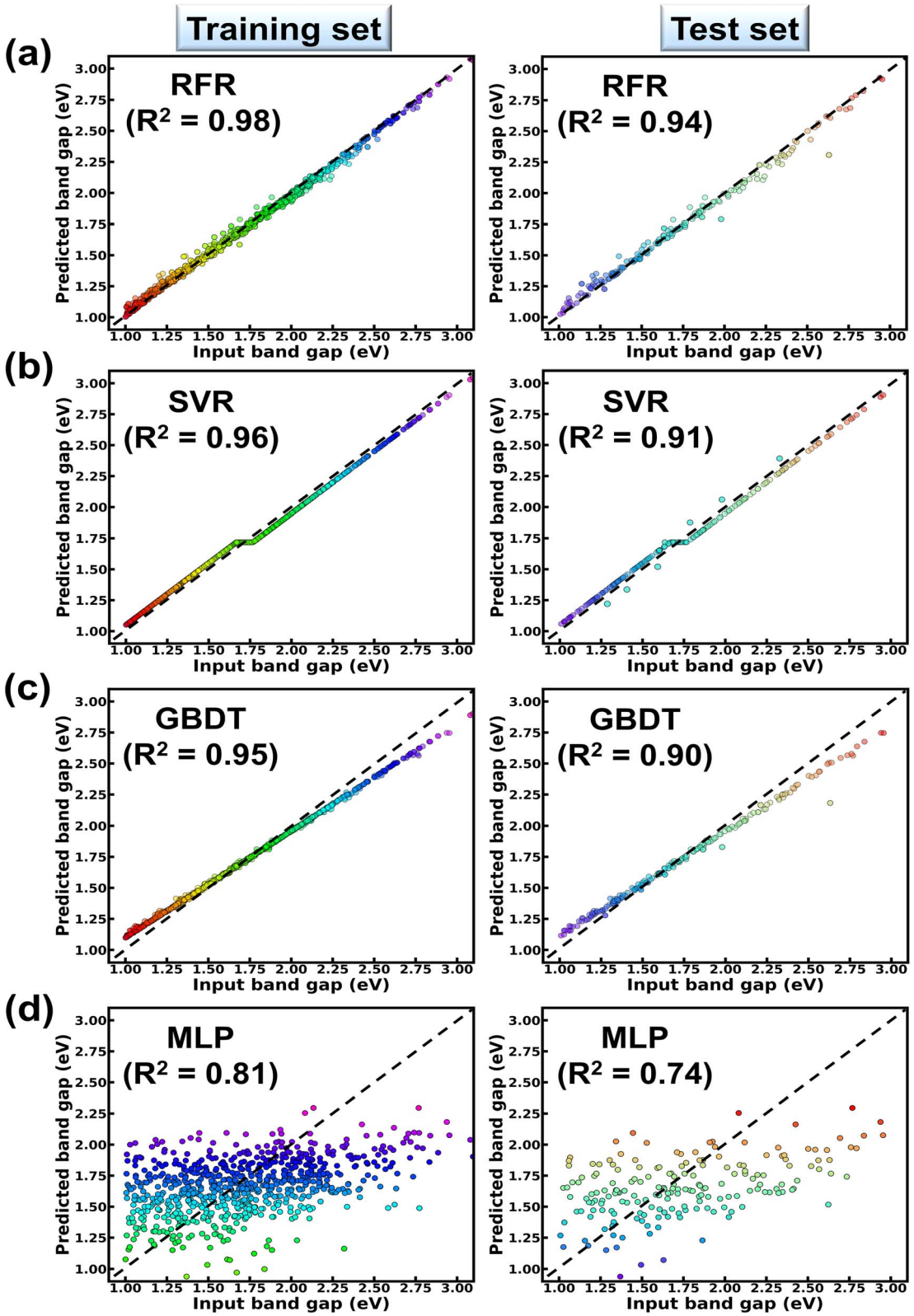

Fig. 3 Fitted bivariate plots showing the variations of predicted and input band gaps of ABN_3 perovskites for both the training and test datasets as obtained from (a) RFR (b) SVR (c) GBDT and (d) MLP models.

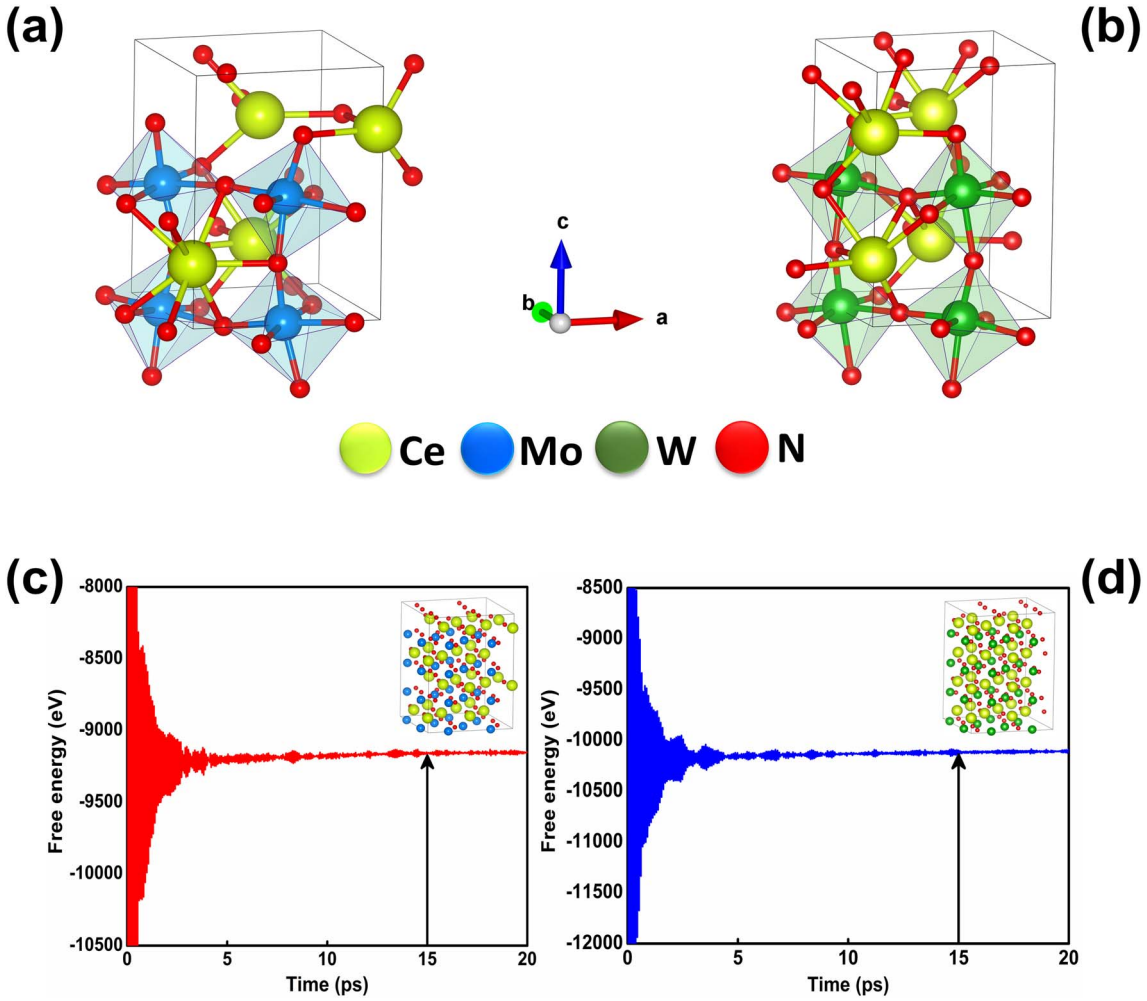

Fig. 4 Optimized crystal structures of (a) $CeMoN_3$ and (b) $CeWN_3$ compounds as obtained from DFT calculations. Free energy as a function of time for (c) $CeMoN_3$ and (d) $CeWN_3$ systems as attained from BOMD simulations. [insets of (c and d) show the respective supercell geometries of $CeMoN_3$ and $CeWN_3$ so obtained from the BOMD simulation run at 15 ps which is marked with vertical arrows].

accuracy of ML model in predicting E_g values of ABN_3 compounds.

3.3. Crystal structures and stabilities of the $CeBN_3$ (B = Mo, W) compounds

At room temperature ($T = 300$ K) and under ambient pressure ($P = 0$ GPa), $CeBN_3$ (B = Mo, W) crystalize to primitive orthorhombic phase and belong to $Pmc2_1$ space group symmetry with space group no. 26. The optimized unitcell geometries of the compounds, as obtained from first-principle DFT calculations with GGA-PBE level of theory, are shown in the upper panel of Fig. 4. The lattice parameters of the $CeMoN_3$ ($CeWN_3$) crystal system have been estimated to be $a = 5.789$ Å (5.686 Å), $b = 5.854$ Å (5.667 Å) and $c = 7.776$ Å (8.027 Å) which are in close agreement with the experimentally determined X-ray diffraction data as reported elsewhere.[28] From Fig. 4(a and b), it is observed that B (=Mo, N) and *N* atoms form several distorted octahedral environments within the crystal structure and B atom, which is located at the center of each BN_6 octahedron, is found to be shifted towards the apical N atom. The distorted octahedron, aka pyramidal coordination and large c/a ratio of $CeBN_3$ may result large spontaneous ferroelectric polarization in the systems under study.[86,87] The ferroelectric polarization values of $CeMoN_3$ and $CeWN_3$ compounds are estimated to be ~47.24 and 49.68 μC cm^{-2} respectively along the direction of crystallographic *c*-axis. To comprehend the thermal stabilities of the compounds at $T = 300$ K, the BOMD simulations have been performed over a time span of 20 ps under time step of 1 fs. Temporal variations of free energies of $CeBN_3$ systems at $T = 300$ K are shown in the lower panel of Fig. 4. The free energies (F) of the compounds have been estimated using the following relation:[88]

$$F(T,\nu) = E(\nu) + F_{el}(T,\nu) + F_{ph}(T,\nu) \quad (12)$$

where E measures the total ground state energy of the supercell, ν signifies the supercell volume at temperature T, $F_{el}(T,\nu)$ and $F_{ph}(T,\nu)$ are the free energies of the electrons and phonons respectively. $F_{el}(T,\nu)$ can be estimated using the following mathematical relation:[89,90]

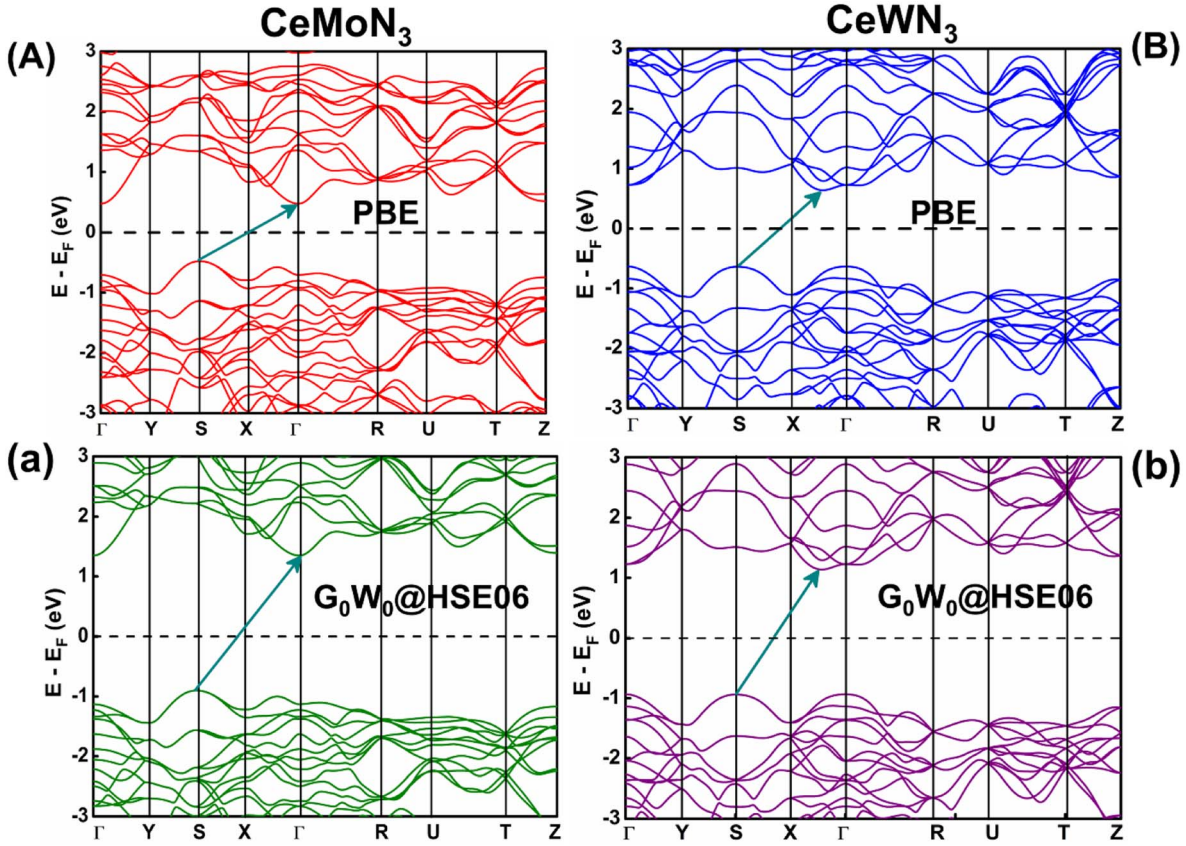

Fig. 5 E–k diagrams of $CeMoN_3$ (left panel) and $CeWN_3$ (right panel) compounds along Γ → Y → S → X → Γ → R → U → T → Z high-symmetry direction as obtained from PBE and G_0W_0@HSE06 level of theories. [Horizontal dashed line and inclined arrow represent Fermi energy level and band gap respectively].

$$F_{el}(T,\nu) = k_B T \int d\upsilon N_{el}(\upsilon)[n\ln n + (1-n)\ln(1-n)] \quad (13)$$

where $N_{el}(\nu)$ is the electronic density of states and n is the Fermi occupation number. $F_{ph}(T,\nu)$ has been calculated under the thermodynamic integration approach[90,91] and is expressed as:

$$F_{ph}(T,\nu) = \int_0^1 d\upsilon \left\langle F_{el}(\{R_I\}) - F_{el}(\{R_I{}^0\}) - \sum_{i,j}\frac{m}{2}u_i u_j D_{ij}(T,\nu) \right\rangle_\upsilon \quad (14)$$

where "$F_{el}(\{R_I\}) - F_{el}(\{R_I{}^0\})$" corresponds to the difference in electronic free energies at a certain point of ionic coordinates $\{R_I\}$. $u_i = \{R_i\} - \{R_i{}^0\}$, m is the atomic mass and D represents the dynamical matrix of the system. "$\langle \ldots\ldots \rangle_\nu$" represents the thermodynamic average and has been estimated using the BOMD simulations. From Fig. 4(c and d) it is found that both the crystal structures attain their respective stabilizing free energy values after a time lapse of ~5 ps. The refined geometries of the compounds, so obtained from the BOMD simulation run at 15 ps, are shown in the inset of Fig. 4(c and d).

3.4. Estimations of E_g values for $CeBN_3$ (B = Mo, W) compounds

The E–k diagrams of $CeBN_3$ systems for B = Mo, W along Γ → Y → S → X → Γ → R → U → T → Z high-symmetry direction have been estimated from DFT calculations at PBE, HSE06, G_0W_0@PBE and G_0W_0@HSE06 level of theories. The results are shown in Fig. 5 and S1 (ESI).† The estimated E_g values of the compounds from the corresponding E–k diagrams are shown in Table 2. Interestingly the E–k diagrams for both $CeMoN_3$ and $CeWN_3$ compounds show the existence of indirect band gaps ranging from 0.94–1.60 and 1.00–1.81 eV, respectively. Presence of indirect band gaps with gap openings in the range 0.94–1.81 eV may render their applications in photovoltaics.[92–96] In this connection it may be relevant to mention that while the PBE functional is known to underestimate the E_g values of the systems in general,[14,33–36,40,41,43] the HSE06 functional on the other hand can predict the E_g values of the compounds in close agreement with the experimental observations.[14,33,40,45,97] The

Table 2 Band gaps of $CeBN_3$ (B = Mo, W) compounds as obtained from DFT calculations at different level of theories

	Band gaps (eV)	
Level of theories	$CeMoN_3$	$CeWN_3$
PBE	0.94	1.00
HSE06	1.57	1.80
G_0W_0@PBE	1.46	1.71
G_0W_0@HSE06	1.60	1.81

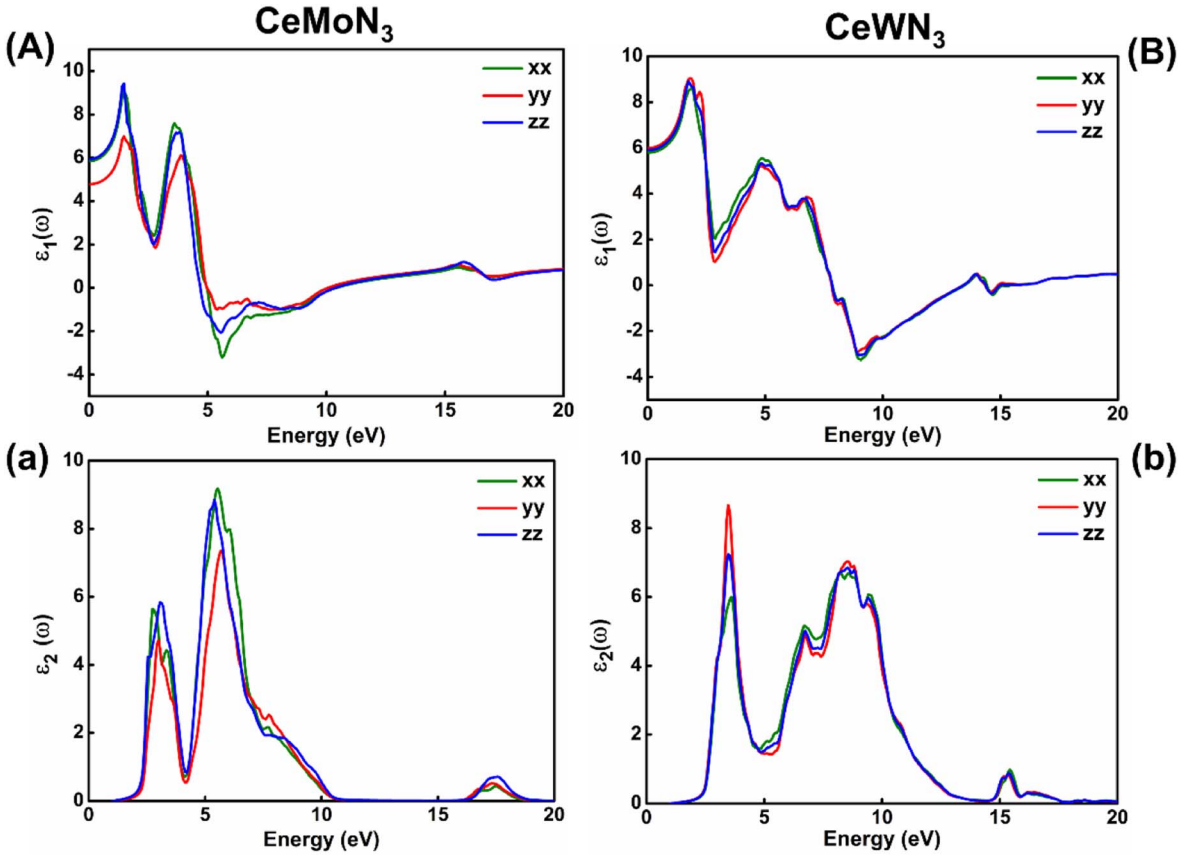

Fig. 6 Left panel: (A) Real and (a) imaginary parts of dielectric function *versus* incident EM wave energy for $CeMoN_3$ compound. Right panel: (B) Real and (b) imaginary parts of $\varepsilon(\omega)$ as a function of EM wave energy for $CeWN_3$ compound.

HSE06 XC energy functional (E_{XC}^{HSE06}) is mathematically expressed as:[98]

$$E_{XC}^{HSE06} = 1/4E_X^{HF,\ SR}(\omega) + 3/4E_X^{PBE,\ SR}(\omega) + E_X^{PBE,\ LR}(\omega) + E_C^{PBE} \quad (15)$$

where "X", "C", "SR" and "LR" symbolize the exchange, correlation, short range and long range terms respectively in the energy functional. "ω (=0.2)" governs the extent of short range interactions. The difference of E_g values between HSE06 and PBE functionals can be rationalized from the fact that the HSE06 functional, which consists of screened Coulomb potential for Hartree–Fock (HF) exchange, considers the exact mixing of both the HF and PBE exchange only for short-range interactions. This mixing allows the exchange hole to become delocalized among its nearest neighbors, which in turn results in E_g values which are reported to be closer to experimental observations in contrast to the same being performed with PBE functional.[98]

The E_g values of $CeMoN_3$ and $CeWN_3$ compounds are predicted to be ~1.55 and 1.76 eV from RFR ML model for the G_0W_0@HSE06 input of 1.60 and 1.81 eV respectively. While the DFT calculations at HSE06 and G_0W_0@HSE06 level of theories can closely predict the experimentally observed E_g values of the systems within <1% error,[40,42,45,48,97,99,100] the predicted E_g values of $CeBN_3$ (B = Mo, W) compounds as obtained from RFR ML model are estimated within an error of ~3% with standard deviation of ~0.035. The selective choice of G_0W_0@HSE06 level of theory in the DFT calculation as input for the prediction of band gaps is thus meaningful, given its efficacy in reproducing the experimental band gaps of many such compounds as reported elsewhere.[14,101–103]

3.5. Optical properties of $CeBN_3$ (B = Mo, W) systems

Electronic band structures are intrinsically linked with the optoelectronic properties of the systems in general. The optoelectronic properties of $CeBN_3$ (B = Mo, W) crystal systems have been estimated from the frequency (ω) dependent complex dielectric function [$\varepsilon(\omega)$]. Since, the $Pmc2_1$ phase of the compounds is structurally anisotropic, the incident electromagnetic (EM) field components along the direction of *a*, *b* and *c*-crystallographic axes are designated as *xx*, *yy* and *zz*, respectively in the consequent calculations. Fig. 6(A) and (B) show the variations of real part of $\varepsilon(\omega)$ [$\varepsilon_1(\omega)$] as a function of incident EM wave energy ($\tilde{E}_M$), so obtained from G_0W_0@HSE06 level of theory, for $CeMoN_3$ and $CeWN_3$ compounds respectively. From the upper panel of Fig. 6, static values of $\varepsilon_1(\omega)$ [$\varepsilon_1(0)$] have been estimated to be ~5.85 (5.80), 4.77 (5.99) and 5.93 (5.90) for $CeMoN_3$ ($CeWN_3$) system along xx, yy and zz polarization directions respectively of the incident EM wave. These non-zero

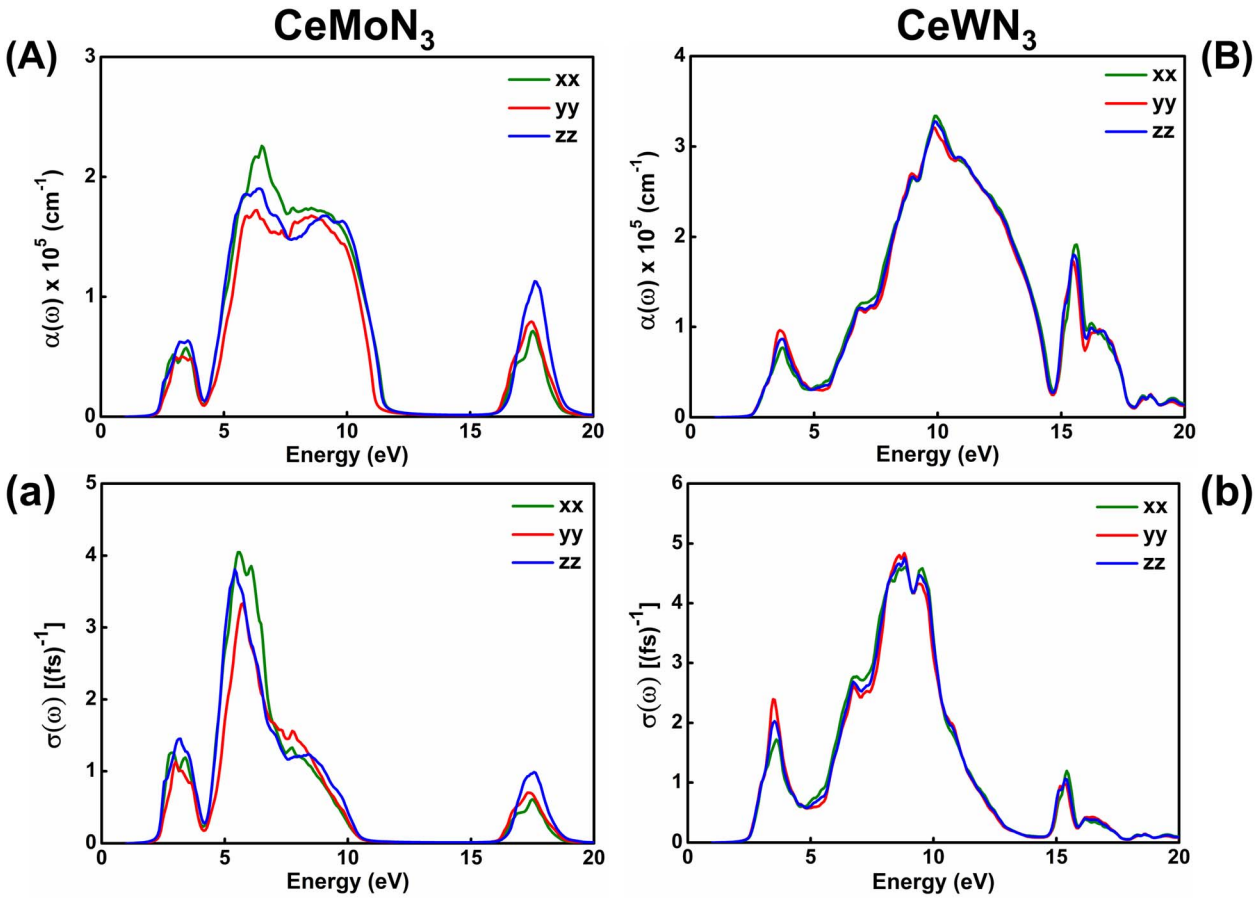

Fig. 7 Left panel: (A) Optical absorption and (a) conductivity as a function of incident EM wave energy for $CeMoN_3$ compound. Right panel: (B) Optical absorption and (b) conductivity as a function of EM wave energy for $CeWN_3$ compound.

values of $\varepsilon_1(0)$ for all the three polarization directions indicate their semiconducting nature so attained from the E–k diagrams [*vide ante*, Fig. 5]. The most intense structure band of $\varepsilon_1(\omega)$ for $CeMoN_3$ ($CeWN_3$) compound is obtained at $\tilde{E}_M$ ~1.45 (1.85) eV which corresponds to maximum dispersion of the EM wave. However, beyond $\tilde{E}_M$ ~3.75 (6.86) eV, $\varepsilon_1(\omega)$ values of $CeMoN_3$ ($CeWN_3$) system gradually decrease and attain negative values within the energy window $\tilde{E}_M$ ~4.72 (7.86)–10.42 (13.39) eV. The negative values of $\varepsilon_1(\omega)$ signify metallic Drude – like behaviour of the compounds within the said energy windows.[42,43,104]

$\varepsilon_2(\omega)$ is known to correlate directly with the band gaps of the compounds in general. Fig. 6(a) and (b) depict the variations of $\varepsilon_2(\omega)$ as a function of $\tilde{E}_M$ for $CeMoN_3$ and $CeWN_3$ systems respectively, so attained from G_0W_0@HSE06 level of theory. From Fig. 6(a and b) the critical or take-off values of $\varepsilon_2(\omega)$ have been observed at $\tilde{E}_M$ ~1.60 (1.81) eV for $CeMoN_3$ ($CeWN_3$) compound for all the three polarization directions. The critical or take-off values of $\varepsilon_2(\omega)$ are in exact agreement with the E_g values of the systems, as obtained from the G_0W_0@HSE06 level of theory (*vide ante*, Table 2). Interestingly, the take-off values of $\varepsilon_2(\omega)$ are found to be independent of polarization directions of EM wave. Moreover, finite values of $\varepsilon_2(\omega)$ between $\tilde{E}_M$ ~2.30 (2.40) and 10.01 (12.50) eV for $CeMoN_3$ ($CeWN_3$) crystal corroborate strong attenuation of the incident EM wave inside the crystal systems within the said energy window.[42,43]

The response of strong attenuation of the incident EM wave inside the $CeBN_3$ (B = Mo, W) compounds, so reflected in the $\varepsilon_2(\omega)$–$\tilde{E}_M$ plots (Fig. 6), can also be attributed from their absorption coefficients [$\alpha(\omega)$] and optical conductivities [$\sigma(\omega)$]. Fig. 7 shows the variations of $\alpha(\omega)$ and $\sigma(\omega)$ as function of $\tilde{E}_M$ for the referred systems. Akin to $\varepsilon_2(\omega)$–$\tilde{E}_M$ plots, the critical values of both $\alpha(\omega)$ and $\sigma(\omega)$ are found at $\tilde{E}_M$ ~1.60 (1.81) eV for $CeMoN_3$ ($CeWN_3$) crystal system for all the three polarization directions. Hence the estimations of $\alpha(\omega)$ and $\sigma(\omega)$ help to recheck the E_g values as obtained from electronic band structures and $\varepsilon_2(\omega)$–$\tilde{E}_M$ plots. From Fig. 7, finite values of $\alpha(\omega)/\sigma(\omega)$ have been observed within $\tilde{E}_M$ ~2.30/2.30 to 11.43/10.01 eV, 16.47/16.55 to 18.77/18.64 eV and 2.40/2.40 to 17.90/12.50 eV for $CeMoN_3$ and $CeWN_3$ compounds, respectively. The finite values of $\alpha(\omega)$ and/or $\sigma(\omega)$ within the specified energy window signify large opacity and high optical conductivity of the said systems.[42,43] Moreover, the high transparency of $CeMoN_3$ ($CeWN_3$) compound within the energy window ~0–1.60 eV (0–1.81 eV) has also been noticed in $\alpha(\omega)$–$\tilde{E}_M$ and $\sigma(\omega)$–$\tilde{E}_M$ plots (Fig. 7). The high transparency of the said systems covering visible and Infrared (IR) regions of the EM wave may promote them as potential candidates for optical luminescent materials and IR detectors.[43,105,106]

4. Conclusions

The band gaps of ABN_3 perovskites have been predicted from ML models based on the feature descriptors. The dataset of 1563 ABN_3 perovskites, which show $E_f < -0.026$ eV and E_g values spanning in the range from 1.0 to 3.1 eV, have been selected from initial 5566 samples for ML model evaluation. The E_g values of the compounds are found to be linked with 117 feature descriptors. The top 10 feature descriptors have been selected by eliminating those features which show absolute correlation values <0.89 and low rank of importance. Correlations between the band gap and the topmost 3 features such as electronegativity, mean covalent radius and d valence electrons have also been discussed. Four supervised ML models such as MLP, GBDT, SVR and RFR have been considered to predict the band gaps of these nitride perovskite compounds. The accuracy of each model has been tested from MAE, RMSE and R^2 values. The RFR algorithm shows lowest RMSE (=0.11 eV) and highest R^2 (=0.94) values in comparison to other models. R^2 values and the corresponding bivariate plots suggest the superiority of RFR algorithm as an effective ML model is predicting the band gaps of ABN_3 perovskites in contrast to SVR, GBDT and MLP algorithms. Two newly synthesized ABN_3-type perovskites $CeBN_3$ (B = Mo, W) have been further chosen and their electronic band structures and optoelectronic properties have been studied from DFT calculations. The E_g values of $CeBN_3$ (B = Mo, W) compounds have been estimated from DFT calculations at PBE, HSE06, G_0W_0@PBE and G_0W_0@HSE06 level of theories. The E_g values of $CeMoN_3$ and $CeWN_3$ compounds have been predicted to be 1.55 and 1.76 eV from RFR algorithm for the G_0W_0@HSE06 input of 1.60 and 1.81 eV respectively. The E_g values of the systems have also been verified from their respective optoelectronic parameters such as $\varepsilon_2(\omega)$, $\alpha(\omega)$ and $\sigma(\omega)$. We believe that this study will help to unveil the efficacy of ML models in predicting the band gaps of nitride perovskites which in turn will bear potential applications as photovoltaic and optical luminescent materials.

Data availability

The data and codes that support the findings of this study are available on reasonable request from corresponding author.

Conflicts of interest

There are no conflicts of interest to declare.

Acknowledgements

Authors would like to thank the National Supercomputing Mission (NSM) for providing computing resources of 'PARAM Kamrupa' at IIT Guwahati, which is implemented by C-DAC and supported by the Ministry of Electronics and Information Technology (MeitY) and Department of Science and Technology (DST), Government of India. Swarup Ghosh sincerely acknowledges the University Grants Commission (UGC), Government of India for providing the senior research fellowship (NET) award.

References

1 Z. Shi and A. H. Jayatissa, *Materials*, 2018, **11**, 729.
2 P. Tonui, S. O. Oseni, G. Sharma, Q. Yan and G. Tessema Mola, *Renewable Sustainable Energy Rev.*, 2018, **91**, 1025–1044.
3 M. Aldamasy, Z. Iqbal, G. Li, J. Pascual, F. Alharthi, A. Abate and M. Li, *Phys. Chem. Chem. Phys.*, 2021, **23**, 23413–23427.
4 B. V. Politov, E. P. Antonova, E. S. Tropin, D. A. Osinkin, A. Y. Suntsov and V. L. Kozhevnikov, *Renewable Energy*, 2023, **206**, 872–878.
5 Y. Zhou, X. Guan, H. Zhou, K. Ramadoss, S. Adam, H. Liu, S. Lee, J. Shi, M. Tsuchiya, D. D. Fong and S. Ramanathan, *Nature*, 2016, **534**, 231–234.
6 A. Raj, S. Sharma, D. V. Singh, A. Kumar, R. K. Chourasia, J. M. Siqueiros, O. R. Herrera, A. Anshul and M. Kumar, *Phys. B*, 2024, **673**, 415504.
7 L. Polavarapu, M. A. Loi, H. Zeng and J. M. Luther, *Nanoscale*, 2023, **15**, 15075–15078.
8 A. Balilonda, Z. Li, Y. Fu, F. Zabihi, S. Yang, X. Huang, X. Tao and W. Chen, *J. Mater. Chem. C*, 2022, **10**, 6957–6991.
9 R. Wang, J. Wang, S. Tan, Y. Duan, Z.-K. Wang and Y. Yang, *Trends Chem.*, 2019, **1**, 368–379.
10 D. Luo, X. Li, A. Dumont, H. Yu and Z.-H. Lu, *Adv. Mater.*, 2021, **33**, 2006004.
11 H. C. Koo, S. B. Kim, H. Kim, T.-E. Park, J. W. Choi, K.-W. Kim, G. Go, J. H. Oh, D.-K. Lee, E.-S. Park, I.-S. Hong and K.-J. Lee, *Adv. Mater.*, 2020, **32**, 2002117.
12 M. Kepenekian and J. Even, *J. Phys. Chem. Lett.*, 2017, **8**, 3362–3370.
13 M.-Y. Liu, Q.-Y. Chen, C. Cao and Y. He, *Phys. Chem. Chem. Phys.*, 2019, **21**, 2899–2909.
14 S. Ghosh and J. Chowdhury, *Mod. Phys. Lett. B*, 2023, **38**, 2330003.
15 C. Gui, J. Chen and S. Dong, *Phys. Rev. B*, 2022, **106**, 184418.
16 J. A. Flores-Livas, R. Sarmiento-Pérez, S. Botti, S. Goedecker and M. A. L. Marques, *JPhys Mater.*, 2019, **2**, 025003.
17 B. F. Grosso, D. W. Davies, B. Zhu, A. Walsh and D. O. Scanlon, *Chem. Sci.*, 2023, **14**, 9175–9185.
18 V.-A. Ha, H. Lee and F. Giustino, *Chem. Mater.*, 2022, **34**, 2107–2122.
19 R. Sarmiento-Pérez, T. F. T. Cerqueira, S. Körbel, S. Botti and M. A. L. Marques, *Chem. Mater.*, 2015, **27**, 5957–5963.
20 T. K. Ng, J. A. Holguin-Lerma, C. H. Kang, I. Ashry, H. Zhang, G. Bucci and B. S. Ooi, *J. Phys. D: Appl. Phys.*, 2021, **54**, 143001.
21 M.-C. Jung, K.-W. Lee and W. E. Pickett, *Phys. Rev. B*, 2018, **97**, 121104.
22 M. Kim, E. Pallecchi, R. Ge, X. Wu, G. Ducournau, J. C. Lee, H. Happy and D. Akinwande, *Nat. Electron.*, 2020, **3**, 479–485.
23 I. Ashraf, S. Rizwan and M. Iqbal, *Front. Mater.*, 2020, **7**, 181.
24 W. Lengauer, *J. Phys. Chem. Solids*, 1988, **49**, 59–63.
25 Y. M. Shy, L. E. Toth and R. Somasundaram, *J. Appl. Phys.*, 2003, **44**, 5539–5545.

26 S. P. Chockalingam, M. Chand, J. Jesudasan, V. Tripathi and P. Raychaudhuri, *Phys. Rev. B: Condens. Matter Mater. Phys.*, 2008, **77**, 214503.
27 V. M. Pan, V. G. Prokhorov, V. A. Komashko, G. G. Kaminsky, M. A. Kousenetsov and C. G. Tretiatchenko, *IEEE Trans. Magn.*, 1989, **25**, 2000–2003.
28 R. Sherbondy, R. W. Smaha, C. J. Bartel, M. E. Holtz, K. R. Talley, B. Levy-Wendt, C. L. Perkins, S. Eley, A. Zakutayev and G. L. Brennecka, *Chem. Mater.*, 2022, **34**, 6883–6893.
29 N. E. Brese and F. J. DiSalvo, *J. Solid State Chem.*, 1995, **120**, 378–380.
30 K. R. Talley, C. L. Perkins, D. R. Diercks, G. L. Brennecka and A. Zakutayev, *Science*, 2021, **374**, 1488–1491.
31 S. D. Kloß, M. L. Weidemann and J. P. Attfield, *Angew. Chem., Int. Ed.*, 2021, **60**, 22260–22264.
32 S. Bandyopadhyay, A. Paul and I. Dasgupta, *Phys. Rev. B*, 2020, **101**, 014109.
33 S. Ghosh, R. R. Banik and J. Chowdhury, *Indian J. Theor. Phys.*, 2021, **69**, 43–68.
34 V. I. Anisimov, J. Zaanen and O. K. Andersen, *Phys. Rev. B*, 1991, **44**, 943–954.
35 H. Xiao, J. Tahir-Kheli and W. A. Goddard III, *J. Phys. Chem. Lett.*, 2011, **2**, 212–217.
36 I. N. Yakovkin and P. A. Dowben, *Surf. Rev. Lett.*, 2007, **14**, 481–487.
37 D. S. Lambert and D. D. O'Regan, *Phys. Rev. Res.*, 2023, **5**, 013160.
38 S. Tomić and N. M. Harrison, *AIP Conf. Proc.*, 2010, **1199**, 65–66.
39 D. Wing, G. Ohad, J. B. Haber, M. R. Filip, S. E. Gant, J. B. Neaton and L. Kronik, *Proc. Natl. Acad. Sci. U.S.A.*, 2021, **118**, e2104556118.
40 S. Ghosh, S. Sarkar and J. Chowdhury, *Mater. Chem. Phys.*, 2022, **276**, 125379.
41 R. Ray Banik, S. Ghosh and J. Chowdhury, *Phys. Scr.*, 2023, **98**, 045920.
42 S. Ghosh and J. Chowdhury, *Mater. Sci. Eng., B*, 2022, **284**, 115903.
43 R. R. Banik, S. Ghosh and J. Chowdhury, *Phys. Scr.*, 2023, **98**, 105914.
44 S. Śmiga and L. A. Constantin, *J. Phys. Chem. A*, 2020, **124**, 5606–5614.
45 A. J. Garza and G. E. Scuseria, *J. Phys. Chem. Lett.*, 2016, **7**, 4165–4170.
46 H. Einollahzadeh, R. S. Dariani and S. M. Fazeli, *Solid State Commun.*, 2016, **229**, 1–4.
47 J. M. Crowley, J. Tahir-Kheli and W. A. Goddard III, *J. Phys. Chem. Lett.*, 2016, **7**, 1198–1203.
48 Y. Duan, L. Qin, L. Shi and G. Tang, *Comput. Mater. Sci.*, 2015, **101**, 56–61.
49 S. Chowdhury, S. Ghosal, D. Mondal and D. Jana, *J. Phys. Chem. Solids*, 2022, **170**, 110909.
50 E. Bedolla, L. C. Padierna and R. Castañeda-Priego, *J. Phys.: Condens. Matter*, 2021, **33**, 053001.
51 S. Chibani and F.-X. Coudert, *APL Mater.*, 2020, **8**, 080701.
52 C. Gao, X. Yang, M. Jiang, L. Chen, Z. Chen and C. V. Singh, *Phys. Chem. Chem. Phys.*, 2022, **24**, 4653–4665.
53 Y. Zhang, W. Xu, G. Liu, Z. Zhang, J. Zhu and M. Li, *PLoS One*, 2021, **16**, e0255637.
54 A. Halder, A. Ghosh and T. S. Dasgupta, *Phys. Rev. Mater.*, 2019, **3**, 084418.
55 Y. Zhuo, A. Mansouri Tehrani and J. Brgoch, *J. Phys. Chem. Lett.*, 2018, **9**, 1668–1673.
56 Y. Tang, H. Chen, J. Wang and X. Niu, *Phys. Chem. Chem. Phys.*, 2023, **25**, 18086–18094.
57 M. Gao, B. Cai, G. Liu, L. Xu, S. Zhang and H. Zeng, *Phys. Chem. Chem. Phys.*, 2023, **25**, 9123–9130.
58 H. J. Kulik, T. Hammerschmidt, J. Schmidt, S. Botti, M. A. L. Marques, M. Boley, M. Scheffler, M. Todorović, P. Rinke, C. Oses, A. Smolyanyuk, S. Curtarolo, A. Tkatchenko, A. P. Bartók, S. Manzhos, M. Ihara, T. Carrington, J. Behler, O. Isayev, M. Veit, A. Grisafi, J. Nigam, M. Ceriotti, K. T. Schütt, J. Westermayr, M. Gastegger, R. J. Maurer, B. Kalita, K. Burke, R. Nagai, R. Akashi, O. Sugino, J. Hermann, F. Noé, S. Pilati, C. Draxl, M. Kuban, S. Rigamonti, M. Scheidgen, M. Esters, D. Hicks, C. Toher, P. V. Balachandran, I. Tamblyn, S. Whitelam, C. Bellinger and L. M. Ghiringhelli, *Electron. Struct.*, 2022, **4**, 023004.
59 O. Allam, B. W. Cho, K. C. Kim and S. S. Jang, *RSC Adv.*, 2018, **8**, 39414–39420.
60 F. Wang, Z. Yang, F. Li, J.-L. Shao and L.-C. Xu, *RSC Adv.*, 2023, **13**, 31728–31737.
61 V. Gladkikh, D. Y. Kim, A. Hajibabaei, A. Jana, C. W. Myung and K. S. Kim, *J. Phys. Chem. C*, 2020, **124**, 8905–8918.
62 G. Pilania, A. Mannodi-Kanakkithodi, B. P. Uberuaga, R. Ramprasad, J. E. Gubernatis and T. Lookman, *Sci. Rep.*, 2016, **6**, 19375.
63 A. Talapatra, B. P. Uberuaga, C. R. Stanek and G. Pilania, *Commun. Mater.*, 2023, **4**, 46.
64 V. Vakharia, I. E. Castelli, K. Bhavsar and A. Solanki, *Phys. Lett. A*, 2022, **422**, 127800.
65 S. Priyanga G, M. N. Mattur, N. Nagappan, S. Rath and T. Thomas, *J. Mater.*, 2022, **8**, 937–948.
66 Z. Wan, Q.-D. Wang, D. Liu and J. Liang, *New J. Chem.*, 2021, **45**, 9427–9433.
67 F. Pedregosa, G. Varoquaux, A. Gramfort, V. Michel, B. Thirion, O. Grisel, M. Blondel, P. Prettenhofer, R. Weiss, V. Dubourg, J. Vanderplas, A. Passos, D. Cournapeau, M. Brucher, M. Perrot and É. Duchesnay, *Mach. Learn. Res.*, 2011, **12**, 2825–2830.
68 J. Hauke and T. Kossowski, *Quaest. Geogr.*, 2011, **30**, 87–93.
69 P. Giannozzi, O. Baseggio, P. Bonfà, D. Brunato, R. Car, I. Carnimeo, C. Cavazzoni, S. de Gironcoli, P. Delugas, F. Ferrari Ruffino, A. Ferretti, N. Marzari, I. Timrov, A. Urru and S. Baroni, *J. Chem. Phys.*, 2020, **152**, 154105.
70 P. Giannozzi, O. Andreussi, T. Brumme, O. Bunau, M. Buongiorno Nardelli, M. Calandra, R. Car, C. Cavazzoni, D. Ceresoli, M. Cococcioni, N. Colonna, I. Carnimeo, A. Dal Corso, S. de Gironcoli, P. Delugas, R. A. DiStasio, A. Ferretti, A. Floris, G. Fratesi, G. Fugallo, R. Gebauer, U. Gerstmann, F. Giustino, T. Gorni, J. Jia,

M. Kawamura, H. Y. Ko, A. Kokalj, E. Küçükbenli, M. Lazzeri, M. Marsili, N. Marzari, F. Mauri, N. L. Nguyen, H. V. Nguyen, A. Otero-de-la-Roza, L. Paulatto, S. Poncé, D. Rocca, R. Sabatini, B. Santra, M. Schlipf, A. P. Seitsonen, A. Smogunov, I. Timrov, T. Thonhauser, P. Umari, N. Vast, X. Wu and S. Baroni, *J. Phys.: Condens. Matter*, 2017, **29**, 465901.

71 P. Giannozzi, S. Baroni, N. Bonini, M. Calandra, R. Car, C. Cavazzoni, D. Ceresoli, G. L. Chiarotti, M. Cococcioni, I. Dabo, A. Dal Corso, S. de Gironcoli, S. Fabris, G. Fratesi, R. Gebauer, U. Gerstmann, C. Gougoussis, A. Kokalj, M. Lazzeri, L. Martin-Samos, N. Marzari, F. Mauri, R. Mazzarello, S. Paolini, A. Pasquarello, L. Paulatto, C. Sbraccia, S. Scandolo, G. Sclauzero, A. P. Seitsonen, A. Smogunov, P. Umari and R. M. Wentzcovitch, *J. Phys.: Condens. Matter*, 2009, **21**, 395502.

72 D. F. Shanno, *Math. Comput.*, 1970, **24**, 647–656.

73 D. Goldfarb, *Math. Comput.*, 1970, **24**, 23–26.

74 R. Fletcher, *Comput. J.*, 1970, **13**, 317–322.

75 C. G. Broyden, *IMA J. Appl. Math.*, 1970, **6**, 76–90.

76 A. Dal Corso, *Comput. Mater. Sci.*, 2014, **95**, 337–350.

77 J. P. Perdew, A. Ruzsinszky, G. I. Csonka, O. A. Vydrov, G. E. Scuseria, L. A. Constantin, X. Zhou and K. Burke, *Phys. Rev. Lett.*, 2008, **100**, 136406.

78 A. Benassi, *PWSCF 's epsilon.x user's manual*, **https://www.researchgate.net/profile/Nowzar-Soltani/post/Can_anyone_answer_this_question_on_the_optical_properties_of_the_Epsilon_calculations/attachment/59d623046cda7b8083a1d75b/AS%3A310495943299072%401451039409313/download/eps_man.pdf**.

79 A. Jain, S. P. Ong, G. Hautier, W. Chen, W. D. Richards, S. Dacek, S. Cholia, D. Gunter, D. Skinner, G. Ceder and K. A. Persson, *APL Mater.*, 2013, **1**, 011002.

80 J. Hu, S. Stefanov, Y. Song, S. S. Omee, S.-Y. Louis, E. M. D. Siriwardane, Y. Zhao and L. Wei, *npj Comput. Mater.*, 2022, **8**, 65.

81 L. Ward, A. Agrawal, A. Choudhary and C. Wolverton, *npj Comput. Mater.*, 2016, **2**, 16028.

82 K. Li, Y. Li and D. Xue, *Funct. Mater. Lett.*, 2011, **04**, 217–219.

83 A.-S. Om Kumar, V. Shukla and S. K. Srivastava, *J. Sci.: Adv. Mater. Devices*, 2019, **4**, 158–162.

84 K. Li, C. Kang and D. Xue, *Mater. Res. Bull.*, 2012, **47**, 2902–2905.

85 M. Rahm, P. Erhart and R. Cammi, *Chem. Sci.*, 2021, **12**, 2397–2403.

86 S. Bandyopadhyay and I. Dasgupta, *Phys. Rev. B*, 2021, **103**, 014105.

87 T. Ahmad, K. Jindal, M. Tomar and P. K. Jha, *Phys. Chem. Chem. Phys.*, 2023, **25**, 5857–5868.

88 S. Ghosh and J. Chowdhury, *Phase Transitions*, 2023, **96**, 446–463.

89 R. Phillips, *Crystals, Defects and Microstructures: Modeling across Scales*, Cambridge University Press, Cambridge, 2001.

90 B. Grabowski, P. Söderlind, T. Hickel and J. Neugebauer, *Phys. Rev. B: Condens. Matter Mater. Phys.*, 2011, **84**, 214107.

91 B. Grabowski, T. Hickel and J. Neugebauer, *Phys. Status Solidi B*, 2011, **248**, 1295–1308.

92 J. Kangsabanik, M. K. Svendsen, A. Taghizadeh, A. Crovetto and K. S. Thygesen, *J. Am. Chem. Soc.*, 2022, **144**, 19872–19883.

93 S. Halder, R. A. Kumar, R. Maity and T. P. Sinha, *Ceram. Int.*, 2023, **49**, 8634–8645.

94 O. I. Malyi and C. M. Acosta, *J. Phys. Chem. C*, 2020, **124**, 14432–14438.

95 R. Anbarasan, J. K. Sundar, M. Srinivasan and P. Ramasamy, *Comput. Condens. Matter*, 2021, **28**, e00581.

96 Y. Kang, Y. Youn, S. Han, J. Park and C.-S. Oh, *Chem. Mater.*, 2019, **31**, 4072–4080.

97 R. R. Pela, M. Marques and L. K. Teles, *J. Phys.: Condens. Matter*, 2015, **27**, 505502.

98 J. Heyd, G. E. Scuseria and M. Ernzerhof, *J. Chem. Phys.*, 2003, **118**, 8207–8215.

99 P. Borlido, J. Schmidt, A. W. Huran, F. Tran, M. A. L. Marques and S. Botti, *npj Comput. Mater.*, 2020, **6**, 96.

100 S. Matsuishi, D. Iwasaki and H. Hosono, *J. Solid State Chem.*, 2022, **315**, 123508.

101 P. Bhumla, D. Gill, S. Sheoran and S. Bhattacharya, *J. Phys. Chem. Lett.*, 2021, **12**, 9539–9546.

102 K. Demmouche and J. Coutinho, *Int. J. Mod. Phys. B*, 2018, **32**, 1850328.

103 Y. Kang, G. Kang, H.-H. Nahm, S.-H. Cho, Y. S. Park and S. Han, *Phys. Rev. B: Condens. Matter Mater. Phys.*, 2014, **89**, 165130.

104 M. I. Naher and S. H. Naqib, *Sci. Rep.*, 2021, **11**, 5592.

105 R. Reisfeld, *Opt. Mater.*, 2010, **32**, 850–856.

106 L. Su, X. Fan, T. Yin, H. Wang, Y. Li, F. Liu, J. Li, H. Zhang and H. Xie, *Adv. Opt. Mater.*, 2020, **8**, 1900978.